Relativistic few-body systems: from B decays to bound states in Minkowski space

Facoltà di Scienze Matematiche, Fisiche e Naturali

Dottorato di Ricerca in Fisica – XXXII Ciclo

Candidate

Jorge Henrique de Alvarenga Nogueira
ID number 1781873

Thesis Advisors

Dr. Giovanni Salmè (INFN, Roma)
Prof. Tobias Frederico (ITA/Brazil)

July 2019

Thesis defended on November 6, 2019
in front of a Board of Examiners composed by:

Prof. Brett Vern Carlson (ITA)

Prof. Wayne Leonardo Silva de Paula (ITA)

Prof. Marco Nardecchia (Rome U. "La Sapienza")

Prof. Mauro Papinutto (Rome U. "La Sapienza")

A minha família é a base de tudo e possibilitou toda e qualquer conquista que eu tenha alcançado. Graças à minha mãe, uma guerreira que enfrentou todas as dificuldades para criar os seus filhos. Ao meu pai, que infelizmente não está mais entre nós, mas nos guiou com muito amor, doçura e sabedoria. À minha linda irmã, com sua encantadora meiguice e admirável força de vontade. Ao meu cativante irmão, que muito me ensina com seu lídimo ponto de vista. Agradeço aos meus tios, Rosane e Carlos, que contribuíram de várias maneiras. Dedico também à todos os familiares, amigos e colegas que fizeram parte dessa jornada.

Abstract

Few-body degrees of freedom (dof) have their hallmark in hadron and nuclear physics, even before quantum chromodynamics was established, and still today are used to guide phenomenological interpretations of hadronic observables. The aim of the thesis is the attempt to develop a relativistic framework where the aforementioned dof can be phenomenologically investigated, still retaining as many general principles as possible and living in Minkowski space. An appealing motivation for elaborating such an effort is given by the challenging analysis of the charge-parity violation (CPV) in the three-body decay of the B meson, as illustrated in the thesis. In particular, the phenomenological study of CPV, using only hadronic degrees of freedom, is carefully carried out in the B decay, obtaining the remarkable outcomes of (i) an explicitly CPT invariance formalism for addressing final state interactions, which satisfactorily describes the CPV in the three-body phase space of coupled decay channels; and (ii) a simple method which predicts a substantial CPV suppression in two-body decays involving pseudoscalar and vector mesons, that in turn is a quantitative outcome to be investigated in forthcoming experiments planned at the several B-factories all over the world. The necessity of representing the meson vertexes in the quark-level diagrams paved the way to the study of the Bethe-Salpeter equation for bound states. A non-perturbative framework was developed to deal with two- and three-body bound states. Firstly, the two-boson equation is solved in Minkowski space by means of the Nakanishi integral representation and light-front projection, and then the effect of truncating the interaction kernel of the Bethe-Salpeter equation is explored, assessing the impact of the cross-ladder diagrams on several dynamical observables. The evaluation of their effect when color dof are present has been also performed, obtaining a clear support for the rainbow-ladder truncation widely adopted in the investigation of strongly interacting systems. Furthermore, the three-boson Faddeev-Bethe-Salpeter equation with zero-range interaction is solved, for the first time, both in Euclidean and Minkowski spaces, without relying on a three-dimensional reduction or any ansatz for representing the Bethe-Salpeter amplitude. The variation of two-body scattering length enables to find a Borromean ground state, missed in previous relativistic calculations. Finally, a substantial improvement, has been achieved by including spin dof. It has been investigated a system composed by a fermion and a scalar particle, as well as a fermion-antifermion bound state. Applications to several dynamical observables are presented and discussed, in view of the possible extension of the relativistic framework, whose development has contributions from this thesis, to the analysis of decays where the relativistic effects can play a relevant role, as it happens in the CPV three-body decays of the B-meson.

Sommario

I gradi di libertà dei sistemi a pochi corpi mostrano il loro segno caratteristico sia in fisica adronica che nucleare, ben prima dell'avvento della Cromodinamica Quantistica, ed ancora oggi sono utilizzati per guidare l'interpretazione fenomenologica degli osservabili adronici. Lo scopo della tesi è il tentativo di sviluppare un approccio relativistico attraverso cui i menzionati gradi di libertà possano essere indagati fenomenologicamente, verificando il maggior numero possibile di principi generali ed utilizzando lo spazio di Minkowski. Una motivazione interessante per elaborare tale sforzo è data dall' analisi della violazione della invarianza di CP nel decadimento a tre corpi del mesone B, che risulta essere arduo e stimolante allo stesso tempo, come illustrato nella tesi In particolare, lo studio fenomenologico dettagliato della violazione di CP nei decadimenti del mesone B, utilizzando solo i gradi di libertà adronica, ha permesso di ottenere notevoli risultati, tra cui: 1) un formalismo, che contiene esplicitamente il vincolo dettato dalla invarianza di CPT, e permette sia di affrontare lo studio delle interazioni di stato finale sia di descrivere in modo soddisfacente la violazione di CP, nello spazio di fase dei canali di decadimento accoppiati; 2) un metodo semplice che predice una sostanziale soppressione della violazione CP nei decadimenti a due corpi che coinvolgono mesoni pseudoscalari e vettoriali, e che a sua volta fornisce una predizione da indagare quantitativamente nei prossimi esperimenti pianificati nelle diverse B-factory, presenti nel mondo. La necessità di descrivere i vertici mesonici nei diagrammi a livello di quark ha aperto la strada allo studio dell'equazione Bethe-Salpeter per gli stati legati. È stato sviluppato un approccio non-perturbativo per trattare gli stati legati a due e tre corpi. In primo luogo, l'equazione a due bosoni è stata risolta nello spazio di Minkowski per mezzo della rappresentazione integrale di Nakanishi e della proiezione sul fronte-luce, e in seguito è stato esplorato l'effetto di troncamento dell'operatore di interazione presente nell'equazione integrale di Bethe-Salpeter, stimando l'impatto dei diagrammi cross-ladder su diversi osservabili dinamici. È stato effettuato anche un attento esame del loro effetto in presenza di gradi di libertà di colore, ottenendo una chiara evidenza in favore del troncamento che viene utilizzato nella così detta approssimazione rainbow-ladder, ampiamente adottata nello studio di sistemi fortemente interagenti. Inoltre, l'equazione di Faddeev-Bethe-Salpeter con interazione puntiforme è stata risolta, per la prima volta, sia nello spazio Euclideo che in quello di Minkowski, senza basarsi su una riduzione tridimensionale o su una qualsiasi Ansatz per l'ampiezza di Bethe-Salpeter. Lo studio di come varia la lunghezza di diffusione di due corpi ha permesso di trovare uno stato fondamentale borromeano, che i precedenti calcoli relativistici non avevano individuato. Infine, un sostanziale miglioramento è stato ottenuto includendo i gradi di libertà di spin. È stato studiato sia un sistema composto da un fermione e da una particella scalare, sia uno stato legato fermione-antifermione. Nella tesi vengono presentate e discusse applicazioni che coinvolgono diversi osservabili dinamici, in vista della possibile estensione del nostro approccio relativistico all'analisi dei decadimenti dove gli effetti relativistici possono giocare un ruolo rilevante, come accade p.e. nei decadimenti del mesone B a tre corpi che violano l'invarianza di CP.

Acknowledgments

I am indebted to the many people that directly or indirectly influenced on my journey and learning through all the years of study and research that lead to this thesis. Following my memories back, I will try to chronologically mention some important people that marked my journey.

Since my first contact with Prof. Tobias Frederico, just after the admission exams for São Paulo and Rio de Janeiro graduation programs, I was already impressed with his facility on going through different physical concepts with a coherent thinking and with his admirable intuition for interpreting physical phenomena. After these years of intense interaction, I can tell that having him as one of my PhD supervisors was a determining factor to my scientific grow. He gave me all the possibilities to learn, to discover and to challenge myself. He believed in me in every situation, from giving talks in notorious conferences to starting new collaborations in different subjects. Always supportive and extremely helpful, his guidance through all the challenges I had to face during the development of my research deserves my wholehearted gratitude. I am extremely thankful to Prof. Frederico for his supervision.

In practice, I had some other supervisors during my thesis that deserve to be mentioned. Firstly, Prof. Ignacio Bediaga, who I have closely collaborated with and that resulted in the first chapter of this thesis, as well as in other five publications. I also thank Prof. Odilon Lourenço, a very helpful, hard-working and pleasant person for our collaborative work. Furthermore, I thank Patrícia Magalhães, who I had the pleasure to work with in what was presented in Sec. 2.2.

I am thankful to Vitor Gigante for accepting teaching me about the Bethe-Salpeter equation and the Nakanishi representation when I was making my first steps on the field. He believed that I could contribute and accepted my proposal for collaborating when I barely had knowledge in the subject. Our interaction went beyond research and I am glad to have made such a great friend. We, together with Cristian Gutiérrez and Emanuel Ydrefors, have spent a great and intense period collaborating at "Sala 1630" of ITA. Our group, which also included Prof. Vladimir Karmanov, who was visiting ITA at the time, had a fruitful research. That was possible thanks to the tireless efforts of all those involved, working from Monday to Monday and trying our best to learn and produce high-quality research.

I would like to stress my gratitude to Emanuel Ydrefors, most likely my closest collaborator during the PhD, for his great contribution to the fertile work presented here and to the close friendship that we have developed along these years.

I thank to Prof. Vladimir Karmanov, for the rewarding collaboration and his willingness to teach. He acted as an informal supervisor in a considerable part of the work that resulted in this thesis.

I would like to specially thank Dr. Giovanni Salmè, for being my scientific supervisor at La Sapienza and for close guidance through the many challenges that I had to surmount during my studies in Rome. Among other people, I highlight Valerio Gherardi and Cédric Mezrag, for our collaboration and friendship during my period in Rome. The enjoyable time I had in Europe contributed significantly to change the way I think. I had numerous personal experiences, on and off the academia, that shaped my character and taught me about defining goals and choosing priorities.

Contents

List of publications

- J. H. Alvarenga Nogueira, I. Bediaga, A. B. R. Cavalvante, T. Frederico and O. Lourenço, *CP violation: Dalitz interference, CPT and final state interactions*, Phys. Rev. D **92**, 054010 (2015). arXiv:1506.08332 [hep-ph];

- J. H. Alvarenga Nogueira, I. Bediaga, T. Frederico, P. Magalhães and J. Molina Rodriguez, *Suppressed $B \to PV$ CP asymmetry: CPT constraint*, Phys. Rev. D **94**, 054028 (2016). arXiv:1607.03939 [hep-ph];

- J. H. Alvarenga Nogueira, T. Frederico and O. Lourenço, *$B^+ \to K^-\pi^+\pi^+$: three-body final state interactions and $K\pi$ isospin states*, Few Body Syst. **58** no.2, 98 (2017). arXiv:1609.01568 [hep-ph];

- V. Gigante, J. H. Alvarenga Nogueira, E. Ydrefors, C. Gutierrez, V. A. Karmanov and T. Frederico, *Bound state structure in Minkowski space: beyond the ladder approximation*, Phys.Rev. D **95** (2017) 056012. arXiv:1611.03773 [hep-ph];

- E. Ydrefors, J. H. Alvarenga Nogueira, V. Gigante, T. Frederico and V. A. Karmanov, *Three-body bound states with zero-range interaction in the Bethe-Salpeter approach*, Phys.Lett. B **770** 131-137 (2017). arXiv:1703.07981 [nucl-th];

- J. H. Alvarenga Nogueira, Chueng-Ryong Ji, E. Ydrefors and T. Frederico, *Color-suppression of non-planar diagrams in bosonic bound states*, Phys. Lett. B **777**, 207-211 (2018). arXiv:1710.04398 [hep-th];

- E. Ydrefors, J. H. Alvarenga Nogueira, V. A. Karmanov, T. Frederico, *Solving the three-body bound-state Bethe-Salpeter equation in Minkowski space*, Phys. Lett. B **791** 276-280 (2019);

- J. H. Alvarenga Nogueira, V. Gherardi, T. Frederico, G. Salmè, D. Colasante and E. Pace, *Solving the Bethe-Salpeter equation in Minkowski space for a fermion-scalar system*, Phys. Rev. D **100**, 016021 (2019). arXiv: 1907.03079 [hep-ph];

- J.H. Alvarenga Nogueira, I. Bediaga, A. B. R. Cavalvante, T. Frederico and O. Lourenço, Charmless Three-Body B-decays: final state interaction and CP violation. Proceedings of the XIII International Workshop on Hadron Physics – XIII Hadron Physics. J. Phys.: Conf. Ser. **706**, 042010 (2016);

- T. Frederico, J. H. Alvarenga Nogueira, I. Bediaga, A. B. R. Cavalvante and O. Lourenço, CPT, FINAL STATE INTERACTION AND CP VIOLATION. "Summary of the 2015 LHCb workshop on multi-body decays of D and B mesons", arXiv:1605.03889 (2016);

- J. H. Alvarenga Nogueira, T. Frederico, I. Bediaga and P. C. Magalhães *CP Violation in the three-body $B^{\pm}$ phase-space*, Proceedings of the 38th International Conference on High Energy Physics. PoS ICHEP2016, 635 (2016);

- V. Gigante, C. Gutierrez, J. H. Alvarenga Nogueira and E. Ydrefors, *A short review about the Bethe-Salpeter equation and the solution for the $\chi^2\phi$ model in Minkowski space*, Proceedings of the 38th International Conference on High Energy Physics. PoS ICHEP2016, 1107 (2017);

- V. Gigante, J. H. Alvarenga Nogueira, E. Ydrefors and C. Gutierrez, *Study of the bound-state Bethe-Salpeter equation in 2+1 Minkowski space*, Proceedings of the 7th International Workshop on Astronomy and Relativistic Astrophysics. Int. J. Mod. Phys. Conf. Ser. 45, 1760055 (2017). arXiv:1703.07808 [hep-ph];

- J. H. Alvarenga Nogueira, E. Ydrefors, T. Frederico, G. Salmè, *Relativistic Studies of Few-Body Systems Using the Bethe–Salpeter Approach*, Few Body Syst. **59** (2018) no.5, 94;

- E. Ydrefors, J. H. Alvarenga Nogueira, V. A. Karmanov and T. Frederico, *Bethe-Salpeter approach to three-body bound states with zero-range interaction.* Proceedings of the XXII International Conference on Few-Body Problems in Physics, submitted to Few Body Systems (2018);

- A. R. Castro, E. Ydrefors, W. de Paula, T. Frederico, J. H. Alvarenga Nogueira, P. Maris, *The Bethe-Salpeter approach to bound states: from Euclidean to Minkowski space.* Proceeding of the XLI Brazilian Meeting on Nuclear Physics, to appear in Journal of Physics: Conference Series (JPCS) (2019), arXiv:1901.04266 [hep-ph].

- A. R. Castro, E. Ydrefors, W. de Paula, T. Frederico, J. H. Alvarenga Nogueira, P. Maris, *Connecting the Bethe-Salpeter amplitude, the Nakanishi integral representation, and the valence light-front wave function*, in preparation.

- J. H. Alvarenga Nogueira, T. Frederico, E. Pace, G. Salmè and E. Ydrefors, in preparation (2019).

- W. de Paula, J. H. Alvarenga Nogueira, E. Ydrefors, C. Mezrag, H. Moutarde, G. Salmè and T. Frederico, in preparation (2019).

- E. Ydrefors J. H. Alvarenga Nogueira, V. A. Karmanov, and T. Frederico, in preparation (2019).

Chapter 1

Introduction

The benchmark to investigate elementary particles and their interactions is the Standard Model (SM) of particle physics [1]. The outstanding knowledge enclosed in such a fundamental theory has been the result of unprecedented efforts from both theoretical and experimental sides. Quantum field theory defines the theoretical framework, giving the guidelines to construct physical models for understanding experimental data. In the last decades several laboratories and research groups have been settled around the world aiming for exploring the hadron structure and phenomena involving fundamental particles. Undoubtedly the European Organization for Nuclear Research (CERN) is one of the most important experimental research centers, comprising the largest and most powerful particle collider on Earth, the Large Hadron Collider (LHC) [2]. Seven detectors are there settled intending to test the Standard Model and its extensions. Among those detectors, the one known as LHCb is a specialized b-physics experiment, particularly in charge-parity (CP) violation in interactions of heavy particles containing a bottom quark, known as B mesons. The noteworthy question under investigation is the imbalance between matter and antimatter observed in the Universe. The CP symmetry breaking mechanism is described within the Standard Model through the unitary matrix introduced by Cabibbo, Kobayashi and Maskawa, the CKM matrix [3]. The CKM matrix provides the strength of the quark-flavor change by means of weak interactions and can be parameterized according to the number of quark generations. For the SM the quark mixing matrix requires 4 independent parameters to be described, as there are $N = 3$ quark generations, of which three are called quark mixing angles and one is the CP-violating complex phase [4]. This complex phase is expected to include the observed asymmetry in the Dalitz plot[1] of three-body charged B meson decays, studied by the LHCb collaboration.

In 1964, the possibility of CP symmetry breaking had its first evidence for neutral kaons oscillating into their antiparticles, in a work that honoured Val Logsdon Fitch and James Cronin with the Nobel prize [5]. The CP symmetry breaking puzzled the particle physics community back then, but later brought to the conclusion that a third operation, time reversal T, would give a fundamental symmetry of physical laws, namely the conservation of CPT symmetry. The asymmetry seen in 1964 comes from the fact that the $K^0 - \bar{K}^0$ oscillation does not happen with the same probability in

---

[1]The Dalitz plot is a visual representation of the phase space of a three body decay.

both directions. The leading contributions to the neutral kaon oscillation amplitude comes from the box diagrams involving the $W^\pm$ bosons. On the other hand, the first evidence for CP noninvariance in charged systems was pointed out by Bander, Silverman and Soni [6] (so-called BSS model), being based on the interference between the tree and penguin Feynman quark-level diagrams. Although this is the main mechanism used for performing calculations of CP asymmetry in B meson decays, interferences at the hadronic level can contribute considerably to the asymmetry distribution. One possibility, extensively explored in the literature [7, 8, 9, 10, 11], is the interference between different intermediate states that occupy the same kinematical region and have the same final states.

Another alternative involves inelastic final state rescattering, which couples different decay channels and distribute CP violation (CPV) among them [12, 13, 14, 15, 16]. Therefore, besides the quark-level mechanism manifested by means of the BSS model, it becomes necessary to extend the description by considering final state interactions among the mesons in the final state of the decay process. The latter is also called "compound" contribution to CP violation [17]. With the aforementioned ideas in mind, Wolfenstein proposed, in 1991, a CP violation formalism based on unitarity and CPT constraint, including the effect from final state interactions [12]. CPT invariance in this context means the equality between particle and its charge conjugate lifetimes, and, therefore, when partial decay widths of charge conjugate channels are different, some other decay channels must have an equal total amount of CPV, but with opposite sign. In this way the sum of the partial decay widths results in identical total widths for the particle and its antiparticle, ensuring that CPT is not violated. This constraint, although very fundamental, is not explicitly taken into account by the majority of the CPV calculations in the literature, under the argument that multiple decay channels, with various numbers of final mesons, would need to be considered to verify the CPT constraint for a given decaying particle.

Based on Wolfenstein's approach, a phenomenological model was developed in Ref. [16] to take into account the effect from final state interactions by including the $\pi\pi \to KK$ inelastic scattering amplitude. The limited experimental data available back then was analyzed for the decays $B^\pm \to K^\pm K^+ K^-$ and $B^\pm \to K^\pm \pi^+ \pi^-$, as the two channels have a significant part of their CP distribution located in an area where hadronic channels are strongly coupled. The dependence on the quark-level tree and penguin amplitudes, responsible for the so-called short distance contribution to CPV, was reduced to a final overall normalization to be fixed by the experimental data. Despite of the simplified model, a remarkable evidence for the connection between the CPV in the two considered channels was seen, supporting the statement that CPT is a practical constraint that must be explicitly taken into account in every calculation. It is worth to mention that the approach proposed in Ref. [16] was developed for a three-body decay amplitude where two particles interact while the third one is free.

The PhD thesis research started by exploring the CP violation in the B meson decay into three light mesons aiming to further develop the model of Ref. [16] by encompassing more of the dynamics observed through the experimental data. For this purpose, the studied decays were the charged channels $\pi^\pm \pi^+ \pi^-$, $\pi^\pm K^+ K^-$, $K^\pm K^+ K^-$ and $K^\pm \pi^+ \pi^-$ of the $B^\pm$ meson. The CPV in those channels was measured with great accuracy for their entire phase spaces by LHCb collaboration [18]. The

three types of interference mechanisms mainly known as CPV sources in charmless three-body charged B decays are: 1) the BSS model at quark-gluon level; 2) the interference between two final states with different weak phases coupled by final state interactions, which is constrained by CPT invariance [12]; and 3) the interference between resonances that share the same phase space region [7, 8, 9, 10, 19]. In the PhD research, the main two-body resonant structures below the KK threshold seen experimentally were included, namely through the $M\rho$ and $Mf_0(980)$ channels ($M = K, \pi$), and keeping the final state interaction coupling in the $\pi\pi$ and KK channels. The partonic decay amplitudes[2] are represented with a slightly more elaborated parametrization than in Ref. [16], but are still far from representing their full complexity. All the possible interferences are included in the amplitude, with each term of the CPV formula having an overall parameter to be fixed by fitting the experimental data. The whole region below two-body invariant masses of 1.6 GeV is taken into account [20], exploring beyond the phase space area previously considered. Another important advance made in this thesis is the analysis of the two extra channels $\pi^{\pm}\pi^{+}\pi^{-}$ and $K^{\pm}K^{+}\pi^{-}$, with different sources of CPV in their phase space consistently explained within the model [20, 21, 22, 23]. Moreover, it was published in Ref. [24] a remarkable consequence of the CPT invariant model: the suppression of the CPV in two-body B decays involving a pseudoscalar P meson and a vector V one. A simple experimental method was then proposed for extracting the CPV in the $B \to PV$ decays from the three-body phase space, without resorting to a full amplitude analysis. By performing toy Monte Carlo simulations, it was shown that the method indeed corroborates the aforementioned suppression.

The CPV model discussed so far only includes two-body interactions in the three-body decay amplitude and developing a framework to investigate the rescattering involving all the final state mesons is essential. For that reason, the decay amplitude was then formulated in a fully three-body context [25], based on the Faddeev decomposition of the three-body inhomogeneous Bethe-Salpeter equation (BSE) [26] on the light-front (LF) [27, 28]. The decay amplitude of the $B^{+} \to K^{-}\pi^{+}\pi^{+}$ process is built and the integral equation is perturbatively solved, with the $K\pi$ T-matrix parametrization fixed through the experimental scattering data. This model still needs to be consistently merged with CPV model of Ref. [20], namely by keeping CPT invariance. Nevertheless, the robust three-body framework in which the model is based has several branches to be explored, presenting a promising approach for phenomenological applications.

A fundamental limitation of the above mentioned approaches is the lack of a proper partonic description. As discussed, the decay amplitudes involving quarks and gluons as degrees of freedom (dof) were merely parametrized, with its relevant information being fitted to experimental data, without any microscopic characterization of the partonic process. For describing fully the content of the decay amplitudes, it is necessary to also evaluate the microscopic decay amplitudes, where the CKM weak phase resides, by taking into account the quark and gluon degrees of freedom. These partonic amplitudes govern the formation of the mesons in the decay channel, including possible intermediate resonances, therefore call for the knowledge of mesonic bound state amplitudes. Appropriately addressing these amplitudes in

---

[2]The partonic amplitudes are the quark-level diagrams that enter through the BSS mechanism.

an already complicated formalism is highly non-trivial, since it requires a whole new path of complications in the non-perturbative context.

In quantum field theory the covariant homogeneous Bethe-Salpeter equation (BSE) [26, 29] is one of the most well-accepted tools to deal with bound states in the non-perturbative domain. This is a singular four-dimensional integral equation for bound states in Minkowski space. For several decades after its proposal, in 1951, the main practice to avoid its singular nature was relying on the Wick-rotation ($k_0 \rightarrow ik_4$) [30], leading to an equation in Euclidean space. Considering that the dynamical observables are defined in Minkowski space, one needs to explicitly take into account the contributions that arise from poles/cuts (branch points) in the complex-momentum plane. This structure is challenging to be taken into account in the leading approaches available in the literature, e.g. lattice quantum chromodynamics (QCD) and Dyson-Schwinger equation (DSE) approach [31], as in most cases they have Euclidean-based formulations. As an illustration of such sensitivity, within the Bethe-Salpeter (BS) approach [32] it was shown that the elastic electromagnetic form factor can vary while comparing calculations with the BS amplitude computed in Minkowski or Euclidean spaces, if the analytic structure is not properly handled. Therefore, further efforts towards solving the BSE directly in Minkowski space are valuable to better understand those formal steps while computing physical observables. This is the main purpose of the rest of the thesis.

The following parts of the thesis were devoted to explore solutions of the homogeneous BSE in order to build a feasible framework to phenomenologically investigate hadron observables, which can be used for more realistic descriptions of CPV and other hadronic phenomena. Needless to say that, given the complexity of the problem outlined above, the following research is part of a big project with the long-term goal of dealing with non-perturbative problems fully in Minkowski space. This ongoing development will enable to study realistic few-body systems, such as hadrons, nucleons and light nuclei, in a fully relativistic framework and with direct access to any observable. Historically, the first case solved within the approach that will be adopted here was the $\chi\phi^2$ model, i.e a two-scalar system interacting through a massive scalar exchange in the ladder approximation, overcoming the limitation of the honored Wick-Cutkowsky model [30, 33], that managed to solve the BSE analytically but for a massless exchange. For getting actual solutions for the scalar system, Kusaka and Williams [34] numerically applied the technique based on the so-called Nakanishi Integral Representation (NIR) [35] for the BS amplitude. The NIR can be seen as a spectral representation, as in this case the spectral function, called the Nakanishi weight function, is an unknown quantity to be found numerically. The method combines the analysis of the n-leg transition amplitude carried out by Nakanishi [35] within a diagrammatic framework and the freedom offered by the unknown weight function. The diagrammatic analysis determines an explicit structure in the complex plane and lead to a real weight function, which depends upon a set of compact and non compact variables. In the last decade, the method was made more effective by exploiting the light-front (LF) framework [36], what allowed to develop a more robust approach [37, 38, 39] and represented a breakthrough in the field. Particularly, appealing for the physical intuition, it is the use of the so-called LF projection, that corresponds to the integration over the external momentum $k^- = k^0 - k^3$ component of the BS amplitude, and eliminates the LF relative time

between the two particles. Thereby, the four-dimensional singular equation becomes a three-dimensional non-singular one, as the LF projection amounts in practice to Cauchy integrations, hence being able to take into account the involved singularities that NIR makes explicit in the BS amplitude. Besides simplifying the algebraic manipulations to derive an integral equation for the weight function, the integration over k^- of the BS amplitude also gives direct access the valence LF wave function.

Although extremely challenging, this approach leads to phenomenological covariant models to explore not only the spectra, but also the dynamics inside hadrons. The first question addressed in the thesis is the relevance of the truncation of the BSE 4D interaction kernel [40, 41, 42]. In particular, for a two-scalar system, it is shown that the cross-ladder kernel has a sizable effect on dynamical observables, e.g the valence LF wave function and the electromagnetic form factor. Moreover, the asymptotic behavior of the form factor is analyzed in detail both analytically and numerically. In the analysis it is included the crossed contribution beyond the impulse approximation of the form factor, necessary to keep the formulation consistent with the higher order diagram of the interaction kernel. The notable impact seen by the inclusion of only the second order of the interaction kernel indicates that the BSE should be essentially reformulated in order to give reasonable results when applied to QED without taking into account the whole set of irreducible diagrams contributing to the kernel. The question is whether the same persists within a theory with different degrees of freedom, like for dealing with hadron physics. To accomplish this, in the thesis the study has been extended to a scalar QCD model, where the color factors appear differently for each diagram of the interaction kernel [43, 44]. It is seen that the inclusion of the color degree of freedom produces a remarkable suppression of the cross-ladder diagrams even if the number of colors is fixed at $N_c = 3$. This finding is extremely important for further developments of phenomenological QCD models, since it supports the ladder truncation of the BSE as a viable tool for studying hadron dynamics.

A further step is to generalize the approach to include more particles in the bound state. A first attempt to explore the dynamics of a three-body system, within the BSE framework, has been therefore carried out [45]. A three-boson system, interacting through a zero-range interaction, is described by means of: (i) the Wick-rotated BSE, i.e in Euclidean space; (ii) and the BSE projected onto the LF hyperplane, in Minkowski space but truncated at the valence component. Although the approaches are defined in different spaces, there are quantities that can be compared, e.g. binding energies and transverse amplitudes. In particular, it is shown an effect from the higher-Fock components remarkably sizable for three-body systems, as effective three-body forces also take place. Another notable finding is that the Thomas collapse, a well-known phenomena in the non-relativistic context which makes scale invariant equations not bounded from below, disappears in the spectrum. This is related to the different nature of the relativistic dispersion relation, which already plays the role of a regulator. However, it is still noticed that, although a finite value is found, it does not correspond to a physical ground state as its squared mass is negative.

Although interesting conclusions could be found from the above-mentioned studies, the three-body BSE still needs to be solved fully in Minkowski space with access to the content beyond the valence component, as done in the two-body

case. Recalling that, the investigation of the zero-range three-body BSE is fully done in Minkowski space, now without relying on NIR ansatz or LF projection but by integrating directly the singularities [46]. It is desirable to extend the approach based on the NIR and LF projection also to this case. Indeed, the direct integration method for integrating the singularities, developed for two-scalar scattering and bound states in the ladder approximation in Ref. [47], could be a possible alternative to the NIR plus LF projection, at least when the spin dof are not considered. Furthermore, although a considerable part of the singularities is analytically tractable, the final equation still has singularities to be evaluated, but with a notable numerical effort. However, the solution has been obtained and the comparison of the suitable observables with the corresponding ones evaluated from the Wick-rotated equation has been performed. The comparison confirms for both binding energy and transverse amplitude that the solutions are correct, despite the challenging numerical implementation. Due to the complexity of the method, generalizing for other systems would make things barely unsolvable. For this reason, an ansatz for the integral representation supplemented by uniqueness conjecture, following what was developed in Ref. [38], is an ongoing research that will also be presented in this thesis. The NIR (or a similar integral representation) together with uniqueness or with the LF framework (both in its standard form [27] or in the explicitly covariant formulation [28]) seems quite appealing, given the peculiar feature of plainly exhibiting the analytic structure of the BSE. Indeed, one expects that this method will require less effort to achieve the numerical stability.

In order to deal with spin dof and gain physical intuition on the three-body case, desirable for describing mock baryons through an effective two-body quark-diquark model, the NIR together with LF projection has been applied to develop a fully covariant framework in Minkowski space for a scalar-fermion bound state, interacting through one-boson (scalar or vector) exchange [48]. This solution can be interesting for effectively modeling a three-body system, eventually elaborating a quark-diquark description of baryons. This is an important step in the direction of describing a three independent quark system interacting through a finite-range interaction. The observables obtained for this system would, inter alia, give an interesting input for representing baryonic states present in some decay channels of the B meson which present CP violation, e.g. $B^+ \rightarrow p\bar{p}K^+$ [1]. As it is presented in what follows, the new idiosyncrasies of the problem bring new challenging aspects. For instance, extremely interesting phenomena, such as the consequence of the scale invariance property of the integral equation with the vector exchange kernel, is seen in the observables.

The closing point of the research regards the solution of the BSE for a fermion-antifermion system interacting through a massive vector boson [49, 50, 51]. The first phenomenological application of the actual solutions of the BSE within this approach is made in an attempt to extract observables for a mock pion [51], like the electromagnetic form factor and the Generalized Parton Distributions (GPDs). Although the approach still need to be further developed for describing a realistic QCD bound state, this is the first step for building an environment where the evaluation of the partonic amplitudes with a proper representation of the involved mesons can be carried out. Indeed, such development is extremely important for evaluating the partonic decay amplitudes that enter in the CPV model since this

model for the pion BS amplitude can straightforwardly applied to compute the $B^{\pm} \to \pi^{\pm}\pi^{+}\pi^{-}$, by considering the tree and penguin Feynman diagrams with the BS amplitude as an input for the pion vertexes.

The thesis is organized as follows. Chap. 2 is dedicated to the study of CP violation and final state interactions in B meson decays. The BSE for bosonic two-body systems is then investigated in Chap. 3. In Chap. 4, the three-boson system with zero-range interaction is extensively explored. The boson-fermion bound state is considered in Chap. 5. Lastly, in Chap. 6, the fermion-antifermion BSE is solved and used to develop a model for a mock pion. Chap. 7 is devoted to the summary and conclusions. Further details are given in Appendices A to I.

Chapter 2

B-decays: CP violation and FSI

In 1928, the relativistic wave equation proposed by Dirac was the first successful description of massive spin-1/2 particles consistent with both quantum mechanics and special relativity. A remarkable consequence of Dirac's theory is the existence of anti-particles, objects with the same mass as standard particles but with conjugate quantum numbers, e.g. electrical charges. Although the prevailing cosmological model for the Universe expects that same amounts of matter and antimatter were generated in the early moments, this is not what is seen nowadays. Therefore, a key point in particle physics regards the imbalance between matter and antimatter. Knowing that laws of nature do not apply equally to matter and antimatter, the Russian physicist Andrey Sakharov proposed conditions for a preponderant amount of matter [52]. The conditions basically involve nonconservation of baryonic number and charge-parity (CP) symmetry violation. CP violation concentrates the main research efforts due to its role in particle physics. It was first discovered in 1964, linked to the fact that neutral kaons oscillate into their antiparticles with different probability of the transformation in the opposite direction [5]. Years later, "B-factory" experiments observed it also in charged decay processes. The asymmetry involving neutral kaons basically happens because the K^0 oscillation into its conjugate, $\bar{K}^0$, does not happen in the same rate of the oscillation from $\bar{K}^0$ to K^0. In charged decay processes instead, the number of times that a meson decays in a specific channel is different from the one involving the corresponding antimeson decaying into the CP conjugated final state (see [18] for the treatment for three-body B decays).

Particles and antiparticles have symmetry relations connecting their states. The charge conjugation operator C promotes the interchange of all internal quantum numbers, while parity P reverses the sign of the space coordinates, i.e $\vec{x} \to -\vec{x}$. Hence, under CP, a left-handed electron e_L^- would become a right-handed positron e_R^+. If a physical phenomena is not C- and/or P symmetric it means that CP violation is present and laws of Nature distinguish between particle and antiparticle. All fundamental interactions preserve exact CP-symmetry, except by weak interaction processes. Although firstly discovered in neutral K processes, the CP violating effects in B meson decays, only experimentally observed in recent years, are remarkable. Its importance is emphasized by the several B-factories spread around the globe.

An important question that arises while discussing CP violation (CPV) is what is the fundamental composed symmetry enclosing all physical interactions. To answer

that, a third spacetime operator comes into play, time-reversal transformation, $t \to -t$. CP combined with T generates a fundamental symmetry of Nature, preserved by any locally Lorentz-invariant quantum field theory with a Hermitian Hamiltonian. This argument is extremely general and encompasses every single physical process, being confirmed by every experimental observation made so far [1]. This gives a substantial constraint for exploring CP violation within the Standard Model. The question is whether this is a practical constraint, in the sense that it can be explicitly tested for every calculation, or if it involves countless channels, making the explicit verification of CPT in phenomenological calculations of CPV unfeasible.

The CPV dynamics within the SM is strictly related to the quark dynamics. Within the SM, Yukawa interactions with the Higgs condensate generate the masses and mixing of quarks, which are summarized by the following Lagrangian [1]

$$\mathcal{L}_Y = -\frac{v}{\sqrt{2}} \left(Y_{ij}^d \bar{Q}_{Li}^I \phi \, d_{Rj}^I + Y_{ij}^u \bar{Q}_{Li}^I \epsilon_{ij} \phi^* \, u_{Rj}^I + h.c. \right), \tag{2.1}$$

where the indexes $i, j = 1, 2, 3$ are fermion generation labels, $Y^{d,u}$ are the Yukawa coupling matrices, ϕ is the Higgs field, ϵ_{ij} is the Levi-Civita tensor, u_R^I and d_R^I are up- and down-type right-handed quark singlets and the superscript I indicates that the quark fields are conveyed in the interaction basis. The shorthand notation Q_{Li}^I represents a $SU(3)_C$ triplet left-handed $SU(2)_L$ doublet and can be explicitly written as

$$Q_{Li}^I = \begin{pmatrix} u_g^I & u_r^I & u_b^I \\ d_g^I & d_r^I & d_b^I \end{pmatrix}_i = \begin{pmatrix} u_g^I & u_r^I & u_b^I \\ d_g^I & d_r^I & d_b^I \end{pmatrix}, \begin{pmatrix} c_g^I & c_r^I & c_b^I \\ s_g^I & s_r^I & s_b^I \end{pmatrix}, \begin{pmatrix} t_g^I & t_r^I & t_b^I \\ b_g^I & b_r^I & b_b^I \end{pmatrix}. \tag{2.2}$$

The matrices $Y^{d,u}$ are responsible for the quark mixing, i.e the coupling between different quarks, and its diagonalized version $M^f = V_L^f Y^f V_R^f (v/\sqrt{2})$ $(f = u, d)$, also known as mass matrix, gives rise to the physical states. Consequently, u_{Lk} and d_{Lk} quarks couple to charged-current weak interactions, indicated by $W^\pm$, through the following couplings,

$$\frac{-g}{\sqrt{2}} (\bar{u}_L, \bar{c}_L, \bar{t}_L) \gamma^\mu W_\mu^+ V_{CKM} \begin{pmatrix} d_L \\ s_L \\ b_L \end{pmatrix} + h.c., \tag{2.3}$$

where the unitary 3×3 matrix is the Cabibbo-Kobayashi-Maskawa (CKM) [3]. It can be parametrized by three mixing angles and one complex CP-violating phase, and it reads

$$V_{CKM} \equiv V_L^u V_L^{d\dagger} = \begin{pmatrix} V_{ud} & V_{us} & V_{ub} \\ V_{cd} & V_{cs} & V_{cb} \\ V_{td} & V_{ts} & V_{tb} \end{pmatrix} \tag{2.4}$$

This is the only source of CP violation within SM and has been confirmed at B factories measuring CP asymmetry, always in agreement with the CKM phase as a CPV source. The LHCb experiment has been working to confirm measurements previously obtained by other ones, as Belle and BaBar, as well as exploring alternative systems also aiming at exploring possibilities beyond the CKM dynamics (see Ref. [53] for more information).

The focus of the first part of the PhD research has been the heavy meson B decay CP violation which is compatible with the SM. As it is well-known, to have more refined predictions of CPV within SM allows one to improve the ability in recognizing signatures of new physics.

The mechanism for CP violation in weak interactions within the Standard Model is given by a single complex phase of the CKM matrix. As illustrated by Fig. 2.1, quark transitions between members of the same quark generation are more probable, what makes the CKM matrix almost diagonal. A quite useful parametrization of
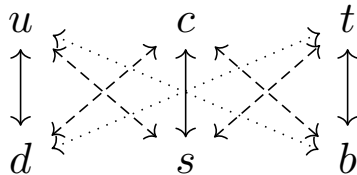
Figure 2.1. Strength of quark transitions among the different generations.

the quark mixing matrix, introduced by Wolfenstein [4], is obtained by expanding the matrix elements in terms of the Cabibbo angle as $\lambda = \sin\theta_{12}$. Equation (2.5) presents the approximation to order λ^3.

$$\begin{bmatrix} V_{ud} & V_{us} & V_{ub} \\ V_{cd} & V_{cs} & V_{cb} \\ V_{td} & V_{ts} & V_{tb} \end{bmatrix} = \begin{bmatrix} 1 - \lambda^2/2 & \lambda & A\lambda^3(\rho - i\eta) \\ -\lambda & 1 - \lambda^2/2 & A\lambda^2 \\ A\lambda^3(1 - \rho - i\eta) & -A\lambda^2 & 1 \end{bmatrix} + \mathcal{O}(\lambda^4) \quad (2.5)$$

The other parameters in terms of the standard Euler angles $\theta_{12}, \theta_{23}, \theta_{13}$ and CP-violating phase δ are $A\lambda^2 = \sin\theta_{23}$ and $A\lambda^3(\rho - i\eta) = \sin\theta_{13}e^{-i\delta}$. This parametrization is helpful in order to quickly identify the order of the coupling between the quarks and the weak bosons, as the magnitude of the matrix elements can be experimentally determined [4]. It is worth emphasizing that the only source of CPV is given by the quantity $(\rho - i\eta)$.

The next sections are composed by three main parts. The goal of Sec. 2.1, presented below, is to build a model explicitly consistent with the CPT constraint for studying CPV. That implies having identical particle and antiparticle lifetimes, even if the partial decay widths can be different for CP conjugate channels due to CP violation. Therefore, in order to fulfill CPT invariance, the total width for particle and antiparticle should be equal and, consequently, the CPV seen in one channel should be seen with opposite sign in other channels.

Within this model the flow of CPV among different channels is given by two-body final state interactions. Inelastic scattering of the type $PP \to P'P'$, with P and P' being light mesons, is the key hadronic effect connecting different decay channels. As anticipated in the introduction, interfering resonances are also important sources of CPV, but in this case within a single decay channel. For this reason the model includes the main resonances experimentally seen for the channels under scrutiny. Although the resonant amplitudes do not distribute CPV among different channels they interfere with the FSI amplitude and change the "compound" CPV flow[1]. In

---

[1]The term compound CPV will be adopted to refer to CPV distributed among different channels by FSI [17].

short, a CP asymmetry formula is derived in the lowest order in the strong interaction scattering matrix and decomposed in terms of the spin of the two-body channels. For the sake of simplicity, only two-body interactions are considered in the model. The kinematical motivation for retaining the interaction in the spectator pair is from the fact that the experimental distribution seen for the three-body phase space is largely located at low energies [18]. The structure observed in the experimental Dalitz plot, given in Ref. [18], is parameterized by the isobar model, where Breit-Wigner distributions outline the main resonances, namely ρ and $f_0(980)$, plus a non-resonant background. Furthermore, the inelastic scattering amplitude $\pi\pi \leftrightarrow KK$, connecting the coupled channels, is incorporated in the description of the three-body decay amplitude.

Sec. 2.2 is devoted to present a simple application of the aforementioned model, where it is possible to see a suppression of the CPV in decays like $B \to PV$, where $P = \pi$ or K and V is a vector meson. The approach allows one to analyze the three-body phase-space in resonant regions without relying on a full amplitude analysis and has as outcome that, around regions arising from intermediate states like PV, the CPV should be very low.

The third part, presented in Sec. 2.3, is devoted to build a model for the three-body decay amplitude with FSI effects including all the mesons in the final state. This model is based on the inhomogeneous Bethe-Salpeter equation projected onto the LF and solved perturbatively. Finally, issue of the partonic (or source) amplitudes is presented, showing that the need of a full approach for embedding the quark-level amplitudes moves the research work into a much broader area: the proper description of non-perturbative systems in quantum field theory. That paves the way of the rest of the thesis, where the homogeneous Bethe-Salpeter approach is developed and solved for some relevant bound systems.

2.1   CP violation and the CPT constraint

As mentioned in the introduction, the first evidence of CPV in charged systems was shown by Bander, Silverman and Soni in Ref. [6], where it was proposed what is known as the BSS mechanism. The hadron decay amplitude is proposed to be a sum of two terms as

$$\mathcal{A}^{\pm} = A_\lambda + B_\lambda e^{\pm i\gamma}, \tag{2.6}$$

where A_λ, B_λ are, in a general scenario, complex functions invariant under CP and $e^{\pm i\gamma}$, the CP-violating phase, which enters linearly at lowest order in the decay amplitude. CP conjugation changes only the sign multiplying the weak phase γ in Eq. (2.6). The two terms, at leading order, can be associated with the tree and penguin diagrams that interfere producing measurable asymmetries in reactions involving the b quark, as shown by Bander, Silverman and Soni. Figure 2.2 shows the tree and penguin diagrams for a generic reaction $b \to f + q + \bar{q}$ associated to the terms of Eq. (2.6), with f (d or s), q and $\bar{q}$ denoting quark flavors.

The goal now is to formulate a decay amplitude consistent with CPT invariance that takes into account the BSS mechanism presented in Eq. (2.6). The notation adopted in this section to derive the B meson decay amplitude consistent with
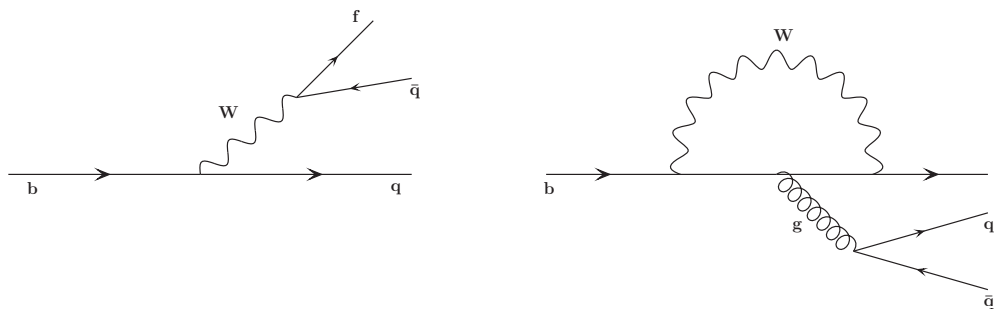
Figure 2.2. Tree (left) and penguin (right) diagrams for the reaction $b \to fq\bar{q}$, where $f = d, s$.

the CPT constraint follows Refs. [14, 15, 16, 20], where topics related to the ones discussed here are treated.

As it is well known in quantum field theory, the CPT transformation has a status of fundamental symmetry, with the straightforward consequence that any Hamiltonian within the SM conserves CPT, i.e

$$(\mathcal{CPT})^{-1} H_w \, \mathcal{CPT} = H_w \quad \text{and} \quad (\mathcal{CPT})^{-1} H_s \, \mathcal{CPT} = H_s, \tag{2.7}$$

where H_w and H_s are, respectively, the weak and strong Hamiltonians. Representing the initial hadron state by $|h\rangle$ and the interacting final state by $|\lambda_{out}\rangle$, the weak decay amplitude is simply given by the following matrix element

$$\langle \lambda_{out} | H_w | h \rangle = \langle \lambda_{out} | (CPT)^{-1} H_w \, \mathcal{CPT} | h \rangle = \chi_h \chi_\lambda \langle \bar{\lambda}_{in} | H_w | \bar{h} \rangle^*, \tag{2.8}$$

where $\chi_{h,\lambda}$ are complex phases coming from the CPT operator applied to the states, e.g. $\mathcal{CPT} |\phi\rangle = \chi_\phi \langle \bar{\phi} |$, and λ_{in} denotes the initial state affected by the strong interaction. Now introducing the completeness relation of the interacting states, $\sum_{\bar{\lambda}'} |\bar{\lambda}'_{out}\rangle\langle\bar{\lambda}'_{out}| = \mathbb{1}$, in Eq. (2.8) and taking into account that H_w is a Hermitian operator, one gets

$$\langle \lambda_{out} | H_w | h \rangle = \chi_h \chi_\lambda \sum_{\bar{\lambda}'} S_{\bar{\lambda}', \bar{\lambda}} \langle \bar{\lambda}'_{out} | H_w | \bar{h} \rangle^*, \quad S_{\bar{\lambda}', \bar{\lambda}} = \langle \bar{\lambda}'_{out} | \bar{\lambda}_{in} \rangle = S_{\lambda', \lambda}, \tag{2.9}$$

where $S_{i,j}$ represents S-matrix elements.

The fundamental constraint of the model, the CPT invariance, is implemented in practice by requiring that the sum over all the partial widths to be the same for the hadron $|h\rangle$ and its CP conjugate, since particle and antiparticle must have equal mean lifetimes by CPT. This consequence of Eq. (2.9) and the hermiticity of the weak Hamiltonian operator can be summarized through the following expression

$$\sum_\lambda |\langle \lambda_{out} | H_w | h \rangle|^2 = \sum_{\bar{\lambda}} |\langle \bar{\lambda}_{out} | H_w | \bar{h} \rangle|^2. \tag{2.10}$$

The decay amplitude discussed above within CPT invariance carries the strong interaction present in the final state. It can be related to the BSS mechanism, from Eq. (2.6), by

$$\mathcal{A}_\lambda^- = \langle \lambda_{out} | H_w | h \rangle, \quad \mathcal{A}_\lambda^+ = \langle \bar{\lambda}_{out} | H_w | \bar{h} \rangle. \tag{2.11}$$

Therefore, writing the BSS decay amplitude consistently with CPT invariance gives the following expression

$$A_\lambda + e^{\mp i\gamma}B_\lambda = \chi_h\chi_\lambda \sum_{\lambda'} S_{\lambda',\lambda}\left(A_{\lambda'} + e^{\pm i\gamma}B_{\lambda'}\right)^*, \tag{2.12}$$

which establishes a connection between the amplitudes A_λ, B_λ and their conjugates.

The CPT constrain of Eq. (2.10) sums over the decay widths Γ_λ of the final state channels, denoted by $\bar{\lambda}$, of the kinematically allowed phase-space and can be written in a more convenient notation by

$$\sum_\lambda \Gamma(A_\lambda^-) = \sum_{\bar{\lambda}} \Gamma(A_{\bar{\lambda}}^+). \tag{2.13}$$

After the formation of the final state hadrons, the mesons can interact through final state interactions. It is useful to introduce the expansion of the strongly interacting state in terms of the free state $|\lambda_0\rangle$ and the states carrying the FSI effects in higher orders, i.e $|\lambda_{out}\rangle = |\lambda_0\rangle + \dots$ where the dots indicate the interacting states with the FSI corrections. The expansion allows one to rewrite Eq. (2.9) as

$$\langle\lambda_{out}|H_w|h\rangle = \chi_h\chi_\lambda \sum_{\bar{\lambda}'} S_{\bar{\lambda}',\bar{\lambda}}\langle\bar{\lambda}_0'|H_w|\bar{h}\rangle^* + \dots = \sum_{\lambda'}\left(\delta_{\lambda',\lambda} + i\,t_{\lambda',\lambda}\right)\langle\lambda_0'|H_w|h\rangle + \dots ,$$

where the scattering matrix are written in terms of the T-matrix $t_{\lambda',\lambda}$.

The only source of mesonic strong interactions at leading order (LO) is from the T-matrix. In this formalism, the FSI effect enters simply in LO in the decay amplitude and will be introduced by replacing $A_\lambda \to A_{0\lambda}$ and $B_\lambda \to B_{0\lambda}$, where $A_{0\lambda}$ is the decay amplitude related to the tree (left panel of Fig. 2.2) and $B_{0\lambda}$ to the penguin (right panel of Fig. 2.2) diagrams. These diagrams and their higher orders compose the BSS model. Hence Eq. (2.12) turns into

$$A_{0\lambda} + e^{\mp i\gamma}B_{0\lambda} = \chi_h\chi_\lambda\left(A_{0\lambda} + e^{\pm i\gamma}B_{0\lambda}\right)^* + i\,\chi_h\chi_\lambda \sum_{\lambda'} t_{\lambda',\lambda}\left(A_{0\lambda'} + e^{\pm i\gamma}B_{0\lambda'}\right)^*. \tag{2.14}$$

Another important point to bear in mind is that only two-body interacting terms are taken into account in this formalism, as in what follows the T-matrix is restricted to its lowest order. Taking into account the CPT constraint as

$$\langle\lambda_0|H_w|h\rangle = \chi_h\chi_\lambda\langle\bar{\lambda}_0|H_w|\bar{h}\rangle^*, \tag{2.15}$$

one gets that the partonic amplitudes should be related as $A_{0\lambda}(B_{0\lambda}) = \chi_h\chi_\lambda A_{0\lambda}^*(B_{0\lambda}^*)$. Consequently, the decay amplitude up to the leading order in $t_{\lambda',\lambda}$ reduces to a simpler form, more common in the literature. [12, 13],

$$\mathcal{A}_{LO}^\pm = A_{0\lambda} + e^{\pm i\gamma}B_{0\lambda} + i\sum_{\lambda'} t_{\lambda',\lambda}\left(A_{0\lambda'} + e^{\pm i\gamma}B_{0\lambda'}\right). \tag{2.16}$$

Obtaining the CP asymmetry means calculating the difference $\Delta\Gamma_\lambda = |\langle\lambda_{out}|H_w|h\rangle|^2 - |\langle\bar{\lambda}_{out}|H_w|\bar{h}\rangle|^2$, which computed to leading order in the hadronic interaction, gives

$$\Delta\Gamma_\lambda = 4(\sin\gamma)\,\mathrm{Im}\left\{(B_{0\lambda})^* A_{0\lambda} + i\sum_{\lambda'}\left[(B_{0\lambda})^* t_{\lambda',\lambda} A_{0\lambda'} - (B_{0\lambda'} t_{\lambda',\lambda})^* A_{0\lambda}\right]\right\}, \tag{2.17}$$

where λ' labels each state coupled to the decay channel λ by the strong interaction.

In the RHS of Eq. (2.17), the two terms between square brackets, that contain the scattering matrix elements, correspond to the so-called "compound" CP asymmetry [17], i.e the one coming from the flow among different decay channels. This contribution, enclosing the FSI effects, is notated by $\Delta\Gamma_\lambda^{FSI}$. When summing over all the possible decay channels and integrated over the phase-space, these two contributions cancel each other resulting in $\sum_\lambda \Delta\Gamma_\lambda^{FSI} = 0$, due to the CPT condition. Another essential consequence of CPT is the constraint at microscopic level, accounted by

$$\sum_\lambda \text{Im}\left[(B_{0\lambda})^* A_{0\lambda}\right] = 0.$$

In the situation where particle and antiparticle amplitudes conserve CP for all decay channels, this is a trivial condition as it does not involve the flux of CPV among different channels owing to FSI. Although it was not taken into account by Wolfenstein [12], the condition is worth to be explicitly tested in practice. In the situation where only two channels, λ and λ', are coupled by FSI, Eq. (2.17) reduces to

$$\Delta\Gamma_\lambda = 4(\sin\gamma)\,\text{Re}\Big\{ (B_{0\lambda})^*\, t_{\lambda',\lambda}\, A_{0\lambda'} - (B_{0\lambda'}\, t_{\lambda',\lambda})^*\, A_{0\lambda} \Big\} = -\Delta\Gamma_{\lambda'}\,. \qquad (2.18)$$

Equation (2.18) was applied to analyze the large CP violation observed by LHCb collaboration [54] in the $B^\pm \rightarrow K^\pm K^+ K^-$ and $B^\pm \rightarrow K^\pm \pi^+ \pi^-$ decay channels [16]. The observed large CPV was on the low $K^+ K^-$ and $\pi^+ \pi^-$ mass regions between 1 and 1.6 GeV, where those channels are known to be coupled by strong interactions [55, 56]. Giving the dominance of the s-wave scattering and after manipulations, the final expression, apart from a phase-space factor, is simply proportional to

$$\sqrt{1 - \eta^2}\cos\left(\delta_{KK} + \delta_{\pi\pi} + \Phi\right),$$

where η is the inelasticity parameter and $\delta_{\pi\pi(KK)}$ the s-wave phase-shifts. These functions are given by the parametrization of the $\pi\pi \rightarrow KK$ scattering amplitude proposed in Ref. [57].

An interesting particular case of Eq. (2.18) is when the contribution from the diagram that does not carry the weak phase is insignificant, e.g. $A_{0\lambda} = 0$ (notice that the corresponding amplitude of the coupled channel, $A_{0\lambda'}$, is not considered to be negligible in this scenario), for which

$$\Delta\Gamma_\lambda = 4(\sin\gamma)\,\text{Re}\{(B_{0\lambda})^*\, t_{\lambda',\lambda}\, A_{0\lambda'}\}\,.$$

This expression shows that CP violation still can arise, in this case as a consequence of the interference between the decay amplitudes in the channels λ and λ' (coupled by strong interactions), and the diagram which carries the weak phase $e^{\pm i\gamma}$. Thereby, CPV can still exist in a $B^\pm$ decay channel, λ, where the penguin (or tree) contribution is negligible while in the corresponding coupled channel, λ', the tree (or penguin) contribution can be neglected. As a consequence, only one channel may carry the weak CP violating phase. For measurable CPV, the interference needs to happen between amplitudes originating in different channels, coupled by the strong

interaction. In such an example, the CPV interference effects will be predominantly coming from FSI, as it would be the only mechanism linking different channels.

As previously discussed, this formalism aims to deal with three-body decays but so far taking into account two-body interactions. Therefore the decay amplitude always assume a non-interacting particle, not affected by FSI. Three-body FSI it is not yet included in this formalism, but will be discussed in the next sections. The formalism is similar to the one developed for the $D^\pm \to K^\pm \pi^+ \pi^-$ decay in Refs. [58, 59, 60], where the rescattering via three-body FSI was shown to be small when compared to two-body scattering contributions.

Another important process to take into account is the formation of intermediate resonances. In order to do that, the formalism needs to explicitly label the spin of the two-body state. Certainly, the decomposition in other quantum numbers also needs to be properly included, but those are kept implicit in the formalism in pursuit of keeping the notation clean, as no ambiguity happens in terms of them in the later analysis. The spin is expressed here by the index J, which appears in the decomposition of the amplitudes $A_{0\lambda}$ and $B_{0\lambda}$, as well as in the $t_{\lambda',\lambda}$ matrix. Identifying the angular momentum of the outgoing channel allows one to introduce the main resonances experimentally seen in the measured phase-space. Decomposing the decay amplitude of Eq. (2.16) in terms of J,

$$\mathcal{A}_{LO}^\pm = \sum_J \left(A_{0\lambda}^J + e^{\pm i\gamma} B_{0\lambda}^J \right) + i \sum_{\lambda',J} t_{\lambda',\lambda}^J \left(A_{0\lambda'}^J + e^{\pm i\gamma} B_{0\lambda'}^J \right), \qquad (2.19)$$

where, recalling, $\lambda\,(\lambda')$ are the two-body channels in the final mesonic state. Although not explicitly shown, the amplitude includes dependence on the energy-momentum of the spectator hadron, as well as on other quantum numbers, but this will be displayed only when necessary for the sake of simplicity. The decomposed CP asymmetry is, consequently

$$\Delta\Gamma_\lambda = \Gamma\left(h \to \lambda \right) - \Gamma(\overline{h} \to \overline{\lambda}) = 4(\sin\gamma) \times \qquad (2.20)$$

$$\times \sum_{J\,J'} \mathrm{Im} \left\{ \left(B_{0\lambda}^J \right)^* A_{0\lambda}^{J'} + i \sum_{\lambda'} \left[\left(B_{0\lambda}^J \right)^* t_{\lambda',\lambda}^{J'} A_{0\lambda'}^{J'} - \left(B_{0\lambda'}^{J'} t_{\lambda',\lambda}^{J'} \right)^* A_{0\lambda}^J \right] \right\},$$

where the states λ' are the ones coupled by FSI to the decay channel λ.

Everything discussed under the angular momentum decomposition still satisfies the CPT condition as stated before. Therefore, the CP asymmetry summed over all the possible decay channels will result in the following

$$\sum_\lambda \Delta\Gamma_\lambda = 4(\sin\gamma) \sum_{\lambda J} \mathrm{Im} \left[\left(B_{0\lambda}^J \right)^* A_{0\lambda}^J \right] + \sum_\lambda \Delta\Gamma_\lambda^{FSI} = 0, \qquad (2.21)$$

where the $\Delta\Gamma_\lambda^{FSI}$ corresponds to the CPV arising from the flow due to FSI and explicitly fulfills,

$$\sum_\lambda \Delta\Gamma_\lambda^{FSI} = 4(\sin\gamma) \times \qquad (2.22)$$

$$\times \sum_{\lambda'\lambda J} \mathrm{Re} \left[\chi_h \chi_{\lambda J} \left(B_{0\lambda}^J \right)^* t_{\lambda',\lambda}^J \left(A_{0\lambda'}^J \right)^* - \chi_h^* \chi_{\lambda'J}^* B_{0\lambda'}^J \left(t_{\lambda',\lambda}^J \right)^* A_{0\lambda}^J \right] = 0.$$

Recalling that one proves Eq. (2.22) by using $A_{0\lambda}(B_{0\lambda}) = \chi_h\chi_\lambda A^*_{0\lambda}(B^*_{0\lambda})$, the symmetry property $t^J_{\lambda,\lambda'} = t^J_{\lambda',\lambda}$, and the fact that different CP eigenstates are not mixed by strong interactions, i.e $\chi_{\lambda J} = \chi_{\lambda' J}$.

2.1.1 Resonances, interferences and CPV formula

Resonance formation corresponds to an essential contribution in the decay process. It can happen both at the partonic amplitude level, as well as a hadronic effect, while the mesonic rescattering process is going on. Resonances are particularly important due to their influence on the dynamics of the phase-space, as they interfere with neighboring areas. The first step to introduce the resonant structure into the formalism is to separate the source amplitudes in resonant (R) and non-resonant (NR) parts in the decay amplitude of Eq. (2.19), i.e

$$
\begin{aligned}
\mathcal{A}^\pm_{LO} &= \sum_J \left[\sum_R A^J_{0\lambda R} + A^J_{0\lambda NR} + e^{\pm i\gamma}\left(\sum_R B^J_{0\lambda R} + B^J_{0\lambda NR}\right)\right] \qquad (2.23)\\
&+ i\sum_{\lambda',J} t^J_{\lambda',\lambda}\left[\sum_R A^J_{0\lambda' R} + A^J_{0\lambda' NR} + e^{\pm i\gamma}\left(\sum_R B^J_{0\lambda' R} + B^J_{0\lambda' NR}\right)\right].
\end{aligned}
$$

As said, $A^J_{0\lambda R}$ and $B^J_{0\lambda R}$ do not take into account the physical processes happening at the hadronic level. The entire two-meson rescattering process is fully encoded within the T-matrix, so that double counting the processes is avoided. The aim is to identify the resonant amplitudes analogously to how it is performed in the isobar model [61] and, therefore, it is useful to establish the following relations

$$(1 + i\,t^J_{\lambda\lambda})A^J_{0\lambda R} \rightarrow a^R_0 F^{BW}_{R\lambda} P_J(\cos\theta); \quad (1 + i\,t^J_{\lambda\lambda})B^J_{0\lambda R} \rightarrow b^R_{0\lambda} F^{BW}_{R\lambda} P_J(\cos\theta), \ (2.24)$$

where $F^{BW}_{R\lambda}$ are Breit-Wigner amplitudes, J is the spin of the resonance and $P_J(\cos\theta)$ the Legendre polynomial, defined in terms of the helicity angle θ (see Fig. 2.3) between the equally charged particles. This is in agreement with the Gottfried-Jackson frame [62], which is used by the experimentalists [63]. Important to recall that although the formalism is still completely general, in the forthcoming applications the interest will be on resonances decaying to two spin zero particles.
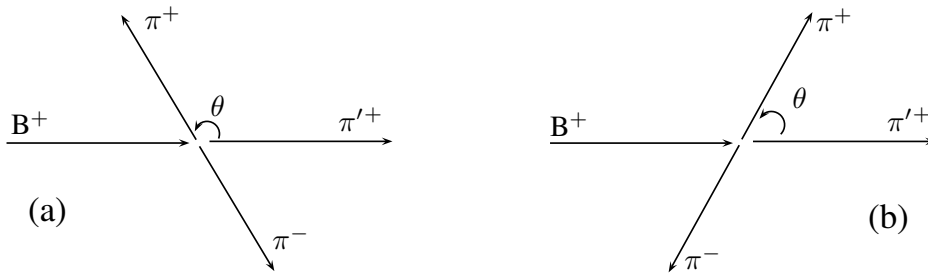
Figure 2.3. Diagram representing the definition of the helicity angle, θ. As an example, the $B^+ \rightarrow \pi^+\pi^+\pi^-$ decay, where π'^+ is the non-interacting particle. (a): $\cos\theta < 0$ ($\theta > \frac{\pi}{2}$). (b): $\cos\theta > 0$ ($\theta < \frac{\pi}{2}$).

Introducing the relations given in Eq. (2.24), the decay amplitude can be written as

$$
\begin{aligned}
\mathcal{A}_{LO}^{\pm} &= \sum_{J\,R}\left(a_{0\lambda}^{R} + e^{\pm i\gamma}b_{0}^{R}\right)F_{R\lambda}^{BW}P_{J}(\cos\theta) + \sum_{J}\left(A_{0\lambda NR}^{J} + e^{\pm i\gamma}B_{0\lambda NR}^{J}\right)\\
&+ i\sum_{\lambda',J}t_{\lambda',\lambda}^{J}\left(A_{0\lambda' NR}^{J} + e^{\pm i\gamma}B_{0\lambda' NR}^{J}\right),
\end{aligned}
\tag{2.25}
$$

where the first two terms on the RHS correspond to the isobar model, the first one enclosing all the resonant structures and the second being the partoninc process when it leads directly to the final state. The two-body hadronic final state interactions are, naturally, in the third term where the scattering matrix elements appear. This term is supposed to also carry the possibility of the resonance being formed during the rescattering process, e.g. $P'P' \to R \to PP$.

From the decay amplitude of Eq. (2.25) the final CP asymmetry formula reads

$$
\Delta\Gamma_{\lambda} = \Gamma\left(h \to \lambda\right) - \Gamma(\overline{h} \to \overline{\lambda}) = 4(\sin\gamma)\ \times
\tag{2.26}
$$

$$
\begin{aligned}
\times\ & \sum_{J\,J'}\mathrm{Im}\left\{\left(\sum_{R}b_{0\lambda}^{R}F_{R\lambda}^{BW}P_{J}(\cos\theta) + B_{0\lambda NR}^{J}\right)^{*}\left(\sum_{R'}a_{0\lambda}^{R'}F_{R'\lambda}^{BW}P_{J'}(\cos\theta) + A_{0\lambda NR}^{J'}\right)\right.\\
+\ & i\sum_{\lambda'}\left(\sum_{R}b_{0\lambda}^{R}F_{R\lambda}^{BW}P_{J}(\cos\theta) + B_{0\lambda NR}^{J}\right)^{*}t_{\lambda',\lambda}^{J'}\left(\sum_{R'}a_{0\lambda'}^{R'}F_{R'\lambda'}^{BW}P_{J'}(\cos\theta) + A_{0\lambda' NR}^{J'}\right)\\
-\ & i\sum_{\lambda'}\left.\left(\sum_{R'}b_{0\lambda'}^{R'}F_{R'\lambda'}^{BW}P_{J'}(\cos\theta) + B_{0\lambda' NR}^{J'}\right)\left[t_{\lambda',\lambda}^{J'}\right]^{*}\left(\sum_{R}a_{0\lambda}^{R}F_{R\lambda}^{BW}P_{J}(\cos\theta) + A_{0\lambda NR}^{J}\right)\right\}.
\end{aligned}
$$

This expression still depends explicitly on two variables in the three-body decay context, e.g. the two-body invariant masses m_{12}^{2} and m_{23}^{2}, and the index λ that indicates the decay channel and includes all the possible kinematical regions. As the Breit-Wigner distributions were introduced by hand to relate the formalism with the isobar model, it is essential to explicitly check the CPT constraint while performing the experimental data analysis. There might be terms which are not consistent with the CPT constraint, thus Eq. (2.26) needs to be integrated over the phase-space and summed over all decay channels after the fitting procedure, showing that $\int dm_{12}^{2}\,dm_{23}^{2}\sum_{\lambda}\Delta\Gamma_{\lambda} = 0$ is still satisfied [20].

Equation (2.26) represents the final formal step of the derivation, and describes, in a general manner, the CP asymmetry in a weak decay channel λ enclosing partonic effects, resonant structures, final state interactions and interference terms. All the interactions are at two-body level. The CPT constraint needs to be verified in every calculation, which is easily achievable within the formalism. Now it is time to specify the cases which will be treated with the CPV formula. Two three-body decays will be analyzed with the formula in this study, namely $B^{\pm} \to \pi^{\pm}\pi^{+}\pi^{-}$ and $B^{\pm} \to K^{\pm}\pi^{+}\pi^{-}$. As it was shown experimentally [63, 64, 65], the vector $\rho(770)$ and the scalar $f_{0}(980)$ resonances are the dominant ones in the dynamics of those decays for low invariant $\pi^{+}\pi^{-}$ masses. These resonances are assumed to decay always in the $\pi\pi$ channel. Moreover, it is also known that the s-wave coupling between the strongly interacting channels $\pi\pi$ and KK is very large [56], being the exception as early experiments have shown that the elastic regime is predominant in the low $\pi\pi$ and $K\pi$ mass regions [55]. This knowledge on the suppression of inelastic transitions makes

reasonable to assume that transitions between different channels are uncommon. Therefore, the aforementioned resonances will be the ones included, as well as their interference with the non-resonant background and $t_{\pi\pi \to KK}^{J=0}$ amplitude.

The partonic amplitudes now can be explicitly identified by the specific structures of the decays under study as

$$A_{0\lambda R} = a_0^\rho F_\rho^{\text{BW}} k(s) \cos\theta + a_0^f F_f^{\text{BW}}, \quad B_{0\lambda R} = b_0^\rho F_\rho^{\text{BW}} k(s) \cos\theta + b_0^f F_f^{\text{BW}},$$

$$A_{0\lambda NR} = \frac{a_{0\lambda}^{nr}}{1 + \frac{s}{\Lambda_\lambda^2}}, \quad B_{0\lambda NR} = \frac{b_{0\lambda}^{nr}}{1 + \frac{s}{\Lambda_\lambda^2}}, \tag{2.27}$$

where the Breit-Wigner distribution, representing the decay of a resonance R, takes the form [1]

$$F_R^{\text{BW}}(s) = \frac{1}{m_R^2 - s - i m_R \Gamma_R(s)}, \tag{2.28}$$

where m_R, a fixed input parameter, is the resonance mass and $\Gamma_R(s)$, given by

$$\Gamma_R(s) = \frac{\left(\frac{s}{4} - m_\pi^2\right)^{1/2} m_R \Gamma_R'}{\left(\frac{m_R^2}{4} - m_\pi^2\right)^{1/2} s^{1/2}}, \tag{2.29}$$

denotes the energy dependent relativistic width and where Γ_R' is the resonance width.

All the masses and widths are experimentally known in the literature. Particularly, the resonance masses are given by $m_\rho = 0.775$ GeV and $m_f = 0.975$ GeV, and the widths are fixed as $\Gamma_\rho' = 0.150$ GeV and $\Gamma_f' = 0.044$ GeV [1, 66] in the analysis published in Ref. [20], that will be as follows. More explicitly, the resonant and non-resonant terms of the $B^\pm \to \pi^\pm \pi^+ \pi^-$ and $B^\pm \to K^\pm \pi^+ \pi^-$ decays, takes the form

$$\begin{aligned} \mathcal{A}_{0\lambda}^\pm &= a_0^\rho F_\rho^{\text{BW}} k(s) \cos\theta + a_0^f F_f^{\text{BW}} + \frac{a_{0\lambda}^{nr} + b_{0\lambda}^{nr} e^{\pm i\gamma}}{1 + \frac{s}{\Lambda_\lambda^2}} \\ &+ [b_0^\rho F_\rho^{\text{BW}} k(s) \cos\theta + b_0^f F_f^{\text{BW}}] e^{\pm i\gamma}, \end{aligned} \tag{2.30}$$

where $k(s) = \sqrt{1 - \frac{4m_\pi^2}{s}}$ is a kinematical factor that takes into account the threshold behavior of the ρ p-wave amplitude. The angle θ, illustrated in Fig. 2.3, is conveniently defined, for the subsequent experimental data, as the angle between the non-interacting with its equally charged particle in the final state. Therefore, $-1 \leq \cos\theta \leq 1$ is related to the spin of the ρ resonance. This is one of variables that characterize the three-body decay phase-space, as it will be seen later.

Another ingredient considered in the modeled amplitude is the form factor $\left(1 + \frac{s}{\Lambda_\lambda^2}\right)^{-1}$, which parametrizes the squared mass dependence in the non resonant partonic amplitude. The quark-level tree and penguin diagrams, which composes the partonic decay amplitude, depend on the structure of the mesons involved in the diagram, i.e on their wave functions. In favor of simplicity, the form factor is chosen

to depend on only one of the independent Mandelstam variables, but still accounts the power-law behavior expected from the hard momentum structure of the involved mesons [67]. The value of the Λ parameters should, roughly, be scaled by Λ_{QCD}, though this is just an empirical guide for fixing them. The values chosen here were $\Lambda_\lambda = \Lambda_{\pi\pi} = 3.0$ GeV and $\Lambda_{\lambda'} = \Lambda_{KK} = 4.0$ GeV. Worth to say that no significant change is seen in the fitting with changes up to 50% of these parameters. As it is known, the partonic amplitudes are very complicated to be properly described, although it deserves a deeper understanding. However this simple model will be adopted, as its characterization is beyond the scope of the present study.

The CP asymmetry given by Eq. (2.26) can be written for the specific decay amplitude discussed above (2.30) as

$$
\begin{aligned}
\Delta\Gamma_\lambda \;=\; & 4(\sin\gamma)\mathrm{Im}\Bigg[\left(b_0^\rho F_\rho^{\mathrm{BW}}k(s)\cos\theta + b_0^f F_f^{\mathrm{BW}} + \frac{b_{0\lambda}^{nr}}{1+\frac{s}{\Lambda_\lambda^2}}\right)^{*}\times \\
& \hspace{4cm}\times\left(a_0^\rho F_\rho^{\mathrm{BW}}k(s)\cos\theta + a_0^f F_f^{\mathrm{BW}} + \frac{a_{0\lambda}^{nr}}{1+\frac{s}{\Lambda_\lambda^2}}\right)\Bigg] \\
& +\;4(\sin\gamma)\,\mathrm{Re}\Bigg\{\sum_{\lambda'}\Bigg[\left(b_0^\rho F_\rho^{\mathrm{BW}}k(s)\cos\theta + b_0^f F_f^{\mathrm{BW}} + \frac{b_{0\lambda}^{nr}}{1+\frac{s}{\Lambda_\lambda^2}}\right)^{*}t_{\lambda',\lambda}^{J=0}\,\frac{a_{0\lambda'}^{nr}}{1+\frac{s}{\Lambda_{\lambda'}^2}} \\
& -\left(\frac{b_{0\lambda'}^{nr}}{1+\frac{s}{\Lambda_{\lambda'}^2}}\,t_{\lambda',\lambda}^{J=0}\right)^{*}\left(a_0^\rho F_\rho^{\mathrm{BW}}k(s)\cos\theta + a_0^f F_f^{\mathrm{BW}} + \frac{a_{0\lambda}^{nr}}{1+\frac{s}{\Lambda_\lambda^2}}\right)\Bigg]\Bigg\}, \quad (2.31)
\end{aligned}
$$

where λ designates the different regions of the phase-space for a given decay channel and λ' are the corresponding coupled channels, i.e. πKK or KKK coupled, respectively, to $\pi\pi\pi$ and $K\pi\pi$. It has already been placed $J=0$ for the T-matrix, since only the *s*-wave channel will be considered. The CPV from the coupling between different decay channels, originated by FSI and its interferences with resonant and non resonant amplitudes, are fully concentrated in the terms between curly brackets.

The last ingredient missing to write down the explicit formula for the CP asymmetry is the $\pi\pi \to KK$ rescattering amplitude. It is given by the *s*-wave isoscalar inelastic T-matrix, corresponding to the off-diagonal S-matrix elements. The two-channel S-matrix can be written as

$$
S = \begin{bmatrix} \eta e^{2i\delta_{\pi\pi}} & i\sqrt{1-\eta^2}\,e^{i(\delta_{\pi\pi}+\delta_{KK})} \\ i\sqrt{1-\eta^2}\,e^{i(\delta_{\pi\pi}+\delta_{KK})} & \eta e^{2i\delta_{KK}} \end{bmatrix}, \quad (2.32)
$$

where $\eta(s)$ is the inelasticity parameter and $\delta_{\pi\pi}(s)$ the $\pi\pi$ phase-shift. The explicit form of these expressions are presented in Ref. [57], which incorporate the requirements of analyticity and unitarity, and being fully consistent with the known $\pi\pi$ scattering experimental data. In Eq. (2.32), the inelasticity parameter reads

$$
\eta(s) = 1 - \left(\epsilon_1\frac{k_2}{s^{1/2}} + \epsilon_2\frac{k_2^2}{s}\right)\frac{M'^2 - s}{s}; \quad k_2 = \frac{\sqrt{s - 4m_K^2}}{2}, \quad (2.33)
$$

where the phase shift is written as

$$
\delta_{\pi\pi}(s) = \frac{1}{2}\cos^{-1}\left\{\frac{\cot^2[\delta_{\pi\pi}(s)] - 1}{\cot^2[\delta_{\pi\pi}(s)] + 1}\right\}; \quad \cot(\delta_{\pi\pi}) = c_0\frac{(s - M_s^2)(M_f^2 - s)}{M_f^2 s^{1/2}}\frac{|k_2|}{k_2^2}. \quad (2.34)
$$

The input parameters involved in the equations above, as fixed in Ref. [57], are quantified as follows: $m_K = 0.494$ GeV, $M_s = 0.92$ GeV, $M' = 1.5$ GeV, $M_f = 1.32$ GeV, $\epsilon_1 = 2.4$, $\epsilon_2 = -5.5$, and $c_0 = 1.3$, Important to note that, for simplicity, the central values of the parameters are used, without considering their uncertainties as given in [57]. Therefore, one source of uncertainty in this model are the errors in the parametrization of the $\pi\pi$ phase shift and inelasticity parameter. The model aims to describe the main CPV dynamics, but not the whole rich structure observed in the full phase-space. The pion mass is assumed to be degenerated for $\pi^\pm$ and given by $m_\pi = 0.138$ GeV. An assumption made here is that the phase-shifts are comparable for both $\pi\pi$ and KK amplitudes between 1 and 1.6 GeV, i.e. $\delta_{KK} \approx \delta\pi\pi$.

With all the ingredients in hand, the CP asymmetry formula (2.31) can be further elaborated, by using simple relations between complex numbers as presented in Appendix A. The goal is to turn all the source amplitudes into coefficients in each term, as they will be unknown parameters to be found through the fitting procedure. Using the formulas presented in Appendix A, one can write the explicit formula for the fitting as

$$
\begin{aligned}
\Delta\Gamma_\lambda(s,\theta) =\ & \frac{\mathcal{A}}{\left(1+\frac{s}{\Lambda_\lambda^2}\right)^2} + \frac{\{\mathcal{B}\cos[2\delta_{\pi\pi}(s)] + \mathcal{B}'\sin[2\delta_{\pi\pi}(s)]\}\sqrt{1-\eta^2(s)}}{\left(1+\frac{s}{\Lambda_\lambda^2}\right)\left(1+\frac{s}{\Lambda_{\lambda'}^2}\right)} + \mathcal{C}|F_\rho^{\mathrm{BW}}(s)|^2 k^2(s)\cos^2\theta \\
&+ |F_\rho^{\mathrm{BW}}(s)|^2 k(s)\cos\theta \left\{ \frac{\mathcal{D}'\sqrt{1-\eta^2(s)}\{m_\rho\Gamma_\rho(s)\cos[2\delta_{\pi\pi}(s)] - (m_\rho^2-s)\sin[2\delta_{\pi\pi}(s)]\}}{1+\frac{s}{\Lambda_{\lambda'}^2}} \right.\\
&+ \frac{\mathcal{D}(m_\rho^2-s)}{1+\frac{s}{\Lambda_\lambda^2}} + \frac{\mathcal{E}m_\rho\Gamma_\rho(s)}{1+\frac{s}{\Lambda_\lambda^2}} + \left.\frac{\mathcal{E}'\sqrt{1-\eta^2(s)}\{(m_\rho^2-s)\cos[2\delta_{\pi\pi}(s)] + m_\rho\Gamma_\rho(s)\sin[2\delta_{\pi\pi}(s)]\}}{1+\frac{s}{\Lambda_{\lambda'}^2}} \right\} \\
&+ |F_\rho^{\mathrm{BW}}(s)|^2|F_f^{\mathrm{BW}}(s)|^2 k(s)\cos\theta\times \\
&\times \left\{ \mathcal{F}[(m_\rho^2-s)(m_f^2-s) + m_\rho\Gamma_\rho(s)m_f\Gamma_f(s)] + \mathcal{G}[(m_\rho^2-s)m_f\Gamma_f(s) - m_\rho\Gamma_\rho(s)(m_f^2-s)] \right\} \\
&+ |F_f^{\mathrm{BW}}(s)|^2 \left\{ \frac{\mathcal{H}(m_f^2-s)}{1+\frac{s}{\Lambda_\lambda^2}} + \frac{\mathcal{H}'\sqrt{1-\eta^2(s)}\{m_f\Gamma_f(s)\cos[2\delta_{\pi\pi}(s)] - (m_f^2-s)\sin[2\delta_{\pi\pi}(s)]\}}{1+\frac{s}{\Lambda_{\lambda'}^2}} \right. \\
&+ \frac{\mathcal{P}m_f\Gamma_f(s)}{1+\frac{s}{\Lambda_\lambda^2}} + \left.\frac{\mathcal{P}'\sqrt{1-\eta^2(s)}\{(m_f^2-s)\cos[2\delta_{\pi\pi}(s)] + m_f\Gamma_f(s)\sin[2\delta_{\pi\pi}(s)]\}}{1+\frac{s}{\Lambda_{\lambda'}^2}} \right\} + \mathcal{Q}|F_f^{\mathrm{BW}}(s)|^2,
\end{aligned}
\tag{2.35}
$$

where λ designates the decay channels, $\pi^\pm\pi^+\pi^-$ or $K^\pm\pi^+\pi^-$, and the subindex λ' corresponds to the respective coupled channels, $\pi^\pm K^+K^-$ or $K^\pm K^+K^-$. As explicitly studied in Ref. [20], the terms containing the parameters $\mathcal{A}$, $\mathcal{C}$, $\mathcal{H}$, $\mathcal{P}$ and $\mathcal{Q}$ are not CPT invariant, either locally or globally, and have to be zero. Moreover, as done in Ref. [20], the parameter $\mathcal{B}'$ is chosen to be zero, so the whole effect of the rescattering term is concentrated in the term containing the parameter $\mathcal{B}$. In summary, the free parameters to be fitted in Eq. (2.35) are $\mathcal{B}$, $\mathcal{D}$, $\mathcal{D}'$, $\mathcal{E}$, $\mathcal{E}'$, $\mathcal{F}$, $\mathcal{G}$, $\mathcal{H}'$ and $\mathcal{P}'$. It is important to keep in mind that $\Lambda_\lambda = 3$ GeV and $\Lambda_{\lambda'} = 4$ GeV are fixed parameters associated to the size of the incoming bound state, as explained in detail below Eq. (2.30). The inelasticity, $\eta(s)$, and phase shift, $\delta_{\pi,\pi}(s)$, are fixed by the $\pi\pi \to KK$ scattering experimental data following the parametrization given in Ref. [57] (see Eqs. (2.33) and (2.34)). Furthermore, F_R^{BW} is the Breit-Wigner distribution, given by Eq. (2.28), and Γ_R is the energy dependent relativistic width, given by Eq. (2.29). All the masses of the particles $(m_\pi, m_K, m_\rho, m_f, m_B)$

and particle widths $(\Gamma'_\rho, \Gamma'_f)$ involved in Eq. (2.35) are fixed by the well-known experimental measurements listed in Ref. [1].

Worth mentioning that in Eq. (15) of Ref. [16] only the terms of parameters $\mathcal{B}$ and $\mathcal{B}'$ were present and, therefore, all the other structures of Eq. (2.35) besides those were introduced for the first time in the research performed in this thesis. The content of these new structures included here account for the amplitudes of the resonances ρ and $f_0(980)$, the non resonant background amplitude and all the possible interference terms among the involved amplitudes. None of these structures were ever taken into account in an explicitly CPT invariant model before, with this being the first time that the whole three-body phase space of the channels $B \to \pi\pi\pi$ and $B \to K\pi\pi$ was studied in detail with such a CPT invariant model, as in Ref. [16] it was only considered the region of two-body invariant masses between 1 and 1.6 GeV. This is also the first CPT invariant model compatible with the isobasic model, widely used by experimentalists.

The expression above, before used to fit the experimental data [63], needs to be expressed only in terms of the low invariant mass $\sqrt{s} = m_{\pi^+\pi^-}$. Moreover, experimentally the phase-space was defined in two regions, namely the ones defined by $\cos\theta < 0$ and $\cos\theta > 0$. One can write the dependence of the angle θ through the kinematics of the decay, e.g. for the $B^+ \to \pi^+\pi^+\pi^-$ case, as[2]

$$\cos\theta = \frac{2m^2_{\pi'^+\pi^-} - m^2_B - 3m^2_\pi + s}{2\left(s - 4m^2_\pi\right)^{1/2}\left[\frac{(m^2_B - m^2_\pi - s)^2}{4s} - m^2_\pi\right]^{1/2}}, \tag{2.36}$$

where $m_B = 5.279$ GeV is the B meson mass [1]. Therefore, it is necessary to perform the integration $\Delta\Gamma(s) \equiv \int \Delta\Gamma_\lambda(s, m^2_{\pi'^+\pi^+})\, dm^2_{\pi'^+\pi^+} = \Delta\Gamma(s)^{(\cos\theta < 0)} + \Delta\Gamma(s)^{(\cos\theta > 0)}$, eliminating the dependence on $m^2_{\pi'^+\pi^+}$ and separating the phase space. This process is done in the appendix of Ref. [20]. The remaining Mandelstam variable, s, is the interacting pair square mass. Notice that, although Eq. (2.35) is long, every term in it correspond to one possible interference within the phase space, under the ingredients considered in the model. The whole set of coefficients, i.e. $\mathcal{A}, \mathcal{B}, \cdots, \mathcal{Q}$, is presented in its original form, as obtained through the derivation, in Appendix A.

It is worth stressing that a different but equivalent form of the $t^{J=0}_{\pi\pi \to KK}$ amplitude can be written, namely $|K_\lambda|\cos(\delta_\lambda + \delta_{\lambda'} + \Phi_\lambda)$, where $K_\lambda = B^*_{0\lambda}A_{0\lambda'} - B_{0\lambda}A^*_{0\lambda'}$ and $\Phi_\lambda = -i\ln(K_\lambda/|K_\lambda|)$. This was the form presented in Ref. [16], where it was assumed that $\Phi_\lambda = 0$. Here, instead, the same amplitude was written in terms of $\mathcal{B}$ and $\mathcal{B}'$, where a zero phase would correspond to $\mathcal{B}' = 0$. This condition is later on obtained in the fitting procedure. Just as an illustration, but eliminating all the terms that violate CPT in Eq. (2.35), as they must vanish once the asymmetry is integrated over the phase-space, and eliminating the terms shown by the fitting procedure to be suppressed, one gets for the $B^\pm \to \pi^\pm\pi^+\pi^-$ decay

---

[2]See the complete derivation in Ref. [20].

$$
\begin{aligned}
\Delta\Gamma_\lambda \quad &= \frac{\mathcal{B}\cos[2\delta_{\pi\pi}(s)]\sqrt{1-\eta^2(s)}}{\left(1+\frac{s}{\Lambda_\lambda^2}\right)\left(1+\frac{s}{\Lambda_{\lambda'}^2}\right)} + |F_\rho^{\mathrm{BW}}(s)|^2 k(s)\cos\theta \left\{ \frac{\mathcal{D}(m_\rho^2 - s)}{1+\frac{s}{\Lambda_\lambda^2}} + \frac{\mathcal{E} m_\rho \Gamma_\rho(s)}{1+\frac{s}{\Lambda_\lambda^2}} \right\} \\
&+ \quad F_\rho^{\mathrm{BW}}(s)|^2 |F_f^{\mathrm{BW}}(s)|^2 k(s)\cos\theta \times \\
&\times \quad \left\{ \mathcal{F}[(m_\rho^2 - s)(m_f^2 - s) + m_\rho \Gamma_\rho(s) m_f \Gamma_f(s)] + \mathcal{G}[(m_\rho^2 - s)m_f \Gamma_f(s) - m_\rho \Gamma_\rho(s)(m_f^2 - s)] \right\}.
\end{aligned}
$$
(2.37)

which is a much simpler formula. For the $B^\pm \to K^\pm \pi^+ \pi^-$ decay, the same formula is valid but with the term multiplying $\mathcal{D}'$ in Eq. (2.35) also appearing as non-zero in the fit. It is straightforward to notice that Eq. (2.37) simply presents the interferences among the non-resonant background, the resonances $\rho(770)$ and $f_0(980)$ and the s-wave $KK \to \pi\pi$ amplitude. The coupling between channels in the $B^\pm$ decays to $\pi^\pm K^+ K^-$ and $K^\pm K^+ K^-$ is an outcome of the fitting and, since it presents purely compound CPV, only $\mathcal{B}$ is non-zero.

2.1.2   Analyzing the CPV experimental data

The aim now is to use Eq. (2.35), integrated in one of the two-body invariant masses as explained in the previous section, to analyze the experimental data, for the difference between the B^- and B^+ differential decay rates of Ref. [63]. For the two decay channels, namely $B^\pm \to \pi^\pm \pi^+ \pi^-$ and $B^\pm \to K^\pm \pi^+ \pi^-$, the CPV distributions given by Eq. (2.35) are fitted. Following the way how the data was presented [63], the fit is over the CPV distribution on the $\pi^+ \pi^-$ invariant mass, $m_{\pi^+\pi^-} = \sqrt{s}$, where the resonant structure, as well as the compound CPV, is more prominent. For the $B^\pm \to \pi^\pm \pi^+ \pi^-$ decay, the fitting is performed in the region of the space where $\cos\theta > 0$.

The fitting procedure to find the relevant parameters compatible with the experimental data follows the χ^2 method. Important to notice that the θ angle definition in the formalism derived for the $B^\pm \to \pi^\pm \pi^+ \pi^-$ decay is the opposite as the definition followed in Ref. [63], i.e. $\cos\theta > 0 \to \cos\theta < 0$ and $\cos\theta < 0 \to \cos\theta > 0$. With the parameters fixed, the CP asymmetry is plotted for $\cos\theta < 0$ and compared with the data. For the $B^\pm \to K^\pm \pi^+ \pi^-$ decay instead, the fit was performed in the $\cos\theta < 0$ region.

The CPV of the corresponding coupled channels, $B^\pm \to \pi^\pm K^+ K^-$ and $B^\pm \to K^\pm K^+ K^-$, are compared with the formula where the coefficient of the term carrying FSI, namely the one multiplying $\mathcal{B}$, has been fixed by the previous fitting of the respective coupled channels. All the CPV in the coupled channels is assumed to be coming from the two-body rescattering and, therefore, only $\mathcal{B}$ is non-zero for them. This assumption is supported by the features of the experimental data, as no resonant interference is measured in the region between 1 and 1.6 GeV. Important to mention that the model developed here includes only specific ingredients and, therefore, other contributions, as well as the $B^\pm \to \pi^\pm \pi^+ \pi^-$ decay amplitude symmetrization, are lacking and would be interesting to be considered to describe more details of other regions of the phase space [63].

2.1.3 $B \to \pi\pi\pi$ **decay**

The first step is to carry out the fit of the integrated Eq. (2.35) to the measured CPV distribution over the low $\pi^+\pi^-$ invariant mass projection for the $B^\pm \to \pi^\pm\pi^+\pi^-$ decay in the region $\cos\theta > 0$. This decay channel has two identical pions in its final state and, as discussed, the necessary symmetrization effects are not taken into account in the developed model. It is expected that this deficiency of the model might spoil some regions of the fitting and, hence, some study to minimize the negative impact is needed. This can be done by examining Fig. 2.4, from where it is possible to conclude that the CP asymmetry is mostly affected for $\cos\theta < 0$ when $m_{\pi^+\pi^-}$ is high, while the effect is minimum for $\cos\theta > 0$. The angle θ, as already mentioned (see Fig. 2.3), is the angle between the equally-charged pions, i.e. π'^+ and π^+. The CP symmetry is sensitive to the invariant mass of the system (π'^+, π^-), but if it is correctly symmetrized θ and $\pi - \theta$ should produce the same result. Figure 2.4 shows that when $\cos\theta < 0$ the invariant mass of the pair containing
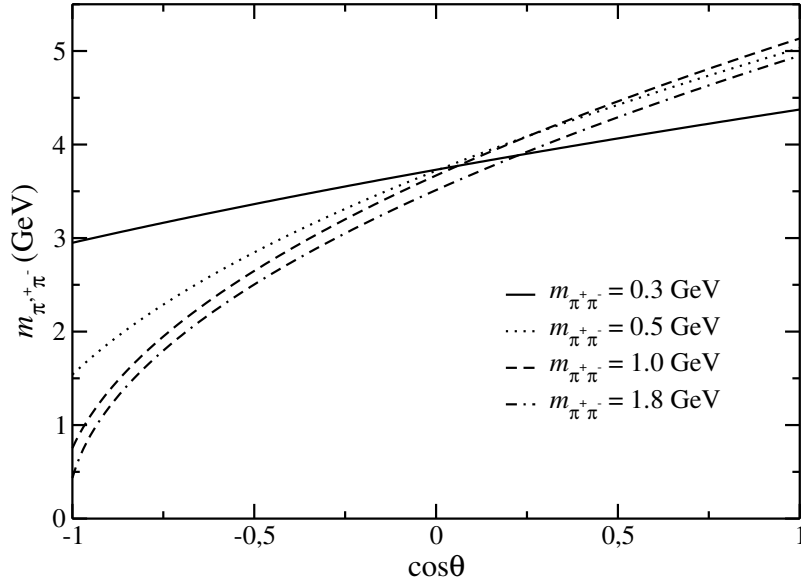
Figure 2.4. $m_{\pi'^+\pi^-}$ as a function of $\cos\theta$ for some particular values of $m_{\pi^+\pi^-}$.

the bachelor particle stays below ≈ 3 GeV. The plot shows the invariant mass of the system (π'^+, π^-), for fixed invariant mass of the system (π^+, π^-), that contains the interaction. Since the region of interest here is under 1.6 GeV, it can be affected by the lack of symmetrization of the decay amplitude if the fit is performed for $\cos\theta < 0$. Meanwhile, for $\cos\theta > 0$, $m_{\pi'^+\pi^-} \gtrsim 3$ GeV, what reduces the lack of symmetrization effects in the range under study $(m_{\pi'^+\pi^-} < 1.6$ GeV). Choosing the less affected region is, obviously, a palliative measure and the symmetrization effects need to be studied with more care in the future. The symmetrization of the decay amplitude could considerably increase the number of free parameters if the relations between the partonic amplitudes are not carefully considered, as twice as many terms will be present in the CPV expression. Moreover, following the discussion above, not using the data for $\cos\theta < 0$ to find the fitting parameters will ensure more reliable results, even if the model misses the Bose symmetrization of the decay amplitude.

The fitting outcome is shown in Fig. 2.5a, while the right side of Fig. 2.5 displays each individual non-zero term. All these contributions are locally consistent with CPT, as explained in detail in Ref. [20], which means that the integration over the phase space of each contribution is vanishing individually. More explicitly, these terms are: 1) the $\pi^+\pi^- \to K^+K^-$ rescattering amplitude, with coefficient $\mathcal{B}$; 2) both real and imaginary parts of the interference between the ρ Breit-Wigner and the non-resonant amplitudes, corresponding to the $\mathcal{D}$ and $\mathcal{E}$ parameters; and 3) the interference between the imaginary part of the ρ and the $f_0(980)$ Breit-Wigner amplitudes, where the coefficient is $\mathcal{G}$. It is notable the fact that each term contributing to the fitting is clearly related to a particular structure in the CPV dynamics. As measured by LHCb, ρ is the main resonance in the $\pi\pi\pi$ phase space and its spin structure is clearly seen in Figs. 2.5 and 2.6, with the CP asymmetry changing sign almost exactly at the ρ mass. This structure is also locally CPT invariant, as it vanishes when the term of $\mathcal{D}$ integrated over $m_{\pi^+\pi^-}$ and when the term of $\mathcal{E}$ is integrated over the whole phase space (including over $\cos\theta$). The presence of the amplitude related to the scalar meson $f_0(980)$ is also consistent with the known dynamics and, analogously, the term of $\mathcal{G}$ vanishes when integrated over the phase space. Exploring the dynamics at this level of detail for these decays within an explicitly CPT invariant model was never considered before in the literature.
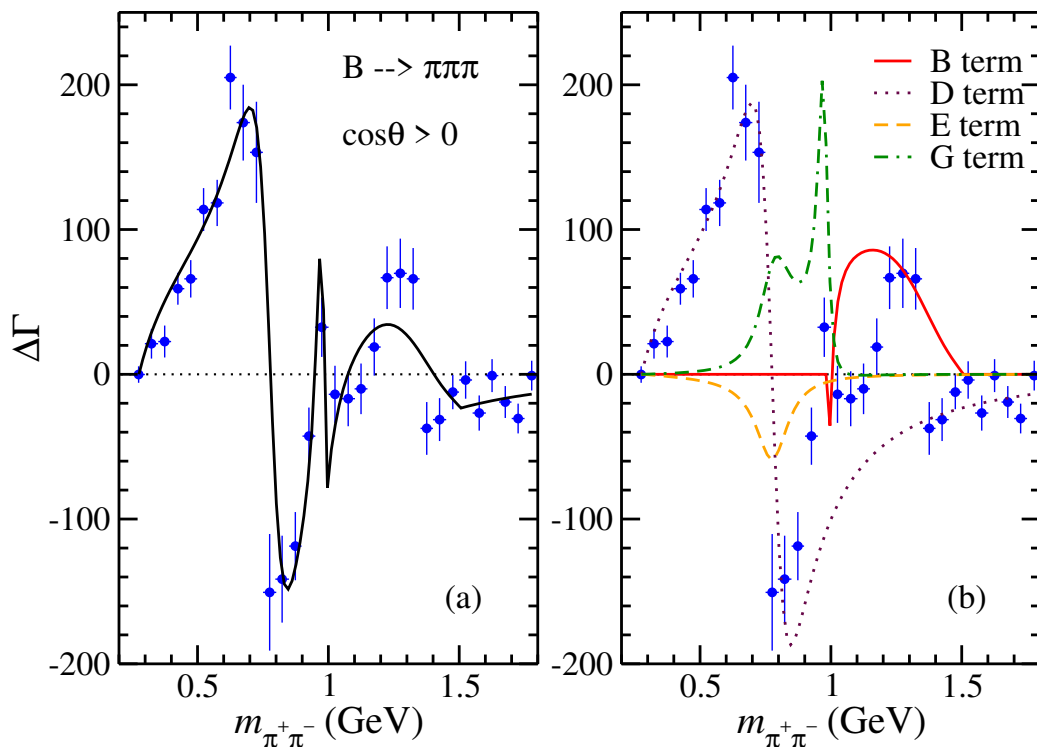
Figure 2.5. CP violation distribution in the $B^\pm \to \pi^\pm\pi^+\pi^-$ decay. Solid line: fit of the experimental data by using the integrated Eq. (2.35) ($\cos\theta > 0$). (a) total and (b) individual contributions. Dots: experimental data from Fig. 4c of Ref. [63]. Notice that B, D, E and G are the same as, respectively, $\mathcal{B}$, $\mathcal{D}$, $\mathcal{E}$ and $\mathcal{G}$.

All the explicit values of the non zero parameters obtained in the fit are presented

in Table 2.1. The contributions from the amplitudes of the parameters $\mathcal{D}$ and $\mathcal{E}$ are related to the ρ meson and are especially significant for the real part of the Breit-Wigner, while $f_0(980)$ appears only in the interfering term with ρ, that is related to $\mathcal{G}$. In the rescattering region, i.e. between 1 and 1.6 GeV, the $\pi^+\pi^- \to K^+K^-$ amplitude ($\mathcal{B}$ term) dominates, as anticipated in Ref. [16]. The asymmetry related to the rescattering amplitude, unlike the other terms, is not locally CPT invariant[3] and, therefore, does not vanish when integrated over the phase space. Due to the inelastic scattering, this CPV is distributed between different channels, as previously explained. The key coupled channel in this case is $B^\pm \to \pi^\pm K^+K^-$, and should have an equal amount of CP asymmetry as $B^\pm \to \pi^\pm\pi^+\pi^-$ between 1 and 1.6 GeV but with an opposite sign. This will be checked as follows.

$\mathcal{B}$	-24.02 ± 3
$\mathcal{D}$	7.82 ± 0.6
$\mathcal{E}$	-1.23 ± 1
$\mathcal{G}$	-0.534 ± 0.3
χ^2/ndf	$42.48/26$

Table 2.1. Non zero parameters, outcome of the fitting procedure for Fig. 2.5. All the other parameters of Eq. (2.35) are zero. The value of χ^2 for the fitting is also presented. The errors of the parameters give a rough estimate on how important the correspondent term in Eq. (2.35) is to the fit. This combination of free parameters is the one that gives the best fit, all the others are zero, either due to CPT invariance or for decreasing the quality of the fit.

One can use the parameters found through the fitting procedure to fix Eq. (2.35) and compare it with the data in the $\cos\theta < 0$ region. It is expect that this region will not be perfectly represented, due to the issues mentioned above, but it is interesting to check if the main physical features can be represented. This is done in Fig. 2.6a, where it is seen that, although with discrepancies, the plot is mostly in fair agreement with experimental data. Mainly two regions are not reproduced, specifically: below the $\rho(770)$ meson mass and just above 1 GeV, where the main contribution comes from the $\pi^+\pi^- \to K^+K^-$ rescattering amplitude. Following the symmetrization arguments obtained through Fig. 2.4, the main suspicion is that the disagreements are related to an interference between ρ and $\pi^+\pi^- \to K^+K^-$ amplitudes in the crossing channels, since for the data above 1 GeV the $m_{\pi'^+\pi^-}$ invariant mass for $\cos\theta \lesssim -0.75$ can be even below 1 GeV in the crossing channel. Again, the contributions term-by-term, which are the same as before but now for negative $\cos\theta$, are also shown in Fig. 2.6b.

Besides the ones already mentioned, other structures could improve the model and its representation of the data in the region below the ρ mass. For instance, the explicit inclusion of the s-wave $\pi\pi$ elastic scattering amplitude also given in [57]. Furthermore, the scalar resonance $f_0(500)$ [68], also called σ resonance, could improve the matching of the model with the data for low two-body invariant mass, as

---

[3]The asymmetry is not locally CPT invariant if it does not vanish when integrated over the phase space of the decay channel under scrutiny.
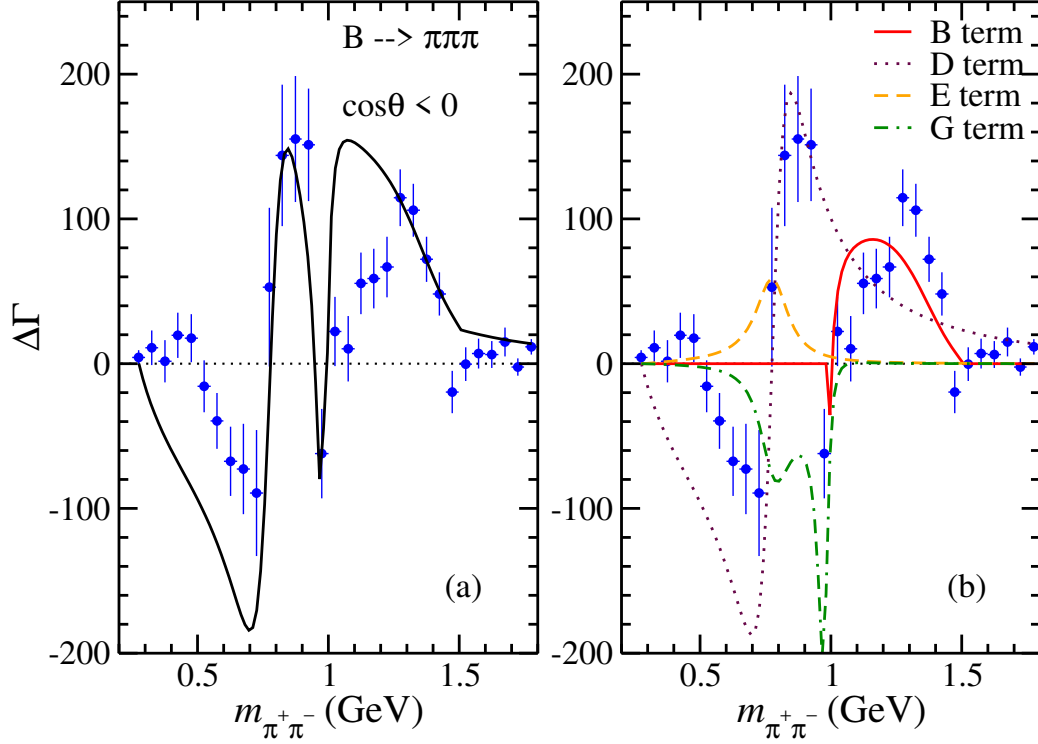
Figure 2.6. CP violation distribution in the $B^{\pm} \to \pi^{\pm}\pi^{+}\pi^{-}$ decay from the integrated Eq. (2.35) ($\cos\theta < 0$) compared with the experimental data (dots). (a) total and (b) individual contributions. Experimental data from Fig. 4d of Ref. [63]. Notice that B, D, E and G are the same as, respectively, $\mathcal{B}$, $\mathcal{D}$, $\mathcal{E}$ and $\mathcal{G}$.

suggested in Ref. [69]. Worth noting that including such structures in the formalism needs to be done with care, in order to avoid double counting.

Just as an exercise, the simplified Eq. (2.37) can be used in the fitting, but now without the form factors $\left(1 + \frac{s}{\Lambda_{\lambda}^2}\right)^{-1}$, what can be done, for instance, by making $\Lambda_{\lambda} \to \infty$. It is seen in Fig. 2.7 that the form factor hardly changes the shape of the fit, which is good since its simple structure should not affect the main points under study.

2.1.4 $B \to \pi KK$ decay

After fixing the parameters through the fitting of the $\pi\pi\pi$ channel, the CP asymmetry in the respective coupled channel is obtained as an outcome that can be compared with experimental data. The CP violation formula for the coupled channel, $B^{\pm} \to \pi^{\pm}K^{+}K^{-}$, derived from Eq. (2.26) and integrated over $\cos\theta$, reads

$$\Delta\Gamma_{\pi KK}(s) = -\frac{2\mathcal{A}}{a'(s)\sqrt{s - 4m_K^2}\left(1 + \frac{s}{\Lambda_{\lambda'}^2}\right)^2} - \frac{2\mathcal{B}\sqrt{1 - \eta^2(s)}\cos[2\delta_{\pi\pi}(s)]}{a'(s)\sqrt{s - 4m_K^2}\left(1 + \frac{s}{\Lambda_{\lambda}^2}\right)\left(1 + \frac{s}{\Lambda_{\lambda'}^2}\right)},$$

$$(2.38)$$
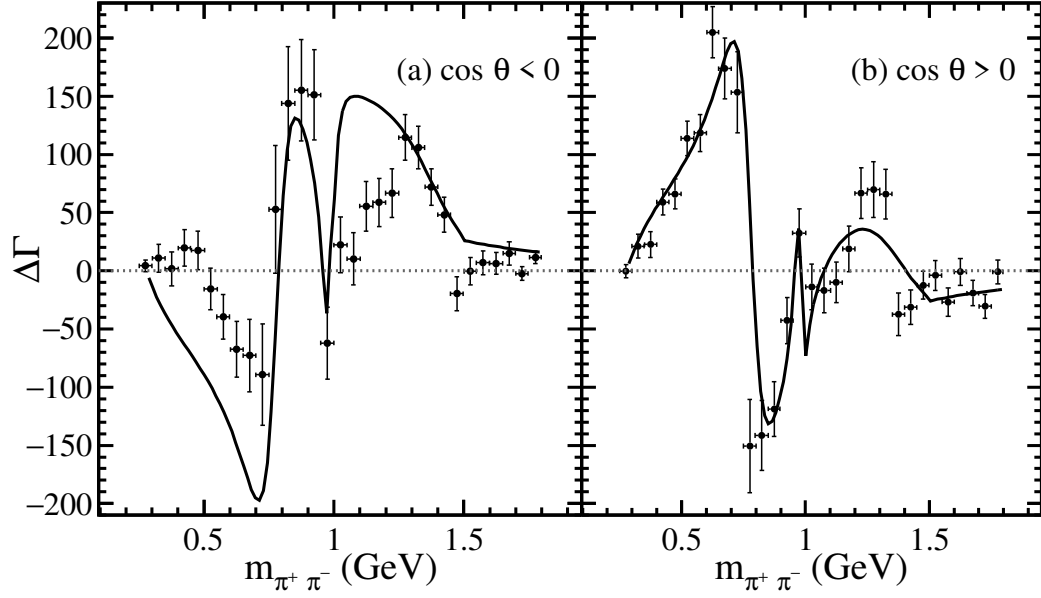
Figure 2.7. Same as Figs. 2.6a (left) and 2.5a (right), but without the partonic amplitude form factor in the integrated CP asymmetry (solid lines) formula (2.37).

where $a'(s)$ is the the kinematical factors coming from the angular integration and is written as

$$a'(s) = \frac{1}{(s - 4m_K^2)^{1/2} \left[\frac{(M_B^2 - m_\pi^2 - s)^2}{4s} - m_\pi^2 \right]^{1/2}}, \qquad (2.39)$$

where the factor $\sqrt{s - 4m_K^2}$, namely the kaon momentum in the rest frame of the KK subsystem, is the main difference with respect to the kinematical factor of the $\pi\pi$ channel. Due to the fact that the formalism fulfills the CPT constraint, by integrating the decay width of Eq. (2.35) over $\cos\theta$ one gets precisely Eq. (2.38) integrated over the phase space but with opposite sign, i.e. $\Delta\Gamma_{\pi\pi\pi} = -\Delta\Gamma_{\pi KK}$. Evidently, this is valid only above the KK threshold, since only in that region the channels are coupled by the $\pi\pi \to KK$ rescattering. As in this region there are no resonant effects, the only two remaining terms are the ones with parameters the $\mathcal{A}$ and $\mathcal{B}$ in Eq. (2.35), of which only $\mathcal{B}$ is non-zero from the fitting procedure.

As opposed to the $\pi\pi\pi$ channel case, Eq. (2.38) is not separated into two kinematical regions and is simply obtained by adding the contributions detailed in Figs. 2.5 and 2.6 for the term which contains the $\pi^+\pi^- \to K^+K^-$ amplitude. The reason is that LHCb presented the sum of events in the $\cos\theta < 0$ and $\cos\theta > 0$ regions for this decay. The result is compared with the experimental data in Fig. 2.8. The figure shows a fair agreement between the outcome of the model and the experimental data. Although a small discrepancy is seen, it is essential to bear in mind that there is an uncertainty present in the model, coming from the $t_{\pi\pi\to KK}$ parametrization, that is not explicitly shown in the plot. Worth repeating that CPT is conserved, what can be demonstrated by summing all CP asymmetry contributions

obtained for $B^\pm \to \pi^\pm \pi^+ \pi^-$ and $B^\pm \to \pi^\pm K^+ K^-$ decays within the model, in the region of two-body invariant mass ($m_{\pi^+\pi^-}$ and $m_{K^+K^-}$) below 1.6 GeV. This is remarkable, showing that, at least for some cases, not many decay channels need to be considered in order to verify explicitly CPT invariance.
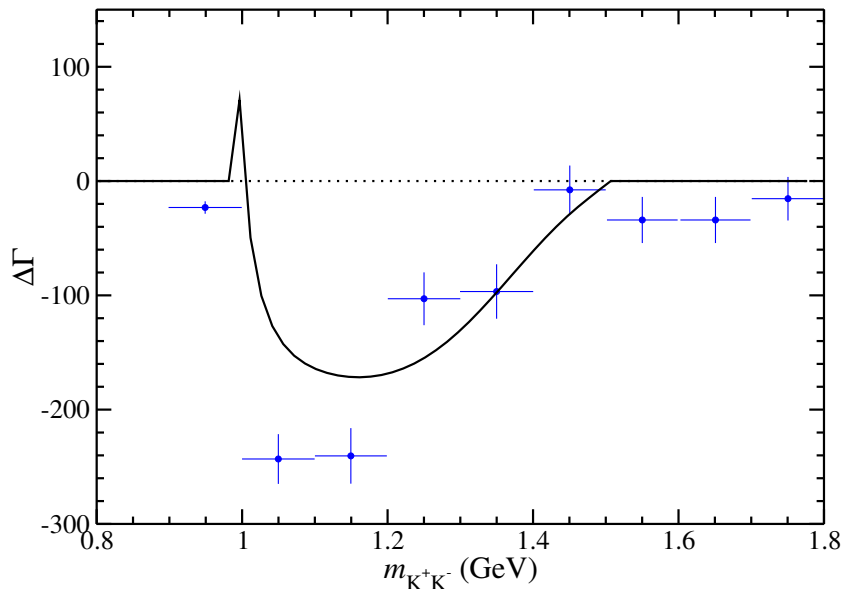
Figure 2.8. CP violation distribution $\Delta\Gamma$ given by Eq. (2.38) compared with the experimental data (points) for the $B^\pm \to \pi^\pm K^+ K^-$ decay. Experimental data from Fig. 7b of Ref. [63].

The same procedure can be followed for the two other channels measured in Ref. [63], i.e. $B^\pm \to K^\pm \pi^+ \pi^-$ and its coupled channel $B^\pm \to K^\pm K^+ K^-$. In these decays, the number of measured events is about an order of magnitude bigger than the ones analyzed before, what enables a more reliable and constrained fit. Additionally, no symmetrization effect occurs in the fitted channel, $K\pi\pi$, which makes irrelevant which region of $\cos\theta$ is chosen for obtaining the partonic amplitudes $(\mathcal{A}, \cdots, \mathcal{Q})$. In this decay the most stable region for the fitting is $\cos\theta < 0$, given that this part of the phase space emphasizes better the structures included in the model. Further investigation needs to be done on the $\cos\theta > 0$ region of the phase space, as its dynamics presents a new feature not yet clarified. A suggestion made in Ref [16], within the confines of the present formalism, is the possible existence of double charm meson rescattering extending to high two-body invariant mass. This would mean that strong coupling of type $\pi\pi \to D\overline{D}$ or similar would be distributing CPV between channels, $D\overline{D}K \to KKK$ or $K\pi\pi$, in that region. As this effect is far from the KK threshold and above 1.6 GeV, under investigation here, and can be avoided by neglecting the $\cos\theta < 0$ distribution, only $\cos\theta > 0$ will be treated here.

2.1.5 $B \to K\pi\pi$ decay

The best fit for the $K\pi\pi$ channel of the integrated Eq. (2.35) includes the terms with the following parameters: 1) $\mathcal{B}$, which refers to the CPV flow to the coupled channel KKK; 2) $\mathcal{F}$ and $\mathcal{G}$, associated to the real and imaginary parts of the interference

between the ρ and $f_0(980)$ resonances; and 3) $\mathcal{D}$, which is related to the interference of the F_ρ^{BW} real part with the non-resonant partonic amplitude. This is shown in Fig. 2.9a, where the best fit to the $\cos\theta < 0$ region is presented. In Fig. 2.9b the individual components are displayed. Again the same exercise as before can be done, by integrating each contribution over the phase space to verify CPT invariance, and all the present contributions vanish except the term of $\mathcal{B}$. This is a consequence of the CP asymmetry in that region being distributed to a different channel, which should have an equal amount, with opposite sign, of CPV events. As mentioned, the coupled channel in this case is $B^\pm \to K^\pm K^+ K^-$.

The main resonant structure present in the $B^\pm \to \pi^\pm \pi^+ \pi^-$ decay, as pointed out experimentally, is $f_0(980)$, although ρ exists in smaller amounts. Following the BSS mechanism and thinking on the possible partonic diagrams for this amplitude one also notices the possibility of quark transitions where $f_0(980)$ appears in the final state. It is evident from the fit that this resonant structure appears as expected. Looking at Fig. 2.9b one notices that the interference between real parts of ρ and $f_0(980)$ is the dominant term. Although present, the imaginary part is less relevant. Above the KK threshold, as usual, the term that contains the $t_{\pi^+\pi^- \to K^+K^-}$ amplitude dominates, with the amplitudes associated to the ρ resonance appearing with smaller contributions. The explicit values of the non zero parameters obtained in the fit are shown in Table 2.2.
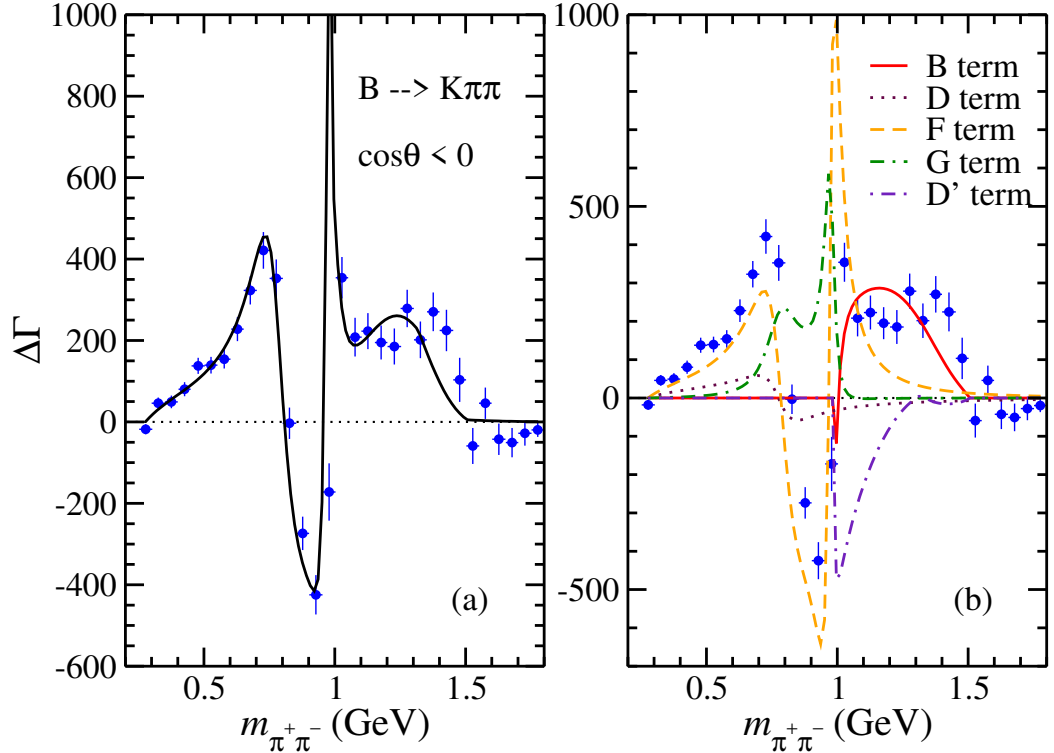
Figure 2.9. CP violation distribution for the $B^\pm \to K^\pm \pi^+ \pi^-$ decay ($\cos\theta < 0$ region) through the integrated Eq. (2.35) fitted to the experimental data (points), presented in Fig. 5c of Ref. [63]. (a) total and (b) individual contributions. Notice that B, D, F, G and D' are the same as, respectively, $\mathcal{B}$, $\mathcal{D}$, $\mathcal{F}$, $\mathcal{G}$ and $\mathcal{D}'$.

$\mathcal{B}$	-80.23 ± 8
$\mathcal{D}$	-2.437 ± 1
$\mathcal{F}$	-4.48 ± 0.6
$\mathcal{G}$	1.541 ± 0.3
$\mathcal{D}'$	57.41 ± 13
χ^2/ndf	$31.18/25$

Table 2.2. Non zero parameters, outcome of the fitting procedure for Fig. 2.9. All the other parameters of Eq. (2.35) are zero. The value of χ^2 for the fitting is also presented. The errors of the parameters give a rough estimate on how important the correspondent term in Eq. (2.35) is to the fit. This combination of free parameters is the one that gives the best fit, all the others are zero, either due to CPT invariance or for decreasing the quality of the fit.

2.1.6 $B \to KKK$ decay

Once the parameters are fixed through the fitting, it is time to compare the outcome of the rescattering term with the coupled channel to check if it can describe the data and provide CPT invariance in that region, i.e. $\Delta\Gamma_{K\pi\pi} = -\Delta\Gamma_{KKK}$. From the B^- and B^+ event distribution, the measured CP violation enclosing the sum of events for $\cos\theta < 0$ and $\cos\theta > 0$ provided by LHCb, as done for the $B^\pm \to \pi^\pm K^+ K^-$ decay, is compared to the model in Fig. 2.10. As seen in the figure, for the experimental data concentrated in the region above 1 GeV the shape of the curve is the same of Eq. (2.38). The only difference in this case, due to the different mesons in the final state, is in the kinematical factor $a'(s)$ (2.39) which needs the substitution $m_\pi \to m_K$ in order to be consistent with the new case. Again, the only non-zero parameter in the region is $\mathcal{B}$ of Eq. (2.35), fixed by the fitting of the CP asymmetry performed for the $B^\pm \to K^\pm \pi^+ \pi^-$ decay channel. The agreement is clear and gives a robust evidence of the importance of the strong coupling between the channels under discussion. The connection between the CP asymmetry of these channels was explored for the first time in this study and is another notable indication of the strong coupling between channels by final state interactions.

2.1.7 The main input: scattering matrix

At this point, the formalism showed to be very successful in the description of CP violation distributions in heavy meson three-body decays. Evidently this was verified studying specific decay channels and taking into account their essential features. The major lessons learned are: CPT can be a practical constraint and strong interaction among the final state mesons can distribute the CPV among specific decay channels, sometimes even only two of them. This is remarkable and allows one to think about other examples that could be explored within this idea. As discussed at the end of Sec. 2.1.4, strong couplings of the type $D\overline{D}K \to KKK$ or $K\pi\pi$ could be related to the interference seen in the CP asymmetry pattern of the decay $K\pi\pi$ in a region of the phase space. The successful application of the model for the studied decays opens the way for exploring the strong coupling through final state interactions in other decays, and the goal of this section is to discuss simple alternatives to promote
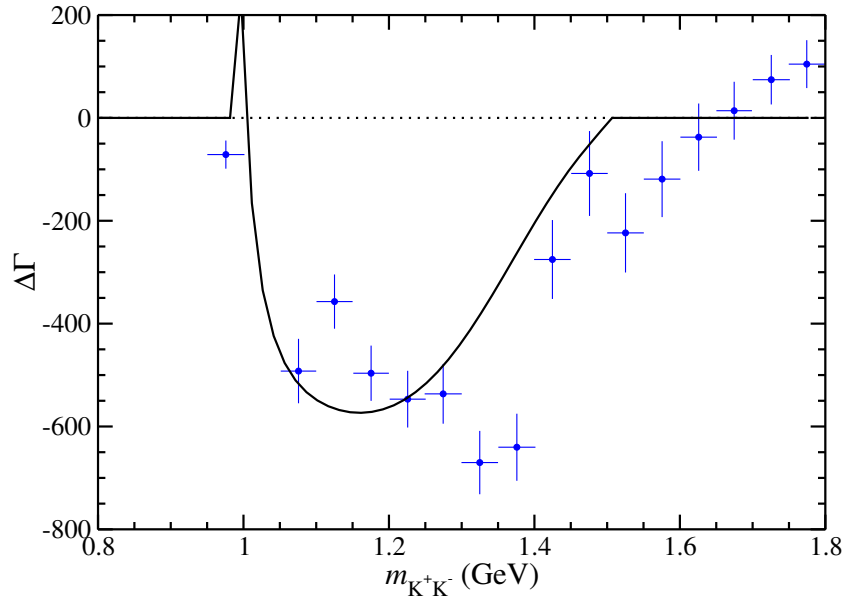
Figure 2.10. CP violation distribution for the sum of both $\cos\theta$ regions in the $B^{\pm} \rightarrow K^{\pm}K^{+}K^{-}$ decay. Experimental values (points) from Figs. 6c and 6d of Ref. [63].

this study. The aim is to discuss this idea still in the context of B decays in three light pseudoscalars, but now for two-body invariant mass around 4 GeV, i.e. above the $\bar{D}D$ threshold, always taking into account final state interactions and the CPT constraint.

In a general manner, while two-body B decays are extensively explored in the literature, three-body ones still have a lot to be understood. Considering the $2+1$ factorization, i.e. a three-body decay with a non-interacting particle, the properties of two-body decays can be used to explore three-body decays. Obviously, that involves neglecting three-body rescattering effects, as done in the formalism treated in the previous sections. The dynamics in three-body decays, even when considering only two-body interactions, is far more challenging, since their phase space, also called Dalitz plot, depends on two kinematical variables that can assume various values. If soft final state interactions, meaning the ones happening once the final state hadrons are formed, are relevant for specific two-body scattering processes, one can assume that it might contribute to three-body decays with same final state mesons. That is possible as the B meson initial energy can be more distributed between the meson pair and the non interacting particle, allowing the pair to rescatter to different configurations. Some examples and discussions from the literature, which brings possible arguments while supporting FSI of the type $DD' \rightarrow PP'$, (D, $D' \equiv$ charmed mesons, P, $P' \equiv K, \pi$), will be discussed in what follows.

Bander-Silverman-Soni, in their seminal paper [6], already put into discussion quark reactions from the b−quark involving $c\bar{c}$ intermediate states. For instance, within the BSS mechanism the process $b \rightarrow c\bar{c}s \rightarrow u\bar{u}s$ emerges contributing to the absorptive part, i.e. strong phase, of the penguin diagram. Low-energy hadronic FSIs could play that role if the $c\bar{c}$ pair is understood as a double charm meson which connects two different channels through inelastic scattering. As previously

shown, that transition allows CPV consistent with CPT constraint in the formalism developed here, even if the BSS mechanism is not explicitly taking CPT invariance into account.

The discussion involving CPT invariance within the BSS mechanism was only later properly introduced, by Gérard and Hou in Ref. [70]. The study by Gérard and Hou treated m_c, the charm quark mass, as a free parameter to study how an intermediate channel of the type, e.g., $b \rightarrow sc\bar{c}$ opens. Thereafter, they could examine the absorptive part, from the timelike gluon propagator, arising, depending on whether or not the internal legs goes on-shell for $q^2 > m_c^2$ [71]. Although their study was not directly associated to soft FSIs, it shows the concern of implementing the fundamental CPT symmetry into CP violation studies.

One essential discussion is whether the effects from the penguin absorptive parts, also known as hard FSI, are surpassed by hadronic FSI in two-body modes. As discussed in Ref. [70], that would make it even more challenging to describe exclusive partial rate asymmetries, given that the involved inelastic phase-shifts are problematic to be measured. Hadronic FSIs causing CPV in B meson decays was firstly pointed out by Wolfenstein, in 1991 [12], where the idea was to carry out the partial wave decomposition of the scattering amplitude, taking into consideration strong phase shifts to write down the decay amplitude. This is, of course, an inspiration of the model developed in Refs. [16, 20]. Wolfenstein's formalism was also particularly interesting for conserving CPT explicitly. This type of formalism, although very promising and theoretically consistent, depends on the knowledge of the possible mesonic rescatterings, i.e. on the S-matrix, which can end on the final state under study to understand the CPV distribution in that specific decay channel.

Although various intermediate transitions can influence the CPV dynamics in three-body decays, as for example when involving double charm mesons as $D\bar{D} \rightarrow PP$, inelastic rescattering processes of the type are poorly explored in the literature, both theoretically and experimentally. However, there are some relevant studies performed in the two-body decay context that could be used to understand three-body decays. For instance, the initial pictorial idea for the $B \rightarrow \pi\pi$ decay was the B meson decaying into a colorless $q\bar{q}$ state with high relative momentum, what would bring small FSI effects in the $\pi\pi$ channel [72]. Nevertheless, that was indicated to be inaccurate in Ref. [73], where it was shown that the meson-meson s-wave interaction at m_b energies can be large, as soft FSI can eventually grow for high energies. The main point is that perturbative calculations usually miss this feature, as the process has a purely non-perturbative nature. Ref. [74] also discusses the relevance of hadronic FSI in heavy meson decays, where it was shown that the strong phase estimated from the inelastic scattering amplitude can turn significant if the decay ratio of the involved final states are high. The possibility of large effects from scattering phase-shift in two-body B decays was also discussed in Ref. [75]. As a last example, Ref. [76] also discusses inelastic rescattering contributions in the context of coupled-channel approaches, Regge exchanges, as well as the use of other hadronic models applied to study two- and three-body decays.

Many well-known approaches in the literature to deal with heavy meson decays are based on effective field theories, as QCD factorization, perturbative QCD and soft-collinear effective theory. Although they allow deep studies of B meson decays, some aspects are still not clear, particularly in three-body decays. Usually soft

FSI effects are understood to be suppressed in the heavy quark limit, because of cancellations occurring between many intermediate states [77]. However, this was shown to not be always the case for physical values of m_b [78], especially when involving intermediate states with high branching fractions [79]. Ref. [17] brings an interesting set of two-body decays being analyzed under the effects of hadronic final state interactions, with a similar formalism being used to explore the $B \to KK$ decay in [80]. Briefly, their idea is that soft FSI can enhance considerably color-suppressed neutral modes, what affects considerably the CP violation distribution from pure short-distance physics. It means that intermediate hadronic channels, e.g. $B \to D_s \bar{D} \to K\pi$ and $B \to D\bar{D} \to \pi\pi$, can produce sizable impact on the CP asymmetry. If this type of process can be relevant at the two-body level, one could expect even higher contributions to three-body decays as the rescattering process can happen for different relative energies between the mesons and affect the dynamics in broad regions of the phase space. As said, obtaining the scattering amplitude is the major challenge while trying to take into account rescattering processes in the decay amplitude. However, models like the one in Ref. [17] can shed some light on the soft FSI dynamics, even if obtained only for two-body decays as it can be used to settle the normalization of the scattering matrix element. In the three-body context, the hadronic transition has to be known with its dependence on the scattering energy, starting from the opening channel threshold energy, e.g. DD', preferably over the whole phase-space. It is a quite intriguing task the development of models that can describe that dynamics. One promising path, based on lattice QCD calculations, has been the study such as the one done for the P-wave $\pi\pi \to KK$ coupled-channel, and some others, in Ref. [81]. Worth mentioning some other papers dealing with the parametrization of matrix elements to take into account long-distance effects [82] and a discussion on allowed regions for soft FSI within QCD factorization [83].

Given the need of new S-matrix models bringing the necessary inputs for CP violation studies under the effect of final state interactions, a simple idea is sketched below. This might be a useful start to account for the contribution coming from coupled channels involving two light pseudoscalars and two charmed mesons, which can be playing a role in the CPV distribution recently released by LHCb for high KK, $\pi\pi$, $K\pi$ invariant masses of three-body B decays [18].

The goal is to sketch a simple relativistic S-matrix model that describes inelastic meson-meson rescattering. The parametrization should consider relevant physical ingredients involved in the process. Firstly, thinking about the S-matrix modulus, the two-meson inelastic collision is simply approximated by the annihilation of the initial hadronic states producing a $q\bar{q}$ pair which recombines and generates the final state particles. Implementing the idea is based on three assumptions: 1) the intermediate propagation has a damping factor like s^{-1}; 2) the meson breakup into the $q\bar{q}$ pair, which creates an imbalance in the relative momentum, goes as $\approx \sqrt{s}$; and 3) a factor going as s^{-1} related with the threshold behavior. The threshold behavior also depends on the relative momentum of the intermediate $q\bar{q}$ pair, as well as on its valence wave function asymptotic behavior (for energies $\approx m_b$). One can use Ji's [84] idea on the s-wave valence light-cone wave function to fix its asymptotic behavior, which goes as $k_\perp^{-2}$ in the transverse momentum. For the sake of simplicity, his can be translated into a s^{-1} damping factor. All the aforementioned factors together suggest that the S-matrix element should have a suppression that goes as s^{-3}. One can

now include the threshold energy, s_{th}, obtaining for the Lorentz invariant S-matrix element a dependence as $\mathcal{N}\sqrt{s - s_{th}}/s^{3.5}$, where $\mathcal{N}$ is a normalization factor to ensure the matrix element to meet unitarity. This parametrization, although simple, is consistent with the s-wave isospin-zero $\pi\pi \to \pi\pi$ scattering matrix obtained in Ref. [85], being able to reproduce the respective experimental data if taken into account the proper parameters, as shown in Fig. 2.11. Worth mentioning that the parametrization is also perfectly consistent with the inelastic scattering transition of Ref. [57]. Once the modulus has its shape developed, it is time to discuss the
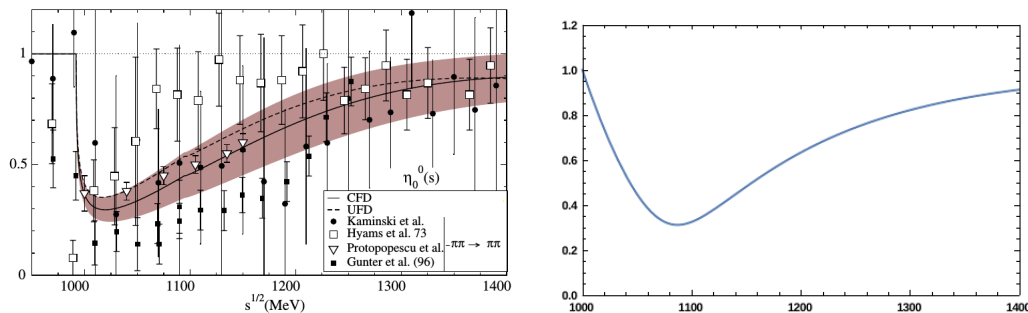
Figure 2.11. (Left panel) Comparison of the s-wave $I = 0$ $\pi\pi$ inelasticity parameter proposed in [85] with the experimental data. Figure taken from Ref. [85]. (Right panel) The simple parametrization suggested in the text.

phase-shift parametrization. The scattering matrix, assuming only two channels, is a unitary SU(2) matrix with three unknown independent parameters, i.e. the inelasticity η and the two phase shifts, for say $\delta_{PP'}$ and $\delta_{DD'}$. One usual way of writing the S-matrix diagonal element in terms of the phase-shift and consistent with unitarity is given by

$$S_\lambda = \eta e^{2i\delta_\lambda} = \frac{k\cot\delta_\lambda + ik_\lambda}{k\cot\delta_\lambda - ik_\lambda}, \tag{2.40}$$

where $k_\lambda = \sqrt{s - s_{th\lambda}}/2$ is the kinematical factor that takes into account the λ channel threshold.Two channels, represented by the $S_{DD'}$ and $S_{PP'}$ matrix elements, are considered. In its explicit form, the S-matrix is then assumed to have a pole in $k\cot\delta$ with momentum $s = s_0$, i.e.

$$k\cot\delta_{PP'} = -\frac{c}{(1 - k_{PP'}/k_{0PP'})}, \tag{2.41}$$

where $k_{0PP'} = \sqrt{s_0 - s_{th\,PP'}}/2$. The pole represents a node in the projected CP violation distribution or, physically, a virtual bound state in the charmed two-meson decay channel. At the threshold momentum this virtual bound state actually exists, as shown in the previous sections and also in Ref. [20]. The c parameter has dynamical origin as it constitutes the residue of the pole in $k\cot\delta$ of the PP' (light pseudoscalars) phase-shift. The remaining parameter, for the $S_{DD'}$ matrix element, is introduced as a (virtual or real) bound state represented by a scattering length and introduce a node in the PP' channel. In the unitary limit, the scattering length can take the limit $a \to \infty$ with no changes in the result.

The aforementioned idea, of introducing a zero in the S-matrix, is inspired by its non-relativistic counterpart known as the Ramsauer-Townsend effect. The effect manifests precisely as a minimum (or a zero) in the scattering amplitude. Although simple, the parametrization developed above can be further explored and used to fit the experimental data. It can also have its parameters fixed from models available in the literature in order to determine the non-diagonal strong S-matrix elements, which is the main ingredient to explore the compound CP violation. Efforts in this direction, using elements of the parametrization explained, have been made recently in Refs. [86].

2.2 CPT and CP asymmetry suppression in $B \to PV$ decays

As mentioned before, the main theoretical approaches in the literature nowadays applied to perform calculations on CP violation for B decays are based on short distance factorization and do not incorporate CPT invariance explicitly. Apart from that, if the CP asymmetry does not vanish after integrated over the phase space of a decay channel it must exist an equal sum, with opposite sign, distributed among other decay channels. Depending on how many existing coupled channels, verifying that explicitly can be very challenging. However, the mechanism responsible to distribute the CPV among different channels, that is to say final state interactions, is in general quite restrictive. In particular, for processes involving one pseudo-scalar and one vector particle in the final state, i.e. $B \to PV$, the CPV from quark-level processes might be suppressed if CPT invariance is explicitly taken into account.

This section presents a simple and straightforward consequence of the CPT invariant model developed previously. The content presented in this section was published in Ref. [24], where a simple model was developed to analyze CPV in regions of three-body phase spaces involving intermediate vector mesons. The model is particularly interesting due to its simple and practical structure, avoiding the need of a full amplitude analysis.

Short distance approaches are based on the fact that the strong coupling constant is small, due to the nature of the process mainly dominated by high energy interactions, thus allowing the use of pertubation theory techniques. Nevertheless, most QCD processes involve color confinement, particularly when hadrons are formed, requiring a non-perturbative treatment. To account for that, the idea is to break the decay amplitude into two parts, one perturbatively calculable, enclosing the short distance portion, and the other one taking part of the non-perturbative long distance physics. The latter effects are usually obtained from global fits to experiments, as theoretical calculations are quite challenging. The factorization idea applied to B meson decays started with the so-called Naive factorization approach (NF) [87], which combined with ideas of the seminal paper by Lepage and Brodsky [88] originated the leading frameworks in use nowadays, i.e. QCD factorization (QCDF) [89], perturbative QCD (pQCD) [90] and soft- collinear effective theory (SCET) [91]. Although attempts to include hadronic effects has been done [92], those approaches focus mostly on the quark-level perturbative processes. It is worth also mentioning that mostly the non-perturbative frameworks explored in the literature are based on

the flavour $SU(3)$ symmetry approach used in Refs. [93].

One common characteristics of the aforementioned approaches is that they hardly discuss the consequences that CPT invariance imposes on the decay amplitude, hoping that many hadronic channels, involving various numbers of final state mesons, would be coupled through rescattering processes. This supported the idea that CPT is hardly verifiable in practice for charmless B decays [94]. As discussed beforehand, experimental data has been extensively suggesting that multi-meson rescattering is unlikely to be the ruling process in charmless multi body B decays [16, 20]. As also has been discussed here for three-body B decays, LHCb measurements [18] show that mostly two-body interactions and low mass resonances are the dominant leading processes, causing the event distribution to occupy mainly the edges of the phase space.

The noteworthy compilation carried out in Ref. [95] brings results of CP asymmetries and branching ratios for several two-body charmless B decays and constitutes an interesting indication for the CP asymmetry suppression idea presented here. The disagreement between the experimental data and theoretical calculations, arising from different frameworks, highlights a poor understanding of the CP asymmetries, particularly for decays like $B \to PV$. This is remarkable and suggests that something special happens for decays involving one pseudoscalar and one vector meson. Another peculiarity of this kind of decays is that their observables are effectively measured from three-body phase spaces, making three-body data also useful to indirectly study two-body decays involved in the phase space dynamics. Following the discussion above, the idea is to consider in a general manner the possible hadronic processes involved in $B \to PV$ decays, as well as to build a simple formula to extract their CP asymmetry from the three-body phase space without relying on complicated amplitude analysis.

Dealing with more specific cases, available theoretical calculations of $B \to PV$ decays are restricted to the ones including low mass vector resonances, like $\rho(770)$, $K^*(890)$ and $\phi(1020)$. The $\rho(770)$ and $K^*(892)$ vector resonances decay always to $\pi\pi$ and $K\pi$, respectively, while $\phi(1020)$ has a considerable branching fraction to $K\bar{K}$ but also decays significantly to three pions through $\pi\rho(770)$ [1]. Moreover, all the approaches, e.g isobar model and K-matrix, applied for the three-body amplitude analysis use the (2+1) factorization, i.e. do not consider three- body final state interaction effects. Therefore, the third particle, the non interacting one, does not affect the intermediate resonances and the CPT constrained model presented in the last section suggests that CP violation could not be possible for the processes involving $V = \rho(770)$ or $K^*(890)$. For charmless B meson three-body decays, this is not a particularly groundless approximation, as the event distribution is almost completely concentrated on the edge of the phase space [18]. Meanwhile, for decays with $V = \phi(1020)$, one could expect perceptible CP asymmetry, though that seems unlikely as the small contribution of tree diagrams suppresses the CPV coming from the BSS mechanism. The last effect that could cause CP asymmetry is the presence of hadronic FSI, which is by itself a constraint regardless what happens at quark-level. The goal below is to discuss the arguments to support, using simple theoretical concepts, that eventual rescattering between mesons in the final state is also suppressed in $B \to PV$ decays.

Even though three-body final state interaction effects are not explicitly taken

into account in the experimental approaches, this is evidently one possible hadronic mechanism that could produce CP asymmetry in $B \to PV$ decays. In this process the rescattering with the non interacting particle would distribute the CP asymmetry among different regions of the three-body phase space. This effect deserves more attention, since one needs a formalism which explicitly takes into account three-body final state interactions and is still CPT invariant. Although this has not been done yet, a formalism for three-body decays based on the Bethe-Salpeter equation will be presented in Sec. 2.3. Within this approach, which is based on the Faddev decomposition, three-body final state interactions are intrinsically deemed and the integral equations are solved perturbatively. The result shows that the three-body final state interaction effect is considerably small with respect to the driving partonic amplitude [25]. Moreover, similar results within the same approach were already obtained for the $D^+ \to K^-\pi^+\pi^+$ decay [58, 59, 96].

Another possibility that can produce CP asymmetry is the inelastic rescattering of the type $PV \to P'X$, with P' and X representing the outbound particles in the scattering process. Analogously, the reverse process could happen, i.e. $XP' \to PV$, where the PV is the outcome of a hadronic rescattering. Calculating the probability for this transition amplitude would require an enormous effort carried out within the QCD framework. However, one can simplify the discussion using the unitary scattering matrix idealized in Sec. 2.1.7, which can already give an idea on whether or not the effect is suppressed. As the probability of the transition is given by the modulus square of the off-diagonal S-matrix element, the phase will not enter in this discussion. In other words, the quantity of interest is the inelasticity, given by $\eta(s) = \sqrt{1 - |S_{PV \to P'X}(s)|^2}$. Following that same discussion, the transition amplitude $S_{PV \to P'X}(s)$ should carry a damping factor that goes, at least, as

$$S_{PV \to P'X}(s) \sim \mathcal{N}\sqrt{s/s_{th} - 1}/(s/s_{th})^{3.5}. \qquad (2.42)$$

As already said, this formula is consistent with other parametrizations made in the literature, as the one for the $s-$wave isospin zero $\pi\pi \to KK$ amplitude of Ref. [57]. As a matter of fact, that amplitude also drops rapidly above $\sqrt{s} \sim 1.6$ GeV. From the S-matrix unitarity, the maximum value that the transition element can reach is constrained. With the purpose of fixing the normalization, one can suppose, for instance, that the maximum value for a particular $PV \to P'X$ process is ~ 0.87, what imposes that $\mathcal{N} = \Lambda^6 = (1.24)^6$. If the threshold is located at $\sqrt{s_{th}} = 2$ GeV, one gets that at the B meson mass $S_{PV \to P'X'}(m_B) \sim 0.014$, suggesting a substantial suppression of the inelastic transition amplitude under consideration. Although the chosen number for the parameters $\mathcal{N}$ and s_{th} are quite arbitrary, it is a conservative estimate and allows to say that no other choices would prevent such a suppression. In short, based on the above simple arguments, one can expect that any hadronic rescattering processes are expected to produce small effects on the CP asymmetry distribution for the $B \to PV$ decay.

2.2.1   A method to extract A_{CP} for $B \to PV$ decays

The model presented below is a particular case of Eq. (2.35) where the hadronic rescattering amplitude is neglected, as this term is meant to be suppressed in the

actual scenario. As an extensive discussion on the model was already made, this section targets to be straightforward. As said, the model aims at circumventing complicated amplitude analysis while obtaining CP asymmetry parameters for decays involving one pseudoscalar and one vector meson. Following the ingredients of the formalism introduced in Sec. 2.1, the key point is to explore the angular distribution coming from the spin one vector meson (2.24) and its interferences with the surroundings on the three-body phase space. This interference usually happens with the resonant amplitudes from light scalar resonances, e.g. the σ, κ, $f_0(980)$ resonances, and can also involve the non-resonant background. The specific type of process which is the main object of interest here is a decay like $B^{\pm} \to P_b^{\pm}(V \to P_1^+ P_2^-)$, where P_b is the bachelor particle and $P_{b,1,2} = \pi$ or K, i.e. the same kind of processes investigated in the previous subsections. Therefore, the decay amplitude is the same as before (2.30), but a new parametrization, more familiar to experimentalists for performing Monte Carlo simulations, will be considered now, namely

$$\mathcal{A}_{0\lambda}^{\pm} = a_{\pm}^V e^{i\delta_{\pm}^V} F_V^{BW} \cos\theta(s_{\perp}, s_{\parallel}) + a_{\pm}^S e^{i\delta_{\pm}^S} F_S^{BW}, \qquad (2.43)$$

where, following the prevalent convention used by experimentalists[4], the dependence on the phase space variables is written in terms of $s_{\parallel} = (p_{P_1} + p_{P_2})^2$ and $s_{\perp} = (p_{P_b} + p_{P_1})^2$. The function $F_{V,S}^{BW}$ is the Breit-Wigner amplitude, Eq. (2.28), meant to account for the scalar (S) and vector (V) resonant amplitudes, while the phases $\delta_{\pm}$ come from the partonic amplitude representing the three-body final state production. Worth mentioning that the second term on the RHS of Eq. (2.43) could instead be a non-resonant background if written as $a_{\pm}^{nr} e^{i\delta_{\pm}^{nr}} F^{NR}$, where F^{NR} represents an arbitrary non-resonant amplitude, without changing the possible applications of the method. The strong phase coming from the hadronic rescattering process is not accounted for those phases. The relations between the parameters of Eq. (2.43) and the decay amplitude introduced previously, of Eq. (2.30), are simply $a_{\pm}^V e^{i\delta_{\pm}^V} = a_0^V + b_0^V e^{\pm i\gamma}$ and $a_{\pm}^S e^{i\delta_{\pm}^S} = a_0^S + b_0^S e^{\pm i\gamma}$.

As discussed before for the $B \to \pi\pi\pi$ decay (2.36), it is convenient to use the phase space variables, $s_{\parallel}$ and $s_{\perp}$, to express the angular distribution related to the vector meson spin of Eq. (2.24), i.e. $\cos\theta(s_{\perp}, s_{\parallel})$. Assuming that the vector meson is in the $s_{\parallel}$ channel, the relation reads [97]

$$\cos\theta(s_{\perp}, s_{\parallel}) = \frac{(m_B^2 - s_{\parallel} - m_{P_b}^2)(s_{\parallel} + m_{P_1^+}^2 - m_{P_2^-}^2) + 2\,s_{\parallel}(m_{P_b}^2 + m_{P_1^+}^2 - s_{\perp})}{\sqrt{\lambda(m_B^2, s_{\parallel}, m_{P_b}^2)}\,\sqrt{\lambda(s_{\parallel}, m_{P_1^+}^2, m_{P_2^-}^2)}}\,,$$
$$(2.44)$$

where m_B is the B meson mass, $m_{P_b}, m_{P_1^+}$ and $m_{P_2^-}$ are the final state meson masses and $\lambda(x, y, z)$ is the triangle (or Källén) function, given by

$$\sqrt{\lambda(x, y, z)} = \left[x - (\sqrt{y} + \sqrt{z})^2\right]\left[x - (\sqrt{y} - \sqrt{z})^2\right].$$

For an illustration of the angle θ, see Fig. 2.3. The formula of Eq. (2.44) is the same that enters in Eq. (2.35) used in the last section, but now not integrated over $s_{\perp}$.

---

[4]For the interested reader, Ref. [97] brings more details on the kinematics of the Dalitz plot.

As usual, to obtain the CP asymmetry formula one needs to simply subtract the B^+ and B^- decay amplitudes square modulus, i.e.

$$
\begin{aligned}
|\Delta\Gamma|^2 &= |\mathcal{A}_{0\lambda}^+|^2 - |\mathcal{A}_{0\lambda}^-|^2 \\
&= [(a_+^V)^2 - (a_-^V)^2]|F_V^{\mathrm{BW}}|^2 \cos^2\theta + [(a_+^S)^2 - (a_-^S)^2]|F_S^{\mathrm{BW}}|^2 + 2\cos\theta|F_V^{\mathrm{BW}}|^2|F_S^{\mathrm{BW}}|^2 \times \\
&\quad \{[(m_V^2 - s)(m_S^2 - s) - m_V\Gamma_V m_S\Gamma_S][a_+^V a_+^S \cos(\delta_+^V - \delta_+^S) - a_-^V a_-^S \cos(\delta_-^V - \delta_-^S)] \\
&\quad -[m_V\Gamma_V(m_S^2 - s) - m_S\Gamma_S(m_V^2 - s))][a_+^V a_+^S \sin(\delta_+^V - \delta_+^S) - a_-^V a_-^S \sin(\delta_-^V - \delta_-^S)]\},
\end{aligned}
$$
(2.45)

which is simply a special case of Eq. (2.35) before the integration over $s_\perp$. Notice that $\cos\theta$ is a shorthand for $\cos\theta(s_\perp, s_\parallel)$. Eq. (2.45) would carry the same essential features if instead of the scalar resonant amplitude a non-resonant amplitude would have been considered, i.e. the coefficients related to BSS mechanism and the interference term would carry the same dependence on $\cos\theta(s_\perp, m_V^2)$.

The method now consists in studying the resonance vicinity, in other words $s_\parallel \approx m_V^2$, where $V = \rho(770)$, $K^*(892)$ and $\phi(1020)$. The function $\cos\theta$ is expected to be quite stable with respect to $s_\perp$, around the fixed value of $s_\parallel = m_V^2$, which is illustrated, for a specific case, in Fig. 2.4. This means that the helicity angle can be explored in a small area around the resonance, assumed to vary only with respect to $s_\perp$, i.e. $\cos\theta(s_\perp, m_V^2 \pm \epsilon) \approx \cos\theta(s_\perp, m_V^2)$.

All the unknown parameters of Eq. (2.45) are meant to be extracted directly from experimental data, through the fitting of the square amplitudes with a quadratic function of $\cos\theta(s_\perp, m_V^2)$. However, it is important to interpret the terms in Eq. (2.45) in order to understand the method. The coefficients depending on $a_\pm^{V,S}$ of the first two terms on the RHS are related to the direct partonic CP asymmetry, explained by the BSS mechanism. Meanwhile, the proportionality to $\cos^2\theta(s_\perp, m_V^2)$ in the first one arises from the interference with the vector resonance angular structure. These two terms violate CPT, as they do not vanish if Eq. (2.45) is integrated over the whole phase space, and, therefore, it must be imposed that they do not contribute in order to be consistent with CPT. One simple solution for this is having the same coefficients from B^+ and B^- for these amplitudes. Anyway one could also expect them to be different and canceling out after the integration over the phase space. The term linear in $\cos\theta(s_\perp, m_V^2)$ is the interference term. The CP violation distribution in this term is associated to the mixing between the real and imaginary parts of the Breit-Wigner distributions of the vector and scalar resonances. By studying the cosine signature when looking at the distribution in $s_\perp$ one identify the specific type of CP asymmetry source according to the model.

The quantity of interest of the method is the CP asymmetry inherent to the BSS mechanism around the vector resonance region, as it corresponds to the intermediate PV channel. This is extracted after obtaining the parameters associated with the vector partonic amplitude through the fit of the resonance area in the three-body phase space. The aforementioned CP asymmetry can be written as

$$
A_{CP}^V = \frac{(a_-^V)^2 - (a_+^V)^2}{(a_-^V)^2 + (a_+^V)^2}.
$$
(2.46)

As discussed, these parameters are mainly associated with a CPT violating term of Eq. (2.45). If one expects to verify CPT invariance locally in this context, i.e.

assuming that the arguments of the last section for the suppression of inelastic rescattering effects distributing CPV among different channels are valid, the data analysis should give $A_{CP}^V \to 0$.

It is relevant to notice that resonances are also present in the crossed channel, i.e. as functions of $s_\perp$, and, therefore, can make the analysis of the angular distribution, $\cos\theta(s_\perp, m_V^2)$, quite challenging, as other sources of CP asymmetry might exist. Nonetheless, the resonances in the perpendicular channel are also located in the low mass region of the phase space, concentrating the interferences there. Experimentalists can then, without serious consequences, exclude these interference regions from the analysis, due to the huge available phase space of charmless three-body B decays. The measured value for A_{CP}^V from the fitted parameters might still have good resolution and limited errors if the available experimental data has significant statistics.

The straightforward conclusion from the discussion above is that if the CPT constraint is explicitly carried out, the CP asymmetry can be suppressed for some charmless $B \to PV$ decays. This feature was never suggested in the literature, as mostly short distance approaches indicate a substantial direct CP distribution in these decays. Specifically, for three-body decays involving three pseudoscalar mesons (i.e. the situation where the subsequent decay of the vector meson that leads to a three-body state, $B \to PV \to PPP$) in the final state, two experimental characteristics reinforce those constraints: i) charmless B decays have their phase spaces mostly populated around the edges, what encourage the (2+1) approximation accounting for two-body resonances and a non interacting meson. ii) the elastic regime dominates the $\rho(770)$ and $K^*(890)$ resonances, making the coupling through FSI with other channels unlikely. These two features combined with the CPT constraint practically gives no place for CP violation effects in $B \to PV$ decays. Important to highlight that, although unlikely, the possibility of inelastic rescattering contributions generating direct CP violation needs to be further explored with more reliable calculations.

For the reader interested in more explorations of the model, a Toy Monte Carlo simulation using the equations discussed above can be found in Ref. [24]. The potential information that can be extracted through this method can shed some light on the disagreements among the theoretical calculations and experimental measurements of A_{CP} for $B \to PV$ decays presented in the compilation of Ref. [95]. However, this simple method is unable to substitute the refined amplitude analysis and their complexity, since the access to, e.g., the resonance branching fractions, are not reachable within the model.

2.3 Three-body FSI in B decays

One of the most important effects not embedded in the model formulated earlier is three-body rescattering, i.e. hadronic interactions involving all the final state mesons of the three-body decay. The idea of this section is to develop a decay amplitude that includes final state interactions among all the involved mesons, however in a completely independent formalism. An interesting exercise for future explorations is to find a formal way to merge the formalism present in what follows with the CPT

invariant CP asymmetry formula of Eq. (2.35).

The goal is to present a fully relativistic model to account for three-body final state interactions, and subsequently apply it to the process $B^+ \to K^- \pi^+ \pi^+$. The formalism presented here follows closely what was developed in Ref. [59] for the D meson decay in the same channel. The model aims at formulating the decay amplitude and exploring its structure outputs without going deep into the details. As there is no experimental amplitude analysis available for this channel the model is meant to be further explored in the future. The study presented in this section was published in Ref. [25].

The three-body decay amplitude within this model is based on the Faddeev decomposition of the Bethe-Salpeter equation, taken care in the light-front framework [27, 28]. The two-body interaction kernel is given by the s-wave scattering amplitude for the $K\pi$ system, with the 1/2 and 3/2 isospin channels being considered. The outcome is a set of inhomogeneous integral equations that are expanded perturbatively and then solved numerically. It is worth emphasizing that partonic processes, part of the source amplitudes, are not addressed, neither the large absorption to the several decay channels present in the huge B decay phase space. The convergence of the rescattering perturbative series is tested numerically, being achieved in the expansion up to two-loops. These kind of investigation, even if not ultimate, has its value as the main approaches available in the literature, mostly based on QCD effective field theories within heavy quark expansions [89, 90, 91], are drawn up on the factorization of the hadronic matrix elements, mainly considering short-distance physics. Separating the problem in the long- and short-distance physics, through, e.g., the operator product expansion of the weak effective Hamiltonian, is a quite difficult task and new methods can help to understand the involved physics.

FSI effects play an important role in heavy meson weak decays, even in strongly suppressed channels. As an example, a recent experimental study of the charmless B_c decay to the $KK\pi$ channel, which within the Standard Model can only occur by weak annihilation diagrams, shows some events in the phase space of this suppressed channel [98]. This unexpected measurement can be associated to inelastic hadronic rescattering transitions related with that final decay channel. This type of interactions are usually considered as suppressed non-factorizable effects in the QCD factorization, but even within this approach it was shown that the b-quark mass m_b is not large enough to suppress the decay, mainly, in the center of the phase space [83].

The perturbative expansion is allowed if the strong coupling constant, α_s, is expected to be small in the treated high-energy process. Nonetheless, the long-distance physics and its non-perturbative nature leads to amplitudes complicated to deal with, both analytically and numerically. Solving the final equation needs to be done, in principle, without relying on any perturbative expansion. At this first attempt, in order to keep things simple, the perturbative approach will be adopted and the convergence verified numerically. For the moment, this will quantify the reliability of the present approach, but similar equations (for the bound state) will be properly treated later in the coming chapters.

The convergence of the series expansion is checked going up to third order terms of the two-body transition matrix, i.e. up to three-loops. The numerical results for the $B^+ \to K^- \pi^+ \pi^+$ decay amplitude comprising three-body FSI and $K\pi$ interactions in the $I = 1/2$ and 3/2 isospin states are the outcome. The transition

amplitude is parametrized by the LASS experimental data [55], which gives the resonant structure as well as the corresponding scattering amplitude poles only in the isospin 1/2 channel.

It is relevant also to point out other developments of relativistic models for the three-body FSI that were applied to the $D^+ \to K^- \pi^+ \pi^+$ decay [59, 58, 99], since the formalism shown here carry many ingredients from those references. More specifically, in Ref. [59], the isospin projection of the decay amplitude was performed to study different isospin state contributions to the $K^- \pi^+$ rescattering. The formulation starts from the three-body Bethe-Salpeter equation and uses its Faddeev decomposition. The decay amplitude was separated into a smooth term and a three-body interaction contribution. Moreover, the amplitude was factorized as a two-meson amplitude times a reduced complex amplitude for the non interacting meson, which carries the three-body FSI effect. The desired off-shell bachelor amplitude[5] is the solution of an inhomogeneous Faddeev type integral equation. Its input is the two-body s-wave isospin 1/2 and 3/2 $K^- \pi^+$ T-matrix. The two-body amplitude included in the kernel accounts for effective three-body interactions, no irreducible three-body force (a ϕ^6 term in the Lagrangian) is included in the relativistic equation. The light-front projection of the Faddeev-Bethe-Salpeter equations [100] was performed, as it reduces the four-dimensional equations to three-dimensional ones due to the $k^- = k^0 - k^3$ integration, simplifying its structure and the subsequent numerical calculations. Interactions between identical charged pions were neglected, as this impact is expected to be suppressed. The aforementioned procedure, followed in Ref. [59], is the same as the one used below.

This is a single channel model and, therefore, not including directly three-body absorptive interactions. The absorption due to the coupling to other channels is introduced here by a finite $i\varepsilon$ parameter in the free LF three-body propagator. The stability with respect to this parameter is also studied. This is a naive way of considering absorptive effects due to the coupling to other channels, which are needed for three-body unitarity to be satisfied. Consequently, the loss in probability flux is given by a finite width in the free three-body propagator.

2.3.1 $B^+ \to K^- \pi^+ \pi^+$ decay amplitude with FSI

The $B^+ \to K^- \pi^+ \pi^+$ decay amplitude, solution of a Bethe-Salpeter equation, enclosing the $3 \to 3$ transition matrix in its kernel is given by

$$\mathcal{A}(k_\pi, k_{\pi'}) = B_0(k_\pi, k_{\pi'}) + \tag{2.47}$$
$$+ \int \frac{d^4 q_\pi d^4 q_{\pi'}}{(2\pi)^8} T(k_\pi, k_{\pi'}; q_\pi, q_{\pi'}) S_\pi(q_\pi) S_{\pi'}(q_{\pi'}) S_K(K - q_{\pi'} - q_\pi) B_0(q_\pi, q_{\pi'}),$$

where, S_i $(i = \pi, \pi', K)$ are scalar propagators, B_0 is the source amplitude, k_π, $k_{\pi'}$ the pions four-momenta and K denotes the total momentum of the system. Following this notation, the two-body invariant mass of the $K\pi$ system is defined as $M_{K\pi}^2 = (K - k_{\pi'})^2$. The meson propagators read $S_i(q_i) = i(q_i^2 - m_i^2 + i\epsilon)^{-1}$ and do not take into account dressing effects. The short-distance physics resides in the $B_0(k_\pi, k_{\pi'})$ amplitude and its computation involves the evaluation of the

---

[5]The bachelor particle amplitude is the one describing the non interacting meson.

quark-level amplitudes contributing to the decay channel. The off-shell interaction kernel $T(k_\pi, k_{\pi'}; q_\pi, q_{\pi'})$ consists of an infinite sum of rescattering diagrams and is considered in ladder approximation. The complete scattering matrix enclosing FSI is a solution of the fully off-shell four-leg transition amplitude. More details on its formalism can be found in Ref. [38]. The kernel will include only two-body irreducible diagrams involving all the final state mesons, except by the interference between the pions. The interaction kernel encloses the $K\pi$ transition matrix, which sums over all respective $2 \to 2$ collision terms. Writing the interaction kernel in terms of the two-body rescattering matrix, one gets

$$T_i(k'_j, k'_k; k_j, k_k) = (2\pi)^4 \tau_i(s_i)\, S_i^{-1}(k_i)\, \delta(k'_i - k_i) \;, \qquad (2.48)$$

where δ is a four-momentum conserving delta function and the Mandelstam variable $s_i = (k_j + k_k)^2$ is the only dependence considered. The amplitude $\tau_i(s_i)$ is the unitary s-wave scattering amplitude involving the particles j and k. This term brings to the model the long-range physics.

Using the separable form of Eq. (2.48) the problem is reduced to a four-dimensional integral equation in one momentum variable for the Faddeev components of the vertex function. Applying Eq. (2.48), the decay amplitude of the $B^+ \to K^-\pi^+\pi^+$ process, excluding the $\pi^+\pi^+$ interaction, reads

$$\mathcal{A}_0(k_\pi, k_{\pi'}) = B_0(k_\pi, k_{\pi'}) + \tau(M_{K\pi}^2)\xi(k_{\pi'}) + \tau(M_{K\pi'}^2)\xi(k_\pi) \;, \qquad (2.49)$$

where the subindex in $\mathcal{A}_0$ denotes the angular momentum of the s-wave two-meson scattering, $M_{K\pi}^2 = (K - k_{\pi'})^2$, $M_{K\pi'}^2 = (K - k_\pi)^2$ and the on-mass-shell momentum of the non interacting pion is given by

$$|\mathbf{k}_\pi|^2 = \left(\frac{M_B^2 + m_\pi^2 - M_{K\pi'}^2}{2\, M_B}\right)^2 - m_\pi^2 \;. \qquad (2.50)$$

Decomposing the decay amplitude in terms of a complex phase and an amplitude is convenient for the forthcoming amplitude analysis. It reads

$$A(M_{K\pi'}^2) = \frac{1}{2}\langle K\pi\pi|B_0\rangle + \langle K\pi\pi|\tau(M_{K\pi'}^2)|\xi(k_\pi)\rangle = a_0(M_{K\pi'}^2)e^{i\Phi_0(M_{K\pi'}^2)}, \quad (2.51)$$

which is a function of only $M_{K\pi'}^2$ and $|K\pi\pi\rangle$ represents the state in isospin space. The amplitude $\xi(k_i)$ represents the non interacting particle and carries the three-body rescattering effect, being written in its general form as the solution of a Faddeev-like equation.

For the specific decay under scrutiny, where two of the particles are identical and no interaction between them, the inhomogeneous integral equation for the spectator amplitude is a function only of the momentum of the non interacting particle (see [59]),

$$\xi(k) = \xi_0(k) + \int \frac{d^4q}{(2\pi)^4} \tau\left((K - q)^2\right)\, S_K(K - k - q)\, S_\pi(q)\, \xi(q), \qquad (2.52)$$

where the first term, i.e. the driving term of the perturbative expansion, will be identified as

$$\xi_0(k) = \int \frac{d^4q}{(2\pi)^4} S_\pi(q) S_K(K - k - q) B_0(k, q), \qquad (2.53)$$

where the partonic decay amplitude, $B_0(k, q)$, is written with its general dependence for now. Bear in mind that, since the interaction between the identical pions is not taken into account in the model, the non interacting particle will be always a π^+. All the other possible interactions are of the type $K\pi$ and are included by iteration.

The rescattering series comes from the solution of Eq. (2.52), where the second term encloses the higher order loop diagrams. Both amplitude and phase are enclosed by Eq. (2.52), depending only on the bachelor meson on-mass-shell momentum. The main ingredients of the decay amplitude are the well behaved function $B_0(k_\pi, k_{\pi'})$, which will naively treated as an overall normalization, and the scattering amplitude, $\tau\left(M_{K\pi'}^2\right)$. The operator τ will be conveniently decomposed into two isospin states, namely, $1/2$ and $3/2$.

The scattering amplitude is meant to include the $K\pi$ s-wave resonances present in the decay. Its explicit form will be obtained through a parametrization that reproduces the $K\pi$ s-wave scattering LASS experimental data [55]. It will be followed the same procedure as in Ref. [59], where the $K\pi$ s-wave elastic scattering amplitude was introduced in the resonant $I_{K\pi} = 1/2$ and non-resonant $I_{K\pi} = 3/2$ isospin states. The parametrization includes the three main low-mass resonances of the channel, $K_0^*(1430)$, $K^*(1630)$ and $K_0^*(1950)$. The $K_0^*(1630)$ and $K_0^*(1950)$ resonances are included following the LASS data, whereby the kinematical phase space was fitted up to 1.89 GeV. See appendix B.1 for the explicit form of the adopted parametrization. In addition, the $I = 3/2$ channel is covered with a s-wave parametrized scattering amplitude, by using the first two terms in the effective range expansion, due to its simpler structure. As said, the $\pi\pi$ interaction is neglected, as considered in Ref. [59], since it involves identical particles and, for this reason, is expected to be considerably suppressed.

The form presented in Eq. (2.52) is not yet convenient to be solved numerically due to the singular structure of the propagators when expressed in Minkowski space. One way of simplifying it is by the projection onto the light-front hyperplane, what is done in practice by integrating the equation over $q^- = q^0 - q^3$. The projection transforms the four-dimensional coupled equations into a three-dimensional set, structurally simpler to handle numerically. Such technique is widely used in the literature [27, 28] as it gives a notable alternative to bypass the Minkowski space singularities keeping the consistency with its dynamics. Nevertheless, it is important to mention that the projection as it is predominantly done in the literature retains only the valence component of the amplitude, what can be a limitation particularly for three-body relativistic systems [44, 45]. This light-front Fock-space truncation to the three-meson valence component is present in the model under consideration.

One of the main advantages of performing the LF projection is the suppression of Z-diagrams in the kernel [27]. In addition, the projected integral equations are covariant under seven LF kinematical transformations, namely the ones that keep the null-plane invariant, including three translations, a rotation around the z-direction, two other kinematical boosts and, finally, the boost along the z-direction. Moreover, the truncation of the LF Fock-space is stable under kinematical boosts [101]. In contrast, the Fock-space truncation in the instant form has three translations, three rotations and no boosts.

For further details on the derivation of the equation suitable for the numerical solution, see Appendix B.2. The interaction among the final state mesons needs to

include two possibilities, considering that $\pi^+\pi^+$ interaction is discarded. Therefore, the symmetrization of the decay amplitude with respect to the identical pions becomes simply given by

$$\mathcal{A}_0 = A_0(M^2_{K\pi'}) + A_0(M^2_{K\pi}). \tag{2.54}$$

Performing the isospin projection (see Appendix B.2 for more details) on each term leads to

$$A_0(M^2_{K\pi'}) = \sum_{I_T, I_{K\pi'}, I_T^z} \left\langle K^-\pi^+\pi^+ \middle| I_T, I_{K\pi'}, I_T^z \right\rangle \times \tag{2.55}$$

$$\times \left[\frac{1}{2} \left\langle I_T, I_{K\pi'}, I_T^z \middle| B_0 \right\rangle + \tau_{I_{K\pi}}(M^2_{K\pi'}) \xi^{I_T^z}_{I_T, I_{K\pi'}}(k_\pi) \right] = a_0(M^2_{K\pi'}) e^{i\Phi_0(M^2_{K\pi'})},$$

from where one can extract both the modulus, $a_0(M^2_{K\pi'})e$, and the phase, $\Phi_0(M^2_{K\pi'})$, of the decay amplitude.

2.3.2 Perturbative solution

For the sake of simplicity, the problem is solved perturbatively, by iterating Eq. (B.11) starting with the driving term, until convergence is reached. Iterating up to three loops showed to be enough for all the tested sets of parameters, as at this level the contribution is already significantly small. Two sets of equations are solved, the first for the coupled-channel case, where the $I_T = 3/2$ total isospin states are formed by coupling $I_{K\pi} = 1/2$ or $I_{K\pi} = 3/2$ states. The second case is a single channel contribution, with total isospin $I_T = 5/2$, where the $K\pi$ interaction involves isospin $3/2$ states.

For testing the convergence, one can start by only considering the resonant contribution in the $I_{K\pi} = 1/2$ channel, for which the perturbative expansion of the equation (B.11) up to three loops can be written as

$$\xi^{3/2}_{3/2,1/2}(y, k_\perp) =$$

$$= \frac{1}{6}\sqrt{\frac{2}{3}}\xi_0(y, k_\perp) - \frac{i}{3}\left(\frac{1}{6}\sqrt{\frac{2}{3}}\right)\int_0^\Lambda \frac{dq_\perp}{(2\pi)^3} \int_0^{1-y} dx\, K_{1/2}(y, k_\perp; x, q_\perp)\, \xi_0(x, q_\perp)$$

$$- \frac{1}{9}\left(\frac{1}{6}\sqrt{\frac{2}{3}}\right)\int_0^\Lambda \frac{dq_\perp}{(2\pi)^3} \int_0^{1-y} dx\, K_{1/2}(y, k_\perp; x, q_\perp)$$

$$\times \int_0^\Lambda \frac{dq'_\perp}{(2\pi)^3} \int_0^{1-x} dx'\, K_{1/2}(x, q_\perp; x', q'_\perp)\, \xi_0(x', q'_\perp) + \cdots \tag{2.56}$$

where, for simplification, in the driving term it is taken $\alpha^{3/2}_{3/2,1/2} = 1$. The other factors are given in more detail in Refs. [25, 59]. The integration kernel $K_{1/2}$ is defined by Eq. (B.13).

The equation is normalized arbitrarily, since the partonic structure is not properly taken into account in this model. The integration over the transverse momentum is computed by introducing a cut-off of $\Lambda = 0.8$ GeV. This value is considerably smaller than in the D decay case [59]. As checked in this work, the results of Ref. [59] suffer almost no visible change if the cut-off parameter is moved from 2.0 GeV to

0.8 GeV. Nevertheless, in the B case, the use of $\Lambda = 2.0$ GeV is very expensive numerically, probably caused by the large non-physical region, and consequently plenty of numerical noise. As the B meson has a much larger mass, its wave function is expected to be concentrated at low momentum. Moreover, the finite value of the momentum cut-off represents roughly the two-meson interaction range, that is somewhat related to the size of the mesons itself. If the model for the $K\pi$ interaction had a finite range (and not a zero-range one, as it is), it would naturally include a cut-off in the hadronic loop. In the present model, it is instead introduced by the integration momentum cut-off.

On the other hand, concerning the ε parameter, the value used was $\varepsilon = 0.5$ GeV^2, which is considerably larger than the one used in the D decay case. Since the accessible B meson phase space is much larger, it is a known fact that the absorption, due to the several decay possibilities, is higher if compared with the D meson decay. The finite value of the ε parameter can be understood as a way of introducing the absorption effect. Different values of ε were tested, mostly around $\varepsilon = 0.5$ GeV^2, showing a small difference in the results. Important to say that a very small value for this parameter brings a lot of numerical instability. Finally, the subtraction constant in the driving term, $\lambda(\mu^2)$ (see Eq. (B.8)) coming from the regularization procedure is chosen to be zero. The numerical outcomes, the phase-shift and modulus of the bachelor particle amplitude, are outlined in Fig. 2.12.
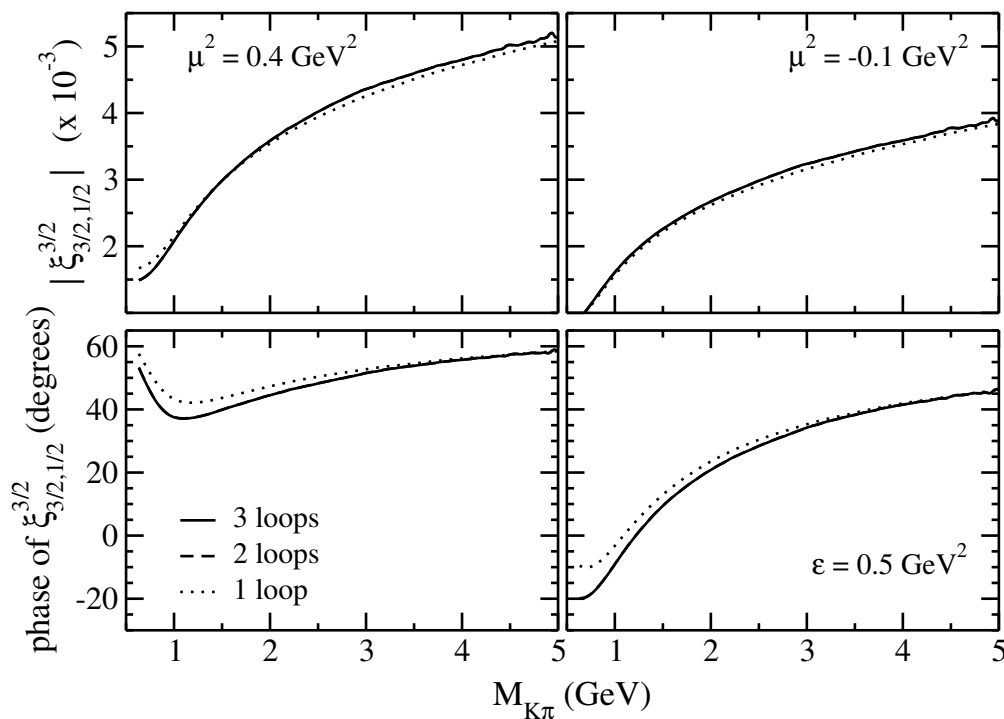
Figure 2.12. Modulus and phase of $\xi_{3/2,1/2}^{3/2}$ for $\varepsilon = 0.5$ GeV^2, $\mu^2 = 0.4$ GeV^2 (left) and $\mu^2 = -0.1$ GeV^2 (right).

Three values of the subtraction point, for the regularization of the kernel, were used in order to verify its effect on the results, namely $\mu^2 = (0.4, -0.1)$ GeV^2. For any tested value of μ^2 it was clear that the two-loop solution is already perfectly

converged for practical applications. Notice that this fact was also observed in the D decay case, but now the convergence is considerably enhanced. The phase is always positive for $\mu^2 = 0.4$ GeV^2, but changes sign for $\mu^2 = -0.1$ GeV^2. It also varies more for $\mu^2 = -0.1$ GeV^2, increasing until reaching a roughly constant region after ≈ 4 GeV. For $\mu^2 = 0.4$ GeV^2, it presents a minimum around 1 GeV and then increases again becoming pretty much unchanged after ≈ 3 GeV. In both cases the modulus increases as the $K\pi$ two-body invariant mass grows.

One can now include both two-body interactions kernels, for $I_{K\pi} = 1/2$ and $I_{K\pi} = 3/2$, and check the convergence for all the components. Including these two isospin channels results in a coupled set of inhomogeneous integral equations, obtained from Eq. (B.11) for $I_T = 3/2$, which reads

$$\xi_{3/2,1/2}^{3/2}(y, k_\perp) = A_w\, \xi_0(y, k_\perp) + \tag{2.57}$$

$$+ \; \frac{iR_{3/2,1/2,1/2}^{3/2}}{2} \int_0^{1-y} \frac{dx}{x(1-y-x)} \int_0^\infty \frac{dq_\perp}{(2\pi)^3} K_{1/2}(y, k_\perp; x, q_\perp)\, \xi_{3/2,1/2}^{3/2}(x, q_\perp)$$

$$+ \; \frac{iR_{3/2,1/2,3/2}^{3/2}}{2(2\pi)^3} \int_0^{1-y} \frac{dx}{x(1-y-x)} \int_0^\infty \frac{dq_\perp}{(2\pi)^3} K_{3/2}(y, k_\perp; x, q_\perp)\, \xi_{3/2,3/2}^{3/2}(x, q_\perp)$$

and

$$\xi_{3/2,3/2}^{3/2}(y, k_\perp) = B_w\, \xi_0(y, k_\perp) + \tag{2.58}$$

$$+ \; \frac{iR_{3/2,3/2,1/2}^{3/2}}{2} \int_0^{1-y} \frac{dx}{x(1-y-x)} \int_0^\infty \frac{dq_\perp}{(2\pi)^3} K_{1/2}(y, k_\perp; x, q_\perp)\, \xi_{3/2,1/2}^{3/2}(x, q_\perp)$$

$$+ \; \frac{iR_{3/2,3/2,3/2}^{3/2}}{2} \int_0^{1-y} \frac{dx}{x(1-y-x)} \int_0^\infty \frac{dq_\perp}{(2\pi)^3} K_{3/2}(y, k_\perp; x, q_\perp)\, \xi_{3/2,3/2}^{3/2}(x, q_\perp).$$

For $I_T = 5/2$ only the interaction for $I_{K\pi} = 3/2$ appears, resulting in a single channel equation from Eq. (B.11), which reads

$$\xi_{5/2,3/2}^{3/2}(y, k_\perp) = C_w\, \xi_0(y, k_\perp) + \tag{2.59}$$

$$+ \; \frac{iR_{5/2,3/2,3/2}^{3/2}}{2} \int_0^{1-y} \frac{dx}{x(1-y-x)} \int_0^\infty \frac{dq_\perp}{(2\pi)^3} K_{3/2}(y, k_\perp; x, q_\perp)\, \xi_{5/2,3/2}^{3/2}(x, q_\perp),$$

where the isospin states related to the partonic amplitude projection, defined in Eq. (B.10), bring the weights A_w, B_w and C_w, which depends on the Clebsch-Gordan and recoupling coefficients $(R_{I_T, I_{K\pi}}^{I_T^z})$ The weights are defined by

$$A_w = \langle I_T = 3/2, I_{K\pi} = 1/2, I_T^z = 3/2|\, B_0 \rangle, \quad B_w = \langle 3/2, 3/2, 3/2|\, B_0 \rangle$$
$$\text{and} \quad C_w = \langle 5/2, 3/2, 3/2|\, B_0 \rangle. \tag{2.60}$$

More explicitly, the isospin coefficients are

$$A_w = \alpha_{3/2,1/2}^{3/2}(1 + R_{3/2,1/2,1/2}^{3/2}) + \alpha_{3/2,3/2}^{3/2} R_{3/2,1/2,3/2}^{3/2},$$
$$B_w = \alpha_{3/2,3/2}^{3/2}(1 + R_{3/2,3/2,3/2}^{3/2}) + \alpha_{3/2,1/2}^{3/2} R_{3/2,3/2,1/2}^{3/2} \quad \text{and} \tag{2.61}$$
$$C_w = \alpha_{5/2,3/2}^{3/2}(1 + R_{5/2,3/2,3/2}^{3/2}).$$

The coefficients, $\alpha_{I_T,I_{K\pi}}^{I_T^z}$, come from the partonic decay amplitude (B.10) projection onto the isospin space and are defined as

$$\alpha_{3/2,1/2}^{3/2} = \frac{W_1}{2}\, C_{1/2\ 1\ 3/2}^{1/2\ 1\ 3/2}\, C_{1\ -1/2\ 1/2}^{1\ 1/2\ 1/2},$$

$$\alpha_{3/2,3/2}^{3/2} = \frac{W_2}{2}\, C_{1/2\ 1\ 3/2}^{3/2\ 1\ 3/2}\, C_{1\ -1/2\ 1/2}^{1\ 1/2\ 3/2} \quad \text{and} \tag{2.62}$$

$$\alpha_{5/2,3/2}^{3/2} = \frac{W_3}{2}\, C_{1/2\ 1\ 3/2}^{3/2\ 1\ 5/2}\, C_{1\ -1/2\ 1/2}^{1\ 1/2\ 3/2}.$$

The Clebsch-Gordan and recoupling coefficients are $C_{1/2\ 1\ 3/2}^{1/2\ 1\ 3/2} = 1$, $C_{1\ -1/2\ 1/2}^{1\ 1/2\ 1/2} = \sqrt{2/3}$, $C_{1/2\ 1\ 3/2}^{3/2\ 1\ 3/2} = -\sqrt{2/5}$, $C_{1\ -1/2\ 1/2}^{1\ 1/2\ 3/2} = 1/\sqrt{3}$, $C_{1/2\ 1\ 3/2}^{3/2\ 1\ 5/2} = \sqrt{3/5}$, $R_{3/2,1/2,1/2}^{3/2} = -2/3$, $R_{3/2,1/2,3/2}^{3/2} = \sqrt{5}/3$, $R_{3/2,3/2,3/2}^{3/2} = 2/3$, $R_{3/2,3/2,1/2}^{3/2} = \sqrt{5}/3$, and $R_{5/2,3/2,3/2}^{3/2} = 1$. The final forms of the weights, after some manipulations, are $A_w = \sqrt{\frac{1}{54}}(W_1 - W_2)$, $B_w = \sqrt{\frac{5}{54}}(W_1 - W_2)$ and $C_w = \frac{W_3}{\sqrt{5}}$.

Again, convergence of the bachelor amplitude is checked for the coupled-channel case. All Eqs. (2.57), (2.58) and (2.59) appear in the case $I_T = 3/2$. For $I_T = 5/2$, a single channel equation, only Eq. (2.59) contributes. The results are shown in Fig. 2.13, where it is adopted $\varepsilon = 0.5$ GeV^2 and $\mu^2 = -0.1$ GeV^2. The free parameters from the isospin projection of the source term are fixed, following Ref. [59], by $W_1 = 1$, $W_2 = 2$ and $W_3 = 0.2$. As in the single channel case, the convergence is reached
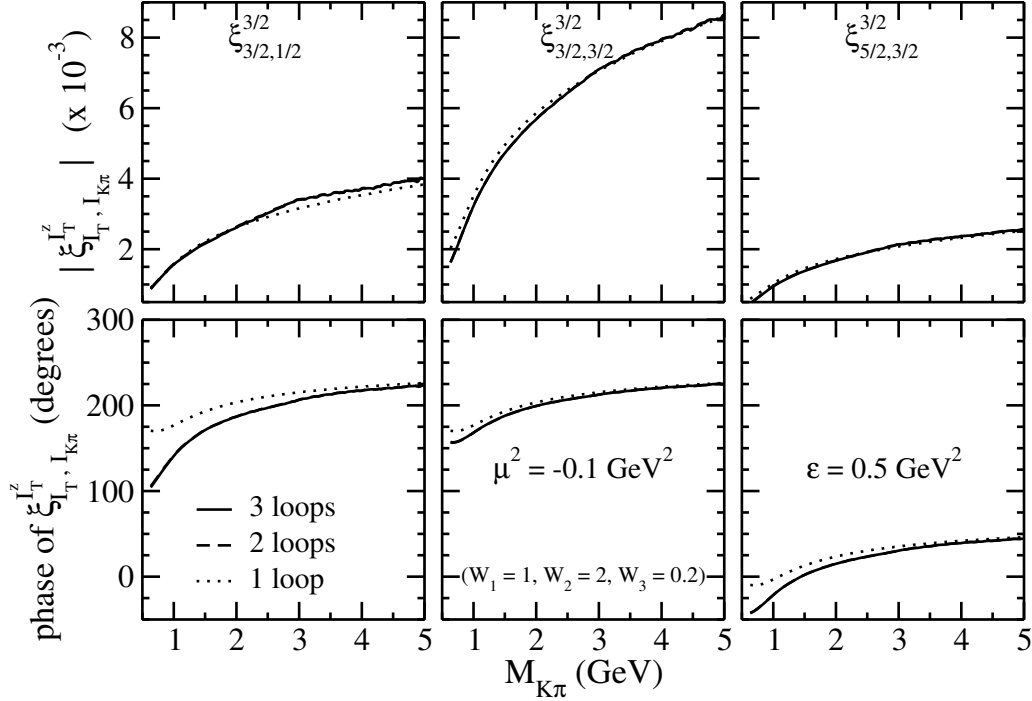
Figure 2.13. Modulus and phase of $\xi_{I_T,I_{K\pi}}^{I_T^z}$ for $\varepsilon = 0.5$ GeV^2 and $\mu^2 = -0.1$ GeV^2 and the parameters $W_1 = 1$, $W_2 = 2$ and $W_3 = 0.2$.

at two-loops, suggesting that higher order terms in the perturbative expansion can be neglected for practical applications. Moreover, both phase and modulus of the

bachelor amplitudes increase with growing $M_{K\pi}$, becoming almost invariant for higher values of the two-body invariant mass, except for the $|\xi^{3/2}_{3/2,3/2}|$ amplitude modulus which keeps increasing. In the channel $I_T = 3/2$, both amplitudes have for their phases similar magnitudes, which are larger than in the $I_T = 5/2$ case and with a similar pattern to the one that was observed for the D decay [59].

2.3.3 Results for the $B^+ \to K^-\pi^+\pi^+$ decay amplitude

Considering that the two-loop result is already enough for the convergence of the perturbative expansion for the bachelor amplitudes, hereafter all the calculations will consider the truncation at that order. For the moment, there is no experimental data available to perform a comparative analysis as done for the D meson decay in Ref. [59], so the goal here is simply to present the general form of the decay amplitude under the current model. The reduced form of the decay amplitude, from where both phase and modulus can be extracted by means of Eq. (2.55), reads

$$A_0(M^2_{K\pi}) = \sqrt{\frac{2}{3}} \left[\frac{1}{12}\sqrt{\frac{2}{3}} + \tau_{1/2}(M^2_{K\pi})\xi^{3/2}_{3/2,1/2}(k_{\pi'}) \right]. \qquad (2.63)$$

The iteration of the coupled equations (2.57)-(2.58) gives the amplitude for the channel $I_T = 3/2$. Meanwhile, for the the $I_T = 5/2$ state, the amplitude is given by the single expression in Eq. (2.59). The resulting s-wave decay amplitude for the coupled-channel case is given by

$$\begin{aligned} A_0(M^2_{K\pi}) &=& C_1\left[\frac{A_w}{2} + \tau_{1/2}(M^2_{K\pi})\xi^{3/2}_{3/2,1/2}(k_{\pi'})\right] + C_2\left[\frac{B_w}{2} + \tau_{3/2}(M^2_{K\pi})\xi^{3/2}_{3/2,3/2}(k_{\pi'})\right] + \\ &+& C_3\left[\frac{C_w}{2} + \tau_{3/2}(M^2_{K\pi})\xi^{3/2}_{5/2,3/2}(k_{\pi'})\right] \end{aligned} \qquad (2.64)$$

where the constants C_i come from the isospin projection onto the state $K\pi\pi$, Eq. (2.55), and are given in Eqs.(2.61) and (2.62). There are two free parameters, which are the weights related with the projected partonic amplitude, namely, $W_1 - W_2$ and W_3 (see Eq. (2.62)). If the first one is zero and the second one nonzero, it means that only the amplitude with total isospin 5/2 contributes and, therefore, the decay amplitude misses the resonant structure, as shown in Ref. [59]. This shows that it is not a good physical choice, since the isospin state contributions are not taken into account in a reasonable way. A more relevant study of the involved weights would be guided by experimental data, as done for the $D^+ \to K^-\pi^+\pi^+$ decay [59], which is not possible for the B decay under study here. For that reason, this work simply follows what was indicated by the D decay analysis, where the authors found a small mixture in the total isospin 5/2 state.

Figure 2.14 shows a comparison between the decay amplitudes from the B and D mesons to the same final state, i.e. $K^-\pi^+\pi^+$. All the parameters involved in the model are adopted to be the same, including the overall normalization. In particular, the subtraction scale was fixed at $\mu^2 = -0.1$ GeV^2, the ε parameter was chosen to be $\varepsilon = 0.5$ GeV^2, and $W_1 - W_2 = -1$ and $W_3 = 0.2$ were used. In order to test the effect of the constants $W_1 - W_2$ and W_3, a second set of parameters was tested, namely, $W_1 - W_2 = 1$ and $W_3 = 0.3$, which was the one used in Ref. [59], but the results showed to be very similar to the ones presented here, with the major change

being a sign flip in the phase (which is not relevant due to the arbitrariness of the complex normalization).

It is quite clear that the amplitude becomes practically constant above $M_{K\pi} \approx 2.6$ GeV. This behavior appears due to the fact that the two-body amplitude of Eq. (B.3) damps quickly for large $M_{K\pi}$ and only the constant partonic amplitude (first term in Eq. (2.48)) dominates. It basically evidence the poor manner how the partonic structure is taken into account in the model, and that the model is not suitable to describe in detail the region beyond the resonant structure. The wavelike behavior of the two-body amplitude in the dominant $I = 1/2$ channel is traced back to the inclusion of resonances below 2 GeV, suggested by the current available experimental information from LASS and the study on the $D^+ \to K^-\pi^+\pi^+$ decay. The intention here was simply to present the model as an alternative to include three-body FSI effects on the decay amplitude, however, the model might not be realistic in its current form for a detailed experimental analysis.
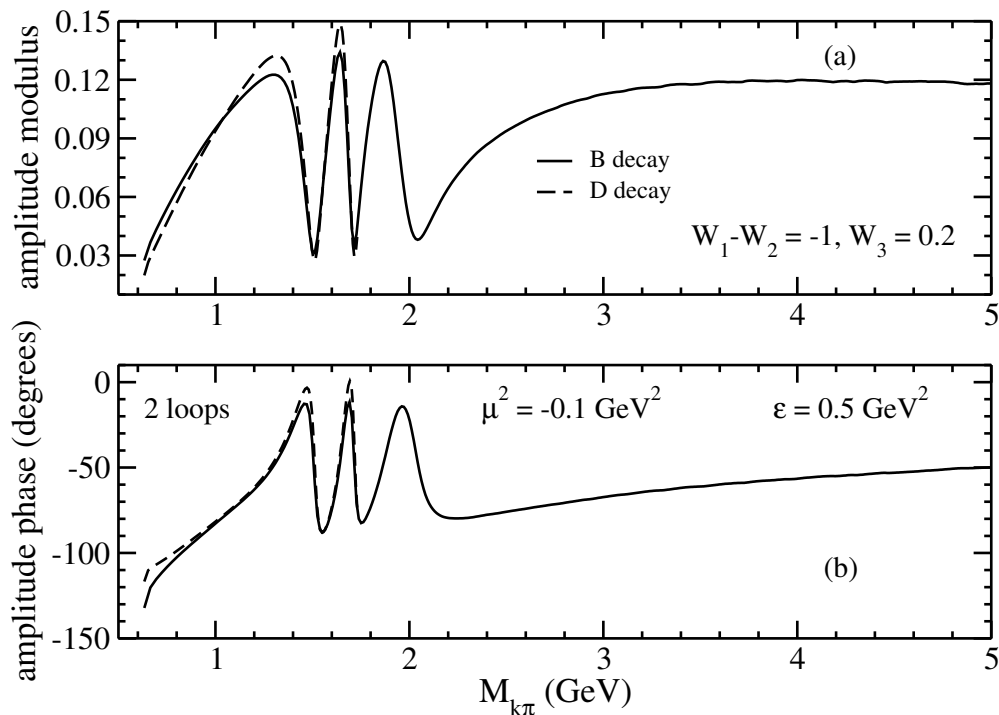
Figure 2.14. Comparison of (a) modulus and (b) phase between $D^+ \to K^-\pi^+\pi^+$ and $B^+ \to K^-\pi^+\pi^+$ amplitudes for a initial state in which $W_1 - W_2 = -1$ and $W_3 = 0.2$.

Figure 2.15 compares both modulus and phase of the $B^+ \to K^-\pi^+\pi^+$ decay amplitude with and without the resonances $K_0^*(1630)$ and $K_0^*(1950)$. The same parameters as before were used. The figure shows that the inclusion of the resonances produces more structure in both modulus and phase. This is clearly related with the resonances contained in the $K\pi$ two-body scattering amplitude, since the peaks are around the resonance masses and below $K_0^*(1430)$ the pattern is different. All the curves have the same tail for increasing two-body invariant masses, what is expected due to the simplistic form adopter for the source amplitudes.
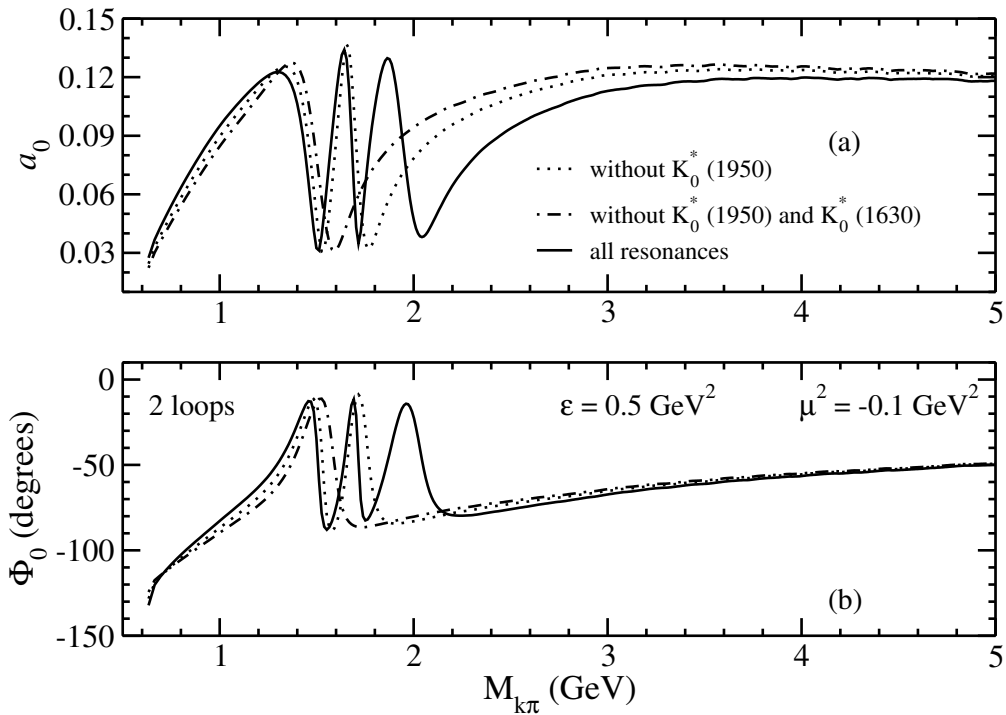
Figure 2.15. Modulus (a_0) and phase (Φ_0) of the $B^+ \to K^- \pi^+ \pi^+$ amplitude, in the notation of Eq. (2.55), comparing cases with all resonances, without $K_0^*(1950)$ and without both $K_0^*(1950)$ and $K_0^*(1630)$.

2.3.4 Concluding remarks and perspectives

The model presented here, although simple, shows to be an interesting alternative to take into account three-body FSI effects in the decay amplitude. Combining this model with the one for CP violation formulated in Sec. 2.1, maintaining CPT invariance, could open interesting possibilities in the study of the three-body phase space. The light-front formulation simplifies the inhomogeneous integral Bethe-Salpeter equations, reducing them to three-dimensional ones. Although they were solved perturbatively in the present work, it would be extremely valuable to explore the structure of the equations without relying on any expansion, as effects of the non-perturbative nature might be lost in the procedure. Including properly the absorption due to other decay channels within a unitary formulation is desirable, since the oversimplified approach of including the ε parameter as in the present model is insufficient if the aim is to perform a realistic amplitude analysis.

The momentum cut-off used in the transverse momentum integration needs also to be further explored, as it would be appealing to find a stable numerical approach where that parameter can be avoided. The amplitudes also need to be properly normalized and experimental data would be useful in order to fix the weights of the three isospin components, that are free parameters for the moment. Another valuable advance would be to solve the equations using a finite-range interaction, where the effective range expansion would be overtaken by the exchanged particle mass, allowing the understanding of the interaction kernel from a broader perspective.

The resonant structure above the $K_0^*(1430)$ resonance is a question that deserves a detailed analysis in the face of future experimental data. While the presence of the $K_0^*(1630)$ resonance is expected to play a role, the influence of the $K_0^*(1950)$ should be better understood.

And last but not least, the source amplitudes, poorly incorporated here and also in the CPT invariant model for the CP asymmetry of Sec. 2.1, deserve proper care by computing the partonic diagrams and including realistic amplitudes for the involved mesons. These are important ingredients and could yield interesting outcomes. Indeed, the parametrized amplitudes adopted in the previous sections were able to give a reasonable description of the CPV effects through the fitting procedure, but a refinement of the description at short distances, i.e. in a non-perturbative regime, opens new windows on the dynamical effects. Unfortunately, computing these amplitudes is a very challenging task, as one needs to evaluate the mesonic vertexes and, preferably, their non-perturbative structure attainable through the theory of quantum chromodynamics (QCD).

This problem leads to a more general question: how to properly represent a mesonic bound state? There are several approaches in the literature, e.g. lattice QCD and Dyson-Schwinger equation, but most of them are based in the Euclidean space. It is interesting to notice that what seemed first a simple problem within a specific context turned out to be a general and fundamental question within hadron physics. This intriguing and challenging problem has motivated the original research, presented in what follows. Next chapters aim at illustrating how to build a sound formalism for addressing a bound system in Minkowski space. The road is long and the ultimate goal is ambitious, however, by starting with simple systems and increasing the complexity little by little it is possible to gather useful knowledge to be exploited for describing hadronic states, in terms of the relevant partonic degrees of freedom.

Chapter 3

Two-boson BSE in Minkowski space

Quantum few-body problems appear throughout physics, as structures and/or reactions involving only a few acting degrees of freedom, like in the case of two and three nucleons systems, hadron structure with quark degrees of freedom, and electron-hole correlations in nano-structured materials. Furthermore, crucial relativistic quantum mechanical correlations, to be investigated within a quantum field-theory framework, often originate from properties of few-body subsystems. Nevertheless, to achieve a thorough description of relativistic few-body systems engaging specific interactions, one should resort to the non-perturbative domain. The predominant tools for dealing with the non-perturbative regime within the field theory are two: the path-integral formulation-based methods, e.g. Lattice QCD, and the covariant integral equation frameworks, e.g the Bethe-Salpeter and Dyson-Schwinger equations. In both cases the calculation procedure most commonly adopted is completely drawn up in Euclidean space [31, 102].

The BS equation, proposed in the early 50s, is an important tool within manifestly covariant non-perturbative quantum field theory. It allows one to describe both bound states, through the homogeneous BS equation, and scattering states, via the inhomogeneous one [26, 29]. The example to be considered here is the two-body Bethe-Salpeter bound-state equation. It is obtained through the on-shell total momentum pole of the four-point Green's function in the energy-complex plane [103]. As a theory in the non-perturbative regime, the kernel must contain all possible two-body irreducible diagrams. However, it has to be emphasized that, even in presence of a truncated interaction kernel, the homogeneous BSE is able to describe a non perturbative regime, since it is the very nature of the integral equation that implicitly generates an infinite set of contributions, and eventually reconstructs a bound state pole in the four-leg Green's function[1]. The refinement of the interaction kernel certainly affects the position of the pole, but its existence is assured by the integral equation one has to solve. The major challenge in Minkowski space, where relativistic observables are formally defined, is due to the existence of singularities and branch points along the real axis of the relative energy in the amplitude as well as in the equation's interaction kernel. Dealing with this cumbersome analytic structure

---

[1]The pole is impossible to be reproduced without an infinite number of interaction exchanges.

when trying to solve the BSE in Minkowski space by brute force is numerically very hard. Indeed, these singularities are integrable due to the infinitesimal dislocation to the complex plane of the poles in the denominators of the propagators, i.e. the $\imath\epsilon$ factor according to the causality constraints. However, their integration is a quite delicate task and requires the use of appropriate analytical as well as numerical methods.

Such technical difficulties in solving the BSE emerge even for the most simple model, like a two-scalar system interacting through a massless scalar particle, and it hampered for a long time the development of a solution for the BSE directly in Minkowski space. The first approach, proposed by Wick [30], was based on the possibility of avoiding the intrinsic singularities through analytical continuation of the BSE to the complex plane, solving the equation in Euclidean space. This method, known as "Wick-rotation", makes the integral equation non-singular and allow its solution by standard numerical methods. Worth mentioning that for the special case of a massless exchanged boson an analytical solution of the BSE is achievable, what is known as the Wick-Cutkosky model [30, 33] and the technique adopted, though in Euclidean space, is quite similar to the one adopted in what follows, namely a suitable integral representation of the BS amplitude. For many years the Wick-rotation was fundamentally the only procedure adopted for solving the 4D BSE (see e.g. Refs. [104, 105, 106, 107, 108, 109]). Also noteworthy that the analytical continuation from Euclidean to the Minkowski space is unstable when done by numerical extrapolation [110].

Despite being widely used, Euclidean BS amplitudes have shortcomings related to its analytical extension to return to Minkowski space, where all dynamical observables are attainable. For example, the naive application of the Euclidean BS amplitude for the calculation of the electromagnetic form factors of bound states solutions of the BSE can lead to inconsistencies [111]. Another example of the necessity of the Minkowski space description appears in the calculation of the of light-like and time-like quantities, like e.g. the parton distribution functions (PDFs).For instance, within the framework based on the BSE plus DSE, the pion distribution has been evaluated in Euclidean space and then extrapolated to Minkowski space in order to get the light-front pion wave function [112]. A calculation fully underpinned by the Minkowskian structure would enable a remarkable corroboration of such extrapolation. However, it should be pointed out that there exist a general issue regarding the calculation of light-like and time-like observables in hadron physics, as shown by the intriguing example of the quasi-parton distributions. As recently proposed, one can calculate quasi-PDFs with moving hadrons in the Euclidean Lattice QCD for large longitudinal momentum to match with parton distribution functions in the infinite momentum frame [113], but unfortunately they are affected by uncontrollable renormalization issues as shown in Ref. [114]. Such an example yields another good motivation of developing non-perturbative tools genuinely Minkowskian.

One of the first successful attempts to provide a thorough numerical investigation of the solutions for the bosonic Bethe-Salpeter equation in Minkowski space was obtained by Kusaka and Williams [34]. They studied a simple model for the bound state of two massive scalar bosons interacting by exchanging another massive scalar boson, the so-called Yukawa model. They used the first order ladder approximation and the Nahanishi Perturbative Integral Representation (PTIR) for the BS ampli-

tude. The PTIR proposed in the early 60's [35], allows one to write *any* perturbative transition amplitude as an integral over a non-singular function of real variables, called Nakanishi weight-function, times a denominator containing the full analytical structure unambiguously determined within the Feynman diagrammatic framework. Since the BS amplitude is a three-leg amplitude, with one leg on its mass-shell, Kusaka and Williams used the Nakanishi integral representation (NIR) as an ansatz for the non-perturbative BS amplitude and solved the BSE, for the first time, directly in Minkowski space. They successfully reproduced the Euclidean space coupling constants computed by Linden and Mitter [104]. Although groundbreaking, their formulation was quite cumbersome to be extended to more complex systems, in particular with spin degrees of freedom or higher-order interaction kernels. Nevertheless, the NIR brings an important input on spelling out the analytical structure of the BS amplitude.

Following their success, in 2006, Karmanov and Carbonell [36] improved the method using a technique formally equivalent to LF projection (which is introduced below), but in spirit it is different. In their approach it is necessary to eliminate the spurious degree of freedom associated to the "auxiliary field", introduced to assure the four-momentum conservation for interacting systems when the interaction is buried in the mass of the system. In such a way, including higher-order contributions into the interaction kernel became possible. The reduction of degrees of freedom, inherent in the approach of Ref. [36], does not spoil the dynamical content of equation, since it is summarized in the Nakanishi weight function, which is the actual quantity to be determined numerically. Indeed, the approach puts in evidence the relation between the BS amplitude and the so-called valence light-front wave function (LFWF). This relation, obtained through a formally exact step, allows one to gain a deeper physical understanding. As a matter of fact, the BS amplitude does not have a probabilistic interpretation, but such a basic feature, helpful for the physical intuition, can be recovered after expanding the interacting state on a Fock basis. The amplitudes of each Fock state are called LFWF and the sum over their square moduli is equal to one. This property is fundamental for introducing the above mentioned probabilistic interpretation. In particular, the 3D restriction of the BS amplitude yields the amplitude of the first Fock state in the expansion, namely the amplitude of the valence component (more details are given below). Through the approach proposed in Ref. [36] a non-singular integral equation for the Nakanishi weight function was derived, enabling the numerical solution even when including a higher-order diagram in the kernel [37] and successfully comparing the results with calculations within Light-Front Dynamics. They were able to obtain the BS amplitude and the valence wave functions, from where any dynamical observable can be directly computed.

By adopting the so-called light-front projection, i.e. the integration on the component $k^- = k^0 - k^3$, allied to the uniqueness conjecture for the PTIR, Frederico *et al.* [38] obtained a non-singular inhomogeneous integral equation to describe the two-body scattering states in Minkowski space, as well as a new form for the homogeneous bound state equation which was solved numerically [39].

A valuable feature of the LF framework applied to the BSE is due to the relations among three essential quantities: the valence light-front wave function, the NIR spectral function and the BS amplitude (see Fig. 3.1). The connections are due to the fact that the Nakanishi integral representation gives the Bethe-Salpeter amplitude Φ
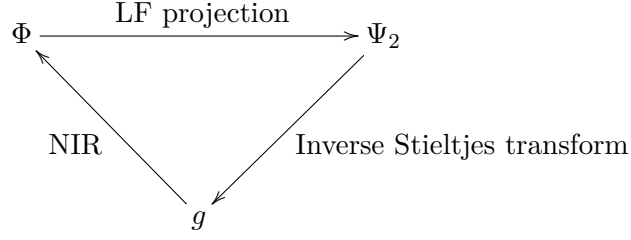
Figure 3.1. Diagram illustrating the connection between the BS amplitude Φ, valence LF wave function Ψ_2 and Nakanishi weight function g (diagram extracted from [116]).

through the weight function g, the light-front projection of the BS amplitude gives the valence light-front wave function Ψ_2 and the inverse Stieltjes transform gives the weight function g from the valence LFWF [115]. This makes quite straightforward to compute any of those quantities once one of them is known.

The main aim from now on is to explore and develop the approach for solving the BSE in Minkowski space, eventually via Light-Front Dynamics (LFD) [28], starting with a bosonic two-body bound state, i.e. the $\chi^2\phi$ model. None of the systems investigated hereinafter includes self-energies or vertex correction effects (for a solution of the $\chi^2\phi$ model including dressed propagators within a framework alike the one by Kusaka and Willians, see Ref. [117]). Following the aforementioned ideas, the main approach to be used here relies on the NIR of the BS amplitudes.The ladder approximation is the truncation of the interaction kernel considered, but other two-body irreducible contributions can be added, as well as different degrees of freedom, e.g. colors, as it is considered in what follows.

Although the method to solve the BSE in Minkowski space is quite general, allowing the inclusion of any order of the interaction kernel, solving the equation become numerically demanding when the interaction kernel is truncated beyond the ladder approximation. For instance, in the form factor calculation, considering the two-body current contribution already involves the computation of a 10-dimensional integral and, consequentially, a significant computational power. For that reason, most of the calculations are performed by using the first order truncated kernel. This hypothesis is intended to be tested here by adding explicitly the cross-ladder diagram to the kernel and studying its impact on the solution. How significant the impact is can depend on the underlying theory and its degrees of freedom. For instance, it turns out that within a scalar QCD model with non planar diagrams, color factors, generated after including the Gell-Mann matrices to each diagram, have a fundamental role for mitigating the influence of the contributions beyond the ladder one. Hence, one expects that the application of the ladder truncation in QCD should be more sound , given the color weights, than in the case of QED, where it is more problematic, as it is well-known. In the context of hadronic and nuclear physics, this outcome supports applications also to hadronic bound and scattering states, after the essential peculiarities of the underlying system under scrutiny are included in the approach.

A brief discussion of the BSE is also done in the context of 2+1 dimensions in Minkowski space. The validity of the NIR for the BS amplitude in $3 + 1$ dimensions has been treated and tested in several works, see e.g. [34, 36, 38]. In Ref. [118], it was shown for the first time that the extension of the NIR of the BS amplitude can be successfully applied to treat the problem of a bound state consisting of two scalar bosons in $2 + 1$ dimensions. The authors presented comparisons between the coupling constants computed in both Euclidean and Minkowski spaces. It was also shown that the BS amplitude in Euclidean space, calculated by means of the Wick-rotation, is in fair agreement with the one computed through the Wick-rotated NIR obtained from the solution in Minkowski space [42]. This is a strong statement in favor of the representation's reliability also in 2+1 dimensions.

It is well-known in non-relativistic quantum mechanics that any attractive short-range force binds a s-wave two-body system, as the radial eigenvalue equation reduced to a Sturm-Liouville problem has an attractive $-1/(2r)^2$ potential [119]. Therefore, it is reasonable to expect an increase in the binding energy of the relativistic bound state if an attractive interaction term is added, like the cross-ladder contribution to the kernel of the BSE. By using the same techniques and numerical methods as in the treatment of the BSE in 3+1 dimensional Minkowski space, the effects of the cross-ladder contribution to the interaction kernel is investigated also in 2+1 dimensions. One observes that, similarly to the case in 3+1 dimensions, the impact on the results is a significant attraction, being even more pronounced for states with large binding energy. One of the most interesting applications of relativistic 2+1 approaches is studying the properties of excitons, i.e. electron-hole bound states, in 2D materials within condensed matter physics. For example, experiments of light absorption by excitons and trions in monolayers of MoS2, material that has an hexagonal structure similar to graphene, could be explored within the relativistic formulation for the excitonic problem. The 2+1 BSE could be applied to model the interaction between the electron and the hole. However, the current status of the developed approach for 2+1 bosonic systems in Minkowski space needs further development to deal with problems at that level of complexity. More details of what will be shown here can be found in Refs. [120, 121].

Although some results for the solution of the BSE in 2+1 dimensions are given in what follows, the aim is to explore the 3+1 BSE towards developing a sound approach to deal with non-perturbative systems in Minkowski space. Once the technical steps are understood within simpler systems, like the scalar two-body one, the BS approach will be adapted to perform a phenomenological description of light mesons. This development gives the inputs for evaluating the partonic source amplitudes which are necessary for a better description of CPV in heavy meson decays, studied in Chap. 2.

3.1   The bound state structure within the BSE

The starting point is the investigation of the effect of the interaction-kernel truncation on the bound state structure of a bosonic two-body system once the BSE (see a diagrammatic sketch in Fig. 3.2) is solved by means of the NIR and light-front projection. The main observables under scrutiny are the valence light-front wave

function and the elastic electromagnetic form factor beyond the impulse approximation, i.e. taking into account the two-body current coming in consequence of the cross-ladder interaction. Adding the two-body exchange is necessary for fulfilling the gauge invariance, as the cross-ladder diagram also contributes to the EM current of the bound state pair. The aforementioned observables are particularly relevant in this context since they are intrinsically linked with the Minkowski space structure. Their asymptotic behaviors (i.e. at large values of the constituent momentum or momentum transfer, respectively, for the LFWF and form factor) are found to be quite independent of the inclusion of the cross-ladder kernel, and, moreover, the form factor's asymptotic tail turns out to decrease in agreement with the analytical result obtained through counting rules.
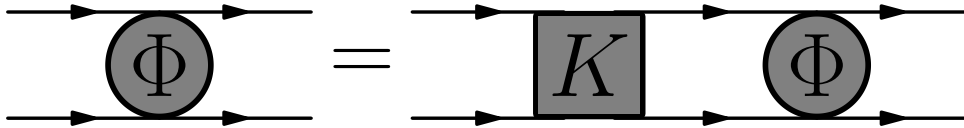
Figure 3.2. Diagrammatic representation of the two-body BSE.

For instance, the leading asymptotic large momentum behavior of hadron elastic form factors are usually calculated using quark counting rules within perturbative QCD [88, 122], while the higher-twist (i.e., beyond the impulse) contributions are expected to be suppressed for high momentum transfer [88]. One interesting example of such a calculation, applied to a spin 1 two-fermion bound state, was performed in Ref. [123], with the subleading power corrections being later considered for both the deuteron [124, 125] and ρ-meson [126] elastic form factors. Given the rich information on the dynamics that one could extract, it is worth carrying out a calculation completely performed in a non-perturbative approach, even for a simple spinless system like the one presented here. This is part of the efforts of this thesis, that aim at establishing a phenomenological framework where hadrons can be studied also in a non-perturbative regime. Understanding the dynamics in simpler scenarios is essential to keep subtleties under control. Here the asymptotic behavior is obtained from the numerical solution of the BSE, as well as analytically from counting rules, both for the valence LF wave function and EM form factor.

The investigation of the cross-diagrams in the interaction kernel was already done within the Minkowski space approach in Ref. [37], but without a detailed exploration of the bound state structure, as the aim was to demonstrate the generality of the method based on the NIR while enclosing different contributions to the interaction kernel truncation. The infinite set of irreducible cross-ladder diagrams for a $\chi^2\phi$ model was previously analyzed within the Feynman-Schwinger representation framework in Ref. [105], showing a huge effect on the binding energy. However, the approach was completely done in Euclidean space. One interesting study beyond the one-body exchange was performed in Ref. [127], where, within a light-front two-body bound-state equation, the full light-front dynamic interaction kernel, including the ladder, cross-ladder, stretched-box, and particle-antiparticle creation/annihilation effects was explored showing in detail contributions of higher Fock states.

It is known that the cross-ladder diagram in its lowest order imposes a significant

net attraction between the two particles in the bound state [37]. This effect is expected to be seen in every observable, but can manifest differently on dynamical ones. Therefore, if the influence of the lowest-order cross-diagram is not negligible, introducing higher order contributions could lead to a sizable effect on the observables. In view of this, understanding quantitatively the dynamics beyond the ladder exchange is an essential step, since to access in detail the range of validity of the ladder approximation is important for extending the description based on the BSE to more complicated systems (e.g. with spin dof or other interaction lagrangian) without facing too cumbersome calculations. The LF framework analysis can be extended to fermionic systems [49, 50] in a quite straightforward way, what would prepare the ground for applications to the study of meson structure. A starting development in this direction will be presented at the end of the thesis.

3.1.1 Bethe-Salpeter Equation and Nakanishi Integral Representation

For two spinless particles, carrying momenta p_1 and p_2, and with a general interaction kernel the BS equation in Minkowski space reads

$$\Phi(k, p) = G(\eta_1 p + k)G(\eta_2 p - k) \int \frac{d^4k'}{(2\pi)^4} iK(k, k', p)\Phi(k', p), \qquad (3.1)$$

where, for $\eta_1 = \eta_2 = 1/2$, $k = (p_1 - p_2)/2$ is the relative momentum, $p = p_1 + p_2$ the total momentum and $M = \sqrt{p^2}$ the total bound state mass. The Feynman propagators $G(p')$ can in general be represented by the Källen-Lehmann spectral representation as [128]

$$G(p') = \int_0^\infty ds \frac{\rho(s)}{p'^2 - s + i\epsilon}. \qquad (3.2)$$

In what follows, $B(n) = 2m - M(n) > 0$ is the binding energy of the $n-$th state. Including the representation for the propagator the equation reads

$$\begin{aligned}
\Phi(k, p) &= \int_0^\infty d\gamma \frac{\rho(\gamma)}{(\eta_1 p + k)^2 - \gamma + i\epsilon} \int_0^\infty d\gamma' \frac{\rho(\gamma')}{(\eta_2 p - k)^2 - \gamma' + i\epsilon} \\
&\times \int \frac{d^4k'}{(2\pi)^4} iK(k, k', p)\Phi(k', p).
\end{aligned} \qquad (3.3)$$

For the further developments the simplest version of the propagator will be considered, i.e. without including self-energy or loop corrections. Therefore, one has that $\rho(\gamma) = \delta(\gamma - m^2)$, and Eq. (3.2) becomes

$$G_0(p') = i \frac{1}{[p'^2 - m^2 + i\epsilon]}. \qquad (3.4)$$

The interaction kernel $iK(k, k', p)$, extensively discussed in Refs. [37, 41, 127] is given by an infinite sum of two-body irreducible Feynman diagrams, being most commonly represented in the ladder approximation.

Solving Eq. (3.1) in terms of the unknown quantity $\Phi(k, p; M^2)$ is generally challenging, as its analytic structure contains singularities that are hard to deal with

numerically. The approach of Refs. [34, 36, 38] proposes to introduce an ansatz for the BS amplitude: the Nakanishi integral representation [35, 34], which for the s-wave amplitude is given by

$$\Phi(k,p) = -i \int_{-1}^{1} dz \int_{0}^{\infty} d\gamma \frac{g(\gamma,z)}{(\gamma + m^2 - \frac{1}{4}M^2 - k^2 - p \cdot k\ z - i\epsilon)^3} \,, \qquad (3.5)$$

where the weight function $g(\gamma,z)$ is a non-singular unknown quantity, to be determined numerically, and the dependence upon the external momenta is explicitly given by the denominator. The representation of Eq. (3.5) is an essential tool in this approach, as it allows one to deal with the singularities and branch cuts analytically, and to know their positions so that it is possible to avoid eventual numerical problems. The NIR is a general representation for N-leg transition amplitudes, originally proposed in the perturbative context.One particular well-known case of the NIR is the Källen-Lehmann spectral representation (see Eq. (3.2)), which corresponds to the 2-point correlation function, and is often used to describe one-particle propagators.

Once all the singularities are known due to the explicit analytic structure, one needs to deal with them, preferably analytically, to make the numerical resolution of the BSE smoother. A very useful technique for that purpose is the light-front projection, which simply relies on introducing the LF variables $k_{\pm} = k_0 \pm k_z$ and $k_{\perp} = (k_x, k_y)$ and perform the integration over the k^- variable.

It is important to notice that such an integration over k^- amounts to restrict the BS amplitude onto the hyperplane $x^+ = 0$, which physically corresponds to eliminate the relative LF time $t + z$ between the constituent particles, and also recovers the probabilistic interpretation. The LF projection allows one to address the light-cone dynamics, since the hyperplane $x^+ = 0$ is tangent to the light-cone (i.e. $x^2 = x^+ x^- - \mathbf{x}_{\perp}^2 = -\mathbf{x}_{\perp}^2 \leq 0$). Formally, the k^- projection corresponds simply to perform Cauchy integration, what ensures a proper treatment of the singularities by taking into account their contributions. This straightforward trick makes the solution of the dynamics of the propagators and amplitudes much simpler [129] and enables a direct connection between the valence light-front wave function, ψ_{LF}, and the BS amplitude through the k^- integration [38], i.e.

$$\begin{aligned}
\psi_{LF}(\gamma,\xi) &= \frac{p^+}{\sqrt{2}}\ \xi\ (1-\xi)\ \int_{-\infty}^{\infty} \frac{dk^-}{2\pi}\ \Phi(k,p) = \\
&= \frac{1-z^2}{4} \int_{0}^{\infty} \frac{g(\gamma',z)d\gamma'}{\left[\gamma' + \gamma + z^2 m^2 + (1-z^2)\kappa^2\right]^2} \,,
\end{aligned} \qquad (3.6)$$

where the transverse momentum is $k_{\perp} = \sqrt{\gamma}$ and the LF longitudinal momentum fraction is $\xi = (1-z)/2$ with $0 < \xi < 1$. The BS equation has physical and abnormal solutions, with the first ones constrained, for identical bosons, by the symmetry property on the weight function, namely $g(\gamma,z) = g(\gamma,-z)$, what should be also seen in the valence wave function.

Combining NIR and LF projection is a robust procedure as it makes the final integral equation non-singular, something that is remarkable regarding solving BSE directly in Minkowski space. Applying the NIR (3.5) on both sides of the spinless BSE (3.1), performing the integration over k^-, and making some transformations [36, 39],

one gets the following compact expression

$$\int_0^\infty \frac{g(\gamma', z; \kappa^2)d\gamma'}{\left[\gamma' + \gamma + z^2 m^2 + (1 - z^2)\kappa^2\right]^2} = \int_0^\infty d\gamma' \int_{-1}^1 dz' \ V(\gamma, z, \gamma', z'; \alpha)g(\gamma', z'; \kappa^2), \quad (3.7)$$

where $\kappa^2 = m^2 - \frac{1}{4}M^2 > 0$, since within the model the bound state mass is constrained by the constituent particle masses, and $V(\gamma, z, \gamma', z'; \alpha)$ is the expression resulting from the interaction kernel K, the boson propagators and the NIR denominator.The weight function g is determined by solving the generalized eigenvalue problem like $Ag = \lambda(\alpha)Cg$, where A and C are the matrices coming from the basis expansion of g on the LHS and RHS of Eq. (3.7), respectively. λ is the eigenvalue and $\alpha = \alpha(B)$ the coupling constant for a fixed binding energy B. More details on the full expressions for $V(\gamma, z, \gamma', z'; \alpha)$ for both ladder and ladder plus cross-ladder kernels see Refs. [36, 37, 121]. The numerical method to solve Eq. (3.7) is quite straightforward, simply involves basis expansions using orthogonal polynomials, namely, Laguerre polynomials for the noncompact dependence on γ and Gegenbauer polynomials for the compact z variable. The numerical procedure is described more explicitly in Sec. I.2 and Refs. [39, 130], for the interested reader. Any other basis expansion can in principle be used as, for instance, splines (see Ref. [36]), but the particular one used here is convenient since it allows an easy implementation of the weight function symmetry for $z \to -z$ and allows to impose orthogonality of the polynomials on the matrices avoiding the need of meshes for interpolating the basis functions.

3.1.2   Coupling constant and valence LFWF

The numerical solution of Eq. (3.7) gives two main quantities for fixed bound state (M) and exchanged boson (μ) masses: the coupling constant $\alpha^{(K)}$ and the weight function $g^{(K)}(\gamma, z)$, both dependent on the adopted truncation for the interaction kernel K. From these quantities all the observables can be obtained. Table 3.1 shows the values of $\alpha^{(L)}$ and $\alpha^{(L+CL)}$, i.e. the coupling constants with Eq. (3.7) solved with the ladder (L) and ladder plus cross-ladder (L+CL) kernels, different values of the binding energy $(B = 2m - M)$ and exchanged boson mass μ. It is clear that adding the cross-ladder kernel brings a strongly attractive effect on the coupling constant reducing its value for a given binding energy. In order to check the effect on a structure observable, the valence LFWF is also computed under both truncations of the interaction kernel and their ratio, $\psi_{LF}^{(L)}/\psi_{LF}^{(L+CL)}$, is given for $\xi = 1/2$ $(z = 0)$ and $\gamma = 500 \, m^2$ (asymptotic region). Analogously, the fifth column of Table 3.1 gives the ratio between the coupling constants, $\alpha_{LF}^{(L)}/\alpha_{LF}^{(L+CL)}$. Comparing the rations of the fifth and sixth columns it is possible to conclude that the impact of the different truncations in the interaction kernel bring the same effect on both quantities. A large value is chosen for fixing γ due to the fact that the LFWF is arbitrarily normalized as $\psi_{LF}^{(L)}(0, 1/2) = \psi_{LF}^{(L+CL)}(0, 1/2) = 1$ in all the cases.

After understanding a bit better the cross-ladder impact on the asymptotic limit, one can look at the overall momentum dependence of the valence wave function. The chosen case is for a strongly bound system, $B = 1.5 \, m$, as there the effect is

B/m	μ/m	$\alpha^{(L+CL)}$	$\alpha^{(L)}$	$\alpha^{(L)}/\alpha^{(L+CL)}$	$\psi_{LF}^{(L)}/\psi_{LF}^{(L+CL)}$
1.5	0.15	4.1399	6.2812	1.5172	1.5774
	0.50	5.1568	7.7294	1.4988	1.5395
1.0	0.15	3.5515	5.3136	1.4961	1.5508
	0.50	4.5453	6.7116	1.4766	1.5094
0.5	0.15	2.5010	3.6106	1.4436	1.4805
	0.50	3.4436	4.9007	1.4231	1.4405
0.1	0.15	1.1052	1.4365	1.2997	1.2763
	0.50	1.9280	2.4980	1.2956	1.2694

Table 3.1. First and second columns present the fixed values for the binding energy and exchanged boson mass, respectively. Third and forth columns give the outputs when solving Eq. (3.7) with ladder (L) and ladder plus cross-ladder (CL) kernels. The last two columns are for comparison between the ratio of the coupling constants, given in terms of $\alpha = g^2/(16\pi m^2)$, corresponding to ladder (L) and ladder plus cross-ladder (L+CL) kernels, with the ratio of the LF wave functions in the asymptotic limit ($\psi(\gamma = 500\,m^2$, $\xi = 1/2$)).

more pronounced. Fig. 3.3 presents the valence LFWF as a function of $\gamma = k_\perp^2$ for fixed longitudinal momentum $\xi = 1/2$ for both ladder (dashed-red) and ladder plus cross ladder (solid-black) kernels. The left and right panels are for $\mu = 0.15\,m$ and $\mu = 0.5\,m$, respectively. Due to the fact that the same normalization was adopted to both cases, it is seen that at low momentum, $\sqrt{\gamma} \lesssim 3\,m$, the curves almost coincide for ladder and ladder plus cross-ladder kernels. Physically, this can be understood as the a behavior dictated by the binding energy, as the coincidence region between the curves is around $\sqrt{\gamma} \sim B = 1.5\,m$. On the other extreme, at large momentum, ladder and ladder plus cross-ladder results are practically proportional, what agrees with the general discussion on asymptotic behavior of the LF wave function in Ref. [88] where it was shown that the large momentum tail should be dominated by the ladder exchange.
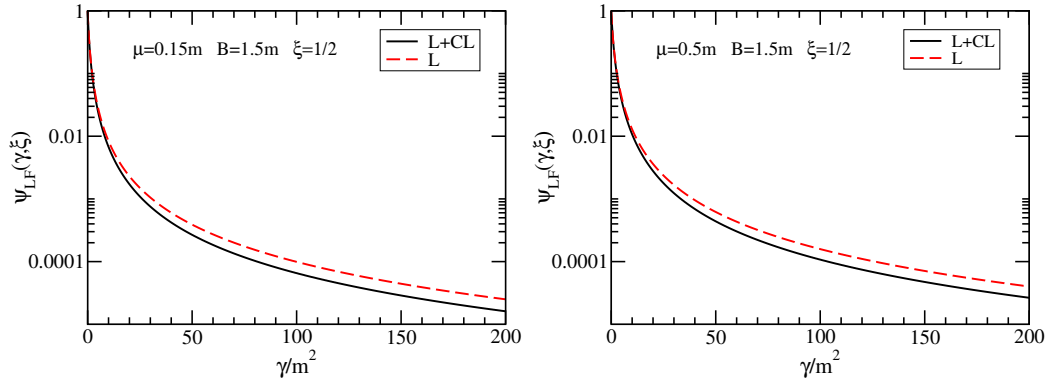
Figure 3.3. LF wave function vs. γ for $\xi = 1/2$ with ladder (L) (dashed lines) and ladder plus cross-ladder (L+CL) (solid lines) interaction kernels for $B = 1.5\,m$ and $\mu = 0.15\,m$ (left-frame) and $\mu = 0.5\,m$ (right-frame).

A simple, but interesting, factorization of the LFWF in terms of its asymptotic

behavior and general longitudinal momentum distribution was given in Ref. [130] for ground and excited states, reading as follows,

$$\psi_{LF}(\gamma, \xi) \to \alpha \; \gamma^{-2} \, C(\xi) \,, \tag{3.8}$$

where the coupling constant, α, is factorized and the asymptotic behavior ($\gamma \to \infty$) is fixed by the generalized counting rule given in Ref. [84], being the same found through the Wick-Cutkosky (WC) model (ladder kernel, zero exchanged mass), where the valence wave function reads [131]

$$\psi_{LF}^{(WC)}(\gamma, \xi) = \frac{C^{(WC)}(\xi)}{2\sqrt{\pi}(\gamma + m^2 - \xi(1 - \xi)M^2)^2}. \tag{3.9}$$

The function $C^{(WC)}$ is given by $C^{(WC)}(\xi) = \xi(1 - \xi)g^{(WC)}(1 - 2\xi)$ and has two different shapes according to the extreme limits of the binding energy, i.e. strongly and weakly bound states. They are explicitly given by

$$C^{(WC)}(\xi) = [\xi(1 - \xi)]^2 \,, \tag{3.10}$$

for $B = 2\,m$, and,

$$C^{(WC)}(\xi) = \xi(1 - \xi)\left(\frac{1}{2} - |\frac{1}{2} - \xi|\right) \tag{3.11}$$

for $B \to 0$. Keeping these functions in mind is helpful to understand more of the $C(\xi)$ behavior in the case under study here.

The aim now is to study the longitudinal asymptotic ($\gamma \to \infty$) distribution $C(\xi)$ under the influence of the interaction kernel. For practical purposes the normalization is arbitrarily fixed at $\psi_{LF}(0, 1/2) = 1$ for all the cases. Formally this constraint for fixing the function $C(\xi)$ should be obtained from the normalization of the BS amplitude [39], nevertheless the precise quantity is not necessary given the goal of the current study. The aim is to explore how $C(\xi)$ changes if the binding energy is kept fixed, knowing that the coupling constant changes due to the cross-ladder attraction and since the high momentum region is unaltered due to the ladder exchange dominance. Fig. 3.4 presents a comparison including $C(\xi)$ computed with the ladder kernel, ladder plus cross-ladder kernel and their shapes when obtained within the WC model (Eqs. (3.10) and (3.11)). The results are presented for weak, $B = 0.118\,m$, and strong, $B = 1.5\,m$, binding energies and compared with the Wick-Cutkosky model for both extremes, $B = 2m$ and $B \to 0$. The exchanged boson mass is here fixed as $\mu = 0.15\,m$. From Table 3.1 it could be concluded that the wave function scales according to α in the asymptotic region. Therefore, for the calculations represented in Fig. 3.4, it was considered the different coupling constants according to their binding energies, as well as the ratio $\psi_{LF}^{(L)}/\psi_{LF}^{(L+CL)}$ for fixed $\gamma = 500\,m^2$ and $\xi = 1/2$ ($z = 0$), which is approximately the same as the ratios between the values of α, i.e. $\alpha^{(L)}/\alpha^{(L+CL)} \approx \psi_{LF}^{(L)}/\psi_{LF}^{(L+CL)}$. This brings a good argument in favor of factorizing α in Eq. (3.8).

Fig. 3.4 shows that the shape of $C(\xi)$ is practically unchanged with B, differently from what is given by the Wick-Cutkosky model between the extreme limits of binding energy. However it is important to point out that the magnitude of $C(\xi)$ decreases by a factor of ≈ 10 from $B = 1.5\,m$ to $0.118\,m$, what is seen on the plot
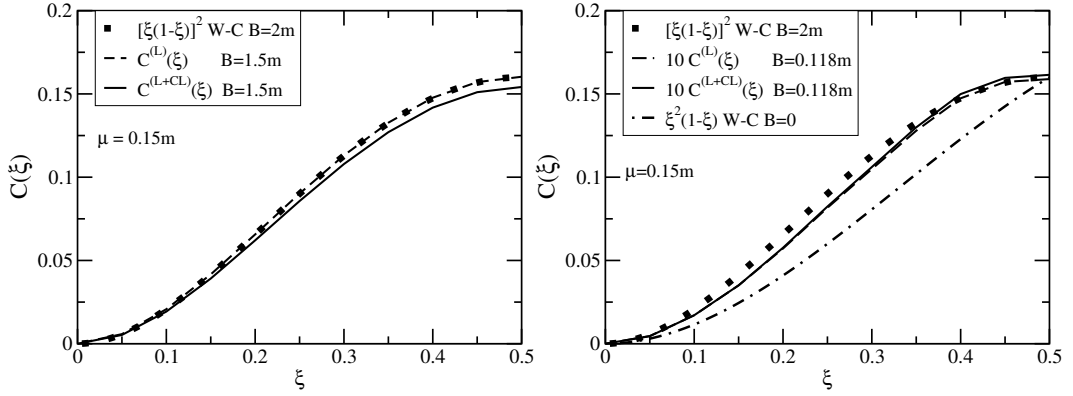
Figure 3.4. Asymptotic function $C(\xi)$ of Eq. (3.8) computed for the ladder, $C^{(L)}(\xi)$ (dashed line), and ladder plus cross-ladder, $C^{(L+CL)}(\xi)$ (solid line), kernels. The results are compared to the functions obtained within the Wick-Cutkosky model for $B = 2m$ (full box) and $B \to 0$ (dash-dotted line, right panel). On the left $B = 1.5\,m$ and on the right $B = 0.118\,m$. Exchanged boson mass of $\mu = 0.15\,m$. For the comparison, the curves for $B = 0.118\,m$ are multiplied by 10.

due to the fact that both curves are normalized to the same value. This significant difference comes from the fact that the wave function decays considerably slower for strongly bound systems. Regarding the comparison with the Wick-Cutkosky model, one can see that the results are better represented by the case where $B = 2\,m$, i.e. $C(\xi)$ can be reasonably well represented by $[\xi(1-\xi)]^\lambda$, where $\lambda = 2$ when $\mu \to 0$. If $\mu \to \infty$, that means a zero-range interaction, the LFWF asymptotic behavior becomes γ^{-1}, with its longitudinal distribution better represented by $C(\xi) = [\xi(1-\xi)]^2$.

This study shows that the form of the longitudinal momentum fraction distribution of the valence LF wave function is quite universal. One can then make up a conjecture that the shape and magnitude of $C(\xi)$, along with the wave function at low transverse momentum, for an arbitrary normalization and given binding energy, are independent on the inclusion of the irreducible cross-ladder contributions in the interaction kernel. Reminding Ref. [105], where the Yukawa model with the complete ladder kernel was solved by means of the Feymman-Schwinger representation, one can use the result for the coupling constant found there to model through Eq. (3.8) the form of the valence wave function with an infinite set of cross-ladder diagrams in the kernel interaction kernel.

Worth mentioning that the Nakanishi weight function, $g(\gamma, z)$, gives the behavior at $z \to \pm 1$, and which is quadratic at the end points. Therefore the behavior of $C(\xi)$ comes from a linear damping of $g(\gamma, z) \sim (1 - |z|)$ for $|z| \to 1$, feature that will be useful later while analytically analyzing the asymptotic form of the EM form factor to demonstrate the consistency of the results with the counting rules.

3.1.3 Space-like elastic EM Form factor

Firstly the electromagnetic current needs to be introduced. In its general case and for a scalar bosonic system it reads

$$J_\mu = (p_\mu + p'_\mu)F_1(Q^2) + (p_\mu - p'_\mu)F_2(Q^2)\,, \tag{3.12}$$

where the total momentum transfer is defined as $Q^2 = -(p - p')^2 > 0$, being greater than zero since only the space-like region will be studied here. Equation (3.12) is reduced to a simpler form in the case that no transition is considered since $F_2 = 0$ due to current conservation in the elastic case. The remnant form factor, F_1, stands for the absorption of a virtual photon by the bound state system. As the cross-ladder interaction kernel is considered in the calculations, due to gauge invariance the EM coupling requires two irreducible contributions to the photon absorption amplitude, leading to two terms of the form factors, i.e.

$$F_1(Q^2) = F_I(Q^2) + F_X(Q^2), \tag{3.13}$$

where F_I represents the usual impulse contribution, related to the triangle diagram on the left of Fig. 3.5, and F_X is linked to the additional two-body current contribution, illustrated in the right side of Fig. 3.5. Applying the Feynman rules to the diagram
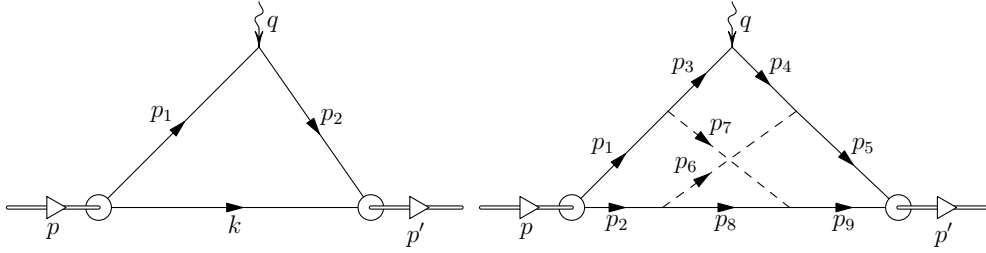
Figure 3.5. Photon absorption amplitude diagramatically represented for the (left) impulse and (right) two-body current contributions.

on the left of Fig. 3.5, one can analytically express the impulse approximation for the EM form factor as

$$(p + p')^\mu F_I(Q^2) = i \int \frac{d^4k}{(2\pi)^4}(p + p' - 2k)^\mu\,(k^2 - m^2)\,\Phi\left(\frac{p}{2} - k, p\right)\Phi\left(\frac{p'}{2} - k, p'\right), \tag{3.14}$$

which is written in terms of the BS amplitude Φ. One can now substitute on the right hand side the NIR for the BS amplitude and contract both sides of Eq. (3.14) with $(p + p')_\mu$ obtaining the following,

$$F_I(Q^2) = \frac{i}{(2\pi)^4}\int_0^\infty d\gamma \int_{-1}^1 dz \int_0^\infty d\gamma' \int_{-1}^1 dz' \int d^4k \left[1 - \frac{2k\cdot(p + p')}{(p + p')^2}\right]$$
$$\times \frac{(m^2 - k^2)\,g(\gamma, z)g(\gamma', z')}{D^3(\gamma, z; \frac{p}{2} - k, p)\,D^3(\gamma', z'; \frac{p'}{2} - k, p')}\,, \tag{3.15}$$

where $D = \gamma + m^2 - \frac{1}{4}M^2 - k^2 - p \cdot k \, z - i\epsilon$ is the denominator of the NIR (3.5). One can easily perform the loop integral in d^4k in Eq. (3.15) through Feynman parametrization, a procedure that is detailed in Refs. [32, 121]. The final expression, after performing the analytical integration, is given by

$$F_I(Q^2) =$$
$$= \frac{1}{2^7\pi^3} \int_0^\infty d\gamma \int_{-1}^1 dz \, g(\gamma, z) \int_0^\infty d\gamma' \int_{-1}^1 dz' \, g(\gamma', z') \int_0^1 dy \, y^2(1-y)^2 \frac{f_{num}}{f_{den}^4}, \quad (3.16)$$

where

$$f_{num} = (6\eta - 5)m^2 + [\gamma'(1-y) + \gamma y](3\eta - 2) + 2M^2\eta(1-\eta) + \frac{1}{4}Q^2(1-y)y(1+z)(1+z')$$

$$\text{and} \quad f_{den} = m^2 + \gamma'(1-y) + \gamma y - M^2(1-\eta)\eta + \frac{1}{4}Q^2(1-y)y(1+z)(1+z'),$$
$$(3.17)$$

with $2\eta = (1+z)y + (1+z')(1-y)$. Eq. (3.16) depends on the weight function $g(\gamma, z)$ which was obtained by solving the BSE (3.7).

The same can be now done for the two-body current, starting by applying the Feynman rules to the diagram on the right of Fig. 3.5. Following the notation of the figure, the photon vertex is now $-i(p_4 + p_3)^\mu$. The full expression can be written as

$$F_X(Q^2) = -i\frac{g^4}{(2\pi)^{12}} \int d^4p_2 d^4p_8 d^4p_9 \left[1 - 2\frac{(p+p')\cdot(p_9 + p_2 - p_8)}{(p+p')^2}\right]$$
$$\times \left[\prod_{i=3,\, i\neq 5}^8 \frac{1}{p_i^2 - m_i^2 + i\epsilon}\right] \Phi\left(\frac{p}{2} - p_2, p\right) \Phi\left(\frac{p'}{2} - p_9, p'\right), \quad (3.18)$$

where $p_3 = p - p_9 - p_2 + p_8$, $p_4 = p' - p_9 - p_2 + p_8$, $p_6 = p_2 - p_8$, $p_7 = p_9 - p_8$, $m_3 = m_4 = m$ and $m_6 = m_7 = \mu$. Naturally, the second term between square brackets in the first lines of Eqs. (3.15) and (3.18) yields zero contributions for the linear terms in k after the 4D loop integrations (further details on the derivation are presented in Ref. [121]).

Again, the NIR should be introduced and the Feynman parametrization used to perform all the three loop integrations. The final formula can be conveniently expressed in a compact form

$$F_X(Q^2) = -\frac{3\alpha^2 m^4}{(2\pi)^5} \int_0^\infty d\gamma \int_{-1}^1 dz \int_0^\infty d\gamma' \int_{-1}^1 dz' g(z', \gamma') g(z, \gamma)$$
$$\times \prod_{i=1}^6 \int_0^1 dy_i \Theta\left(1 - \sum_{j=i+1; i<4}^4 y_j\right)(1-y_5)^2 y_5^2(1-y_6)^2 y_6^3 \frac{f_{num}^X}{\left[f_{den}^X\right]^5}, \quad (3.19)$$

where the lengthy expressions for f_{num}^X and f_{den}^X, dependent of m, y_i, γ, z, γ', z', p' and p, are presented in Ref. [121], where the detailed derivation is also presented. Six Feynman parametric integrations are necessary to perform the loop integrations. Notice that Eq. (3.19) is completely non-singular and can be computed by means of standard numerical methods.

It is valuable to comment briefly on current conservation in this problem. The elastic EM vertex (3.12) is symmetric when permuting $p \leftrightarrow p'$, either for the impulse or for the two-body current contributions. Therefore, the second term of Eq. (3.12), which is antisymmetric under the same permutation, needs to be necessarily zero for the elastic EM vertex, implying $F_2(Q^2) \equiv 0$. The contraction of the EM vertices with $(p - p')^\mu$ (for any individual contribution to the form factor in the elastic case, namely the impulse or two-body current ones in the present case) will lead to zero as a consequence of current conservation $J \cdot q = 0$. This property is even for an isolated irreducible term of the form factor, what does not happen in the inelastic (transition) case (i.e., the non-diagonal matrix elements of $J \cdot q = 0$) where one verifies the current conservation condition after adding all the terms relative to the ones included in the interaction kernel. It would be very interesting to consider this beyond the impulse approximation problem for, e.g., a transition between the ground to an excited case, where finding numerically $J \cdot q = 0$ would depend on the non-trivial cancellation among the contributions to the form factor. One analogous example of the discussion above was presented in Ref. [132], where current conservation for the inelastic form factor of the EM breakup process (bound $\rightarrow$ scattering state) was explicitly obtained numerically. In that case two contributions were necessary for finding the cancellation that produces $J \cdot q = 0$, namely the triangle diagram plus the FSI contribution on the outgoing scattering state.

Thereafter deriving the equation, one can plug in the eigenvector and eigenvalue found by solving Eq. (3.7) with the appropriate kernel, in Eqs. (3.16) and (3.19) and perform the needed integrations to find what is shown in Fig. 3.6. The figure displays the impulse, F_I, and two-body current irreducible contributions, F_X, to the form factor for different sets of input parameters, i.e. binding energy B and exchanged boson mass μ. It is important to have in mind that although there is a truncation involved in the interaction kernel, all the Fock state contributions related to a certain irreducible graph are naturally incorporated in the Bethe-Salpeter approach. Therefore, the form factor presented here present all the contributions beyond the valence component both at ladder and cross-ladder levels.

Trying to cover both strongly and weakly bound state regimes the adopted sets were: $B = 0.1\,m$ and $\mu = 0.15\,m$; $B = 0.1\,m$ and $\mu = 0.5\,m$; $B = 1.5\,m$ and $\mu = 0.15\,m$; $B = 1.5\,m$ and $\mu = 0.5\,m$. Solid curves in Fig. 3.6 represent the total form factor (3.13), i.e. with both contributions added, and its individual contributions are also showed. From the figure one can observe that the two-body current F_X contribution increases for smaller μ when B is fixed, which indicates that when $\mu \rightarrow \infty$ (limit to the contact interaction) the contributions beyond the triangle approximation tends to be suppressed. The total form factor is normalized to one at $Q^2 = 0$, as it should be for the elastic case. Noteworthy that the value of $F_{total}(Q^2 = 0)$ gives the covariant normalization of the BS amplitude. Meanwhile when the binding energy is increased for fixed μ the size of the state is bigger and a slower decay of the form factor is seen, with the crossed contribution also getting more relevant, reaching about 15% of the total at $Q^2 = 0$. Simplistically, based on this toy model, one could expect that strongly bound QED systems would require adding this kind of extra contributions while computing their observables. For QCD systems, as the color degree of freedom comes into play, this expectation is even less obvious, but this will be covered in the next section.
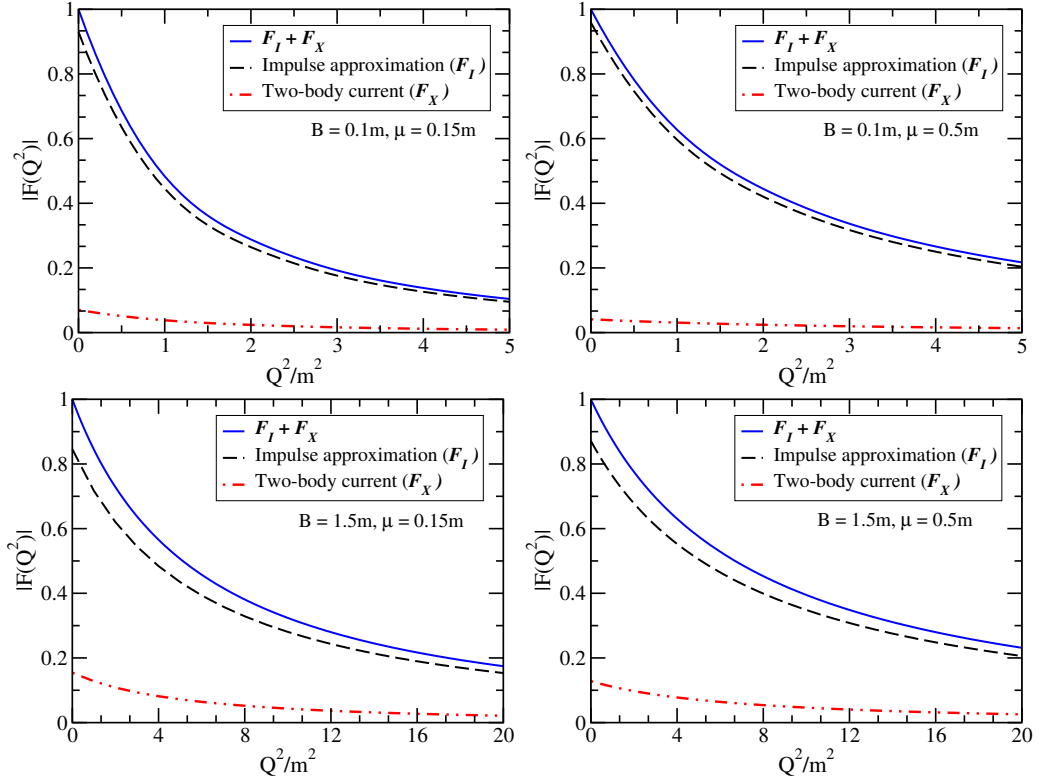
Figure 3.6. EM Form factor vs momentum transfer Q^2 for the BS amplitude with the ladder plus cross-ladder kernel. Total form factor (solid) compared to the impulse contribution F_I (dashed) and to the two-body current F_X (double-dotted dashed) contribution to the vertex. Sets of fixed parameters are (upper-left frame) $B = 0.1\,m$ and $\mu = 0.15\,m$; (upper-right frame) $B = 0.1\,m$ and $\mu = 0.5\,m$; (lower-left frame) $B = 1.5\,m$ and $\mu = 0.15\,m$; (lower-right frame) $B = 1.5\,m$ and $\mu = 0.5\,m$.

Figure 3.6 also shows that as Q^2 grows the impulse approximation gets practically parallel to the total form factor, suggesting that the ladder exchange defines the pattern of the curve for large momentum. This indicates that only the first graph, i.e. the simple triangle diagram, is enough for describing the asymptotic region. Moreover, the bigger μ is, earlier the impulse approximation starts to dominate, what happens also for smaller B with μ fixed (see the upper panels of Fig. 3.6). This enhancement of the two-body current contribution for smaller μ (wider range of the interaction) and larger B (smaller size of the bound state) can be understood by considering that in both cases the overlap between the bound state and the two-body current increases. For the low momentum region, as happens for the valence LFWF, the binding energy (or the bound state mass) is the main quantity shaping the form factor. The asymptotic region concentrates a lot of physics and will be analyzed in detail later in the text.

Another result that corroborates the argument that the structure at the low momentum region is fixed by the binding energy can be seen in Fig. 3.7. To bring a different perspective, all the curves now are normalized to one and a broader interval of Q^2, namely $0 \leq Q^2/m^2 \leq 50$, is shown (logarithmic scale is adopted for a

better visualization). In this figure the form factor in the impulse approximation is computed both with the solution of the BSE corresponding only to the ladder interaction kernel as well as with the solution considering both graphs, i.e. ladder plus cross ladder diagrams, aiming at analyzing the change in the dynamics according to the interaction kernel. Dot-dashed lines present the impulse contribution computed with the BS amplitude obtained by solving the BSE with the ladder truncation, while dashed lines show the impulse contribution with the solution for a ladder + cross-ladder interaction kernel. The results are all for strongly bound systems with $B = 1.5m$ and for two exchanged boson masses: $\mu = 0.15m$ and $\mu = 0.5m$. It is quite clear that at low momentum, typically below $Q \approx B$, all the curves roughly coincide and have similar slopes, what express the bound state size and charge radius. Comparing the left and right panels of the figure one sees that changing μ does not affect that feature. Regarding the tail of the curve, it is possible to see that something similar to what was seen in Table. 3.1, that the valence LFWF asymptotic region scales with the coupling constant, also appears in the form factor.
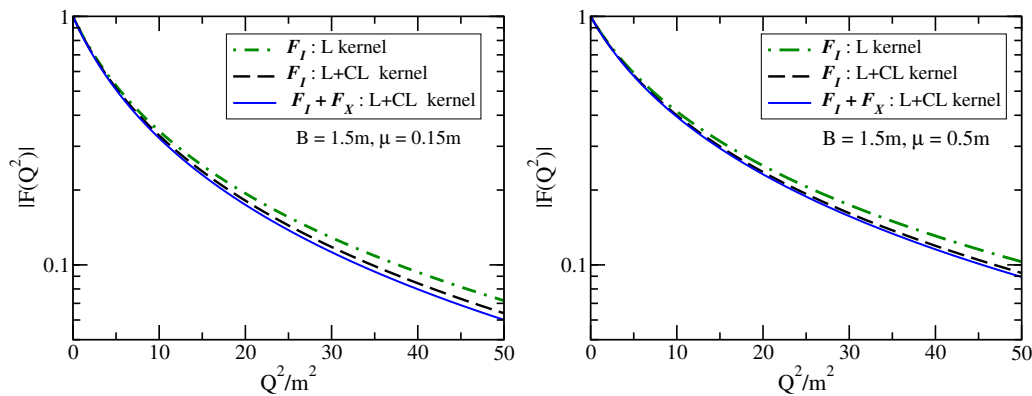
Figure 3.7. EM Form factor vs Q^2. Dot-dashed line: impulse contribution calculated in ladder (L) approximation. Dashed line: the same as the dot-dashed line but adding the cross-ladder (CL) diagrams. Solid line: full calculation. All curves are normalized to $F(Q^2 = 0) = 1$. Binding energy fixed at $B = 1.5\,m$, while two exchanged boson masses are adopted: (left-panel) $\mu = 0.15\,m$ and (right-panel) $\mu = 0.5\,m$.

3.1.4 Asymptotic behavior of the form factor

As commented before, the asymptotic behavior of the form factor is very interesting, among other reasons, due to the fact that this region is extensively discussed in the literature and many properties are known, including from perturbative approaches. The aim here is to explore some properties of the form factor at high momentum both numerically and analytically. Analytically, it is quite useful to obtain the leading behavior of the form factor for $Q^2 \to \infty$ using standard counting rules, as done in the seminal paper by Lepage and Brodsky [88]. Following this idea, the form factors of Eqs. (3.16) and (3.19) should have their leading power-law behavior as dictated by simply counting the Q^2 factors coming from the propagators, and the results are expected to be

$$F_I(Q^2) \sim Q^{-4} \quad \text{and} \quad F_X(Q^2) \sim Q^{-6}, \tag{3.20}$$

discarding logarithmic corrections, which can be found in Ref. [131]. As expected after analyzing Figs. 3.6 and 3.7, the two-body current (also called higher twist contribution) decreases faster than the impulse approximation. The expected behavior of (3.20) can be derived directly from Eqs. (3.15) and (3.18), as follows.

For the sake of simplicity, the Breit reference frame will be adopted, where the constrains are $\vec{p} = -\vec{p'} \equiv \vec{n}\, p_v$, $p_0 = p_0' = \sqrt{M^2 + p_v^2}$, $Q^2 = -(p' - p)^2 = 4\, p_v^2$ and $\vec{n}$ is the direction of the incident momentum $\vec{p}$. Therefore, $p_v = \frac{1}{2}Q$ and $p_0 = p_0' = \sqrt{M^2 + \frac{1}{4}Q^2}$ in Eq. (3.15). Furthermore, the shorthand notation is used: $k_v = |\vec{k}|$. The denominator $D(\gamma, z; \frac{p}{2} - k, p)$ (analogously for $D(\gamma', z'; \frac{p'}{2} - k, p')$) of Eq. (3.15), for $Q \to \infty$, enclosing the aforementioned relations reads

$$D(\gamma, z; \frac{p}{2} - k, p) \propto (1 + z)Q + \delta, \quad D(\gamma', z'; \frac{p'}{2} - k, p') \propto (1 + z')Q + \delta', \quad (3.21)$$

where only the dependence on Q is explicitly displayed, with δ, δ' containing the terms independent of Q. The impulse approximation contribution then becomes

$$F_I(Q^2) \propto \int_{-1}^{1} \frac{g(z)dz}{[(1+z)Q+\delta]^3} \int_{-1}^{1} \frac{g(z')dz'}{[(1+z')Q+\delta']^3} =$$
$$= \frac{1}{Q^6} \int_{-1}^{1} \frac{g(z)dz}{\left(1 + z + \frac{\delta}{Q}\right)^3} \int_{-1}^{1} \frac{g(z')dz'}{\left(1 + z' + \frac{\delta'}{Q}\right)^3}, \quad (3.22)$$

where, again, terms not dependent on Q are omitted, as well as the integration over k, as they bring only finite corrections that become irrelevant for $Q^2 \to \infty$. For the sake of simplicity, one can put $g(z) \equiv 1$, since the aim is to analyze the powers of Q^2. Consequently, the integral gets the form

$$\int_{-1}^{1} \frac{dz}{\left(1 + z + \frac{\delta}{Q}\right)^3} \sim \frac{Q^2}{2\delta^2}, \quad (3.23)$$

which is divergent at $z = -1$ for $\frac{\delta}{Q} = 0$, meaning that the factor $\frac{1}{Q^6}$ in Eq. (3.22) can be compensated by increasing factors at finite Q^2 coming from the integrals. However, considering $g(z) \equiv 1$, which gives $F_I(Q^2) \propto 1/Q^2$ for the form factor asymptotic behavior, is oversimplified. For a proper analyzes one needs to consider the divergent behavior as $Q \to \infty$, i.e.

$$\int_{-1} \frac{dz}{(1+z)^2} = -\frac{1}{1+z}\Big|_{z \to -1}, \quad (3.24)$$

which needs to be properly treated by considering Q large but finite and not discarding the δ/Q term in the denominator, which acts as a cutoff, that means $z = -1 + \frac{\delta}{Q}$. It is important also to consider that $g(z)$ has a general linear behavior close to the end point, i.e. $z \to -1$, as $g(z) \sim (1 - |z|)$, what alters the compensation, i.e.

$$\int_{-1}^{1} \frac{g(z)dz}{\left(1 + z + \frac{\delta}{Q}\right)^3} = \int_{-1}^{1} \frac{(1 - |z|)dz}{\left(1 + z + \frac{\delta}{Q}\right)^3} \sim \frac{2Q}{\delta}, \quad (3.25)$$

providing the expected asymptotic behavior $F_I(Q^2) \propto Q^{-4}$. Therefore, the product of integrals in Eq. (3.22) create an extra factor like $\sim \frac{Q^2}{\delta^2}$ which modifies the fall-off from $\sim \frac{1}{Q^6}$ to $F(Q^2) \propto \frac{1}{Q^4}$. In short, since Eq. (3.15) contains two propagators with 3rd degree denominators like Eq. (3.21), involving terms with p or p' and, consequently, bringing a factor of Q, the asymptotic behavior goes as $\sim \frac{\delta^6}{Q^6}$.

This analysis, although simple, brings an interesting understanding on the asymptotic behavior of the form factor. Subtle corrections to leading asymptotic behavior, as the log-term $\sim \log(Q^2/m^2)$ discussed in Ref. [131] for the Wick-Cutkosky model, are not achievable through such a simple analysis as the one presented here. Nevertheless, the fall-off of $F_I(Q^2) \propto \frac{1}{Q^4}$ found here coincides with the leading order form factor fall-off derived in Ref. [131] for the Wick-Cutkosky model, what corroborate the analysis. The next step is to perform an analogous study for the two-body contribution.

For the crossed contribution, the independent integration variables are, following Eq. (3.18), p_2, p_8, p_9, and in terms of them one can express the conservation vertices as defined in Fig 3.5 $p_1 = p - p_2$, $p_5 = p' - p_9$, $p_6 = p_2 - p_8$, $p_7 = p_9 - p_8$, $p_3 = p - p_2 - p_9 + p_8$ and $p_4 = p' - p_2 - p_9 + p_8$. Hence, the BS amplitudes entering in (3.18) are dependent of $k = \frac{1}{2}(p_1 - p_2) = \frac{1}{2}p - p_2$ and $k' = \frac{1}{2}(p_5 - p_9) = \frac{1}{2}p' - p_9$. For large Q^2, $(p' + p)^2$ and $[(p' + p)^2 - 2(p + p') \cdot (p_9 + p_2 - p_8)]$ can be omitted, as well as propagators depending on p_6, p_7 and p_8.

As in the impulse approximation case, Eq. (3.18) present the cubic denominators coming from the Nakanishi integral representation. Therefore, a term that decays like Q^{-4} also arises in this case, due to the same reasons as before. Nevertheless, now two additional propagators containing p and p' appear, namely the ones with p_3 and p_4. These denominators can be reduced to a similar form as (3.21), anyway in this case the singular behavior due to that $(1 + z)$ and $(1 + z')$ does not appear. Thus, two extra factors as $\frac{1}{Q}$ are present in the two-body contribution case, what makes the leading order asymptotic behavior to be like $F_X(Q^2) \propto Q^{-6}$. It is important to bear in mind that the end-point behavior of the Nakanishi weight function influences the fall-off. Moreover, a more detailed studied would be valuable to understand which kind of correction terms would appear to the asymptotic form.

Figure 3.8 presents, in the left-panel, the impulse (F_I) and two-body current (F_X) contributions to the EM form factor, as well as the multiplication by their asymptotic behaviors as discussed above, in the right-panel. The dependence is displayed in a wide range of Q^2, so that the fall-off becomes more evident. The interaction kernel for the solution of the BSE utilized for these calculations is composed by ladder plus cross-ladder diagrams. In order to properly compare the fall-off of the contributions, both of them are normalized to one at zero momentum transfer. The asymptotic region appear to start around $Q/m \sim 30$, what is reasonably for the weakly bound state under consideration. The asymptotic behavior is also explored under the inclusion of the log correction derived for the Wick-Cutkosky model in Ref. [131], which is naively assumed to be the same in the current case. As seen in Fig. 3.8, $Q^4/\left[1 + (\alpha/2\pi)\log(Q/m)^2\right] F_I$ seems to represent better the asymptotic behavior of the impulse contribution, but not significantly, while for the two-body term $Q^6/\left[1 + (\alpha/2\pi)\log(Q/m)^2\right] F_X$ shows to be considerably more reliable than simply $Q^6 F_X$. Nevertheless, it is notable to see how reasonable results the counting
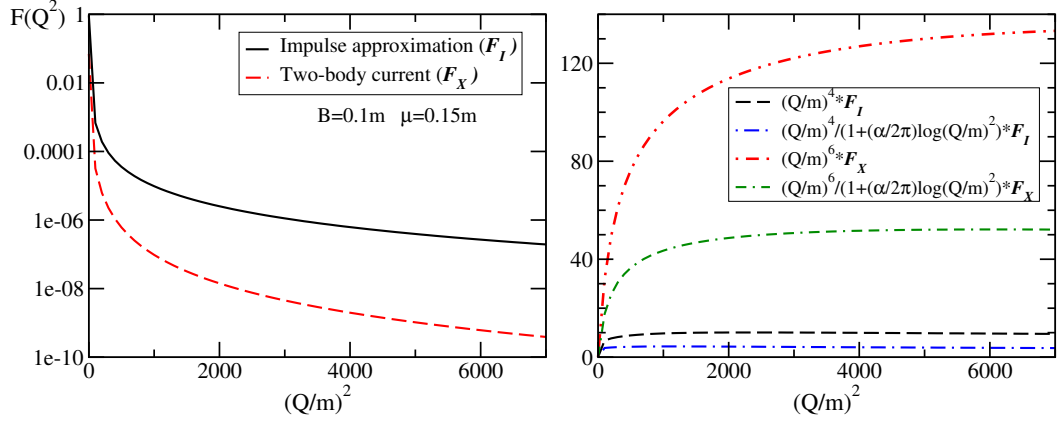
Figure 3.8. Left panel: EM form factor computed numerically with L+CL kernel and shown up to large values of Q^2. Right panel: The impulse and two-body contribution multiplied by the factors shown inset. Input parameters: $\mu = 0.15\,m$ and $B = 0.1\,m$.

rule performed here can provide. Further developments aiming at evaluating also the log-corrections to the fall-off from the massive BSE would be more than welcome.

The study provided so far in this section should be considered as a toy model towards a scalar QCD theory. A natural subsequent question would be how is the response of the Minkowski space structure of the same system within a context more compatible with degrees of freedom typical of the QCD theory. The goal now is to explore how the cross-ladder effect on the observables discussed here changes if a simplified scalar QCD model is considered and the extra factor due to the presence of the Gell-Mann matrices are taken into account.

3.2 The color dof and its suppression on non-planar diagrams

In this section, the aim is to explore the role of the color degrees of freedom within the same approach discussed up to now in the present chapter. After introducing the color factors, one can consider the development as an oversimplified scalar QCD model of a meson. Although the study brings notable results, as it will be shown, this does not exclude the future need of a realistic investigation within QCD theory, so that the conclusions can be tested and their reliability for hadron physics confirmed. As it will be shown, the color factors impose a strong suppression of the irreducible crossed, also known as non-planar, diagrams, creating some hope that they can be discarded for practical purposes where there is no need of refined corrections.

In addition to the analysis of the case of $3 + 1$ spacetime dimensions carried out so far in this chapter, the response of the observables in $2 + 1$ dimensions will be also briefly investigated. The system under scrutiny can be understood in this context as a flavor-nonsinglet bound state of a scalar-quark and a scalar-antiquark with equal masses, exchanging a scalar-gluon with a distinct mass. The underlying framework is essentially the same as the one presented in Sec. 3.1.1. By repeating the calculations of the coupling constants, valence LFWF and EM form factor in the presence of
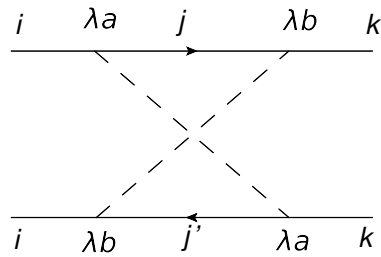
Figure 3.9. Cross-ladder diagram with color matrices.

color factors, one can see that the cross-ladder contribution is already significantly suppressed for $N_c = 3$. This is remarkable considering, e.g., that only the coupling constant is already affected by about 30-50% after introducing merely one crossed irreducible kernel, as shown in Table 3.1. Moreover, if confirmed for more complex systems, would support the use of rainbow-ladder truncations in non-perturbative calculations within the continuous QCD framework (see, e.g. Ref. [102]).

The suppression of non-planar diagrams was already demonstrated long ago, starting with the seminal papers by 't Hooft on developing a planar theory for hadrons in the $N_c \to \infty$ limit (where N_c is the number of colors) [133] and later by explicitly deriving a $SU(N)_c$ theory of QCD in 1+1 dimensions and demonstrating the suppression in the kernel [134]. The later work was further explored in Ref. [135], where a deeper numerical analysis was performed by keeping N_c finite and increasing it step by step in order to follow the evolution of the suppression. Inspired by that work, the aim is to perform an analysis on how the suppression happens in $3 + 1$ and $2 + 1$ spacetime dimensions for different number of colors. The work presented here was published in Ref. [43].

3.2.1 Scalar QCD model

The generalization to include color factors is quite straightforward, starting through the introduction of the Gell-Mann matrices λ_i in the vertices of the interaction kernel diagrams. This is illustrated in Fig. 3.9 for the cross-ladder kernel and the idea is the same for any irreducible graph. Once the diagram is properly defined, it is time to apply the Feynman rules and then perform the trace of the products of color matrices, relative to the colorless composite bound state system. Notice that the resulting color factor is independent on the type of particles involved in the bound state. Following this Ref. [136], the internal boson line factors are replaced by the corresponding $SU(N)$ projection operators. Here $N = N_c$ represents the number of charges or colors of the theory. Following the procedure for the ladder kernel, one gets

$$
\begin{aligned}
tr[(\lambda^a)_{ji}(\lambda^a)_{ij}] &= \sum_a (\lambda^a)_{ji}(\lambda^a)_{ij} = \frac{1}{2} \sum_{i,j=1}^{3} \left(\delta_{jj}\delta_{ii} - \frac{1}{N}\delta_{ji}\delta_{ij} \right) \\
&= \frac{1}{2} \left(N^2 - \frac{1}{N} \sum_{i=1}^{3} \delta_{ii} \right) = \frac{N^2 - 1}{2},
\end{aligned} \tag{3.26}
$$
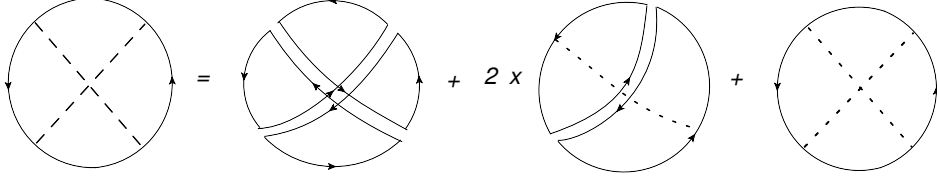
Figure 3.10. Diagrams illustrating the color flow in the cross-ladder graph.

which is a multiplying factor in the ladder kernel iK_L in Eq. (3.5), being the only difference in that equation. For the cross-ladder diagram, as shown by Fig. 3.9, the color factors are the following products: $(\lambda_a)_{ij}(\lambda_a)_{kj'}$ and $(\lambda_b)_{jk}(\lambda_b)_{j'i}$. One important property comes into play in this case [136]

$$\sum_a (\lambda_a)_{ji}(\lambda_a)_{j'k} = \frac{1}{2}\left(\delta_{jk}\delta_{ij'} - \frac{1}{N}\delta_{ij}\delta_{j'k}\right). \tag{3.27}$$

The same process described above for the ladder kernel allied to Eq. (3.27) brings for the color factor of the cross-ladder kernel:

$$tr[\lambda^a\lambda^b\lambda^a\lambda^b] = -\frac{(N^2-1)}{4N}. \tag{3.28}$$

Comparing Eqs. (3.26) and (3.28) it is already clear that for N large enough the cross-ladder kernel will be suppressed by $1/(2N)$. Another interesting difference is the sign flip brought by the color factor, which becomes repulsive instead of attractive as it was shown in Sec. 3.1.2. An interesting way to graphically visualize this result is through the color flow diagrams corresponding to the cross-ladder graph, as shown in Fig. 3.10. The closed loops in the figure can be related with a factor of N, while the dotted lines represent phantom propagators and give factors of $-1/N$ [136]. If one considers, as an exercise, a planar two-boson exchange kernel (i.e. a box diagram, instead of crossed one as in Fig. 3.9) the corresponding factor, obtained by the same procedure described above, would be

$$\frac{N}{4}\left(N - \frac{1}{N}\right)^2 = \frac{1}{4}\left(N^3 - 2N + \frac{1}{N}\right),$$

what reinforces that non-planar graphs are significantly more suppressed than the planar ones. This is in accordance with one of the main conclusions brought by 't Hooft within a QCD_{1+1} model for mesons on the light-front [134]. The question now is how large N needs to be in practice to suppress sufficiently the effect from non-planar graphs on observables. For answering that one needs to introduce the factors computed here in the interaction kernel and solve once again the BSE.

3.2.2   Sensitivity under finite N_c

In the case of the scalar QCD, the procedure adopted for the solution of the BSE is the same as the one described in Sec. 3.1. Figure 3.11 presents for $2+1$, on the left, and $3+1$ dimensions, on the right, the coupling constant, obtained by solving the

BSE with ladder and ladder plus cross-ladder kernels, as a function of the binding energy of the bound state system. The upper panels concern the solution of the bare BSE, i.e. without the inclusion of the color factors, and the lower ones are for the $SU(N)$ BSE, with $N = 2, 3$ and 4 (red, green and purple, respectively). The exchanged boson mass is $\mu = 0.5\,m$ for all the curves. Both for $2 + 1$ and $3 + 1$ dimensions the attractive effect from the cross-ladder kernel for the bare BSE is quite evident, being slightly bigger for the first case, as pointed out at the beginning of Chap. 3. On the other hand, when color factors are introduced the suppression is already quite significant for $N = 2$, since the cross-ladder effect drops from about 47% with no color factor to around 15%. For $N = 3$, the actual number of color charges in QCD theory, the effect is already only 3%, even though a strongly bound system, where the cross-ladder impact is more serious, is being considered. For $N = 4$ the effect is already almost negligible. Another important feature seen in the lower panels in Fig. 3.11 is that g^2 decreases, for a given B, when N increases. This is an expected behavior by 't Hooft's limit, which states that $g^2 N$ should become a constant as $N \to \infty$.
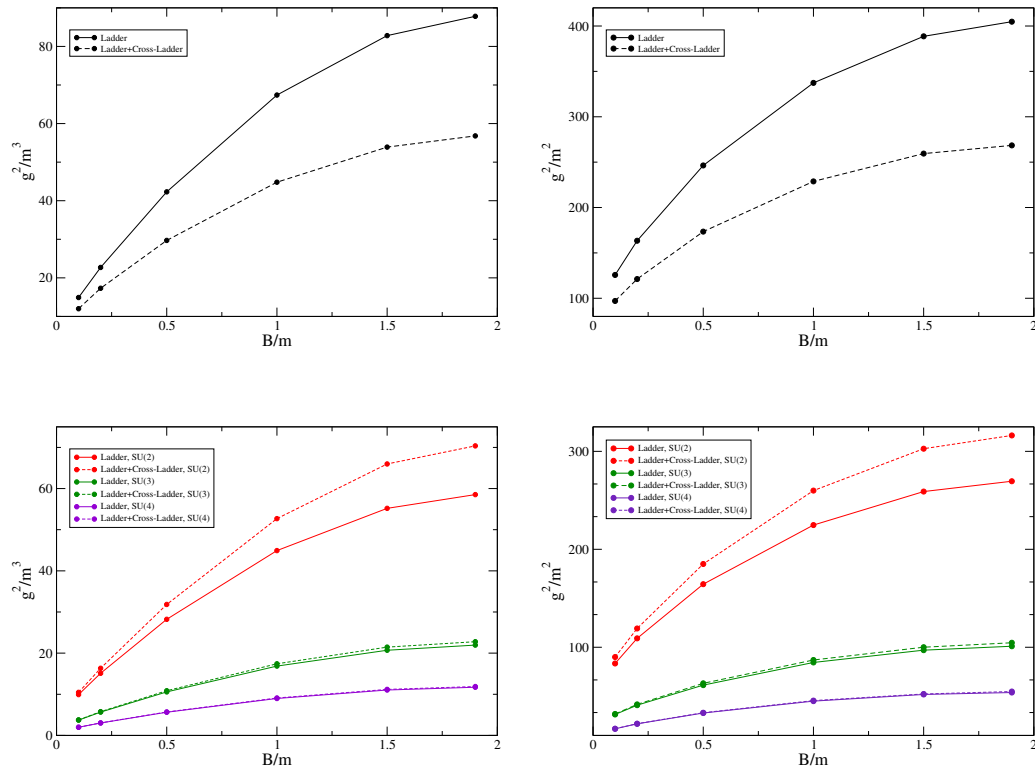
Figure 3.11. Dimensionless coupling constant for various values of the binding energy B obtained by using the Bethe-Salpeter ladder (L) and ladder plus cross-ladder (CL) kernels, for an exchanged mass of $\mu = 0.5\,m$. In the upper panels are shown the results computed with no color factors for 2+1 (left) and 3+1 dimensions (right) respectively. Similarly, in the lower panels are compared the results for $N = 2, 3$ and 4 colors.

In Fig. 3.12, the coupling constant obtained by using the L and L+CL kernels, now only for 3+1 dimensions, is shown for different fixed values of the binding energy.

The interaction boson has its mass fixed at $\mu = 0.15\,m$. The figure presents the results from the BSE without color factors compared with the ones for $N = 2, 3$ and 4. In addition, the Feynman-Schwinger representation (FSR) calculations from Ref. [105], where the infinite sum of irreducible diagrams was included to the interaction kernel of the same system treated here, but without the Gell-Mann matrices at the interaction vertexes, is also presented. Only reasonably weakly interacting systems ($B \lesssim 0.25\,m$) are considered, following what was presented in Ref. [105]. As it was mentioned, this calculation was performed in Euclidean space and the effect on dynamical observables formally defined in Minkowski space were not disclosed. As it can be concluded from the figure, the effect when including the whole set of cross-ladder diagrams is sizable, reaching a factor of three for the largest considered binding energy. For a strongly bound state the difference would be even bigger. Although the effect of the cross-ladder graphs is huge, one could expect that to be significantly suppressed if the color factors are included. Higher order non-planar diagrams would bring even more complex structures than what is shown in Fig. 3.10, with more inner lines and one could expect, consequently, more suppression factors that go like $1/N$ (see the discussion in Sec. 3.2.1). This would mean that at higher orders the effect would be even smaller than the already small impact found here for $N = 3$ including the first crossed diagram. If it turns out to be correct, this would be a strong argument to support rainbow-ladder truncation [31, 102], making calculations for more complicated physical systems (e.g. involving many bodies and more degrees of freedom) feasible as the interaction kernel would be simpler.

It is already interesting to notice that the results including the color factor in Fig. 3.12 get almost parallel to the FSR ones as N increases. This could be a potential indication that the inclusion of color factors in the FSR calculations would give a quite reasonable agreement with the BSE results already at $N = 3$. This expectation should be explicitly tested, as it promises remarkable outcomes. Nevertheless, it is worth mentioning that the scalar ϕ^3 theory contains a sharp shortcoming due to its inherent instabilities from quantum fluctuations, showed in Ref. [137]. Therefore, it would be even more interesting to consider another type of interacting theory, in order to explore the validity of the results in a broader context, closer to, e.g., lattice QCD. An interesting study to be performed is on how the suppression happens when the scalar QCD gluon mass μ becomes closer to zero. This can give a contrast to how the model behaves in the other extremum, i.e. when a long-range interaction takes place. For a clear comparison, Table 3.2 presents the ratios between the coupling constants g_L^2 and g_{L+CL}^2, corresponding to the solutions with the ladder and ladder plus cross-ladder kernels, respectively. Two different values of the exchanged mass are considered, namely $\mu = 0.001\,m$ and $\mu = 0.15\,m$, both for a weakly bound system, where the binding energy is $B = 0.1\,m$, and for a strongly bound one, with $B = 1.5\,m$. The table compares the results obtained through the bare BSE with the ones including $N = 2, 3$ and 4 colors. The suppression shows to be quite strong already for $N = 3$. As the impact from the cross-ladder is less intense for low bindings, the suppression is more severe in this region. The results seem to be quite independent of the exchanged boson mass μ.

Now that the suppression has been seen from different perspectives for the coupling constant, one can look on the effect for different dynamical observables.
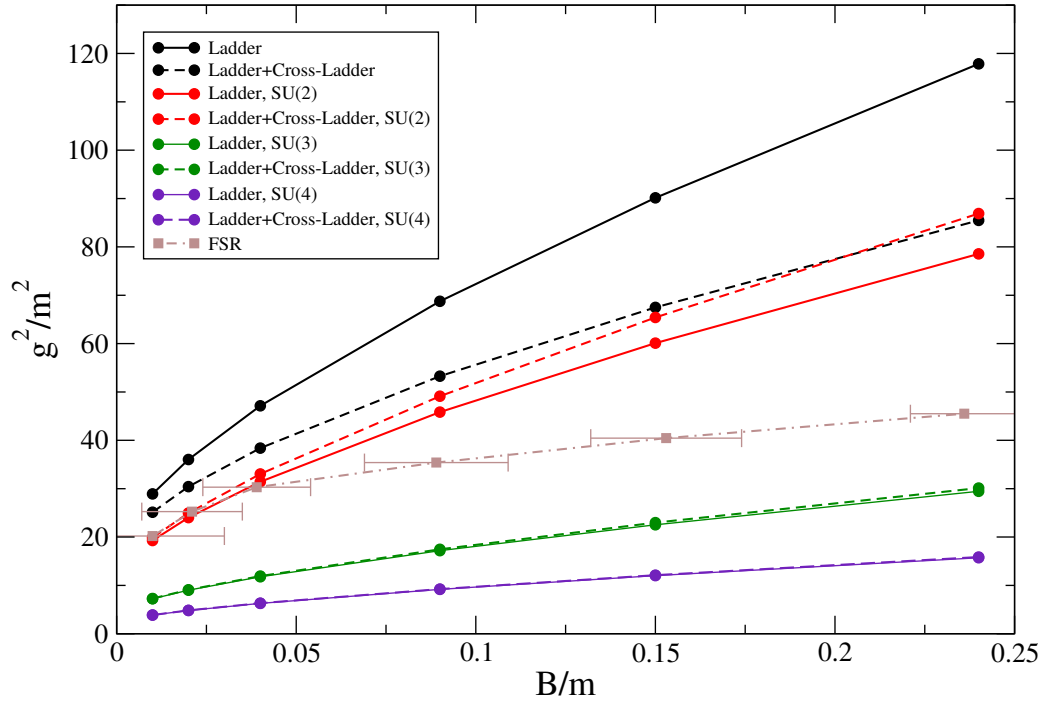
Figure 3.12. Coupling constant as a function of the binding energy B obtained by solving the Bethe-Salpeter equation with ladder (L) and ladder plus cross-ladder (L + CL) kernels in 3+1 dimensions. The exchanged boson mass is $\mu = 0.15\,m$. The results are computed without color factors, as well as for $N = 2, 3$ and 4. The results are also compared with the FSR calculations [105], that contain many types of crossed diagrams, but without GM matrices at interaction vertexes.

B/m	μ/m	$g_{\mathrm{L}}^2/g_{\mathrm{L+CL}}^2$ (BSE)	$g_{\mathrm{L}}^2/g_{\mathrm{L+CL}}^2$ (N=2)	$g_{\mathrm{L}}^2/g_{\mathrm{L+CL}}^2$ (N=3)	$g_{\mathrm{L}}^2/g_{\mathrm{L+CL}}^2$ (N=4)
0.1	0.001	1.3181	0.9246	0.9823	0.9930
0.1	0.150	1.2998	0.9303	0.9835	0.9935
1.5	0.001	1.5199	0.8456	0.9661	0.9867
1.5	0.150	1.5174	0.8467	0.9663	0.9868

Table 3.2. Ratios of the coupling constants calculated with the ladder (g_L^2) and ladder plus cross-ladder (g_{L+CL}^2) kernels. Two binding energies are considered, $B = 0.1\,m$ and $B = 1.5\,m$. The comparison is also made between two exchanged masses, namely $\mu = 0.001\,m$ and $\mu = 0.15\,m$. The results for the no-color BSE are compared with the ones computed with $N = 2, 3$ and 4 colors. Calculations in $3 + 1$ spacetime dimensions.

The starting point is the valence light-front wave function, which was shown to have a sizable effect from the cross-ladder graph on its tail, comparable to the effect seen on the coupling constants as shown in Table 3.1. The result is shown in Figs. 3.13 and 3.14, respectively presenting the dependencies of the wave function with respect to the variables $\gamma = k_\perp^2$ and $z = 2\xi - 1$. The binding energy is fixed at $B = 1.0\,m$

and the two considered exchanged boson masses are $\mu = 0.001\,m$ and $\mu = 0.5\,m$. For the transverse momentum distribution, the longitudinal momentum is fixed at $z = 0$. As done before, the LF wave function normalization is chose to be one at $(z, \gamma) = (0, 0)$. Figure 3.13 shows that there is no difference between the calculation with the colorless ladder kernel (dash-double-dot black line) and the one for $N = 3$ (dashed blue line). This is expected since all the curves are normalized to one, therefore the overall color factor is lost. The appreciable difference is between the calculations for the ladder plus cross-ladder graphs in the interaction kernel without color (dash-dot red line) and with $N = 3$ (solid black line). This shows that the significant suppression also happens for the valence LFWF. In conclusion, for the adopted arbitrary normalization, the full calculations (L+CL) without color factors are remarkably overlapping with the $N = 3$ ladder and ladder plus cross-ladder ones.
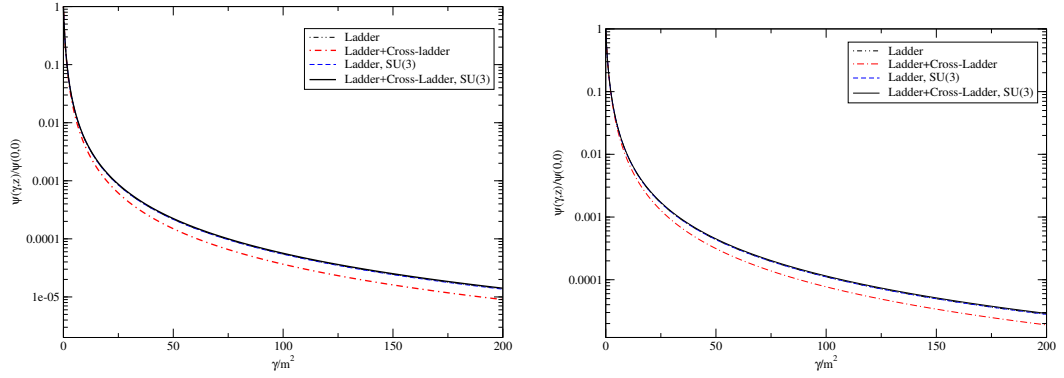
Figure 3.13. Valence LF wave function dependence on $\gamma = k_\perp^2$ computed from the Bethe-Salpeter amplitude for both ladder and ladder plus cross-ladder kernels. The LF wave function obtained with $N = 3$ is compared with the one without color factors for both kernels and they are hardly distinguishable from the full results without Gell-Mann matrixes at the in the vertexes. On the left panel the exchanged mass is $\mu = 0.001\,m$ and on the right it is $\mu = 0.5\,m$. The other fixed input parameters are $B = 1.0\,m$ and $z = 0$.
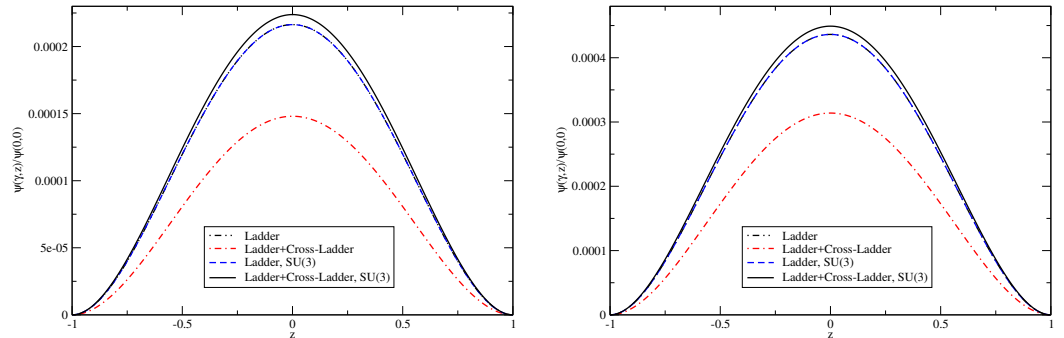
Figure 3.14. Same as in Fig. 3.13, but now was a function of z. The transverse momentum is fixed as $\gamma = 50\,m^2$.

The dependence on z, displayed in Fig. 3.14, is presented for $\gamma = 50.0\,m^2$ (which is already in the asymptotic region, as discussed in Sec. 3.1.2). The binding energy and exchanged boson masses are the same as in Fig. 3.13. The two results for the ladder kernel, with and without the SU(3) color factor, are again on top of each other. The dependence on z is also compared for the BSE results with and without color factor for ladder and ladder plus cross-ladder interaction kernels. It is even more apparent, due to the scale, that the valence light-front wave function also has the cross-ladder effects largely suppressed by the color factor. It is remarkable that $N = 3$ is already enough to enforce a substantial suppression.

For making the results of the last two figures more evident, the ratios between light-front wave functions presented in those figures are shown in Fig. 3.15. In the left panel it is presented the dependence on gamma γ, i.e. $\psi_L(\gamma, z = 0)/\psi_{L+CL}(\gamma, z = 0)$, while the ratio as a function of z, namely $\psi_L(\gamma = 50\,m^2, z)/\psi_{L+CL}(\gamma = 50\,m^2, z)$, is shown on the right panel. In this figure it is clearer that with no color factors the cross-ladder contribution is above 40% for high γ. Nevertheless, when $N = 3$, the cross-ladder effect is reduced to about 3%. Furthermore, the cross-ladder effect on the tail of the ratio between the wave functions turns to be proportional to the ratio of the coupling constant, as discussed in Sec. 3.1.2. What is seen here is analogous, as the suppression is therefore similar in both of those observables. The effects identified in the dependence on z is equivalent.
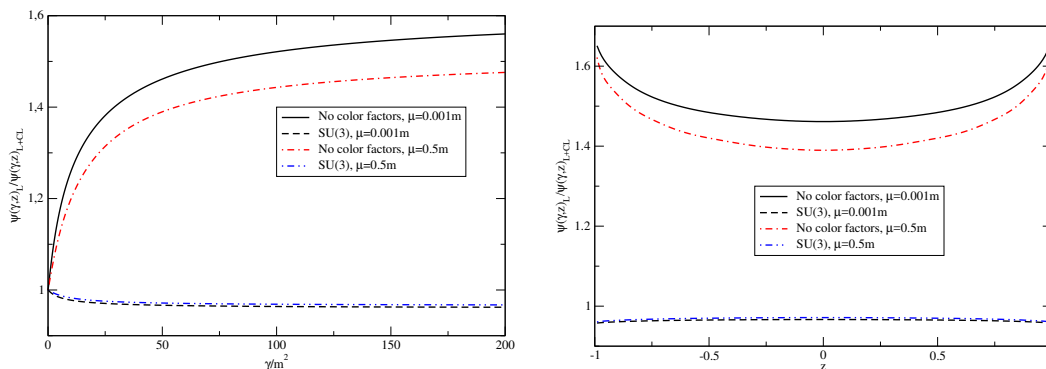
Figure 3.15. Ratios between the valence LF wave functions computed with ladder and ladder plus cross-ladder kernels of Figs. 3.13 (left) and 3.14 (right). In the figures the results for $N = 3$, i.e. SU(3), are compared with the ones obtained without color factors.

Finally, the suppression can be also studied on the elastic EM form factor, since this observable does not involve a Fock-space truncation and shows a different context. Both the impulse approximation and two-body current contributions to the EM current, are shown as functions of the momentum transfer ($Q^2 = -q_\mu q^\mu$) in Fig. 3.16. The binding energy is still fixed as $B = 1.0\,m$, while the exchanged masses are again $\mu = 0.001\,m$ (left) and $\mu = 0.5\,m$ (right). The charge radius (given by the slope of the EM form factor at $Q^2 = 0$) is larger for smaller μ, i.e. for $\mu = 0.001\,m$. This happens since the range of the interaction is longer for smaller exchanged mass. The figure compares the results obtained with $N = 3$ and the ones computed without color factors, showing again a strong suppression.

Analogously to what was presented in Fig. 3.15 for the LFWFs, in Fig. 3.17 are
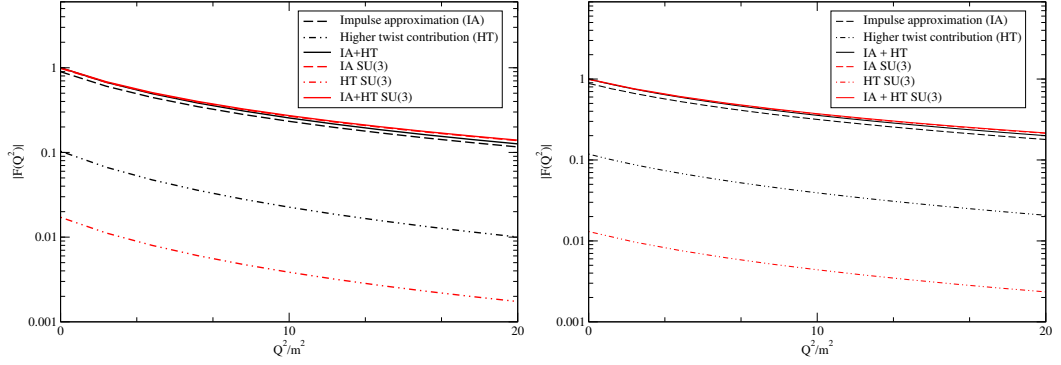
Figure 3.16. EM form factor beyond the impulse approximation (IA), considering the contribution from the first cross graph (right panel in Fig. 3.5), namely, the higher twist (HT) (or two-body current) contribution. $\mu = 0.001\,m$ (left) and $\mu = 0.5\,m$ (right). Comparison with the ones computed with $N = 3$. The binding energy is $B = 1.0\,m$.

displayed the ratios between the two-body current and the impulse-approximation contributions. This figure makes even more clear the suppression of the two-body current contribution when the number of colors is only $N = 3$, again without the need of taking the limit $N \to \infty$ to see a big difference. As an example, for $Q^2 = 0$ the ratio is about 13% without any color factor, while it decreases to 1% when $N = 3$.
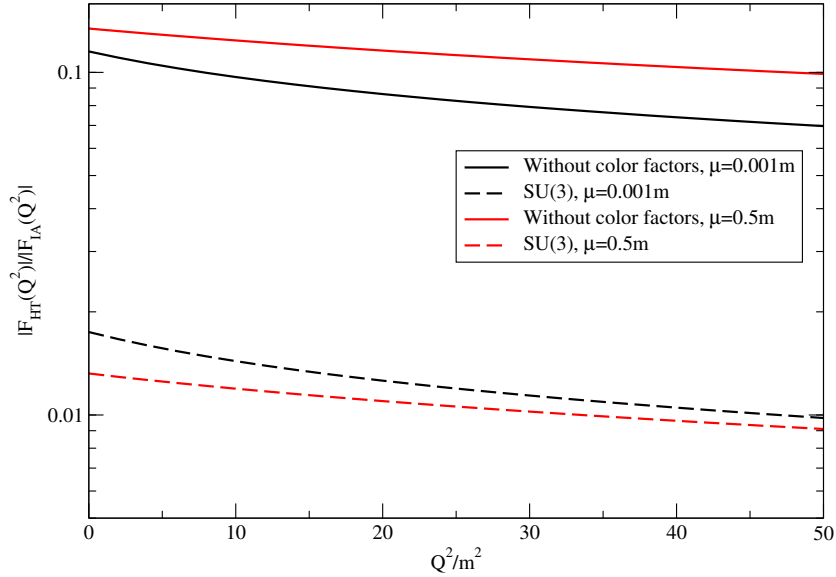
Figure 3.17. Ratio between the higher twist and the impulse approximation contributions to the EM form factor as function of the transferred momentum Q^2. Results without and with (N=3) color factor.

This concludes the analysis of a prototype for the flavor-nonsinglet meson system composed by a scalar-quark and a scalar-antiquark with equal masses. The

non-planar diagrams are shown to be significantly suppressed for all the studied observables already for $N = 3$. If confirmed for realistic QCD systems, this result, which is already assumed in most of the cases seen in the literature and provides a necessary simplification for calculations with the BSE, would be a notable argument on supporting the rainbow-ladder approximation to the continuous QCD [31, 102]. Another extremely interesting study would be to repeat the same calculations for particles with different constituent masses and take the limit where $m_1 >> m_2$. This study is particularly interesting because the effect from cross-ladder graphs is enhanced in this limit.

Chapter 4

Bethe-Salpeter approach to three-boson bound states

This chapter is devoted to study the solution of the three-boson Bethe-Salpeter equation in the case of the two-body zero-range interaction [138]. The equation will be solved both in Euclidean and Minkowski space. Although simpler, the Euclidean case involves several subtleties and was never solved before in the form presented here. The BS equation is also solved within light-front dynamics, as already done in Refs. [139], through its projection onto the LF hyperplane which leads to an equation for the valence part of the Faddeev components of the three-body BS amplitude. By comparing the LF result with the solution of the BSE in Euclidean space one can access effects coming from the higher-Fock contributions to the three-body bound state. As it will be shown, the effect is huge even for weakly bound states. Effective three-body forces act in the system, having a large impact [140]. At the two-body level the truncation at the valence state does not present such dramatic effect [39, 127]. Part of the development presented in this chapter was already published in Refs. [44, 45, 46], while the alternative formalism, using an ansatz for the integral representation, is still under development. Noteworthy that the BSE for three-bosons has a kernel analogous to the quark exchange diagrams in quark-diquark models [102] in the constituent quark picture, making even more appealing the outcomes of the Minkowski space approach to be presented as follows.

Concluding that the effect coming from higher Fock components is sizable leads to raise doubts regarding if valence inspired models, which are widely applied to hadron physics, are appropriate to describe the bound state dynamics, particularly for three-body systems. It is worth mentioning that even for two-boson bound states the valence component can represent only less than about 70% of the strongly bound state (about the same for the mock pion, as it will be presented in Chap. 6), as shown by the valence probabilities calculated in Ref. [39]. The BSE and LFD approaches presented here have already been used as a suitable framework for simplified phenomenological applications. For instance, in the calculation of the light-front amplitudes for a mock pion through the solution of the BSE directly in Minkowski space [51] and the light-front relativistic three-body model for final state interactions of heavy meson decays [25, 59], as presented in Sec. 2.3.

Regarding the BSE in Minkowski space, a new method was recently developed

to access the off-mass-shell scattering amplitude based on the direct integration of the singularities of the propagators and interaction kernel [47]. This method does not resort to the NIR and LF projection, as the one used in this thesis for the bosonic two-body system. The goal is to explore the method for three-body systems. Also, alternative procedures will also be investigated here to solve the three-body Minkowski space equation, aiming at building a robust framework that can be extended to more realistic systems in the future. Even if challenging, the method was able to provide the off-shell BS amplitude for bound and scattering states, allowing to compute highly non-trivial observables like the electromagnetic transition form factor (breakup of the bound state) [132].

As shown in Ref. [140], the comparison of the binding energies calculated within LFD and BSE for a one-boson exchange kernel present a significant difference [140], unlike what happens for two-body systems [106]. The difference between two- and three-body systems basically happens due to the existence of three-body forces of relativistic origin [140]. They found an increasing effect of the three-body forces as μ grows, what is relevant for the zero-range case, which corresponds effectively to $\mu \to \infty$. Although this work is quite instructive, the three-body forces were taken into account perturbatively, producing a significant contribution to the bound state, what indicates the necessity to go beyond perturbation theory. It is essential to obtain the non-perturbative solution of the three-body BSE and LFD equations, including three-body forces, in order to have an thorough understanding of the physical system.

As in this thesis the goal is to address the zero-range interaction case, a major point is the influence of relativistic effects on the stability of the three-body system. In the non-relativistic approach, within the Schrödinger equation, it is well knwon that the binding energy of a three-body system with the two-body zero-range interaction is not bound from below, what is known as the Thomas collapse [141]. As shown in Ref. [138], and further explored numerically in Ref. [139], the relativistic effects result in an effective repulsion at small distances and prevent the Thomas collapse in the relativistic case. This result was found for the valence truncation, within the LFD framework. Exploring the complete amplitude by means of the BSE, which includes higher-Fock contributions is crucial and it was studied for the first time in Ref. [45], as a part of the research in this thesis. In that work, the covariant three-body BSE, proposed in Ref. [138], was solved in Euclidean space for the first time, where it was used the Faddeev decomposition of the full three-boson BS amplitude.

The approach for three-boson systems allows one to explore within the relativistic context a wide and important field of research that is already very well established non-relativistically, known as the Efimov physics [142, 143]. The three-body approach developed here paves the way to explore many interesting phenomena in that direction within the relativistic context and it is expected to bring more remarkable outcomes as further exploration is done.

The study presented in this chapter represents a very nice advance in comparison with the similar approach discussed in Sec. 2.3, as the equations from now on are totally solved non-perturbatively. Future efforts within this framework include the formulation of the three-body decay amplitude for heavy mesons, where the final state interactions among all the outbound mesons can be included. This would be a

considerable progress for the studies presented in Chap. 2.

4.1 Euclidean space and LF dynamics: beyond the valence effects

The starting point is to solve the BSE for three-bosons for a zero-range interaction. The equation is solved for the first time in the form presented in [138], where the Faddeev decomposition was used to obtain one integral equation for the reduced amplitude of the bachelor particle. As the kernel is divergent for the contact interaction, a parameter needs to be introduced in its regularization process of the two-boson transition matrix. This input parameter can be either the two-body scattering length or binding energy. The outputs of the solution are the binding energies, BS amplitudes (when solving the BSE) and valence light-front wave function (when solving the BSE projected onto the LF plane), of the three-body bound state.

By controlling the two-body input parameter one can study three regimes. The first one happens when the two-body interaction is weak enough, for which the three-body system is unbound. The second regime is for stronger two-body interaction, but with the two-body subsystem still virtual, and a three-body bound state appears, what characterize a deeply bound Borromean system [142]. And the last situation, for even stronger two-body interaction and the three-body ground state becomes unphysical, characterized by a negative mass squared. The interesting aspect in this last situation is that the first excited state is physical, and this was the one found previously in light-front calculations, where the ground state was lost. The comparison between BSE and LFD results allow to study the impact of the higher Fock space contributions to the observables, as the BSE implicitly incorporates three-body forces of relativistic origin.

The starting point is to solve, for the first time, the three-body covariant BS equation in the Faddeev decomposition for the zero-range interaction. The Minkowski BSE is transformed into Euclidean space by means of the Wick-rotation in the complex plane. The time-ordered extra graphs incorporating antiparticles within LF dynamics are naturally taken into account in the BS approach [27, 127]. These graphs, as later explained, generate effective three-body forces of relativistic nature. As found in Ref. [140] for a one boson exchange interaction, the intermediate antiparticles are mandatory for generating the three-body forces. The aim is to compare the results found by solving the valence LF and BS equations and to understand the role of dynamics beyond the valence on the properties of relativistic three-body systems with the zero-range interaction. The transverse momenta dependencies of the LF and BS amplitudes are studied and compared, in order to illustrate the impact also on the structure of the relativistic three-boson bound state.

Another remarkable finding is that the three-body state studied in Refs. [138, 139], obtained by adopting the zero-range interaction kernel defined through the constraint of generating a two-body bound state with positive squared two-body mass $M_2^2 > 0$, is not the physical three-body ground state but the first excited one. There exists another low-lying state, which is unphysical, i.e. with negative squared three-body mass M_3^2. This can be understood as a relativistic counterpart of the Thomas collapse. However, differently from the non-relativistic case, M_3^2 is always finite.

By fixing the interaction kernel through the two-body scattering length one can explore different regimes and find a domain where the ground state has $M_3^2 > 0$. In this situation, the excited state found in Refs. [138, 139] is moved to the continuous spectrum. The LF and BS frameworks present this feature, with just the associated values of the scattering length being different due to the action of effective three-body forces. In short, one can conclude that an unbound two-body system is necessary to have a ground state within the framework discussed as follows.

4.1.1 Bethe-Salpeter-Faddeev equation

The solution of the zero-range three-body BSE for three identical spinless particles using the Faddeev decomposition of the full BS amplitude can be reduced to the solution of one single integral equation for the bachelor's vertex function $v(q, p)$ (external propagators are excluded). In the zero-range interaction case $v(q, p)$ depends upon both the total momentum p and on the four-momentum of the spectator particle q. It reads [138]:

$$v(q, p) = 2i\mathcal{F}(M_{12}^2) \int \frac{d^4 k}{(2\pi)^4} \frac{i}{[k^2 - m^2 + i\epsilon]} \frac{i}{[(p - q - k)^2 - m^2 + i\epsilon]} v(k, p). \quad (4.1)$$

Notice that the momentum of the spectator particle, q, determines the effective mass of the two-boson subsystem, M_{12}, due to the four-momentum conservation (see below). Therefore, there is no need to introduce further dependencies in the argument of the vertex function, besides the ones on q and on the total four-momentum p. The other two components can be easily obtained through the cyclic permutation of the momentum of the constituent particles. The full BS amplitude is recovered by multiplying the vertex function by the three external propagators and summing up the components, i.e.

$$i\Phi_M(k_1, k_2, k_3; p) = i^3 \frac{v_M(k_1, p) + v_M(k_2, p) + v_M(k_3, p)}{(k_1^2 - m^2 + i\epsilon)(k_2^2 - m^2 + i\epsilon)(k_3^2 - m^2 + i\epsilon)}, \quad (4.2)$$

where $k_1 + k_2 + k_3 = p$. In the zero-range interaction case, besides the total momentum p, the vertex function depends only on the four-momentum of the spectator particle q. The interaction kernel, is given by $\mathcal{F}(M_{12}^2)$, namely, the relativistic two-body zero-range scattering amplitude. Its derivation in terms of the scattering length a is given (as well as the study of other analytical properties and its numerical behavior) in Appendix C and its final form reads

$$\mathcal{F}(M_{12}^2) = \begin{cases} \dfrac{1}{\frac{1}{16\pi^2 y} \log \frac{1+y}{1-y} - \frac{1}{16\pi ma}}; & M_{12}^2 \leq 0, \\[3ex] \dfrac{1}{\frac{1}{8\pi^2 y'} \arctan y' - \frac{1}{16\pi ma}}; & 0 \leq M_{12}^2 \leq 4m^2, \\[3ex] \dfrac{1}{\frac{y''}{16\pi^2} \log \frac{1+y''}{1-y''} - \frac{1}{16\pi ma} - i\frac{y''}{16\pi}}; & M_{12}^2 \geq 4m^2, \end{cases} \quad (4.3)$$

with

$$y = \frac{\sqrt{-M_{12}^2}}{\sqrt{4m^2 - M_{12}^2}}; \quad y' = \frac{M_{12}}{\sqrt{4m^2 - M_{12}^2}}; \quad y'' = \frac{\sqrt{M_{12}^2 - 4m^2}}{M_{12}}. \quad (4.4)$$

The argument of the zero-range two-body amplitude, M_{12}, is the off-shell two-body effective mass, defined by $M_{12}^2 = (p-q)^2$. One major simplification in Eq. (4.1) happens due to the fact that the interaction kernel does not depend on the loop integration variable k in the zero-range case. Due to that the two-body amplitude factor out in the integral equation, what does not happen for a finite-range interaction kernel like the one-boson exchange or the cross-ladder one, treated in the previous chapter.

The renormalization of the bubble diagram, related to the integral equation for the two-boson scattering amplitude, can be alternatively done through a bound state with the mass M_2 in the two-body system, as done in Appendix C (see also Refs. [138, 139, 144]). Notice that in Refs. [138, 139] the regime $M_{12}^2 \geq 4m^2$ of Eq. (4.3) was not presented, due to the range of the variables considered in those works. The amplitude in terms of the bound state mass, as presented in Refs. [138, 139], can be obtained from Eq.(4.3) (in the physical domain, $0 \leq M_{12} \leq 2m$) by relating M_2 and a ($a > 0$ in this case), using the following formulas

$$a = \frac{\pi y_{M_2}}{2m \arctan y_{M_2}} \quad \text{with} \quad y_{M_2} = \frac{M_2}{\sqrt{4m^2 - M_2^2}}. \qquad (4.5)$$

Such link is very important to understand the range covered by the results obtained previously, in Refs. [138, 139], by considering only the situation where the two-body state is bounded (i.e. $a > 0$, producing a real M_2 through Eq. (4.5)), and the entire region covered by (4.3), including also virtual two-body bound states (i.e. $a \in \mathbb{R}$). In other words, in the region for which $a < 0$ the amplitude $\mathcal{F}(M_{12}^2)$ has no pole in the physical domain and, therefore, the two-body bound state does not exist. The three-body system can still be formed though, as it will be seen, as a Borromean bound state.

Equations (4.1) and (4.3) define the general form of the three-boson Bethe-Salpeter-Faddeev equation in Minkowski space. This equation will be solved in three different ways here: (i) by means of the Wick-rotation, in Euclidean space; (ii) through the LF projection, which truncates the LFWF on the valence component; and (iii) by direct integration in Minkowski space, without a Fock-space truncation. A fourth form will be derived here, by means of the Nakanishi integral representation and the uniqueness assumption[1], but not yet numerically solved.

The Wick-rotation is meant to simplify the solution of Eq. (4.1), avoiding the typical intrinsic singularities of the Minkowski space BS equation. The corresponding integral equation is Wick rotated and defined in Euclidean space, being able to provide correctly the physical spectrum, but not the amplitudes (apart from the transverse one, as it is shown as follows) obtained directly in Minkowski space. As no integral representation is introduced so far to represent $v(q,p)$, its analytic structure is not known a priori. By examining the integral equation, it becomes clear that $v(q,p)$ has the poles of $\mathcal{F}$ as well as the three-body cut originated from the propagators of the integral equation kernel. One expects that, if the Wick-rotation is properly performed, smooth solutions for $v(q,p)$ will be achievable.

The Wick-rotation ($k_0 \to ik_0$) of the integration contour is not always possible, which is the case of Eq. (4.1). It can be shown that the positions of the singularities

---

[1]For a more detailed discussion of uniqueness in the NIR see Refs. [35, 38, 120]

prevent analytic continuation in the complex plane, since the rotating contour crosses the singularities of the propagators. This issue can be, however, overcome by simply shifting the variables and, consequently, the rotation points, so that one avoids crossings by properly moving the rotating contour and the singularity positions. One suggestion that allows the Wick-rotation to be performed in Eq. (4.1) is given by the following shift

$$q = q' + \frac{1}{3}p, \quad k = k' + \frac{1}{3}p, \tag{4.6}$$

which redefine the vertex function as follows

$$\tilde{v}(q', p) = v\left(q' + \frac{1}{3}p, p\right), \quad \tilde{v}(k', p) = v\left(k' + \frac{1}{3}p, p\right).$$

Equation (4.1) under the shift reads

$$\tilde{v}(q', p) = 2i\mathcal{F}(M'^2_{12}) \int \frac{d^4 k'}{(2\pi)^4} \frac{i^2 \tilde{v}(k', p)}{\left[\left(k' + \frac{1}{3}p\right)^2 - m^2 + i\epsilon\right]\left[\left(\frac{1}{3}p - q' - k'\right)^2 - m^2 + i\epsilon\right]}, \tag{4.7}$$

with the appropriate two-body effective mass reading $M'^2_{12} = (\frac{2}{3}p - q')^2$.

One can now make a simple analysis to confirm that the new equation allows the Wick-rotation. For instance, the second propagator of Eq. (4.1) (in the three-particle rest frame) has a complex pole in the variable k'_0 at $k'_0 = k'_{01}$, namely,

$$k'_{01} = \eta' + i\epsilon - q'_0, \quad \eta' = \frac{1}{3}M_3 - \sqrt{(\vec{k} + \vec{q})^2 + m^2}. \tag{4.8}$$

If the three-body bound state is such that $M_3 < 3m$, η' has always a negative value. Rotating the path of integration over k'_{01} by the angle ϕ and making the replacement $q'_0 \to q'_0 \exp(i\phi)$, both the pole and the contour move in such a way that the pole never crosses the contour.

The zero-range amplitude $\mathcal{F}(M'^2_{12})$ also can have a pole, corresponding to the two-body state, when $M'^2_{12} = (p - q')^2 = M_2^2 - i\epsilon$. This generates two poles in the vertex function $\tilde{v}(k', p)$ vs. k'_0. It can be easily checked that if $\frac{2}{3}M_3 < M_2$ (in this situation three-body binding energy per particle is larger than the two-body one, remembering that $M_3/m < 3$.) then the $\tilde{v}(k', p)$ poles also do not affect the Wick-rotation. In conclusion, the Wick-rotation can be safely performed in Eq. (4.7) giving the above condition, where the shifted variables are adopted. It is interesting to notice that the factor of $1/3$ used in this case is related to the fact that the system has three identical particles (analogously to the factor of $1/2$ used for the two-body system in Sec. 3.1). In an unbalanced mass system, i.e. where $m_1 \neq m_2 \neq m_3$, the study needs to be performed to find the correct shift factors. This will be used for the two-body system involving a boson and a fermion later on in this thesis. See Ref. [116] for more details on dealing with the two-body BSE for constituent particles with different masses.

Finally, the Wick-rotation can be performed by an angle $\phi = \pi/2$, making the relevant variables to be transformed as $k_0 = ik_4$, $q_0 = iq_4$. Notice that the primes on the four-momenta are omitted from now on. Thus, the unprimed momenta has a different meaning than in Eq. (4.1). Then the angular integrations (one trivial for

the azimuthal angle and another for the angle between $\vec{k}$ and $\vec{q}$) coming from the d^4k loop integration in Eq. (4.7) can be performed analytically. In the rest frame, the final Euclidean BS equation reads

$$v_E(q_4, q_v) = 2\mathcal{F}(-M'^2_{12}) \int_{-\infty}^{\infty} dk_4 \int_0^{\infty} \frac{dk_v}{(2\pi)^3} \frac{\Pi(q_4, q_v, k_4, k_v)}{\left(k_4 - \frac{i}{3}M_3\right)^2 + k_v^2 + m^2} v_E(k_4, k_v),$$
(4.9)

where $q_v = |\vec{q}|$, $k_v = |\vec{k}|$ and the integration kernel has its final form reading

$$\Pi(q_4, q_v, k_4, k_v) = \frac{k_v}{2q_v} \log \frac{\left(k_4 + q_4 + \frac{i}{3}M_3\right)^2 + (q_v + k_v)^2 + m^2}{\left(k_4 + q_4 + \frac{i}{3}M_3\right)^2 + (q_v - k_v)^2 + m^2}.$$
(4.10)

After the Wick-rotation, the argument of $\mathcal{F}$ becomes complex and is given by $M'^2_{12} = (\frac{2}{3}iM_3 + q_4)^2 + q_v^2$, which moves away the from the real axis. One important property of Eq. (4.9) can be found by performing the complex conjugation of it and by changing $k_4 \to -k_4$, $q_4 \to -q_4$. This enables to conclude that $v_E^*(-q_4, q_v) = v_E(q_4, q_v)$, or more explicitly

$$\text{Re}[v_E(-q_4, q_v)] = \text{Re}[v_E(q_4, q_v)], \quad \text{Im}[v_E(-q_4, q_v)] = -\text{Im}[v_E(q_4, q_v)]. \quad (4.11)$$

This property can be imposed numerically, but this will not be the case here. Therefore the outcome from the numerical solution must present the feature found analytically and expressed in Eq. (4.11). To avoid confusion, it is worth it to mention that, since the two-body amplitude is computed for complex arguments, the expression for $M_{12}^2 < 0$ is used with y replaced by $\tilde{y} = \sqrt{M_{12}^2 - 4m^2 + i\epsilon}/\sqrt{M_{12}^2 + i\epsilon}$, where a finite small ϵ parameter is introduced to ensure the correct branch of square roots and logs. Moreover, for the Euclidean case one should use $-M'^2_{12}$ in place of M_{12}^2.

The integral equation can be solved numerically by standard methods, due to its non-singular form. As in the two-body case (Sec. 3), it can be reduced to a generalized eigenvalue problem like $Av = \lambda(M_3)Bv$, where the vertex function v is expressed through any basis expansion. The one adopted here is the bi-cubic spline decomposition, briefly presented in Appendix D.

4.1.2   Light-front Faddeev-Bethe-Salpeter equation

Another procedure to obtain a non-singular integral equation from Eq. (4.1), but now in Minkowski space, is by performing the integration over k^-, as done in Ref. [138]. Instead of the variable $k = (k_0, \vec{k})$, one can introduce the LF variables, i.e. $k = (k^-, k^+, \vec{k}_\perp)$, where $k^\pm = k_0 \pm k_z$. The valence LF wave function is associated to the integral over k^- of the BS amplitude in Minkowski space. Differently from what was done in Sec. 3.1, now the Nakanishi integral representation is not being introduced, what means that after the projection onto the LF plane only the valence component of the three-boson state is retained. The final equation for the valence component of the three-body vertex reads

$$\Gamma(k_\perp, x) = \mathcal{F}(M_{12}^2) \frac{1}{(2\pi)^3} \int_0^{1-x} \frac{dx'}{x'(1-x-x')} \int_0^{\infty} \frac{d^2k'_\perp}{M_0^2 - M_3^2} \Gamma(k'_\perp, x'), \quad (4.12)$$

where the invariant mass squared of the intermediate three-body state is defined as

$$M_0^2 = \frac{\vec{k'}_\perp^2 + m^2}{x'} + \frac{\vec{k}_\perp^2 + m^2}{x} + \frac{(\vec{k'}_\perp + \vec{k}_\perp)^2 + m^2}{1 - x - x'}. \tag{4.13}$$

Equation (4.12) can be also fully derived within the LFD framework, without relying on the BSE, as done in Ref. [139]. It is important to mention that Eq. (11) of [138] is not the same as (4.12), since the cutoffs incorporated in [138] were discovered to be not necessary later in Ref. [139]. Therefore, the version of the equation presented here (4.12) also does not include those cutoffs. The two-body scattering amplitude $\mathcal{F}(M_{12}^2)$ is the same as in Eq. (4.3), but now the appropriate form of the two-body invariant mass in terms of the LF variables reads

$$M_{12}^2 = (1 - x)M_3^2 - \frac{k_\perp^2 + (1 - x)m^2}{x}.$$

Notice that M_{12} is not taken fixed, as it has the dependence upon the same variables of the vertex function $\Gamma(k_\perp, x)$.

In its most general form, the vertex function depends on three transverse and three longitudinal momenta, namely $\vec{k}_{1,2,3\perp}$ and $x_{1,2,3}$, respectively. However, the relations coming from the conservation laws, $\vec{k}_{1\perp} + \vec{k}_{2\perp} + \vec{k}_{3\perp} = 0$ and $x_1 + x_2 + x_3 = 1$ (see Ref. [139]), reduce the number of independent variables. Another simplification in the case under scrutiny is due to the fact that the three particles are identical and by symmetry properties the general BSE can be reduced to one single integral equation for the vertex function of the spectator particle. Lastly, due to the zero-range interaction kernel, the vertex depends on only one pair of variables, which for the valence LF equation are denoted here by $\vec{k}_\perp$ and x [138].
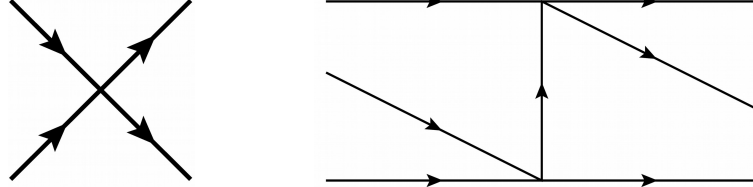
Figure 4.1. The elementary two-body cross graph $2 \to 2$ is shown in the left panel, from which all the Feynman graphs for the zero-range interaction are composed. The graph for the lowest order Feynman three-body amplitude $3 \to 3$, composed by two elementary cross graphs (left panel) is shown in the right panel.

As mentioned, the underlying dynamics is quite different for Eqs. (4.1) and (4.12). The second equation is a truncation of the first one and represents only the valence component of the Fock-space state vector. In order to illustrate the difference, one can start by looking at the diagrammatic representation of the three-body scattering amplitude for the two-body contact interaction (left panel in Fig. 4.1), associated with the two-body amplitude $\mathcal{F}$, which is the most elementary building block to construct all the three-body diagrams in the ladder expansion.

The right panel of Fig. 4.1 shows the Feynman diagram for the lowest order three-body amplitude, which is composed by two two-body elementary graphs. In

the LF all the Feynman diagrams need to have their vertices LF time-ordered, a process that generates the two graphs in Fig. 4.2 when applied to the covariant one on the right panel of Fig. 4.1. For the sake of simplicity, not all diagrams, e.g. graphs including vacuum fluctuation, are being displayed.
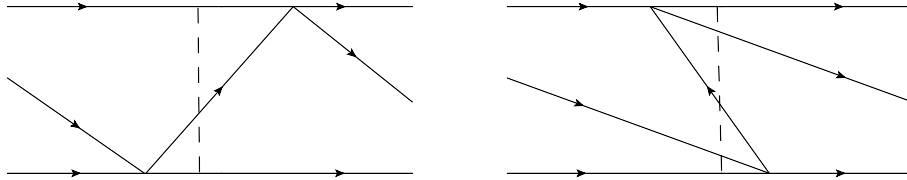
Figure 4.2. The three-body LF graphs obtained by LF time-ordering of the Feynman graph shown in right panel of Fig. 4.1.

The valence LF equation (4.12) incorporates only the graph on the left panel of Fig. 4.2 (and all its reducible iterations containing three-body intermediate states), since a diagram like the one on the right panel already contains intermediate states with more than three particles and therefore it is a contribution beyond the valence one (including antiparticles). It should be pointed out that the irreducible $3 \to 3$ graph including a five-body intermediate state on the right side of Fig. 4.2 is an example of an effective three-body force of relativistic origin, since this contribution has to be explicitly incorporated in the LF framework, as the LF projection of the BSE only retains the valence component, i.e. only 3-particle intermediate states (see e.g. Refs. [37, 127] for an analogous incorporation in two-body systems).

Fig. 4.3 shows examples of other diagrams generating effective three-body forces. Differently from the LF valence equation, the covariant BSE naturally includes those contributions that amount to effective three-body forces. It is worth mentioning that the diagram on the right panel of Fig. 4.1 is not associated with an irreducible three-body forces in the BS equation (4.1), however, it is able to produce effective three-body forces, as it is shown by the LF time ordered diagrams. Notice that the model does not correspond to the full $\lambda\varphi^4$ theory, since Eq. (4.1) contains only the ladder diagrams and does not consider dressed propagators and vertex corrections.
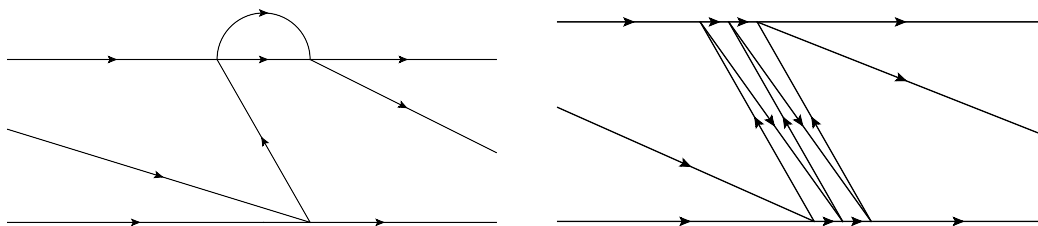
Figure 4.3. Examples of many-body intermediate state contributions to the LF three-body forces.

In conclusion, the whole set of contributions beyond the valence component is what builds the effective three-body forces, only seen within a covariant approach. This was subject of the study, as presented hereafter in the thesis.

4.1.3 Transverse amplitudes

From Euclidean space, if NIR is not used, it might be extremely difficult, or even not possible, to recover the BS amplitude in Minkowski space, since the analytic structure of BS amplitude is hardly reachable through the Euclidean approach. Therefore, for comparing the Euclidean BSE results with the outcomes from the LF equation, defined in Minkowski space, one can rely on the transverse momentum amplitudes to relate the amplitudes in order to explore deeply the dynamical effects. The procedure exposed as follows is analogous to what was found in Ref. [100] and applied in [130] for the two-body system. The relation between the Euclidean BS amplitude and the valence LF wave function comes from the fact that the integrals of the Euclidean BS amplitude over k_4, k_z and of the Minkowski BS one over k^- and k^+ are proportional to each other, differing simply by a Jacobian. For a formal view on the relation between the Bethe-Salpeter amplitude and the light-front wave function.

In order to derive the relation, one should start by considering the full vertex function, which is obtained by the sum of the three Faddeev components. The full three-body LF wave function is also obtained after summing up all the components. As mentioned before, the integral equations presented in Eqs. (4.9) and (4.12) represent the Faddeev component of the vertex function associated with one spectator particle, and the goal is solving them. The full BS amplitude is given by Eq. (4.2). Analogously, the LF wave function is obtained from the vertex by dividing by the LF energy denominator, reading

$$
\psi(\vec{k}_{1\perp}, \vec{k}_{2\perp}, \vec{k}_{3\perp}, x_1, x_2, x_3) = \frac{\Gamma(\vec{k}_{1\perp}, x_1) + \Gamma(\vec{k}_{2\perp}, x_2) + \Gamma(\vec{k}_{3\perp}, x_3)}{M_0^2 - M_3^2}, \qquad (4.14)
$$

where $M_0^2 = (k_1 + k_2 + k_3)^2$ is the same as defined before in Eq. (4.13). Notice that all the four-momenta are on the mass shell, i.e. $k_i^2 = m^2$ and $p^2 = M_3^3$, and satisfy the relation $k_1 + k_2 + k_3 = p$, from the four-momentum conservation law. Eq. (4.14) is written in terms of the variables $\vec{k}_{i\perp}, x_i$, where $\vec{k}_{i\perp}$ is the spacial transverse component of the four-vector $R_i = k_i - x_i p$ and $x_i = k_i/p$. The equation in terms of the variables k_1, k_2, k_3 and p are easily obtained by performing the change of variables (such equation is formally derived in Ref. [139]). Analogous arguments are valid for Eq. (4.2).

In the case of the LF amplitude the situation is very simple, as it is already integrated over k^-. The integration needs to be performed only over two variables, x_1 and x_2 (one analytically), what can be explicitly written as

$$
L^{LF}(\vec{k}_{1\perp}, \vec{k}_{2\perp}) = L_1^{LF} + L_2^{LF} + L_3^{LF}, \qquad (4.15)
$$

$$
L_i^{LF} = -\frac{1}{2}\sqrt{\frac{\pi}{2}} \int_0^1 dx_1 \, \Gamma(\vec{k}_{i\perp}, x_1) \int_0^{1-x_1} \frac{dx_2}{a'x_2^2 + b'x_2 + c'}, \, i = 1, 2, 3
$$

where $a' = E_{1\perp}^2 - x_1 M_3^2$, $b' = -(1 - x_1)E_{1\perp}^2 + x_1[E_{2\perp}^2 - E_{3\perp}^2 + (1 - x_1)M_3^2]$ and $c' = E_{2\perp}^2 - x_1 M_3^2$.

In summary, following the derivation presented in Appendix E.1, one gets for

the L_1 contribution to the Euclidean transverse amplitude

$$
L_1(\vec{k}'_{1\perp}, \vec{k}'_{2\perp}) = - \int_{-\infty}^{\infty} dk'_{1z} \int_{-\infty}^{\infty} dk'_{10} \chi(k'_{14}, k'_{1z}; \vec{k}'_{1\perp}, \vec{k}'_{2\perp}) \tilde{v}(k'_{1v}, k'_{14})
$$
$$
\times \frac{i}{(k'_{14} - i\frac{M_3}{3})^2 + k'^2_{1z} + m_1^2},
$$
(4.16)

where χ is given by Eq. (E.17).

The quantities $L_1^{LF}(\vec{k}_{1\perp}, \vec{k}_{2\perp})$, defined in Eq. (4.15), and $L_1(\vec{k}_{1\perp}, \vec{k}_{2\perp})$, of Eq. (4.16), are supposed to coincide. However, as the LF wave function, found from Eq. (4.12), only retains the valence component of the BS amplitude, of Eq. (4.9), then L_1^{LF} and L_1 are expected to differ due to the different diagrams incorporated in the kernels of Eqs. (4.12) and (4.1). This difference brings a deeper understanding of the effect, since it goes beyond the comparison between the binding energies and provides the impact also on the structure of the relativistic three-body bound state.

The non-relativistic limits for the Euclidean BSE, as well as for the LF one, are presented in Appendix F.

4.1.4 Spectrum and transverse amplitudes

The LF and Euclidean BS integral equations are numerically solved as in the two-body case (Sec. 3), but now by means of a spline decomposition instead of the orthogonal basis used in that case. The main reason is the fact that splines (see appendix D) are local and thus more general functions, being able to represent possibly unknown behaviors of the amplitude. In the two-body case, symmetries of properties of the eigenvector were known and fixing specific polynomials enclosing the system properties was achievable. Moreover, the results presented here are converged with a numerical error of at most about 3%. This accuracy can be further improved by enlarging the number of basis functions or Gaussian points for the integrations, but that would increase the runtime unnecessarily considering the purposes of the study.

The aim is to investigate the low-lying states, considering that the ground state was missed by previous LF calculations [138, 139]. Exploring more about the spectrum can lead to interesting outcomes, particularly regarding the relativistic effects on the Efimov physics[2]. This is an attractive subject for further research within the model. Worth mentioning that studying an unbalanced system [145], with two heavy and one light particle, would make the numerical search of excited states easier since the mass gap between the states would be smaller [142].

The first basic quantity found numerically is the three-body bound state mass. After its solution, the LF equation (4.12) determines the squared mass M_3^2, as well as the BS equation (4.9). Interesting to notice that the change of the sign $M_3 \to -M_3$ is equivalent to the complex conjugation and does not affect the real (i.e.

---

[2]In this context, the Efimov physics has been placed and observed in a variety of quantum few-body systems, mainly studied in non-relativistic quantum mechanics for atomic and nuclear systems. The Efimov physics is studied predominantly for the s-wave three-body equation with short-range interactions, based on scale invariance, which is dynamically broken to a discrete one. Efimov, in 1970, showed how the discrete scaling appears in the several features seen on the observables of the three-boson system. See Refs. [142, 143] for more details.
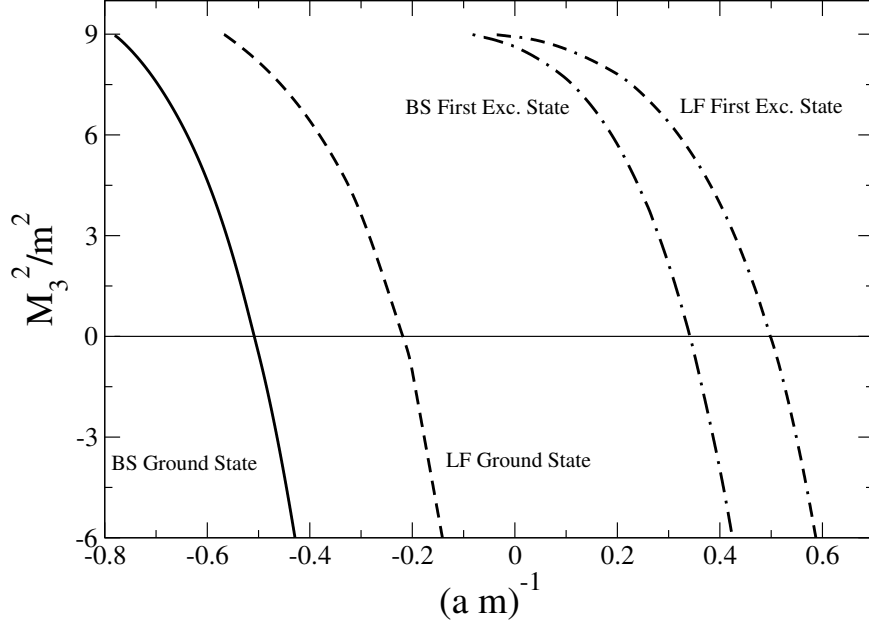
Figure 4.4. Squared three-body mass M_3^2 dependence on the inverse scattering length $(a\,m)^{-1}$. The solid curve is the BS ground state, while the dashed one is the LF ground state. The first excited state of the BSE is represented by the dashed-dotted curve and the LF first excited state through the double-dash-dotted one.

physical) eigenvalues. The value of M_3^2 can be, in principle, found to be both positive or negative while solving the equations, since one can get an unphysical solution depending on the value of the input scattering length a. Although a solution for a given value of a can be non-physical for the ground state, the excited one could still be physical, i.e. with a positive M_3^2. As mentioned before, Refs. [138, 139] found that the relativistic effects eliminate the Thomas collapse from the spectrum, meaning that the eigenvalues M_3^2 never go to $-\infty$. Still M_3^2 can be negative depending on the two-body interaction, what happens already for a two-body state with quite small binding energy. Analogously to what is done to avoid the Thomas collapse in non-relativistic calculations, a cutoff could be introduced to avoid the negative M_3^2. When the two-body interaction becomes weaker, i.e. when the scattering length gets negative and then $|a| \to 0$, the ground state squared three-body mass M_3^2 becomes positive and grows making $B_3 = 3m - M_3 \to 0$, until when the three-body bound states disappear. Figure 4.4 shows this effect through the plot of M_3^2 as a function of the inverse scattering length $(a\,m)^{-1}$. The "LF-excited state" in that figure is the solution found in Refs. [138, 139] as a ground state. The present calculations confirm the values M_3^2 vs. M_2 found in [139], where cutoffs were not used, as can be better seen in Fig. 4.5.

Table 4.1 gives the inverse scattering lengths $(a\,m)^{-1}$ for $M_3^2 = 0$ and $9\,m^2$ (or, respectively, $B_3 = 0$ and $3\,m$). The corresponding values for the inverse scattering lengths are $(a\,m)^{-1} \approx 0.34$, for the BS approach, and $(a\,m)^{-1} \approx 0.50$, in the light-
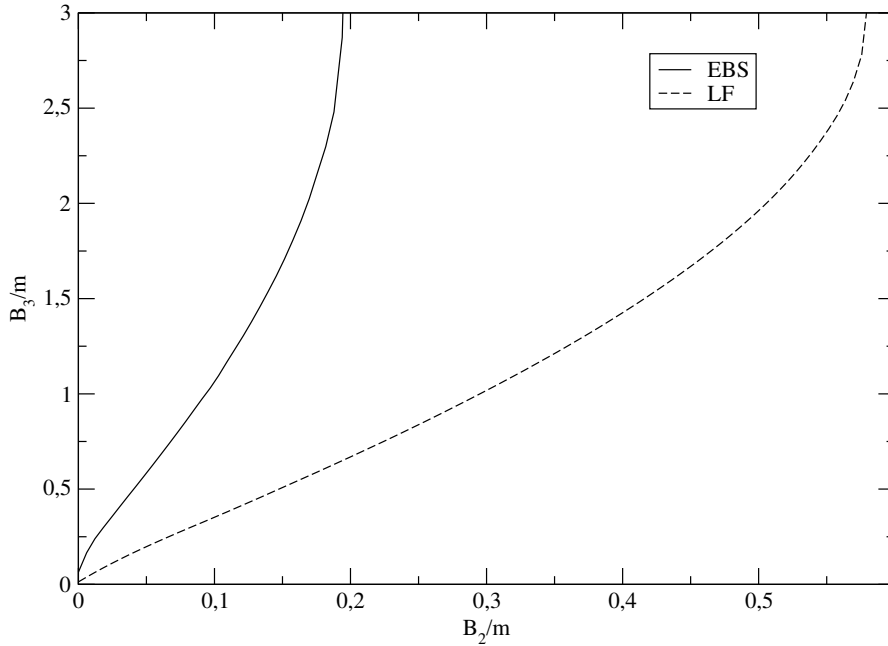
Figure 4.5. Three-body B_3 vs. two-body B_2 binding energy for the first excited state. The solid curve is computed solving the Euclidean BS equation, while the dashed one is obtained from the LF equation.

M_3^2	Inverse scattering length $(a\,m)^{-1}$			
	ground state		excited state	
	BS	LF	BS	LF
$9\,m^2$	-0.78	-0.57	-0.08	-0.04
0	-0.51	-0.21	0.34	0.50

Table 4.1. Limiting values of the inverse scattering length $(a\,m)^{-1}$ for which the curves in Fig. 4.4 cross the bound state thresholds $M_3^2 = 9\,m^2$ and $M_3^2 = 0$.

front, when $M_3^2 = 0$ for the excited state. Using Eq. (4.5) one can find that the two-body binding energies are, respectively, $B_2 \approx 0.194\,m$ and $B_2 \approx 0.582\,m$. For the sake of completeness, for $B_2 = 2m - M_2 \to 0$ the ground state masses are $M_3^2 \approx -94\,m^2$, for the BS equation, and $M_3^2 = -18\,m^2$, for the LF one. In both cases they are extremely over-bounded, and the difference between those values is huge. For the corresponding excited state, still for $B_2 = 0$, the three-body binding energy is $B_3 \approx 0.066\,m$, for the BS equation, and $B_3 \approx 0.013\,m$, for the LF one. The latter value is close to one computed in [139]. In all the cases it is possible to notice the huge difference originated by the higher-Fock components. This result suggests that models using only the valence truncation can be missing relevant information, particularly the ones for three-body systems. From Fig. 4.4 it is also possible to conclude that the three-body mass M_3^2 found in the BS approach is always smaller than the one through the LF equation, showing an attractive and strong impact of the effective three-body forces (see Sec. 4.1.1). This corroborates what was found in

Refs. [106, 140] for the one-boson exchange interaction kernel.

Figure 4.6 shows the amplitudes $\Gamma(k_\perp, x)$ for the two states, ground and excited ones, obtained through the LF equation (4.12) (for the same B_3) and normalized by $\Gamma(0, 1/3) = 1$, for comparison purposes. It is quite evident that they considerably differ from each other, with the characteristic node structure of the excited state being evidently seen.

It is remarkable that the functions $\Gamma(k_\perp, x = 1/3)$ vs. $k_\perp$ have the same fall-off for both ground and excited states. The same asymptotic behavior is expected since both solutions come from the same equation (4.12). The main difference is that for the excited state the amplitude for high momentum is ten times smaller than for the ground state. The asymptotic $k_\perp$-dependence comes from the factor $(M_0^2 - M_3^2) \sim k_\perp^2$, which gives $\Gamma(k_\perp, x) \sim c/k_\perp^2$. That is close to the asymptotic form of both curves shown in the right panel of Fig. 4.6. A logarithmic correction coming from $\mathcal{F}(M_{12}^2)$ also contributes to the asymptotic behavior of the amplitude. However, the non-asymptotic domain of Γ, as well as the factor c, are more sensitive to the details of $\Gamma(k_\perp, x)$ and strongly depend on the state.
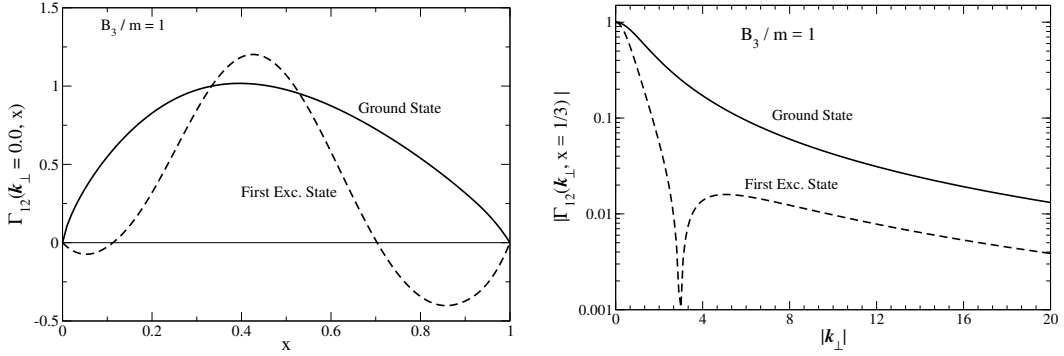
Figure 4.6. The LF vertex function $\Gamma(k_\perp = 0, x)$ of Eq. (4.12) vs. x (left panel) and $\Gamma(k_\perp, x = 1/3)$ vs. $k_\perp$ (right panel). Both panels present the ground state with $B_3 = m$ (solid curve) and the excited state (dashed curve). $B_3 = m$ for all the cases, but for different $(a\,m)^{-1}$ (given in the text).

Figure 4.7 presents the BS vertex amplitudes $v_E(k_4, k_v)$, i.e. the solutions of (4.9), for ground $((a\,m)^{-1} \approx -0.57)$ and excited $((a\,m)^{-1} = 0.25 \to B_2 = 0.093\,m)$ states with the same three-body binding $B_3 = m$. The numerical solutions presents the symmetries expected analytically from Eq. (4.11), namely $\text{Re}[v_E(k_4, k_v = \text{const})]$ vs. k_4 is symmetric relative to $k_4 \to -k_4$ and $\text{Im}[v_E(k_4, k_v = \text{const})]$ is antisymmetric. This is the first time that Eq. (4.9) is fully solved and that the BS vertex amplitude for this model is presented. One can notice that the decay of the BS amplitude for the three-body case with zero-range interaction is quite slow if compared with the amplitudes for the two-body case with an one-boson exchange kernel.

After emphasizing the huge impact that the effective three-body forces impose on the two lowest-lying levels of the spectrum, one can proceed to study the outputs for the transverse amplitudes.Fig. 4.8 shows the comparison of the transverse dependencies of the LF and BS amplitudes, as presented in Sec. 4.1.1. The comparison is made for the Faddeev components given by Eqs. (4.15) (L_1^{LF} - LF approach) and (4.16) (L_1 - Euclidean BS approach). They compose full LF wave function (4.14)
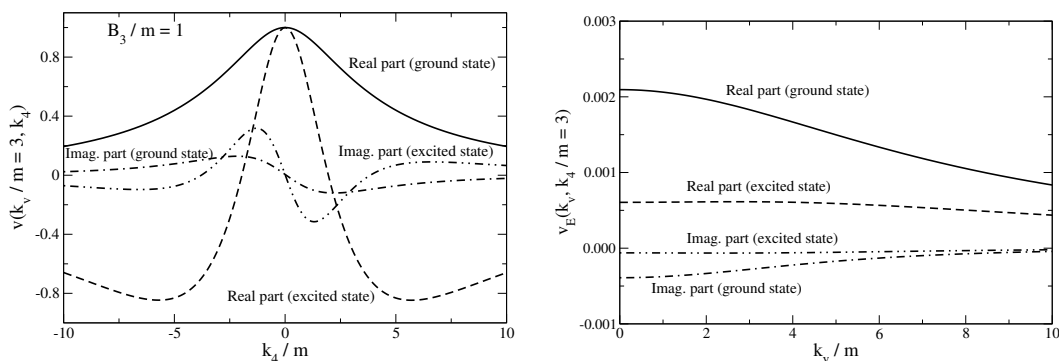
Figure 4.7. The BS amplitude $v_E(k_4, k_v)$ vs. k_4 (left) and vs. k_v (right) normalized to $\mathrm{Re}[v_E(k_4 = 0, k_v/m = 3)] = 1$. Ground (solid curve) and exited (dashed curve) states have their real parts displayed for $\mathrm{Re}[v_E(k_4, k_v/m = 3)]$, in the left panel, and for $\mathrm{Re}[v_E(k_4/m = 3, k_v)]$, in the right one. Analogously, the imaginary parts are presented for $\mathrm{Im}[v_E(k_4, k_v/m = 3)]$, on the left panel, and for $\mathrm{Im}[v_E(k_4/m = 3, k_v)]$, on the right panel. The dot-dashed curve represents the ground state and the dot-dot-dashed curve the exited one.

and the full BS amplitude (4.2). The amplitudes L_i ($i = 1, 2, 3$) have the same functional form due to the Bose symmetry.

The components defined by Eqs. (4.15) and (4.16) depend on two variables, $\vec{k}_{1\perp}$ and $\vec{k}_{2\perp}$. For the comparison shown in Fig. 4.8 it is chosen $\vec{k}_{2\perp} = 0$. Both amplitudes are normalized to one at $k_{1\perp} = 0$, so one can compare their $k_{1\perp}$ dependencies. Again, the binding energy was fixed at $B_3 = m$ for the calculations in both approaches. The node structure of the excited state, already seen in the transverse momentum dependence of the LF vertex function in Fig. 4.6 (right panel), is clearly visible in the figure. The number of nodes is a form of characterization of the states, as the ground state is expected to have no node while the first excited state should present one. Moreover, Fig. 4.8 shows that for the same three-body binding energy, the BS transverse amplitude has a slower fall-off than the LF one. This is one manifestation of the importance of the higher Fock-components to the structure of the amplitude, as the coupling of those components with the valence one is not considered in the LF equation.

A comparison between the transverse amplitudes obtained from Minkowski and Euclidean BS equations without any truncation in the Fock space give exactly the same result, as seen for a two-body system in Ref. [130]. For a given approach (LF or BS), the asymptotic behaviors of both excited and ground states are the same, since their amplitudes are two solutions of the same equation. The high-momentum fall-off is an interesting subject for future research, as it can be studied analytically to understand in detail the leading fall-off and its corrections, as the log correction coming from the two-body scattering amplitude (4.3).

In conclusion, the four-dimensional Bethe-Salpeter Faddeev equation for a zero-range interaction was solved, as well as the three-dimensional reduction in the light-front approach. It was found that the previous LF calculations [138, 139] missed the formal ground state, and the structure of both ground and excited states was exposed in detail. Introducing the renormalization of the two-body amplitude
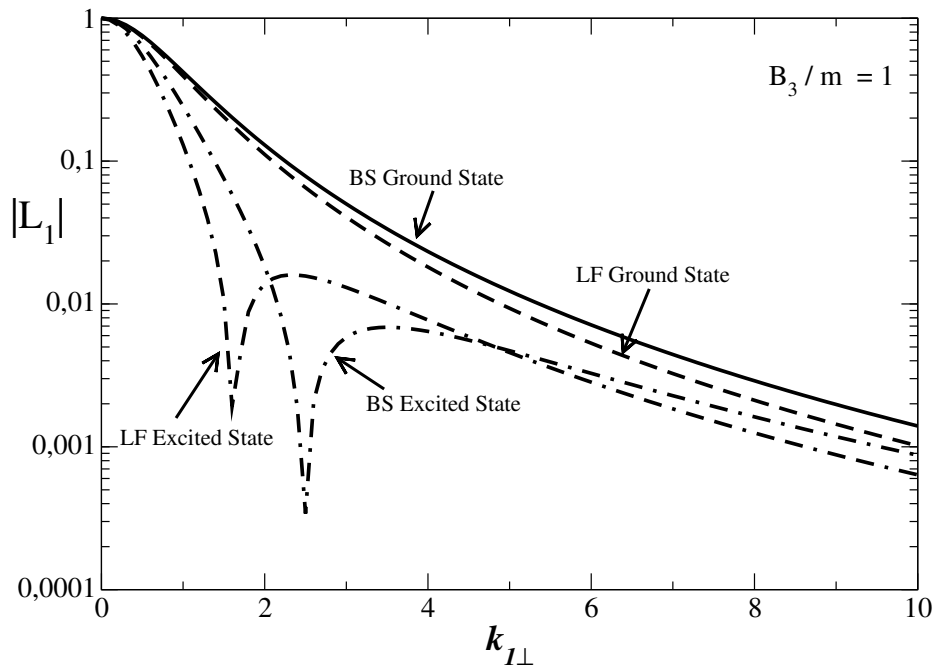
Figure 4.8. Transverse momentum Faddeev components of the LF and Euclidean BS amplitudes. Binding energy fixed at $B_3/m = 1$. The solid (ground state) and dot-dashed (excited state) curves are the BS calculations (Eq. (4.16)), while dashed (ground state) and dash-dash-dotted (excited state) curves are the LF calculations (Eq. (4.15)).

(4.3) by means of the scattering length was essential for that. The results found previously for the excited state in Ref. [139] in the LF framework were confirmed. For negative scattering length, it was found a strongly bound Borromean system. Moreover, it was shown the difference in the dynamical contents of the BS and LF approaches, due to the contribution of the many-body intermediate states which generate effective three-body forces of relativistic origin. A similar effect was also seen for the OBE kernel in Ref. [140]. The relativistic effects in both frameworks also create an effective repulsion, eliminating the Thomas collapse [141] in a three-boson system. Further exploration on the spectrum and the Efimov ratio[3] can be done if the approaches are generalized to systems with non-equal masses [145]. The next step is to solve Eq. (4.1) fully in Minkowski space. Although this is a complex task, finding a reliable method for its solution without any truncation would clear the way to the exploration of complex three-body systems, like baryons.

4.2 BSE in Minkowski space by direct integration

The goal is now to solve the scalar three-body Bethe-Salpeter equation [138], with zero-range interaction, fully in Minkowski space and retaining implicitly the Fock-

---

[3]Efimov predicted that when the two-body binding energy goes to zero the number of three-body bound states increases indefinitely and, in this limit, the ration between two successive states is given by an universal constant, namely $B_3^{(N)}/B_3^{(N+1)} \approx 500$ for the equal mass system. The ratio is at least two orders of magnitude smaller for a system with two heavy and one light particle [142, 143].

space beyond the valence truncation. The adopted method is the direct integration of the singularities of the four-dimensional integral equation, developed recently for the two-body BSE in Ref. [47]. The method does not rely on any ansatz, as e.g. the NIR used for the solution of the two-body equation in Chap. 3. No three-dimensional reduction of the covariant 4D equation, as the one done by performing the projection onto the LF plane, is adopted. Part of what is exposed here was published in Ref. [46]. The results in Minkowski space will be properly compared with the Euclidean space ones, to test the reliability of the method.

One interesting example of calculation within the approach utilized here is the electromagnetic transition form factor, which quantifies the breakup of a two-body bound state. This highly complex calculation was performed through the direct integration method in Minkowski space, using as inputs the solutions, obtained by the same method [47], of the scattering and bound state BS equations. The transition form factor was calculated in the whole kinematical region, including the final state interaction [132], with the non-trivial current conservation explicitly verified numerically.

After presenting and applying the direct integration method, in the next section the NIR will be introduced to turn the three-body equation into a form that could be solved numerically. Developing different methods for the solution fully in Minkowski space is essential to understand the technical difficulties and extend the BSE approach to more complex physical systems.

4.2.1   Three-body Bethe-Salpeter equation in Minkowski space

As already mentioned, Eq. (4.1),

$$v(q,p) = 2i\mathcal{F}(M_{12}^2) \int \frac{d^4k}{(2\pi)^4} \frac{i}{[k^2 - m^2 + i\epsilon]} \frac{i}{[(p-q-k)^2 - m^2 + i\epsilon]} v(k,p), \quad (4.17)$$

is a singular integral equation and solving it numerically is a very challenging task, if not impossible. For that reason, the equation requires a proper treatment to be rewritten in a, at least, less singular form before its numerical solution. The propagators, containing the strongest singularities of the BSE kernel, is represented in the customary form [47]

$$\frac{1}{k^2 - m^2 + i\epsilon} = \frac{1}{k_0^2 - k_v^2 - m^2 + i\epsilon} = PV\frac{1}{k_0^2 - \varepsilon_k^2} - \frac{i\pi}{2\varepsilon_k}[\delta(k_0 - \varepsilon_k) + \delta(k_0 + \varepsilon_k)],$$

$$(4.18)$$

where $\varepsilon_k = \sqrt{k_v^2 + m^2}$, $k_v = |\vec{k}|$ and PV denotes the principal value. The terms like $PV \int \dots \frac{dk_0}{k_0^2 - \varepsilon_k^2}$ contain a singularity that is removed by subtracting integrals from the equation, with appropriate coefficients, in such a way that the final equation is not affected. For that, the following identities are used

$$PV \int_{-\infty}^0 \frac{dk_0}{k_0^2 - \varepsilon_k^2} = PV \int_0^\infty \frac{dk_0}{k_0^2 - \varepsilon_k^2} = 0. \quad (4.19)$$

The second propagator in (4.1) can be integrated over the angles analytically.

Denoting $z = \cos\left(\frac{\vec{k}\cdot\vec{q}}{k_v q_v}\right)$ and recalling that $d^3k = k^2\,dz\,d\varphi$, one can write that

$$\Pi(q_0, q_v, k_0, k_v) = \int \frac{i\,dz\,d\varphi}{[(p-q-k)^2 - m^2 + i\epsilon]} = \frac{i\pi}{q_v k_v}\left\{\log\left|\frac{(\eta+1)}{(\eta-1)}\right| - i\pi I(\eta)\right\}, \tag{4.20}$$

where the integration over the azimuthal angle integration brings simply a factor of 2π. In Eq. (4.20) it was defined

$$I(\eta) = \begin{cases} 1 & \text{if } |\eta| \leq 1 \\ 0 & \text{if } |\eta| > 1 \end{cases}, \tag{4.21}$$

with

$$\eta = \frac{(M_3 - q_0 - k_0)^2 - k_v^2 - q_v^2 - m^2}{2q_v k_v}. \tag{4.22}$$

The kernel of Eq. (4.20) still has log-singularities and discontinuities that will be treated numerically[4].

Once the propagators are expressed as in Eq. (4.18), the principal value singularities are subtracted and the angular integrations are performed, Eq. (4.1) acquires the following form (in the center-of-mass frame, $\vec{p} = 0$)

$$\begin{aligned}
v(q_0, q_v) &= \frac{\mathcal{F}(M_{12}^2)}{(2\pi)^4} \int_0^\infty k_v^2\,dk_v \tag{4.23} \\
&\times \left\{ \frac{2\pi i}{2\varepsilon_k}\left[\Pi(q_0, q_v; \varepsilon_k, k_v)v(\varepsilon_k, k_v) + \Pi(q_0, q_v; -\varepsilon_k, k_v)v(-\varepsilon_k, k_v)\right] \right. \\
&\quad - 2\int_{-\infty}^0 dk_0 \left[\frac{\Pi(q_0, q_v; k_0, k_v)v(k_0, k_v) - \Pi(q_0, q_v; -\varepsilon_k, k_v)v(-\varepsilon_k, k_v)}{k_0^2 - \varepsilon_k^2}\right] \\
&\quad \left. - 2\int_0^\infty dk_0 \left[\frac{\Pi(q_0, q_v; k_0, k_v)v(k_0, k_v) - \Pi(q_0, q_v; \varepsilon_k, k_v)v(\varepsilon_k, k_v)}{k_0^2 - \varepsilon_k^2}\right] \right\}.
\end{aligned}$$

This equation has now, besides the unknown analytical behavior of $v(q_0, q_v)$ which will be discovered numerically, only weak singularities and discontinuities, but unlike (4.1) the singularities in $k_0 = \pm\varepsilon_k$ no longer exist.

The logarithmic singularities of the kernel $\Pi(q_0, q_v, k_0, k_v)$ (4.20) at $\eta = \pm 1$ can be found for fixed values of q_0, q_v and k_v, what makes the numerical treatment in k_0 easier. Their positions with respect to the variable k_0 are

$$\begin{aligned}
k_0 &= (M_3 - q_0) + \sqrt{m^2 + (k_v \pm q_v)^2} \\
k_0 &= (M_3 - q_0) - \sqrt{m^2 + (k_v \pm q_v)^2} \tag{4.24}
\end{aligned}$$

Analogously, the position of the singularities can be found for the variable k_v, so that the integration over this variable can be optimized numerically. The positions of the singularities of $\Pi(q_0, q_v, \pm\varepsilon_k, k_v)$ as a function of k_v are given by

$$k_v = \frac{\pm\sqrt{M_{12}^2(M_{12}^2 + q_v^2)(M_{12}^2 - 4m^2)} \pm q_v M_{12}^2}{2M_{12}^2}, \tag{4.25}$$

---

[4]See Appendix D for more details on the numerical methods.

where $M_{12}^2 = (M_3 - q_0)^2 - q_v^2$. The argument of the square root is positive if $M_{12}^2 \geq 4m^2$ or $M_{12}^2 \leq 0$ and, therefore, for existing real singularities in k_v one needs to ensure one of the following conditions for q_0: $q_0 < M_3 - \sqrt{q_v^2 + 4m^2}$ or $M_3 - q_v < q_0 < M_3 + q_v$ or $q_0 > M_3 + \sqrt{q_v^2 + 4m^2}$. This means that the branching points that needs to be considered while fixing the mesh numerically to separate the regions with and without singularities in k_v are

$$
\begin{aligned}
q_0^{(1)} =& M_3 - \sqrt{q_v^2 + 4m^2}, \quad q_0^{(2)} = M_3 - q_v, \\
q_0^{(3)} =& M_3 + q_v \quad \text{and} \quad q_0^{(4)} = M_3 + \sqrt{q_v^2 + 4m^2},
\end{aligned}
\tag{4.26}
$$

with $q_0^{(1)} < q_0^{(2)} < q_0^{(3)} < q_0^{(4)}$. As it can be seen from Eq. (4.3), these branching points are also present in the two-body amplitude $\mathcal{F}(M_{12}^2)$. More details on the behavior of the $\mathcal{F}(M_{12}^2)$ amplitude can be found in Appendix C.

4.2.2 Transverse amplitude in Minkowski space

As mentioned before, the vertex function $v(q_0, q_v)$ is fundamentally dependent on the metric adopted to define the integral equation. The transverse amplitude, already derived for the Euclidean BS amplitude in Sec. 4.1.3, is instead a quantity useful for comparison between calculations performed in Euclidean and Minkowski spaces. The derivation of the expressions for the Minkowski transverse amplitude is presented below. The final amplitude is expected to coincide with Eq. (4.16), defined in Euclidean space, after computed with the BS amplitude obtained from the solution of the BSE in Minkowski space (4.23).

The BS amplitude can be written in terms of the three vertex components by introducing the external propagators, as given by Eq. (4.2). The transverse amplitude can be defined in Minkowski space, analogously to what was written in (E.7), as

$$
\begin{aligned}
L(\vec{k}_{1\perp}, \vec{k}_{2\perp}) = & L_1(\vec{k}_{1\perp}, \vec{k}_{2\perp}) + L_2(\vec{k}_{1\perp}, \vec{k}_{2\perp}) + L_3(\vec{k}_{1\perp}, \vec{k}_{2\perp}) = \\
& \int_{-\infty}^{\infty} dk_{10} \int_{-\infty}^{\infty} dk_{1z} \int_{-\infty}^{\infty} dk_{20} \int_{-\infty}^{\infty} dk_{2z} i \Phi_M(k_{10}, k_{1z}, k_{20}, k_{2z}; \vec{k}_{1\perp}, \vec{k}_{2\perp}).
\end{aligned}
\tag{4.27}
$$

The final expression for the contribution $L_1(\vec{k}_{1\perp}, \vec{k}_{2\perp})$, after the derivation presented in Appendix E.2, is given by

$$
\begin{aligned}
L_1(\vec{k}_{1\perp}, \vec{k}_{2\perp}) = & -i \int_{-\infty}^{\infty} dk_{1z} \\
& \times \left\{ \frac{i\pi}{2\tilde{k}_{10}} \left[\chi(\tilde{k}_{10}, k_{1z}; \vec{k}_{1\perp}, \vec{k}_{2\perp}) v_M(\tilde{k}_{10}, k_{1v}) + \chi(-\tilde{k}_{10}, k_{1z}; \vec{k}_{1\perp}, \vec{k}_{2\perp}) v_M(-\tilde{k}_{10}, k_{1v}) \right] \right. \\
& - \int_0^{\infty} dk_{10} \\
& \times \frac{\chi(-k_{10}, k_{1z}; \vec{k}_{1\perp}, \vec{k}_{2\perp}) v_M(-k_{10}, k_{1v}) - \chi(-\tilde{k}_{10}, k_{1z}; \vec{k}_{1\perp}, \vec{k}_{2\perp}) v_M(-\tilde{k}_{10}, k_{1v})}{k_{10}^2 - \tilde{k}_{10}^2} \\
& \left. - \int_0^{\infty} dk_{10} \frac{\chi(k_{10}, k_{1z}; \vec{k}_{1\perp}, \vec{k}_{2\perp}) v_M(k_{10}, k_{1v}) - \chi(\tilde{k}_{10}, k_{1z}; \vec{k}_{1\perp}, \vec{k}_{2\perp}) v_M(\tilde{k}_{10}, k_{1v})}{k_{10}^2 - \tilde{k}_{10}^2} \right\},
\end{aligned}
\tag{4.28}
$$

where

$$\tilde{k}_{10} = \sqrt{k_{1z}^2 + \vec{k}_{1\perp}^2 + m^2}. \tag{4.29}$$

Notice that in Appendix E.2 important properties of Eq. (4.28) are discussed, for the interested reader.

4.2.3   Numerical solution

Equation (4.23) is now solved by standard numerical methods, similarly to what was performed in Ref. [47, 46]. The vertex function $v(p, q)$, as done before for the solution of the equation in Euclidean space, represented through the spline decomposition (see Appendix D for more details). The inputs are the scattering length a and the three-body binding energy B_3, the same as in the Euclidean calculations (see Sec. 4.1.4). The equation is numerically represented in the form $Av = \lambda(a, B_3)Bv$, where A is the left-hand side matrix and B is the right-hand side one. The solution is found through iterations such that the eigenvalue fulfills $\lambda(a, B_3) = 1.0$, under a certain precision. The convergence is also verified for the eigenvector v and more iterations are done (or a larger basis is adopted), if needed.

B_3/m	am	λ
0.006	-1.280	$0.999 - 0.054i$
0.395	-1.500	$1.000 + 0.002i$
1.001	-1.705	$0.997 + 0.106i$

Table 4.2. Eigenvalues of the three-body ground state for three values of scattering lengths, a. Three-body binding energies are the same as the ones computed in Euclidean space, through the framework presented in Sec. 4.1.1.

Three results for the eigenvalue are given in Table 4.2, for the following values of the two-body scattering length: $am = -1.280$, $am = -1.500$ and $am = -1.705$[5]. The corresponding three-body binding energies are, respectively, $B_3/m = 0.006, 0.395, 1.001$, as obtained by solving the BSE in Euclidean space. The results for the eigenvalue λ, expected to be real and equal to one, present small deviations from the unity and also an imaginary part. Both of these facts are related to numerical errors, which are about 5% and 10% for the worst cases. These errors could be reduced by increasing the number of splines and Gaussian points for the integrations, but this enhances considerably the runtime and a better precision is not needed for the purposes of the present work.

Nevertheless, it is important to mention another potential source of error: cutoffs were introduced to constrain the domains of the variables q_v and q_0. It is very difficult to reach a reasonable convergence considering the full domains, as the size of the region where the singularities (given by Eqs. (4.24) and (4.25)) appear is enlarged along the axes. Moreover, the asymptotic regions start at larger momenta.

The actual values used to truncate the variables were $q_v^{\max}/m = 6.0$ and $q_0^{\max}/m = 13.0$, for the two smallest binding energies, or $q_0^{\max}/m = 15.0$, for the case where $B_3/m = 1.001$. Regardless, the convergence was reached within

---

[5]Values of $a < 0$ were chosen for simplicity, in order to avoid the pole in $\mathcal{F}(M_{12}^2)$.

about 10% for the worst case. On the other hand, in the Euclidean calculations it is possible to take into account the whole range of the involved variables q_v, q_4, k_v and k_4. The fact that in the Minkowski approach cutoffs were applied while the whole domains were used in the Euclidean calculations make the results not fully comparable. This might be one of the reasons why in λ non-zero imaginary parts appear and for the deviations from 1 obtained in the real part.
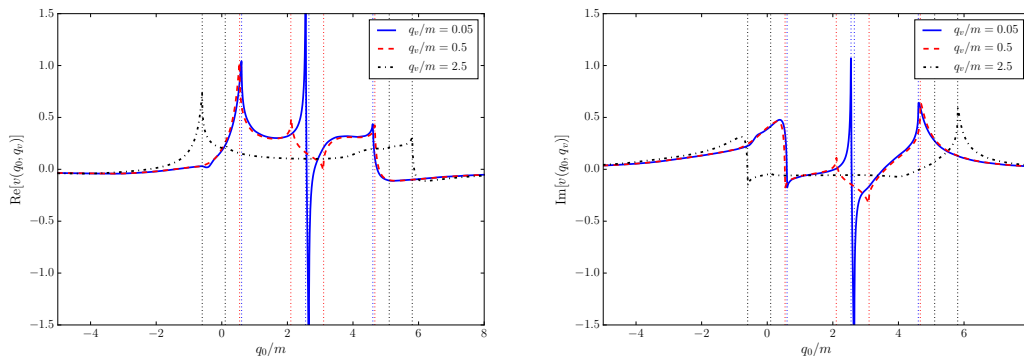
Figure 4.9. Real (left panel) and imaginary (right panel) parts of the vertex function, $v(q_0, q_v)$ with respect to q_0 for $q_v/m = 0.05, 0.5, 2.5$. calculations made with the parameters $am = -1.5$ and $B_3/m = 0.395$. For each value of q_v the analytical positions of the peaks, given by Eq. (4.26), are shown with dotted vertical lines.

.

In Fig. 4.9 it is shown the calculated real and imaginary parts of the vertex function $v(q_0, q_v)$ versus q_0 for three fixed values of q_v, namely $q_v/m = 0.05, 0.5, 2.5$. The results correspond to the binding energy $B_3/m = 0.395$ and $a\, m = -1.5$. In the figure, the analytical positions of the peaks, given by Eq. (4.26), are also shown. For all three cases there is a quite good agreement between the analytical and numerical peak positions. These peaks appear as branching points of the kernel $\Pi(q_0, q_v, \pm\varepsilon_k, k_v)$, defining its singularities, as discussed in Sec. 4.2.1. Interestingly, the aforementioned positions correspond to $M_{12}^2 = 0$ and $M_{12}^2 = 4\, m^2$, which give the branching points of the two-body scattering amplitude $\mathcal{F}(M_{12}^2)$. In Fig. 4.9 it is seen that for small values of q_v a singularity appears at $q_0 \approx M_3$. The distance between the external peaks, corresponding to $M_{12}^2 = 4\, m^2$, is equal to $2\sqrt{q_v^2 + 4m^2}$, an increasing function with respect to q_v. This fact makes things more complicated from the numerical point of view, as for large values of q_v a very wide region of q_0 has to be covered. This requests the need of adopting cutoffs for the variables.

Evidently, it is important to check that the adopted number of basis functions is enough for convergence. For this purpose, Fig. 4.10 shows the real and imaginary parts of $v(q_0, q_v = 0.5m)$, computed by using different number of subintervals N_{q_v} and N_{q_0} (see Appendix D), which vary the number of basis functions for the variables q_v and q_0, respectively. In the calculations it is used the parameters $am = -1.5$ and $B_3/m = 0.395$. It is seen in the figure that for $N_{q_v} \geq 40$ and $N_{q_0} \geq 80$ the solution is well-converged.

Furthermore, in Fig. 4.11, it is displayed the modulus of the contribution $L_1(|k_{1\perp}|, |k_{2\perp}|)$ to the transverse amplitude versus $|k_{1\perp}|$, computed in Minkowski space (symbols). The binding energy is fixed at $B_3/m = 0.395$. The calculations
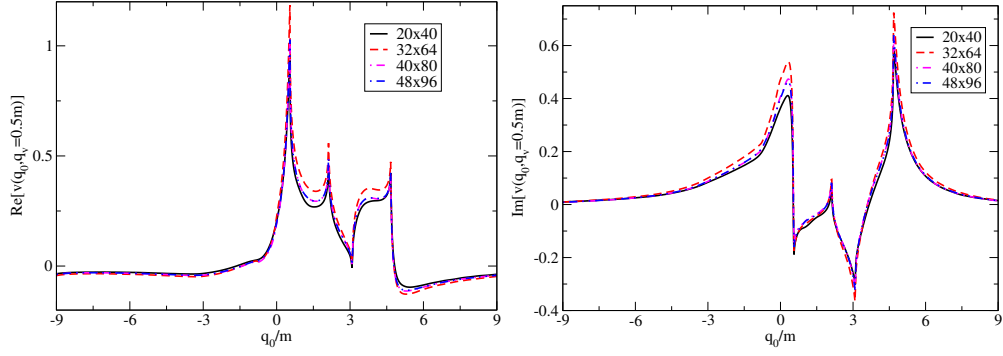
Figure 4.10. Convergence of the real (left panel) and imaginary (right panel) parts of the vertex function $v(q_0, q_v = 0.5m)$ with respect to the size of the basis, $N_{q_v} \times N_{q_0}$. In the calculations it was used $B_3/m = 0.395$.

are made through Eq. (4.28), for three fixed values of $|k_{2\perp}|$, namely $|k_{2\perp}|/m = 0.0, 0.5, 1.0$. The angle between the vectors $k_{1\perp}$ and $k_{2\perp}$ is fixed at $\theta = 0$. It is also shown, for comparison, the corresponding Euclidean results (lines), with the same aforementioned parameters and calculated through Eq. (4.16). It seen that Minkowski and Euclidean results are in fair agreement with each other. The non-smooth behavior of the BSE solution in Minkowski space, shown in Fig. 4.9, makes the agreement even more remarkable.
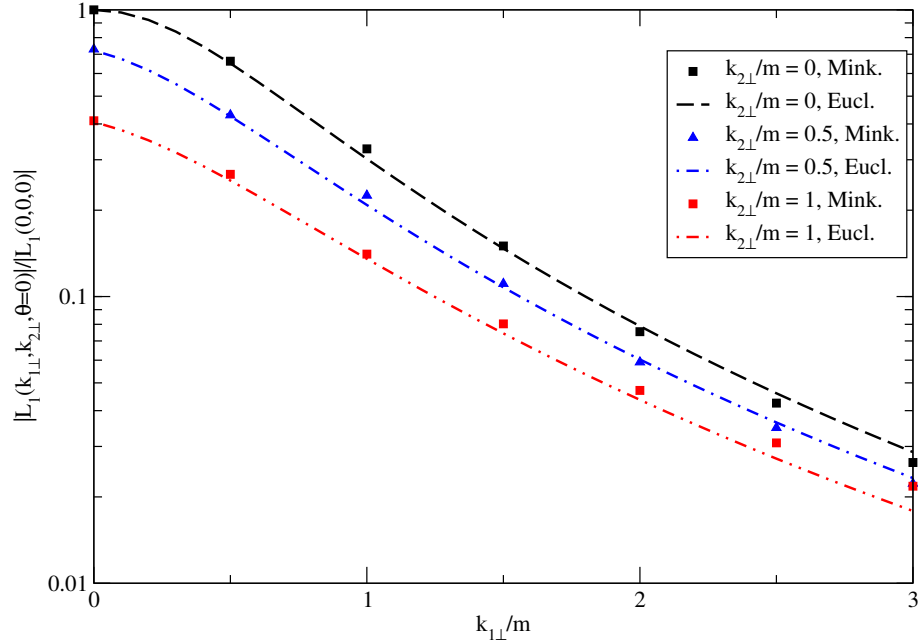
Figure 4.11. Transverse contribution, $L_1(|\vec{k}_{1\perp}|, |\vec{k}_{2\perp}|, \theta = 0)$ versus $|\vec{k}_{1\perp}|$, for $|\vec{k}_{2\perp}|/m = 0.0, 0.5, 1.0$, obtained in Minkowski space (symbols) compared with the ones calculated in Euclidean space (lines), for the parameters $am = -1.5$ and $B_3/m = 0.395$.

The dependence of the transverse contribution L_1 on the angle θ between $k_{1\perp}$ and $k_{2\perp}$ is also displayed, in Fig. 4.12. The following sets of fixed values for the other

variables are used: $(|\vec{k}_{1\perp}|/m, |\vec{k}_{2\perp}|/m) = (0.5, 0.5), (0.5, 2.0)$. For the scattering length and binding energy it is used $am = -1.5$ and $B_3/m = 0.395$, respectively. The modulus of L_1 is a slowly decreasing function with respect to $\cos\theta$. As seen in the figure, a satisfactory agreement is again found between the Euclidean (lines) and Minkowski (symbols) calculations.
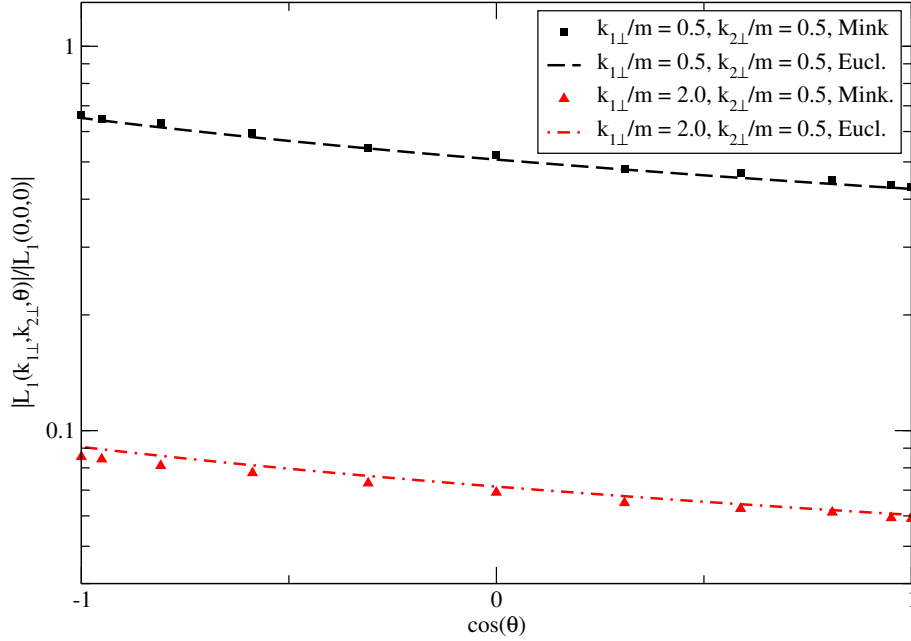
Figure 4.12. Transverse contribution, $L_1(|\vec{k}_{1\perp}|, |\vec{k}_{2\perp}|, \theta)$ with respect to $\cos(\theta)$ for $(|\vec{k}_{1\perp}|/m, |\vec{k}_{2\perp}|/m) = (0.5, 0.5), (0.5, 2.0)$, obtained in Minkowski space compared with the results computed in Euclidean space, for the parameters $am = -1.5$ and $B_3/m = 0.395$.

The results above present, for the first time, the solution of Eq. (4.1) directly in Minkowski space. Although the outcomes are remarkable, showing a non-smooth behavior of the three-body amplitude returning a great agreement with the smooth quantities computed in Euclidean space, the method reveals to be quite challenging to be generalized. For that reason, the next section is dedicated to develop a different way of dealing with the equation in Minkowski space. The Nakanishi integral representation, used for solving the two-boson problem, is adopted as an ansatz and the uniqueness conjecture [35, 38] is introduced to obtain a smooth equation to be solved numerically.

4.3 Minkowski space equation: integral representation and uniqueness

As discussed previously, when solving the three-body BSE by direct integration one still has to deal with a non-smooth equation (4.23) numerically. That brings a notable numerical instability, as well as important sources of errors in the calculations (e.g. the need of using cutoffs to avoid infinite amount of moving weak singularities,

with arbitrarily large distances among them along the real axis). For this reason, a new method was developed in order to solve Eq. (4.1). The method basically consists in expressing the Faddeev component of the vertex function through an ansatz for the integral representation and use the uniqueness theorem to obtain a smooth integral equation for the weight function g. This procedure is similar to the one adopted in Ref. [38] for two-boson scattering and bound state systems. What is presented below is the derivation of the equation and an analytical study of its kernel. The next step, to be performed in the future, consists in exploring the equation numerically.

As discussed in Sec. 4.1.1, as well as in Refs. [45, 46], the zero-range three-body BS equation for the vertex function in the Faddeev decomposition is given by Eqs. (4.1) and (4.3). As the three-body amplitude $v(q, p)$ is now represented by means of an ansatz for the integral representation, the same can be done for the two-body scattering interaction kernel. The two-body amplitude (4.3) can be written in the spectral form as follows

$$\mathcal{F}(M_{12}^2) = \int_{4m^2}^{\infty} \frac{\rho(\gamma) d\gamma}{M_{12}^2 - \gamma + i\epsilon},$$ (4.30)

with the imaginary part given by (c.f. the last line of Eq. (4.3))

$$Im[\mathcal{F}(M_{12}^2)] = -\pi\rho(M_{12}^2) = \frac{\theta(M_{12}^2 - 4m^2)}{16\pi} \frac{y''}{(\frac{y''}{16\pi^2} \log \frac{1+y''}{1-y''} - \frac{1}{16\pi ma})^2 + (\frac{y''}{16\pi})^2}.$$ (4.31)

The spectral function is thus given by

$$\rho(M_{12}^2) = -\frac{\theta(M_{12}^2 - 4m^2)}{16\pi^2} \frac{y''}{(\frac{y''}{16\pi^2} \log \frac{1+y''}{1-y''} - \frac{1}{16\pi ma})^2 + (\frac{y''}{16\pi})^2}.$$ (4.32)

The three-body vertex function, $v(q, p)$, can be written in terms of the following ansatz for the integral representation

$$v(q, p) = \int_0^{\infty} d\gamma \int_{-\frac{4}{3}}^{\frac{2}{3}} dz \frac{g(\gamma, z)}{\gamma - q^2 - (p \cdot q)z - i\epsilon},$$ (4.33)

where $g(\gamma, z)$ denotes the Nakanishi weight function. The denominator is very similar to the one which appears in the Nakanishi representation for the two-body BS amplitude, since it is the Faddeev component for the bachelor particle and considers only two-body interactions. The main difference are the integration limits, basically related with the new denominator and to the fact that the system has three identical particles, with masses $m_1 = m_2 = m_3 = m$. Differently from what was done in Sec. 4.2, the total momentum fraction is chosen to be $p/3$ in the propagators of Eq. (4.1), which is a simple kinematic choice but might be numerically more stable (as seen for the Euclidean case, in Sec. 4.1).

By adopting the NIR of the vertex function and the spectral form of the two-body

amplitude, the BSE (4.1) becomes

$$
\int_0^\infty d\gamma \int_{-\frac{4}{3}}^{\frac{2}{3}} dz \frac{g(\gamma,z)}{\gamma - q^2 - (p\cdot q)z - i\epsilon} = 2i \int_{4m^2}^\infty \frac{\rho(\gamma'')d\gamma''}{(\frac{2}{3}p - q)^2 - \gamma'' + i\epsilon}
$$

$$
\int \frac{d^4k}{(2\pi)^4} \frac{i}{(\frac{p}{3}+k)^2 - m^2 + i\epsilon} \frac{i}{(\frac{p}{3}-q-k)^2 - m^2 + i\epsilon}
$$

$$
\times \int_0^\infty d\gamma' \int_{-\frac{4}{3}}^{\frac{2}{3}} dz' \frac{g(\gamma',z')}{\gamma' - k^2 - (p\cdot k)z' - i\epsilon} =
$$

$$
2i \int_{4m^2}^\infty \frac{\rho(\gamma'')d\gamma''}{(\frac{2}{3}p - q)^2 - \gamma'' + i\epsilon} I(q,\gamma',z';p)g(\gamma',z').
$$

(4.34)

Following the steps detailed in Appendix G, one obtains the following integral equation

$$
g(\gamma,z) = -\frac{2}{(4\pi)^2(z+\frac{4}{3})^4} \int_{-\frac{4}{3}}^{\frac{2}{3}} dz' \left(\frac{2}{3} - z'\right)^2 \theta\left(\left(\frac{2}{3} - z'\right) - \left(z + \frac{4}{3}\right)\right)
$$

$$
\times \int_{4m^2}^\infty \rho(\gamma'')d\gamma'' \int_{\frac{z+\frac{4}{3}}{\frac{2}{3}-z'}}^1 \frac{d\alpha_1}{\alpha_1} \int_0^{\frac{z+\frac{4}{3}}{\frac{2}{3}-z'}} d\alpha_3 \left[\left(z+\frac{4}{3}\right) - \alpha_3\left(\frac{2}{3} - z'\right)\right]
$$

(4.35)

$$
\times \frac{\partial}{\partial\gamma_0}\left[g(\gamma_0(\gamma,z,z',\gamma''),z')\right]\theta(\gamma_0(\gamma,z,z',\gamma'')).
$$

with

$$
\gamma_0(\gamma,z,z',\gamma'') = \frac{p^2}{9} + m^2 - z'\frac{p^2}{3} - \frac{1}{4}\frac{\alpha_3}{\alpha_1}\left(\frac{2}{3} - z'\right)^2 p^2 - \frac{\alpha_1}{\alpha_3}m^2 + \frac{(\frac{2}{3} - z')}{(z+\frac{4}{3})^2}
$$

$$
\times \left[\left(z+\frac{4}{3}\right) - \alpha_3\left(\frac{2}{3} - z'\right)\right]\left[\gamma - (1-\alpha_1)\gamma'' - \frac{2}{3}p^2\left(\frac{2}{3} + z\right)\right],
$$

(4.36)

considering that the following identity was used

$$
\frac{\partial\gamma_0}{\partial\gamma} = \frac{\frac{2}{3} - z'}{(z+\frac{4}{3})^2}\left[\left(z+\frac{4}{3}\right) - \alpha_3\left(\frac{2}{3} - z'\right)\right].
$$

(4.37)

Equation (4.35) is expected to be suitable for numerical treatment.

The condition $\gamma_0 \geqslant 0$ leads to the following constrain on γ''

$$
\gamma'' \leqslant \gamma''_{\max} = \frac{[\gamma - \frac{2}{3}p^2(\frac{2}{3} + z)]}{1 - \alpha_1} + \frac{(z+\frac{4}{3})^2}{(\frac{2}{3} - z')(1-\alpha_1)[(z+\frac{4}{3}) - \alpha_3(\frac{2}{3} - z')]}
$$

$$
\times \left[\frac{p^2}{9} + m^2 - z'\frac{p^2}{3} - \frac{1}{4}\frac{\alpha_3}{\alpha_1}\left(\frac{2}{3} - z'\right)^2 p^2 - \frac{\alpha_1}{\alpha_3}m^2\right].
$$

(4.38)

It is possible to demonstrate that, if the different regions of γ, z plane are considered separately, the Wick-rotation $q_0 \longrightarrow \exp(i\theta)$, with $0 \leqslant \theta \leqslant \frac{\pi}{2}$, can be performed without crossing any singularities for the Nakanishi integral representation used in this derivation (4.33). This is an important fact as the comparison with the Euclidean results is intended to be performed, so that the forthcoming numerical results can be confirmed by previous calculations obtained in Euclidean space [45].

Solving numerically (4.36) and its Wick rotated version is the next step of this ongoing study.

It is worth remarking that the non-smooth behavior of the vertex function, $v(q_0, q)$, seen in Figs. 4.9, could be eventually traced back to the singularities brought by the integral representation proposed in Eq. (4.33). It would be of interest to clarify the relation between the complex cut structure and the branching points originated by Eq. (4.33) and the position of the peaks, which still needs to be investigated in the future. A formal aspect that requires further elaboration is the relation of the integral representation of the vertex function proposed in the section and the NIR of the full three-body BS amplitude of the model (E.3).

Chapter 5

Boson-fermion bound state

After dealing with two- and three-boson systems, it will now be considered a different physical system, enclosing new degrees of freedom. An interesting transition case, which is essentially a two-body system but can be used effectively to explore three-body ones is the one composed by a boson bounded to a fermion. In QCD it is often the case where quark-diquark approaches are developed to deal with baryons [102]. Moreover, considering the bound state systems studied so far in this thesis, that kind of approach brings a new element for the theory framework, as it calls for the necessity to handle an unbalanced mass systems having non-zero spin.

Following the outlook sketched above, this chapter presents the solution of the Bethe-Salpeter equation, for a bound system composed by a fermion and a scalar boson, exchanging a boson that can be either a scalar or vector particle. The fermion-scalar system is built with positive parity, having quantum numbers given as $J^\pi = (1/2)^+$. The equation is solved in Minkowski space through the same procedure as the one used for two-boson systems, i.e. by representing the BS amplitude with the NIR and, subsequently, projecting the BSE onto the LF plane (the method is presented in Sec. 3.1). For the sake of completeness, the equation is also solved in Euclidean space, by means of the Wick-rotation (see Sec. 4.1), so the results can be confirmed by comparing calculations within two independent methods. Vertex corrections and dressing effects are not yet included in this first exploration of the model. The main goal is to extend the BS approach to include a new degree of freedom, the spin, and generalize the framework to include different constituent masses.

Two interaction kernels are considered, namely, a scalar and a vector boson exchange, both in the ladder approximation. With the vector exchange kernel the final equation happens to be scale invariant, enabling intriguing explorations in close analogy with the mathematical origin of the Efimov phenomena, where the conformal invariance is lost [146]. After presenting the integral equation and its solution in Sec. 5.1, the scale invariant regime will be investigated in some detail in Sec. 5.2, in what is an ongoing research. The formal details of the derivation of the non-singular integral equations for the Nakanishi weight functions leading to the BS amplitudes in Minkowski space, its associated valence probabilities and light-front momentum distributions, as well as the numerical results for these solutions, are presented in Refs. [48, 116].

Further analysis of the system within the scale invariance perspective, presented in Sec. 5.2, is foreseen to be organized in a publication in the due course. Moreover, encompassing features to make the framework more realistic, e.g. dressing effects and more complex structures in the interaction kernel, and applying it to hadron physics is a great challenge that must be faced. Although simple, this model can offer a first approach to represent baryons, as e.g. mock protons, involved in B^+ meson decays which contains significant amount of CP violation. Some examples of these decays can be found in [1].

5.1   Boson-fermion BSE

The physical systems subject of the study here are represented by the following simple interacting Lagrangians

$$
\begin{aligned}
\mathcal{L}^s =&\lambda_F^s \bar{\psi}\psi\chi + \lambda_S^s \phi^*\phi\chi \\
\text{and} \quad \mathcal{L}^v =&\lambda_F^v \bar{\psi}V\!\!\!/\psi - i\lambda_S^v \phi^* \overleftrightarrow{\partial}_\mu \phi V^\mu,
\end{aligned}
\tag{5.1}
$$

where $\mathcal{L}^s$ describes the fermion (ψ)-boson (ϕ) system interacting through the exchange of a scalar χ field, while $\mathcal{L}^v$ comprises the vector boson field V^μ. The interacting Lagrangian in the second line of Eq. (5.1) has only dimensionless coupling constants and, therefore, the bound state BSEs are scale invariant in the ultraviolet region, as it will be discussed. This is a quite simple model for describing a mock baryon, as more realistic descriptions, e.g. for the nucleon, would include quark and gluon exchanges consistent with the underlying gauge theory in the interaction kernel [102].

The homogeneous BSE of the aforementioned system can be written, analogously to Eq.(3.1), as follows [48, 116]

$$
\Phi(k,p) = G_0(p/2 - k)S(p/2 + k)\int \frac{d^4k'}{(2\pi)^4}\, i\mathcal{K}^{Ld}(k,k',p)\, \Phi(k',p),
\tag{5.2}
$$

but now with two different propagators, one for the scalar boson G_0, given by (3.4), and the second one for the fermion, explicitly given by

$$
S(q) = i\, \frac{q\!\!\!/ + m_F}{[q^2 - m_F^2 + i\epsilon]}.
\tag{5.3}
$$

As the system under scrutiny in this chapter has non-identical particles, the scalar boson mass will be notated here as m_S instead of m, used in Eq. (3.4). For the interaction kernel $\mathcal{K}^{Ld}$ it is considered the one boson (scalar or vector) exchange truncated at the first ladder diagram, reading as

$$
i\mathcal{K}_s^{Ld}(k,k',p) = -i\,\lambda_S^s\lambda_F^s\,\frac{1}{(k-k')^2 - \mu^2 + i\epsilon}
\tag{5.4}
$$

for the scalar and

$$
i\mathcal{K}_v^{Ld}(k,k',p) = -i\,\lambda_S^v\lambda_F^v\,\frac{(p\!\!\!/ - k\!\!\!/ - k\!\!\!/')}{(k-k')^2 - \mu^2 + i\epsilon}
\tag{5.5}
$$

for the vector boson exchange in the Feynman gauge. In both equations μ represents the exchanged boson mass. The BS amplitude is normalized for both cases and the normalization procedure is described in the Appendix C of Ref. [48].

For solving Eq. (5.2) in Minkowski space it will be adopted the NIR, subsequently projecting the resulting set of integral equations onto the LF, as done for the two-boson case in Sec. 3.1.1. The equation will also be solved in Euclidean space, by simply performing the Wick-rotation, what is enough to ensure a non-singular kernel. Obtaining the solutions through two independent methods allows one to check the reliability of the numerical outcomes. Before the integral equations are built, the BS amplitude needs to be decomposed in terms of its Dirac structures. After imposing the relevant properties for a $1/2^+$ system [48, 116], the BS amplitude can be written as follows

$$\Phi(k,p) = \Big[O_1(k) \ \phi_1(k,p) + O_2(k) \ \phi_2(k,p) \Big] \ U(p,s), \tag{5.6}$$

where the functions ϕ_i are scalar, that can be suitably represented through the NIR, and $U(p,s)$ is the spinor of the whole system with squared mass $M^2 = p^2$, normalized according to $\bar{U}U = \mathbb{1}$. Eq. (5.6) is obtained from the most general decomposition (which includes all the Dirac structures, including the tensor component) by introducing the Dirac equation, $(\not{p} - M)U(p,s) = 0$, and then further exploring the properties following from the discrete symmetries of the BS amplitude[1]. The remaining Dirac structure of the terms are given by the operators $O_1(k) = \mathbb{1}$ and $O_2(k) = \frac{\not{k}}{M}$.

After expanding the BS amplitude through Eq. (5.6), the BSE (5.2) can be written as a set of coupled integral equations for ϕ_1 and ϕ_2, as follows

$$\begin{aligned}
\phi_i^{s(v)}(k,p) = & \frac{i}{(p/2-k)^2 - m_S^2 + i\epsilon} \ \frac{i}{(p/2+k)^2 - m_F^2 + i\epsilon} \int \frac{d^4k'}{(2\pi)^4} \\
& \times \frac{(-i\lambda_S^{s(v)}\lambda_F^{s(v)})}{(k-k')^2 - \mu^2 + i\epsilon} \ \sum_{j=1,2} \mathcal{C}_{ij}^{s(v)}(k,k',p) \ \phi_j^{s(v)}(k',p),
\end{aligned} \tag{5.7}$$

where the coefficients for the scalar exchange (5.4) are given by Eq. (H.1) and for the vector exchange (5.5) by Eq. (H.2), both presented in Appendix H.1 (in the center of mass frame, defined by $\vec{p} = 0$).

The Wick-rotated equation can be obtained by imposing the following relations: $k_E^2 = -(k_4^2 + k^2)$, $p \cdot k_E = iMk_4$, $p \cdot k'_E = iMk'_4$, $k_E \cdot k'_E = -(k_4k'_4 + \vec{k} \cdot \vec{k'})$ and $k_E'^2 = -(k_4'^2 + k'^2)$. The equation for the scalar exchange is derived in the Appendix C.4 of Ref. [116], while for the vector exchange the procedure is described in Appendix H.2.

In Minkowski space the procedure is the same as the one used for the bosonic system of Sec. 3.1.1, i.e. the first step is to introduce the NIR[2] (3.5) in Eq. (5.7) to represent the scalar amplitudes, ϕ_1 and ϕ_2. After that the whole set of integral equations can be integrated over k^-, similarly to what was done for the two-fermion system in Ref. [51]. The procedure is quite straightforward and the resulting equation

---

[1] A detailed examination of the BS equation for the $J^\pi = (1/2)^+$ system is presented in Ref. [116].

[2] Notice that now the system has two particles with different masses and the variable κ is defined as $\kappa = \bar{m}^2 - M^2/4$, where $\bar{m} = (m_F + m_S)/2$.

reads [48]

$$\int_{\gamma_{min}}^{\infty} d\gamma' \frac{g_i(\gamma', z; \kappa^2)}{[\gamma' + \gamma + (1-z^2)\kappa^2 + z^2\bar{m}^2 - i\epsilon]^2} = \frac{\lambda_F \, \lambda_S}{2(4\pi)^2} \frac{1}{\gamma + (1-z^2)\kappa^2 + (\Delta - z\bar{m})^2}$$

$$\times \int_0^1 dv \, v^2 \int_{\gamma_{min}}^{\infty} d\gamma' \int_{-1}^{1} dz' \sum_{j=1,2} g_j(\gamma', z'; \kappa^2)$$

$$\times \left[\frac{(1+z)^2 \, B_{ij}(k_u^-)\theta(z'-z)}{D_u^2(z', z, m_S^2)} + \frac{(1-z)^2 \, B_{ij}(k_d^-)\theta(z-z')}{D_d^2(z', z, m_F^2)} \right],$$

$$(5.8)$$

where the support of the Nakanishi weight function is now defined as [48, 116]

$$\gamma_{min} = -2z\bar{m}|\Delta| + \Delta^2,$$

with $\Delta = (m_S - m_F)/2$. The support is found by imposing that the BS amplitude integrated over k^-, i.e. the LFWF, should not present poles/cuts as it must be for a bound system. Notice that $\gamma_{min} = 0$ for the equal mass case, as it was for the two-boson system. Moreover, the denominator D_u reads

$$D_u(z', z, m_S^2) = v(1-v) \, (z'-z) \left[\gamma - (1-z^2)\frac{M^2}{4} + m_S^2 \right]$$

$$+ (1+z) \left[v(1-v)\left(\gamma + z^2\frac{M^2}{4}\right) + v(\gamma' + \kappa^2) + v^2 z'^2\frac{M^2}{4} + (1-v)\mu^2 \right],$$

$$(5.9)$$

For the second term of the third line in Eq. (5.8) the denominator is given by $D_d(z', z, m_F^2) = D_u(-z', -z, m_F^2)$. The factor $(1+z)^2$ present in the denominators does not represent a problem while solving the equation, as in the limiting case where $z' \to z$ it cancels out with the factor in the numerator.

The coefficients of Eq.(5.8) can be defined, for both interaction kernels, through

$$\begin{aligned} B_{11}(k_{u(d)}^-) &= c_{11}^{(0)} + c_{11}^{(1)} k_{u(d)}^- \, , & B_{12}(k_{u(d)}^-) &= c_{12}^{(0)} + c_{12}^{(1)} k_{u(d)}^- \\ B_{21}(k_{u(d)}^-) &= c_{21}^{(0)} \, , & B_{22}(k_{u(d)}^-) &= c_{22}^{(0)} + c_{22}^{(1)} k_{u(d)}^- \end{aligned} \, , \qquad (5.10)$$

where

$$k_u^- = \frac{M}{2} - \frac{2 \, (\gamma + m_S^2)}{M(1+z)} \quad \text{and} \quad k_d^- = -\frac{M}{2} + \frac{2 \, (\gamma + m_F^2)}{M(1-z)}. \qquad (5.11)$$

The explicit formulas for $c_{ij}^{(0)}$ and $c_{ij}^{(1)}$ are given in Appendix H.1.1.

5.1.1 Numerical outcomes

For solving the Wick-rotated BSE the BS amplitudes are expanded in terms of splines (see Appendix D). The equation is then solved as a eigenvalue problem. In Minkowski space the amplitudes are expanded in terms of an orthonormal basis composed by the product of Laguerre (γ-dependence) and Gegenbauer (z-dependence) polynomials, as done for the bosonic system. The numerical methods applied for a fermion-antifermion system are presented in Appendix I.2. Nevertheless, in contrast to that case the boson-fermion bound state does not present the symmetry under the

Table 5.1. The coupling constant for the scalar exchange case for different values of the binding energy ($B/\bar{m}$). Two masses are considered for the exchanged boson, namely $\mu/\bar{m} = 0.15,\ 0.50$. Constituent particles are considered with equal masses, $m_F = m_S$. The comparison between the Wick-rotated (α^S_{WR}) and the Minkowskian (α^S_M) BS equations is shown.

$B/\bar{m}$	$\alpha^S_M(0.15)$	$\alpha^S_{WR}(0.15)$	$\alpha^S_M(0.50)$	$\alpha^S_{WR}(0.50)$
0.10	1.506	1.506	2.656	2.656
0.20	2.297	2.297	3.624	3.624
0.30	3.047	3.047	4.535	4.535
0.40	3.796	3.796	5.451	5.451
0.50	4.568	4.568	6.404	6.404
0.80	7.239	7.239	9.879	9.879
1.00	9.778	9.778	13.738	13.738

exchange $z \to -z$, equivalent to exchanging the two constituent particles. Thus, both symmetric and antisymmetric Gegenbauer polynomials need to be included in the basis to represent the BS amplitude properly. More details and the specific parameters used in the solution of Eqs. (5.8) can be found in Ref. [48].

As discussed previously for the two- and three-boson cases, the equation is solved as an eigenvalue problem from where the outcomes, after assigning a binding energy, are the coupling constant and the Nakanishi weight functions $g_i(\gamma', z; \kappa^2)$. For the equation with the scalar exchange the coupling constant has a dimensional dependence on the mass, i.e. $\alpha^S = \lambda^s_F\,\lambda^s_S/8\pi m_S$. Meanwhile, the dimensionless coupling constant for the vector case is defined as $\alpha^V = \lambda^v_F\,\lambda^v_S/8\pi$. These definitions are convenient to match the non-relativistic limit to the Born term of the fermion-scalar scattering.

The results for the coupling constant in the scalar exchange case are presented in Table 5.1. Two values are considered for the exchanged boson mass, $\mu/\bar{m} = 0.15$ and 0.5. Moreover, it is considered the equal-mass case, $m_F = m_S$, for several binding energies between $B/\bar{m} = 0.1$ and $B/\bar{m} = 1.0$. The results are obtained through the solution of the Wick-rotated BSE (α^S_{WR}), as well as the ones obtained from Eq. (5.8), in Minkowski space (α^S_M). These are two completely independent methods of solving the BSE (5.7) and the coincidence between the results from the different approaches confirms the reliability of the numerical outcomes. For strongly bound systems, namely beyond $B/\bar{m} \approx 1.2$ for $m_F = m_S$, the numerical results become very unstable and, most likely, the numerical methods have to be further developed to deal with these extreme situations. This problem needs to be better understood through a deeper analysis of the interaction kernel for this system, which present particles with different nature. Further exploration, both analytically and numerically, should be done in the future to clarify the situation.

Furthermore, the Nakanishi weight functions evaluated with the Minkowskian BSE are shown in Fig. 5.1. These quantities do not bring much of the physical features, but are essential since from them any other dynamical observable can be computed. Interesting to point out that the Nakanishi weight functions can have
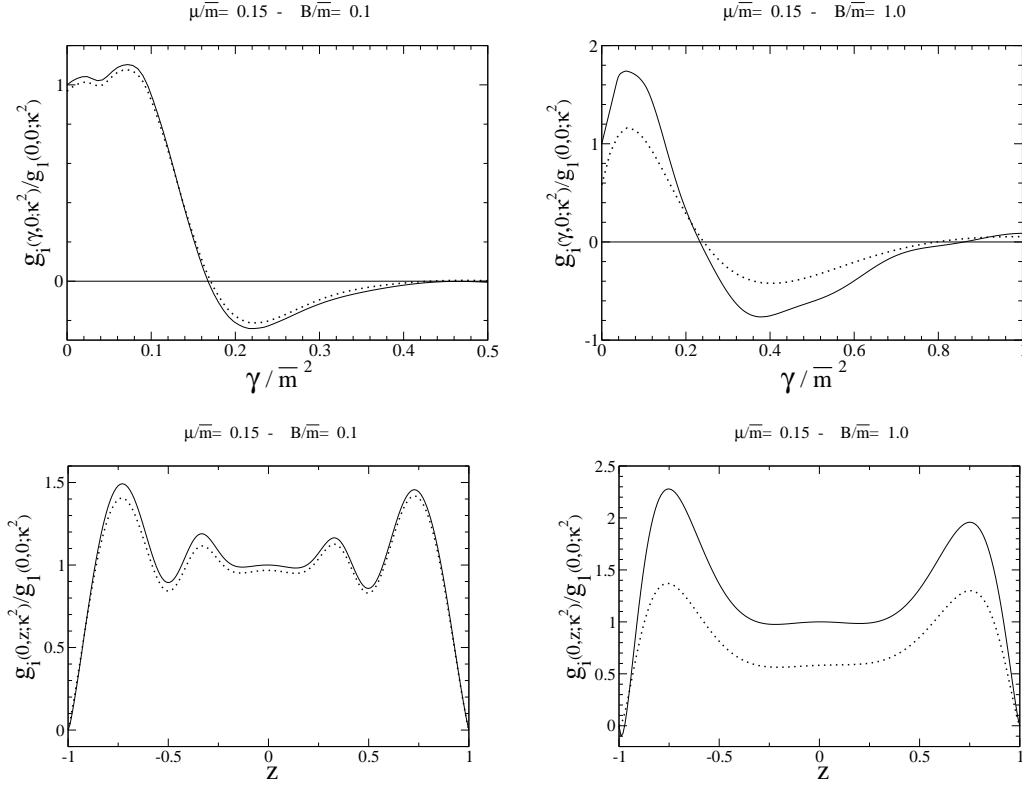
Figure 5.1. Nakanishi weight functions g_1 (solid line) and g_2 (dotted line) as a function of γ, for fixed $z = 0$ (upper panels) and as a function of z, for fixed $\gamma = 0$ (lower panels). It is considered an equal-mass $(1/2)^+$ system, with the scalar exchanged boson mass of $\mu/\bar{m} = 0.15$. On the left side $B/\bar{m} = 0.1$, while on the right one $B/\bar{m} = 1$.

a strongly oscillatory behavior depending on the considered input parameters, but observables obtained from them, e.g. the LFWF, will still have a smooth behavior.

In Fig. 5.1, the considered scalar exchange mass is $\mu/\bar{m} = 0.15$, while the equal-mass case $m_S = m_F$ is again considered. The panels on the left side present the calculations for $B/\bar{m} = 0.1$ and the ones on the right side for $B/\bar{m} = 1.0$. Upper panels present the dependence on γ, for $z = 0$ fixed, while the lower ones show the dependence on z, for $\gamma = 0$ fixed. The normalization factor is adopted to be $g_1(0, 0; \kappa^2) = 1$ for both g_1 and g_2. One interesting feature is that for weakly bounded states the eigenvectors g_1 and g_2 are practically the same, while when the system becomes more relativistic the Nakanishi weight functions start to differ more and more. One simple way of seeing the source of this difference is through the chosen decomposition of the BS amplitude, presented in Eq. (5.6). The Dirac structure multiplying ϕ_2 depends on the mass, i.e. $\not{k}/M$, therefore the amplitude ϕ_2 should decrease when the size of the system decreases and it becomes more relativistic, so that its contribution in Eq. (5.6) does not increase indiscriminately when $M \to 0$.

For the vector exchange, the results for the coupling constant are shown in Table 5.2, for several binding energies up to $B/\bar{m} = 0.5$. Once again the results in Minkowski space (5.8) agree with the Wick-rotated calculations (see Appendix H).

Table 5.2. The coupling constant for the vector exchange for different values of the binding energy ($B/\bar{m}$). Two masses are considered for the exchanged boson, namely $\mu/\bar{m} = 0.15$, 0.50. Constituent particles are considered with equal-masses, $m_F = m_S$. The comparison between the Wick-rotated (α_{WR}^S) and the Minkowskian (α_M^S) BS equations is shown.

$B/\bar{m}$	$\alpha_M^V(0)$	$\alpha_{WR}^V(0)$	$\alpha_M^V(0.15)$	$\alpha_{WR}^V(0.15)$	$\alpha_M^V(0.50)$	$\alpha_{WR}^V(0.50)$
0.10	0.513	0.513	0.608	0.609	0.849	0.854
0.20	0.758	0.761	0.823	0.823	1.009	1.015
0.30	0.936	0.938	0.979	0.978	1.127	1.129
0.40	1.074	1.074	1.107	1.097	1.225	1.216
0.50	1.189	$1.18 \pm .03$	1.214	$1.19 \pm .03$	1.311	$1.28 \pm .04$

As discussed in Sec. 5.1, the integral equation for the $(1/2)^+$ fermion-boson system interacting through a vector boson is scale invariant in the ultraviolet region, what in practice reflects into a maximum value for the coupling constant and beyond that the solution is not stable anymore and requires the introduction of an ultraviolet regulator (see e.g. [49, 107] for the procedure in the two-fermion system). This discussion is very interesting and rich and will be developed in more detail in Sec. 5.2. Noteworthy that, as is the case in the two-fermion bound state [51], the values of the coupling constant are larger for the scalar exchange than the dimensionless ones shown in Table 5.2. In the table, a numerical uncertainty is included for $B/\bar{m} = 0.5$, due to some instabilities when getting close to the limiting case imposed by the breaking of the scale invariance.

Two other quantities, intrinsically defined in Minkowski space and significant for understanding its dynamics, are the valence LF valence distributions. They describe the probability distributions of finding one of the constituent particles with a given longitudinal momentum fraction ξ, denoted by $\phi^F(\xi)$, or of finding it with a transverse momentum $\gamma = |\mathbf{k}_\perp|^2$, namely $\mathcal{P}^F(\gamma)$. For the fermionic constituent they read, respectively,

$$\phi^F(\xi) = \frac{1}{32M\pi^2} \ (1-\xi) \int_0^\infty d\gamma \ \left[\left(\tilde{\phi}_1(\xi,\gamma;\kappa^2) - \frac{z}{2}\tilde{\phi}_2(\xi,\gamma;\kappa^2) \right)^2 + \frac{\gamma}{M^2} \ \tilde{\phi}_2^2(\xi,\gamma;\kappa^2) \right]$$

(5.12)

and

$$\mathcal{P}^F(\gamma) = \frac{1}{32M\pi^2} \ \int_0^1 d\xi \ (1-\xi) \ \left[\left(\tilde{\phi}_1(\xi,\gamma;\kappa^2) - \frac{z}{2}\tilde{\phi}_2(\xi,\gamma;\kappa^2) \right)^2 + \frac{\gamma}{M^2} \ \tilde{\phi}_2^2(\xi,\gamma;\kappa^2) \right].$$

(5.13)

Both Eqs. (5.12) and (5.13) are normalized to the valence probability P_{val}, which can be found in Ref. [48]. The two squared terms in brackets in Eqs. (5.12) and (5.13), i.e.

$$\left(\tilde{\phi}_1(\xi,\gamma;\kappa^2) - \frac{z}{2}\tilde{\phi}_2(\xi,\gamma;\kappa^2) \right)^2 \quad \text{and} \quad \frac{\gamma}{M^2} \ \tilde{\phi}_2^2(\xi,\gamma;\kappa^2)$$

are, respectively, the aligned and the anti-aligned contributions, related to the two possible spin configurations of the system. The functions $\tilde{\phi}_i$ are the components of

the LFWF, defined as

$$\tilde{\phi}_i(\xi, \gamma; \kappa^2) = iM \int_{-\infty}^{\infty} \frac{dk^-}{2\pi} \phi_i(k, p) = \int_{-\infty}^{\infty} d\gamma' \frac{g_i(\gamma', z; \kappa^2)}{[\gamma' + \gamma + (1 - z^2)\kappa^2 + z^2\bar{m}^2 - i\epsilon]^2} \ ,$$

$$(5.14)$$

where $\xi = q_1^+/p^+ = k^+/p^+ + 1/2 = (1 - z)/2$. It is important to bear in mind that the BS amplitude is properly normalized through its covariant normalization condition for computing the LF distributions. The normalization procedure is described in Ref. [48].
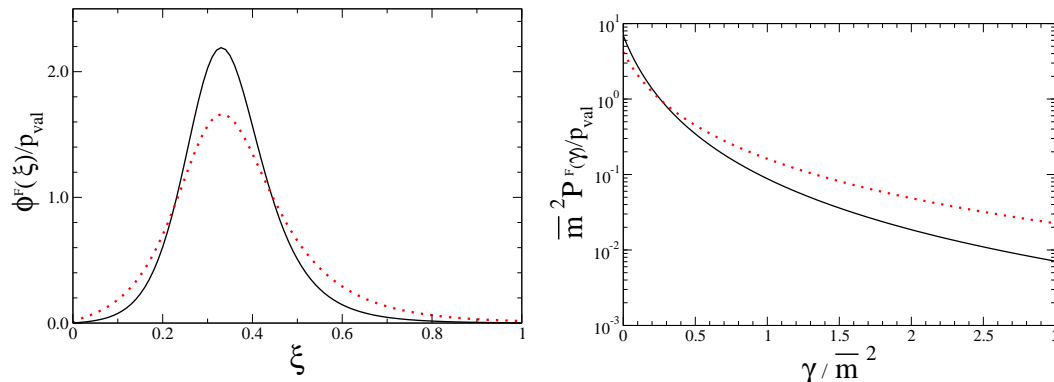
The LF longitudinal and transverse distributions, given by Eqs. (5.12) and (5.13), are displayed, respectively, on the left and right panels of Fig. 5.2. In an attempt of presenting a first investigation towards the description of a mock nucleon, the results were computed for an unbalanced mass with ratio $m_S/m_F = 2$. Two values of the exchanged vector boson mass are considered, namely $\mu/\bar{m} = 0.15$ and $\mu/\bar{m} = 0.50$, while the binding energy is fixed at $B/\bar{m} = 0.1$. For the sake of completeness, the coupling constants associated with the exhibited results are $\alpha^V = 0.648$ ($\mu/\bar{m} = 0.15$) and $\alpha^V = 0.898$ ($\mu/\bar{m} = 0.5$), while the valence probabilities are $P_{val} = 0.75$ ($\mu/\bar{m} = 0.15$) and $P_{val} = 0.77$ ($\mu/\bar{m} = 0.5$). This means that about 25% of the dynamical content is beyond the valence, which is a notable amount considering that the binding energy for the case under scrutiny is quite low. This is in accordance with the results presented for two-bosons in Chap. 3 and in Ref. [39], meaning that valence models for highly relativistic systems, extensively used in the literature, might have a large associated error due to the lack of the dynamics beyond the valence. The fact that the valence distribution $\phi(\xi)$, on the left panel of Fig. 5.2, is not centered around $\xi = 1/2$ but at $\xi = 1/3$ it is a straightforward consequence of the mass asymmetry in this case. It is worth to reinforce that these results could be different for a more realistic approach, that includes, e.g., vertex and self-energy corrections. However, the general shape, before properly applying the evolution to the result at the initial scale, should be the same.

A deep analysis on the LF-momentum distributions of the $(1/2)^+$ model can be found in Ref. [48]. Therein are also presented the valence probabilities and an extensive physical interpretation of the features seen in the results.

The next step is to analyze in detail the asymptotic behavior of the transverse momentum distribution. As it will be seen in the next section, the fall-off of the result obtained from the numerical solution of Eq. (5.7) for the vector exchange coincides with the one predicted by the analytical analysis of the ultraviolet form of the integral equations in the scale invariant regime. The current toy model, although didactic, is quite simple and is lacking more realistic propagators and interaction kernel. Naturally, if considered within QCD theory, the features brought by scale invariance would be deeply changed as the theory has its own intrinsic scale. Therefore, the discussion presented below is limited to the model discussed in this chapter.

5.2   Scale invariance in the fermion-boson system

As discussed before, the coupling constant for fermion-boson system with the vector exchange, $\alpha^V = \lambda_F^v \lambda_S^v/(8\pi)$, is dimensionless, feature that follows from the nature

Figure 5.2. The longitudinal (left panel) and transverse (right panel) light-front distributions of the fermion in the valence component of the state $(1/2)^+$. The considered mass ratio is $m_S/m_F = 2$, while the binding energy is fixed at $B/\bar{m} = 0.1$. Solid lines present results for $\mu/\bar{m} = 0.15$ and dotted ones for $\mu/\bar{m} = 0.50$.

of the interaction Lagrangian (5.1). Therefore, the BSE (5.7) is invariant under a scale transformation in the ultraviolet region, what brings consequences to be studied in the following. The main feature, seen in the results presented in Sec. 5.1.1, is the appearance of an upper-bound for the value of the coupling constant, for given input parameters. As illustrated in Table 5.2, above a certain value of the coupling constant, which varies depending on the fixed values for $B/\bar{m}$ and $\mu/\bar{m}$, the convergence of the numerical solution becomes very challenging. A similar situation occurs in the fermion-fermion bound state, both in Euclidean [107] and in Minkowski spaces [49, 147]. Overcoming this effect passes through the inclusion of a new scale in the integral equation. That can be done, e.g., by means of a form factor at the vertex interaction [49, 51].

It is well-known in quantum mechanics that when the scale invariance is broken it can bring interesting physical phenomena, manifested both in the spectrum and wave function of the corresponding system. For instance, the most classical example, the three-boson bound state with zero-range interaction is not bounded from below, meaning that the three-body system collapses and no finite three-body binding energy can be found as a solution. This was discussed for the relativistic case in Chap. 4. This phenomenon is known as the Thomas collapse [141], and it is closely related to the prominent Efimov phenomena [143], already largely explored in non-relativistic quantum mechanics [142].

As shown in Chap. 4 and in Refs. [45, 138, 139], the relativistic counterpart of the Efimov phenomena present remarkable differences and further study of the features brought by scale invariance are very promising. Therefore, this section is dedicated to explore the fermion-boson equation at high momentum, a regime where all the scales can be disregarded. As it will be seen, properties of the original BSE (5.7) can be predicted in the asymptotic regime. For instance, it can be proven that there is a critical value of the coupling constant and below that the solutions are stable, having a power-law form in the ultraviolet region. An overall view of

this *in progress* study is shown hereinafter. The content of this section is based on Refs. [148, 149].

5.2.1   High momentum limit

The starting point for the present analysis is the BS amplitude as presented in Eq. (5.6). The component ϕ_2 should go to zero for $M \to 0$, in order to keep the BS amplitude finite. To examine if the ratio ϕ_2/M can be finite, one can check the self-consistency of this assumption in the set of coupled integral equations for ϕ_1 and ϕ_2, given by (5.7).

Suppose that one solves the integral equation for ϕ_1 in the limit when $M \to 0$ and $M << m_\psi$. In this case one can assume that $\phi_2/M \to 0$ and solve the uncoupled equation for ϕ_1. The solution for ϕ_1 could be inserted back in the equation for ϕ_2 and, due to the coupling coefficients $c_{21}^{(0),(1)} \propto M$ (see Appendix H.2 for the coefficients of the vector exchange), the inhomogeneous linear equation for ϕ_2 could be solved. The conclusion would be that ϕ_2 is indeed proportional to M and, therefore, the ratio ϕ_2/M is finite. On the other side, such behavior of ϕ_2/M produces a finite contribution to the integral equation for ϕ_1, considering the coupling coefficient $c_{12}^{(0),(1)} \propto 1/M$ for $M \to 0$. This means that $c_{12}^{(0),(1)}\phi_2$ would be finite, which does not support the initial guess of disregarding ϕ_2 to solve the uncoupled equation for ϕ_1. To avoid this contradiction, the coupled equations for ϕ_1 and ϕ_2/M should be solved simultaneously in the limit of $M \to 0$.

Therefore, one has to solve the coupled set of integral equations for ϕ_1 and ϕ_2/M to check whether one of the components vanishes or not. This can be done either in Euclidean or Minkowski space, with the goal of understanding whether the equations remain coupled in the asymptotic regime. Furthermore, the behavior of the coupling constant can be also obtained regardless if the Wick-rotation is adopted.

For the sake of simplicity, the Wick-rotated BSE can be considered first. After performing the limit where $k, k_4 >> \mu, m_\psi, m_\phi, M$ in Eq. (H.10) of the Appendix H, one gets

$$c_{11}^{(0)} \to -k^2 - k_4^2, \quad c_{11}^{(1)} \to -\frac{k^2 + k_4^2}{k^2}, \quad c_{12}^{(0)} \to -i\frac{k_4'}{M}(k^2 + k_4^2),$$

$$c_{12}^{(1)} \to i\frac{k_4}{M}\left(1 + \frac{k_4^2}{k^2}\right), \quad c_{21}^{(0)} \to iMk_4', \quad c_{21}^{(1)} \to -i\frac{M}{k^2}k_4,$$

$$c_{22}^{(0)} \to -k_4'^2 - k'^2, \quad c_{22}^{(1)} \to -\frac{k^2 + k_4^2}{k^2}. \tag{5.15}$$

After the integration on the angular part and in the limit where all the momenta are much larger than the masses, the set of coupled integral equations for the components

of the BSE reads

$$
\phi_1(k_4, k) = -\frac{\alpha}{(2\pi)^2} \int dk_4' dk' \left\{ \frac{b\left(\bar{c}_{11}^{(0)} + \frac{a}{2}\bar{c}_{11}^{(1)}\right) \ln\frac{a+b}{a-b} - b^2 \bar{c}_{11}^{(1)}}{k^2 \left[k^2 + k_4^2\right]^2} \phi_1(k_4', k') \right.
$$
$$
\left. + \frac{b\left(\bar{c}_{12}^{(0)} + \frac{a}{2}\bar{c}_{12}^{(1)}\right) \ln\frac{a+b}{a-b} - b^2 M \bar{c}_{12}^{(1)}}{k^2 \left[k^2 + k_4^2\right]^2} \phi_2(k_4', k') \right\},
$$
$$
\phi_2(k_4, k) = -\frac{\alpha}{(2\pi)^2} \int dk_4' dk' \left\{ \frac{b\left(\bar{c}_{22}^{(0)} + \frac{a}{2}\bar{c}_{22}^{(1)}\right) \ln\frac{a+b}{a-b} - b^2 \bar{c}_{22}^{(1)}}{k^2 \left[k^2 + k_4^2\right]^2} \phi_2(k_4', k') \right.
$$
$$
\left. + \frac{b\left(\bar{c}_{21}^{(0)} + \frac{a}{2}\bar{c}_{21}^{(1)}\right) \ln\frac{a+b}{a-b} - b^2 \bar{c}_{21}^{(1)}}{k^2 \left[k^2 + k_4^2\right]^2} \phi_1(k_4', k') \right\}, \tag{5.16}
$$

where a factor of M in the coefficients was absorbed into the first component of the amplitude, i.e. $M\phi_1(k_4, k) \to \phi_1(k_4, k)$. The auxiliary functions a and b in Eq. (5.16) are, in the limit, given by

$$
a = (k_4 - k_4')^2 + \vec{k}^2 + \vec{k}'^2 \quad \text{and} \quad b = 2\,|\vec{k}||\vec{k}'|. \tag{5.17}
$$

The new coefficients are therefore independent of the masses

$$
\bar{c}_{11}^{(0)} = -k^2 - k_4^2, \quad \bar{c}_{11}^{(1)} = -\frac{k^2 + k_4^2}{k^2}, \quad \bar{c}_{12}^{(0)} = -ik_4'(k^2 + k_4^2),
$$
$$
\bar{c}_{12}^{(1)} = ik_4\left(1 + \frac{k_4^2}{k^2}\right), \quad \bar{c}_{21}^{(0)} = ik_4', \quad \bar{c}_{21}^{(1)} = -i\frac{k_4}{k^2},
$$
$$
\bar{c}_{22}^{(0)} = -k_4'^2 - k'^2, \quad \bar{c}_{22}^{(1)} = -\frac{k^2 + k_4^2}{k^2}. \tag{5.18}
$$

Now one can introduce the following change of variables (analogous for k' and k_4')

$$
k_4 = K\cos\varphi \quad \text{and} \quad k = K\sin\varphi \tag{5.19}
$$

with $0 < \varphi < \pi$. Eq. (5.17) then becomes

$$
a = K^2 + K'^2 - 2K\,K'\cos\varphi\cos\varphi' \quad \text{and} \quad b = 2K\,K'\sin\varphi\sin\varphi'. \tag{5.20}
$$

and for the coefficients the change of variables gives

$$
\bar{c}_{11}^{(0)} = -k^2 - k_4^2 = -K^2, \qquad \bar{c}_{11}^{(1)} = -\frac{k^2 + k_4^2}{k^2} = -\csc^2\varphi,
$$
$$
\bar{c}_{12}^{(0)} = -ik_4'(k^2 + k_4^2) = -iK^2 K'\cos\varphi', \qquad \bar{c}_{12}^{(1)} = ik_4\left(1 + \frac{k_4^2}{k^2}\right) = i\,K\cos\varphi\csc^2\varphi,
$$
$$
\bar{c}_{21}^{(0)} = ik_4' = iK'\cos\varphi', \qquad \bar{c}_{21}^{(1)} = -i\frac{k_4}{k^2} = -\frac{i}{K}\cos\varphi\csc^2\varphi,
$$
$$
\bar{c}_{22}^{(0)} = -k_4'^2 - k'^2 = -K'^2, \qquad \bar{c}_{22}^{(1)} = -1 - \frac{k_4^2}{k^2} = -\frac{1}{\sin^2\varphi} = -\csc^2\varphi.
$$
$$
\tag{5.21}
$$

Considering that the first goal is to find the condition for having real solutions for the coupling constant according to the fall-off in K. For that purpose, one can search for solutions with following asymptotic behavior

$$\phi_1(k_4, k) = K^{\eta+1}\frac{F_1(\varphi)}{\sin^2\varphi} \quad \text{and} \quad \phi_2(k_4, k) = K^{\eta}\frac{F_2(\varphi)}{\sin^2\varphi}. \tag{5.22}$$

After the manipulations detailed in the Appendix H.3, one gets

$$F_1(\varphi) = -\frac{\alpha}{(2\pi)^2}\int_0^\infty dy\, y^{\eta+3}\int_0^\pi \frac{d\varphi'}{\sin\varphi'}$$

$$\times \left\{ \left[-\sin\varphi\left(2 + \left(1 + y^2 - 2y\cos\varphi\cos\varphi'\right)\csc^2\varphi\right)L + 4y\sin\varphi'\right]F_1(\varphi')\right.$$

$$\left. + \left[\csc\varphi\left((1+y^2)\cos\varphi - 2y\cos\varphi'\right)\frac{L}{y} - 4\cos\varphi\sin\varphi'\right]F_2(\varphi')\right\}$$

$$F_2(\varphi) = -\frac{\alpha}{(2\pi)^2}\int_0^\infty dy\, y^{\eta+3}\int_0^\pi \frac{d\varphi'}{\sin\varphi'}$$

$$\times \left\{ \left[-\sin\varphi\left(2y^2 + (1 + y^2 - 2y\cos\varphi\cos\varphi')\csc^2\varphi\right)\frac{L}{y} + 4\sin\varphi'\right]F_2(\varphi')\right.$$

$$\left. + \left[\csc\varphi\left((1+y^2)\cos\varphi - 2y\cos\varphi'\right)L - 4y\cos\varphi\sin\varphi'\right]F_1(\varphi')\right\}, \tag{5.23}$$

where it was considered the change of variables $K' \to K\,y$, as shown in Appendix H.3, and L represents the following logarithmic function

$$L = \ln\frac{a+b}{a-b} = \ln\frac{1 + y^2 - 2y\cos(\varphi+\varphi')}{1 + y^2 - 2y\cos(\varphi-\varphi')}. \tag{5.24}$$

The first step is to analyze the support of $\Re[\eta]$, which defines the region where the integrals in (5.23) are not singular (having in mind the limits $y \to 0$ and $y \to \infty$ of the integrand) and one gets actual solutions. For this purpose, one needs to study the behavior of both the non-diagonal term in the first equation and the diagonal term in the second one, in the limit $y \to 0$. In the first case, for $y \to 0$ the non-diagonal term behaves as follows

$$\left\{\csc\varphi\left((1 + y^2)\cos\varphi - 2y\cos\varphi'\right)\frac{L}{y} - 4\cos\varphi\sin\varphi'\right\}\bigg|_{y\to 0}$$

$$\to -4\,y\,\sin^2\varphi\sin 2\varphi', \tag{5.25}$$

and, in the second case, one has that

$$\left\{-\sin\varphi\left(2y^2 + (1 + y^2 - 2y\cos\varphi\cos\varphi')\csc^2\varphi\right)\frac{L}{y} + 4\sin\varphi'\right\}\bigg|_{y\to 0}$$

$$\to \frac{4}{3}\,y^2\,\sin^2\varphi\,(\sin(3\varphi') - 9\sin\varphi'). \tag{5.26}$$

Then, imposing that the integrals over y in (5.23) converge in the limit $y \to \infty$ and considering the above analysis of the integrand for $y \to 0$, the solution for the equation is found only if the real part of η is constrained by

$$-5 < \Re[\eta] < -4. \tag{5.27}$$

The coupled integral equations (5.23) has two pairs of solutions for F_i, corresponding to the two possible coupling constants, α_1 and α_2. They are found to be

$$F_1(\varphi) = \sin^2 \varphi, \quad F_2(\varphi) = 0 \quad \text{and} \quad F_1(\varphi) = 0, \quad F_2(\varphi) = \sin^2 \varphi. \tag{5.28}$$

This leads to a pair of solutions for the BS amplitude (5.22). The first solution is given by

$$\phi_1(k_4, k) = K^{\eta+1} \quad \text{and} \quad \phi_2(k_4, k) = 0 \,. \tag{5.29}$$

for which the coupling constant reads

$$\alpha_1(\eta) = -\frac{\pi(3+\eta)(5+\eta)(7+\eta)}{4(6+\eta)} \,, \tag{5.30}$$

while the second one is

$$\phi_1(k_4, k) = 0 \quad \text{and} \quad \phi_2(k_4, k) = K^{\eta}., \tag{5.31}$$

which is obtained from the F_1 and F_2 amplitudes related to α_2, i.e.

$$\alpha_2(\eta) = -\frac{\pi(6+\eta)(4+\eta)(2+\eta)}{4(3+\eta)} \,. \tag{5.32}$$

It is worth noticing that one can relate the two couplings through the following formula

$$\alpha = \alpha_1(-9-\eta) = \alpha_2(\eta) \,. \tag{5.33}$$

The support obtained in Eq. (5.27) is better illustrated when one considers Fig. 5.3, where Eqs. (5.30) and (5.32) are shown. As seen in the figure, the range of η that encloses both solutions and still ensures that the kernel of Eq. (5.23) does not diverge when $y \to \infty$ is the one given by Eq. (5.27).
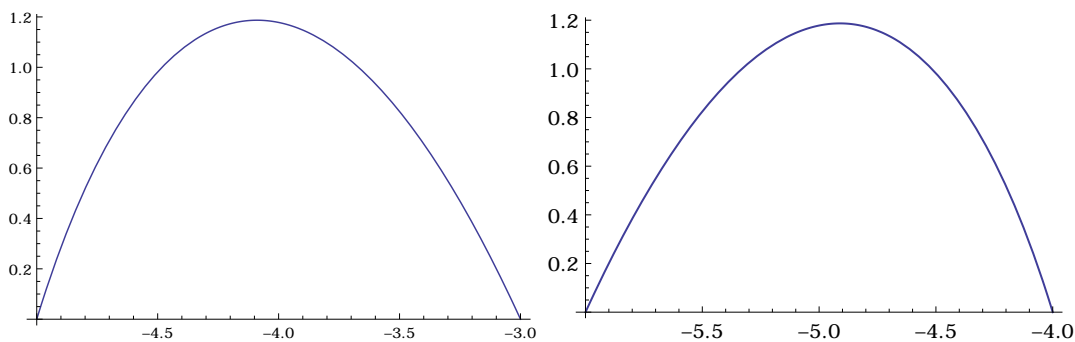
Figure 5.3. α_1 (left panel) and α_2 (right panel) as a function of η from Eqs. (5.30) and (5.32), respectively.

The maximum value of the coupling constant was found to be $\alpha_c \cong 1.187$ for $\alpha_1(\eta_{max})$ at $\eta_{max} \cong -4.089$, and for $\alpha_2(\eta_{max})$ at $\eta_{max} \cong -4.911$. In Fig. 5.3 one observes that for a given value of $\alpha < \alpha_c$ two solutions, $\alpha(\eta_1)$ and $\alpha(\eta_2)$, are found. For the critical value, α_c, there is only one possible solution instead. For α_i above the maximum value, the exponent η is complex and the BS equation in Euclidean

space presents a pair of log-periodic solutions, which demands one extra scale to determine the solution uniquely [142]. Although the study has been done for the large momentum region, the solution of the original set of coupled integral equations (5.7) is also given by the values of η satisfying Eq. 5.27 for a given value of α. This can be confirmed numerically for the general case, but one particular example will be discussed.

The solutions (5.29) and (5.31) were confirmed by solving the integral equations (5.23) numerically. When getting close to the extremes of η, given by Eq. (5.27), obtaining the solution gets more demanding numerically. It was also checked numerically that for the solutions in Eq. (5.28) the terms coupling the integral equations of Eq. (5.23) are very close to zero. Therefore, the equations can be decoupled, obtaining the same aforementioned results (considering that $\phi_2/M \to 0$).

One can now use the results from the Wick-rotated equation and derive the asymptotic behavior of the LFWF. The first step is to obtain the NIR of the BS amplitude in the asymptotic region, i.e

$$\phi_i(k^2) = \int_0^\infty d\gamma \int_{-1}^1 dz \frac{g_i(\gamma, z)}{(k^2 - \gamma + \imath\epsilon)^3} \to \frac{1}{(k^2 + \imath\epsilon)^{-\frac{\eta}{2}}} \,, \tag{5.34}$$

recalling that $z = 1 - 2\xi$. The solution of Eq. (5.34) can be found using the following ansatz

$$g_i(\gamma, z) = \gamma^{2 + \frac{\eta_i}{2}} f_i(z) \,. \tag{5.35}$$

From that, the valence wave function in the asymptotic limit, written in terms of the NIR, is expected to be proportional to the original LFWF, i.e.

$$\begin{aligned} \psi_i(\gamma, z) &= \int_0^\infty d\gamma' \frac{g_i(\gamma', z)}{(\gamma' + \gamma + (1 - z^2)\kappa^2 + z^2\overline{m}^2)^2} \\ &= \int_0^\infty d\gamma' \frac{\gamma'^{2 + \frac{\eta}{2}} f_i(z)}{(\gamma' + \gamma + (1 - z^2)\kappa^2 + z^2\overline{m}^2)^2} \propto \frac{f_i(z)}{(\gamma + (1 - z^2)\kappa^2 + z^2\overline{m}^2)^{-1 - \frac{\eta_i}{2}}} \end{aligned} \tag{5.36}$$

where the function $f_i(z)$ needs to be determined numerically, by solving the BSE equation in the asymptotic limit. Despite of that, it is simple to see that the expected ultraviolet behavior of the light-front wave function is given by

$$\psi_i(\gamma, z) \sim \gamma^{1 + \frac{\eta_i}{2}} \,. \tag{5.37}$$

This result can be compared to the numerical solution of the coupled integral equations (5.8).

One particularly interesting example, where the matching between results from the original equation (5.8) and scale invariant high-momentum regime, is obtained when α reaches its maximum value. In this case $\alpha_c = \alpha_2(\eta) \approx 1.187$ and $\eta = -4.9108$. For this situation, as ψ_1 is expected to have a similar fall-off, it will be presented the results only for ψ_2:

$$\psi_2(\gamma, z) \sim \gamma^{-1.45541} \,. \tag{5.38}$$

The above scaling behavior is expected to be independent of the bound state mass and this should be verified numerically. In Fig. 5.4, it is exemplified the case $\alpha = 1.189$, which very close to the maximum value possible for the coupling constant.

The parameters used are $m_\phi = m_\psi = 1$, $\mu = 0$ and $B = 0.5$. The numerical result is compared in the figure with the following product

$$\gamma^{1.455}\,\psi_2(\gamma, z) \to \ \text{const} \times f_2(z)\,, \tag{5.39}$$

showing that the asymptotic behavior for large γ coincides very well with the result from the numerical solution of the original equation. It is remarkable that the simple analysis for the scale invariant regime can represent so well the asymptotic behavior of the original BSE. Moreover, such agreement supports the result found for the dependence of α on η in Eq. (5.32).

$$\mu/\overline{m}=\ 0.00 \text{ - } B/\overline{m}=\ 0.500 \text{ - } m_F=\ 1.00 \text{ - } m_S=\ 1.00 \text{ - } \xi_0=\ 0.50$$
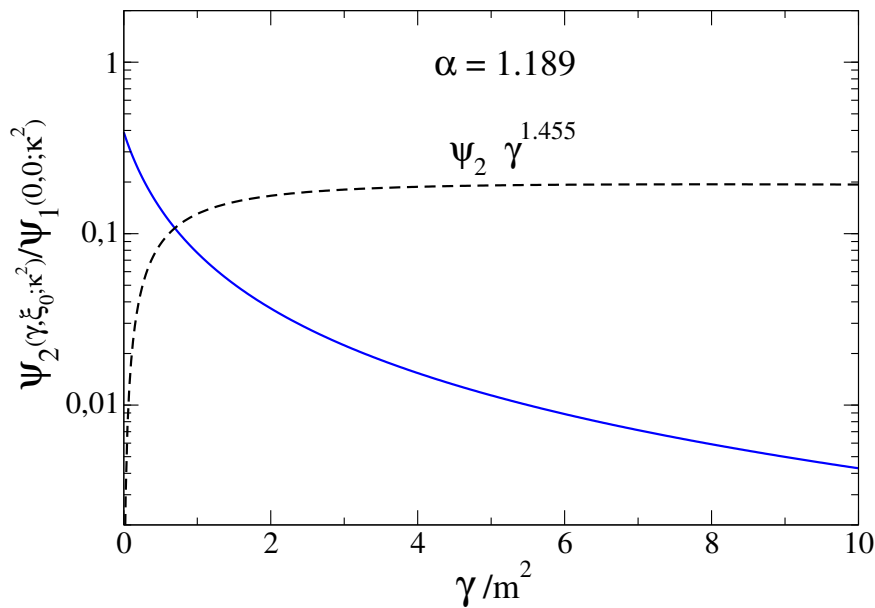
Figure 5.4. The light-front wave function $\psi_2(\gamma, z_0 = 0)$ obtained from the solution of the original equation (5.8) as a function of γ (solid blue curve) and its product with the asymptotic limit found in the high momentum limit (dashed black curve).

Another check of the power-law behavior in the UV limit, discussed in Ref. [48], is on the extension of the numerical calculations for $\gamma/\overline{m}^2 > 40$ for Eq. (5.8). The fall-off for that case can be described by $C_1/\gamma^{2.26}$, for $\mu/\overline{m} = 0.15$, and $C_2/\gamma^{2.43}$, for $\mu/\overline{m} = 0.50$, what is in agreement with the values predicted by the scale invariance analysis presented above.

5.2.2   High momentum limit in the Minkowski space

Next one can consider the asymptotic limit of the integral equation for the Nakanishi weight functions in Minkowski space (5.8). The high momentum limit of the equation is presented in Appendix H.4 where, for simplicity, the derivation is made for ϕ_2, following what was found in Eqs. (5.29) and (5.31). As discussed in the appendix, one can introduce the following ansatz

$$g_2(\gamma, z) = \gamma^r f_2(z) \tag{5.40}$$

where $r = 2 + \frac{\eta}{2}$ with the constraint that $-1 < r < 0$, which is equivalent to (5.27). Following the conclusion of the results obtained from the Wick-rotated equation, the equations can be decoupled and only one of the components can be solved independently. Here it is studied the equation for ϕ_2, but an analogous development could be done for ϕ_1.

Following the derivation detailed in Appendix H.4, the unknown function $f(z)$ is found to obey the following equation

$$f(z) = \frac{1 + |r|}{2 + 4|r|} \int_{-1}^{1} dz' f(z')$$
$$\times \left\{ \left[\frac{1 + z}{1 + z'} \right]^{|r|} \theta(z' - z) + \left[\frac{1 - z}{1 - z'} \right]^{|r|} \left[1 + \frac{4|r|}{(1 - z')} \right] \theta(z - z') \right\}, \tag{5.41}$$

where it was used the relation between α and r obtained in Eq. (5.32) and the subscript 2 in $f(z)$ was dropped out for simplicity. Notice that for $r = 0$ one has that $f(z) = f_0$, where f_0 is a constant, as expected. The numerical solution of Eq.
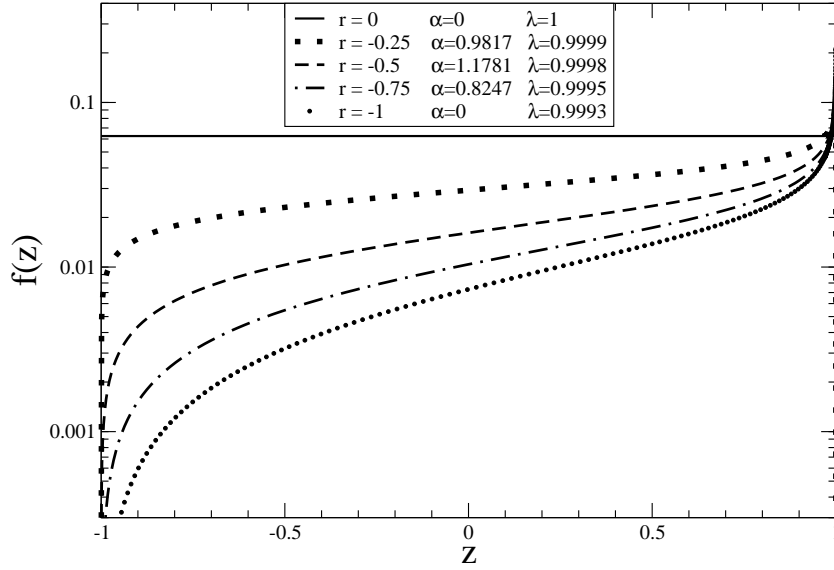
Figure 5.5. $f(z)$ as a function of z for different values of α and corresponding r. The eigenvalue λ is also provided in the figure.

(5.41) is found by solving the following eigenvalue equation

$$\lambda f(z) = \frac{1 + |r|}{2 + 4|r|} \int_{-1}^{1} dz' f(z')$$
$$\times \left\{ \left[\frac{1 + z}{1 + z'} \right]^{|r|} \theta(z' - z) + \left[\frac{1 - z}{1 - z'} \right]^{|r|} \left[1 + \frac{4|r|}{(1 - z')} \right] \theta(z - z') \right\}. \tag{5.42}$$

The eigenstates for real eigenvalues λ close to 1 are shown in Fig. 5.5. The solution needs to be further explored, including the case of complex values of r in order to study the log-periodic solutions which appear beyond the critical value of the coupling constant. In the case studied here, Eq. (5.42) was constrained to real values of r in the numerical solution. The figure indicates an interesting property of $f(z)$, the strong enhancement exhibited close to $z = 1$. This enhancement is also observed in the numerical solutions of the original equation (5.8), studied in detail in Ref. [48]. By further exploring Eq. (5.42), one could find more features of Eq. (5.8), that would help to reach more stability in its numerical solution. This is a study in progress and there are still some stages to be further developed. Nevertheless, it is already remarkable how the scale invariant regime of the equation can bring a deep understanding of features hidden in the original problem. Further exploration of the model within the realm of Efimov physics, namely the scale symmetry breaking to a discrete one [146, 150], is a a next step of this study.

5.2.3 Concluding remarks

The BSE was solved for a boson-fermion system interacting through a scalar or a vector exchange, both in Euclidean and Minkowski spaces. It was found a fair agreement in the comparison between the coupling constants obtained in both Euclidean and Minkowskian equations. The Nakanishi weight functions found numerically, which allows one to recover the BS amplitudes, were also presented. The formalism was developed by considering a generalized NIR for different constituent masses, what can be used for modeling mesons through the fermion-antifermion BSE, presented in the next chapter for the pion phenomenology. One interesting phenomenological application of the solutions for the vector exchange would be to deal with baryons as quark-diquark bound states. As an illustration of that, the longitudinal and transverse LF momentum distributions were presented for the case when $m_S/m_F = 2$ in Sec. 5.1.1. Another interesting application, related to the CPV formulation presented in Chap. 2, is the use of the boson-fermion BSE to model CP-violating partonic decay amplitudes in B decays containing baryons in the final state, as e.g. $B^+ \to p\bar{p}K^+$ [1].

Furthermore, the equation for the vector exchange is scale invariant in the ultraviolet regime. Consequently, the real solutions for the boson-fermion problem with vector interaction are only stable for a certain range of coupling constants, following the analysis of the ultraviolet behavior of the Euclidean BSE.The critical value of the coupling constant was explicitly found $\alpha_c \approx 1.187$, very close to the maximum value of α presented in Table 5.2 for which solving Eq. (5.8) numerically is still possible. For this value of the coupling constant, the asymptotic behavior of one of the components of the LFWF was found to be the same when comparing the one obtained through the solution of the equation and the prediction from the asymptotic region. It is worth mentioning that the this is an ongoing research and needs to be further explored by comparing the asymptotic form of the solutions of the BSE (5.8) for different coupling constants to the analysis of the large transverse momentum region for the LF amplitudes, ψ_1 and ψ_2, made in the previous section.

Chapter 6

Fermion-antifermion bound state: Pion phenomenology

This chapter illustrates to a phenomenological approach to a fermion-antifermion bound state within the Bethe-Salpeter framework in Minkowski space. In view of future applications to hadron physics, one can start by tuning the mass of the bound system to the one of the pion, as well as by adopting the values of other relevant parameters as suggested by lattice calculations (see below). Indeed, for the sake of simplicity, such a system will be called *pion* in what follows, and an extensive overview of dynamical observables, like LF distributions, generalized parton distributions (GPDs) and electromagnetic form factor, will be presented [49, 50, 51]. As discussed before, the dynamical description of the pion, to be presented here, is an essential input to refine the CP violation model presented in Chap. 2, as the light-meson amplitudes are the vertexes of the Feynman diagrams that need to be evaluated in order to obtain the partonic CP-violating decay amplitudes. Particularly, the BS amplitudes presented here can be promptly applied to compute the microscopic decay amplitude of the process $B^{\pm} \to \pi^{\pm}\pi^{+}\pi^{-}$. For the other decays, involving also the kaon meson, the procedure is to use the NIR for unequal mass systems (see Chap. 5 and Refs. [48, 116]) to solve the fermion-antifermion BSE. Once this task will be implemented, all the partonic decay amplitudes of the decays treated in Chap. 2 can be microscopically described. Naturally, for the sake of completeness, it would be interesting to have also the spin-1 fermion-antifermion BSE, for representing the vector intermediate resonances present in those decays, but this is not in the range of the present work.

Regarding the solution of the 0^{-} BSE, once again, the Nakanishi integral representation of the Bethe-Salpeter amplitude and light-front projection of the BSE are used, similarly to what was done in Chaps. 3 and 5. The ingredients of the dynamical model are a phenomenological quark-gluon vertex form factor, effective constituent quarks and a coupling constant obtained as the eigenvalue of the relevant equation with the bound state mass tuned to the pion one. The mass scales of the model are chosen to be around Λ_{QCD}, and an effective gluon mass is also used, being calibrated through such QCD scale, and inspired by lattice QCD calculations, as it will be discussed. Through the BS amplitude, this pion covariant model has, implicitly, besides the valence state, an infinite number of Fock-components built by

$q\bar{q}$ and any arbitrary number of effective gluons.

One of the most fundamental hadrons, the pion presents one of the simplest structures within a constituent quark picture of quantum chromodynamics, but its description is far from being understood and is still not complete, particularly in Minkowski space. Meanwhile, efforts to explore underlying aspects of its dynamics, like the intrinsic transverse motion of valence quarks, are largely based on QCD approaches in Euclidean space (see e.g. [151]). Its dynamics involves basic degrees of freedom and needs a covariant Minkowski space formulation, even phenomenological. The connection with the description of the bound state in terms of a LF wave function, easily achieved in the formalism implemented in this thesis for boson-boson and boson-fermion systems, and already extended to two-fermions [50, 51], is essential for hadron 3D imaging [152, 153, 154].

Generally, research efforts to get a realistic description of hadrons are either carried out through Lattice discretization (LQCD) [155] or continuous QCD techniques, e.g. Dyson-Schwinger and BS equations [156]. Both of these approaches are in Euclidean space and their outcomes, especially for the second one, are used to obtain the light-front Fock-space content of the hadron wave function. One example was the use of the NIR to perform the analytical extension to the Minkowski space from the Euclidean BSE solution to obtain the actual pion valence parton distribution function [112], which was subsequently explored in Refs. [157]. However, extracting the relevant observables that are intrinsically defined in the Minkowski space from Euclidean amplitudes is not yet a well established procedure and calculations fully performed in the physical space are of great interest.

The fermion-antifermion BSE was solved for vector, scalar and pseudoscalar boson exchanges in Minkowski space in Refs. [49, 50, 51], where the formal developments were developed. In this thesis, the fermion-antifermion BSE was solved similarly to what was done in Ref. [51] and all the results presented therein were reproduced. The BS equation is considered in the ladder approximation, following the study of Sec. 3.2, that suggests the suppression of cross-ladder diagrams when color degrees of freedom are included in the BSE kernel for a scalar QCD framework.

The goal here is to use the obtained solutions for a phenomenological study of the pion structure. This is a first step towards the description of hadrons, but extremely important due to the dynamical framework being fully developed in Minkowski space. It is important to highlight that self-energies are discarded and gauge invariance are not considered for the field operators, while the Feynman gauge is used here. Furthermore, the BSE kernel does not enclose confinement. Efforts in that direction are being made, through the inclusion of derivatives of the Dirac delta function in the spectral representation of the propagators, as suggested by Refs. [158]. One great advantage of the approach is that even the BS amplitude with minimal number of legs[1] already present infinite contributions from the light-front Fock-space decomposition of the hadron state vector [159].

Important to point out that the hadron dynamics has been explored through other approaches in Minkowski space, for instance by diagonalizing the light-front QCD Hamiltonian [27], a method known as basis light-front quantization (see e.g. Refs. [160]). The covariant spectator theory has been also used, where a three-

---

[1]I.e., 3 for the two-body bound state, two off-shell and one on-shell.

dimensional reduction of the BSE is explored to develop the formalism in Minkowski space [161]. Light-front models enclosing dynamical chiral symmetry are also being widely used, with great success to describe several features of the hadron spectra [162].

Another benefit of the NIR is that one can easily extend it from Minkowski to the Euclidean space by Wick-rotating the denominator of the representation, where all the dependence upon the external momenta is placed. This allows one to readily compare the results with the ones obtained from Euclidean approaches, e.g. LQCD. A further property of the NIR, already discussed for the two-boson case in Sec. 3.1, is the possibility of achieving the asymptotic transverse momentum form of the valence wave function, since the factorization of the dependencies on x and $k_\perp$ prevail (see Sec. 3.1.2). One can extend such a property to describe the power-law dependence of higher Fock-components of the wave function by means of the NIR [50, 130].

In this chapter, it will be presented new results from the solution of the BSE for a fermion-antifermion bound state interacting through a vector boson exchange. The scales involved in the pion problem are fixed following results found in the literature, .e.g LQCD calculations, and using as a general guideline Λ_{QCD}. Instead of presenting the direct solution, already extensively explored in Refs. [49, 50, 51], the outcomes will be used to compute the pion decay constant, the longitudinal and transverse LF distributions, the GPD and, finally, the EM form factor, which is compared to the experimental data. Although casually called "pion" here, the system can be more precisely understood as a mock pion, since many fundamental aspects, e.g. dynamical chiral symmetry breaking, are still lacking in the model. This ongoing research is being prepared for publication [163].

6.1 The BSE for a 0^- state

The Bethe-Salpeter amplitude for a 0^- fermion-antifermion bound state having total momentum $p = p_1 + p_2$ and total mass $M = \sqrt{p^2}$ obeys the integral equation (see Refs. [49, 50, 51])

$$\Phi(k,p) = S(k+p/2) \int \frac{d^4k'}{(2\pi)^4} F^2(k-k') i S_g^{\mu\nu}(k,k') \Gamma_1 \Phi(k',p) \hat{\Gamma}_2 S(k-p/2), \quad (6.1)$$

where $k = (p_1 - p_2)/2$ denotes the relative momentum and $\Gamma_i = \gamma^\mu$ is the Dirac structure of the interaction vertex. The argument of the form factor F is the the momentum transfer, $q = k - k'$. The interaction kernel $\mathcal{K}$ is assumed to be in the ladder approximation, as suggested by the suppression of the non-planar diagrams when color degrees of freedom are considered, as already seen for $N_c = 3$ in the bosonic example presented in Sec. 3.2. In the interaction kernel it is considered a massive vector boson exchange to mimick the gluon propagator, in the Feynman gauge, which reads

$$S_g^{\mu\nu}(k,k') = -i\, g^2\, \frac{g^{\mu\nu}}{(k-k')^2 - \mu^2 + i\epsilon} \quad (6.2)$$

where g is the coupling constant and μ is an effective gluon mass, fixed by lattice QCD calculations (see e.g. Ref. [164]).

Moreover, in Eq. (6.1) the Dirac propagator S for a fermion of mass m reads

$$S(k) = i\frac{\slashed{k} + m}{k^2 - m^2 + i\epsilon}. \tag{6.3}$$

Furthermore, $\hat{\Gamma}_2 = C\Gamma_2^T C$ and the vertex "quark-gluon" form factor F is of the form

$$F(k - k') = \frac{\mu^2 - \Lambda^2}{(k - k')^2 - \Lambda^2 + i\epsilon}, \tag{6.4}$$

where Λ is a suitable scale for giving the size of the color distribution of the interaction vertex. It is worth mentioning that the form factor F acts as a regulator to avoid the breakdown following from scale invariance in the ultraviolet region that also happens in the present system, similarly to what was discussed in Sec. 5.2 for the boson-fermion bound state.

The BS amplitude can be decomposed as

$$\Phi(k, p) = \sum_{i=1}^{4} S_i(k, p)\phi_i(k, p), \tag{6.5}$$

where each ϕ_i is a scalar function of the invariants k^2, p^2, $k{\cdot}p$. The symmetry property of the scalar functions, i.e. $k \to -k$ for $\phi_i(k, p)$, can be straightforwardly translated to the corresponding properties of the Nakanishi weight function, $g_i(\gamma', z'; \kappa^2)$, which is associated with the exchange $z' \to -z'$. Hence, the weight functions must be even for $i = 1, 2, 4$ and odd for $i = 3$. Moreover, the allowed Dirac structures read

$$S_1(k, p) = \gamma_5, \quad S_2(k, p) = \frac{\slashed{p}}{M}\gamma_5, \quad S_3(k, p) = \Big[\frac{(k \cdot p)}{M^3}\slashed{p} - \frac{1}{M}\slashed{k}\Big]\gamma_5,$$
$$S_4(k, p) = \frac{i}{M^2}\sigma^{\mu\nu}p_\mu k_\nu \gamma_5. \tag{6.6}$$

The NIR can subsequently be applied to each scalar functions, ϕ_i, i.e.,

$$\phi_i(k, p) = \int_{-1}^{1} dz' \int_0^\infty \frac{g_i(\gamma', z'; \kappa^2)}{[k^2 + (p \cdot k)z' - \gamma' - \kappa^2 + i\epsilon]^3} \tag{6.7}$$

with $\kappa^2 = m^2 - M^2/4$.

Noteworthy to mention that the S_i operators of Eq. (6.6), present in the amplitude $\Phi(k, p)$, together with the fermionic propagators (6.3) bring terms that produce extra singularities, not present for the boson-boson or fermion-boson systems.

By inserting Eqs. (6.7) and (6.5) in (6.1), and subsequently performing the light-front projection one can derive the following set of coupled integral equations for the Nakanishi weight functions [50, 51]

$$\int_0^\infty d\gamma' \frac{g_i(\gamma', z; \kappa^2)}{[\gamma + \gamma' + m^2 z^2 + (1 - z^2)\kappa^2]^2} =$$
$$\alpha \sum_{j=1}^{4} \int_{-1}^{1} dz' \int_0^\infty d\gamma' [\mathcal{L}_{ij}^{(ns)}(\gamma, z, \gamma', z') + \mathcal{L}_{ij}^{(s)}(\gamma, z, \gamma', z')]g_j(\gamma', z'; \kappa^2), \tag{6.8}$$

where $\alpha = g^2/(4\pi)$ is the dimensionless coupling constant[2]. Due to the extra singularities, $\mathcal{L}_{ij}^{(s)}(\gamma, z, \gamma', z'; p)$ requires a special treatment to deal with the additional powers of k^-. Within the LF framework, the singular contributions can be singled out in a straightforward way, and rigorously evaluated by the procedure developed in Ref. [165] or using the pole dislocation method given in Ref. [166]. In short, these end-point singularities can be analytically treated by performing the k^- integration as [165]

$$\mathcal{I}(\beta, y) = \int_{-\infty}^{\infty} \frac{dx}{[\beta x - y \mp i\epsilon]^2} = \pm \frac{2\pi i \delta(\beta)}{[-y \mp i\epsilon]}. \tag{6.9}$$

For more details on the application of the method to the 0^- BSE, see Refs. [50, 51]. The kernel of Eq. (6.8) is given in Appendix I. The expressions for the non-singular contributions to the kernel are discussed in the next subsections.

As done in Chaps. 3 and 5, $g_j(\gamma', z'; \kappa^2)$ is expanded as Laguerre (γ) × Gegenbauer (z) polynomials. It is worth mentioning that in the equal mass case the symmetry under the exchange of the particles simplifies significantly the kernel of the equation, as well as the numerics since only the even (for g_1, g_2 and g_4) or odd (for g_3) Gegenbauer polynomials[3] are necessary to account for the z dependence of these Nakanishi weight functions.

For calculating observables, one needs to properly normalize the BS amplitude, so the light-front wave function gives the correct valence probability and momentum distributions. For normalizing the BS amplitude, in the ladder approximation, the following expression needs to be evaluated

$$Tr \left[\int \frac{d^4k}{(2\pi)^4} \frac{\partial}{\partial p'^\mu} \{ S^{-1}(k - p'/2)\bar{\Phi}(k, p)S^{-1}(k + p'/2)\Phi(k, p) \}|_{p'=p} \right] = i\, 2p_\mu\,. \tag{6.10}$$

Introducing Eq. (6.5) and the NIR (6.7) for the ϕ_i amplitudes, performing the trace and the four-dimensional integration, one obtains the normalization condition (derived in Ref. [167])

$$\frac{3}{32\pi^2} \int_{-1}^{+1} dz' \int_0^\infty d\gamma' \int_{-1}^{+1} dz \int_0^\infty d\gamma \int_0^1 dv\, v^2(1-v)^2$$

$$\times \left\{ \frac{g_1(\gamma', z')g_1(\gamma, z) + g_2(\gamma', z')g_2(\gamma, z) - 4\frac{m}{M}g_2(\gamma', z')\, g_1(\gamma, z)}{\left[\kappa^2 + \frac{M^2}{4}\lambda^2 + \gamma'v + \gamma(1-v) \right]^4} \right.$$

$$\left. + \frac{g_3(\gamma', z')g_3(\gamma, z) + g_4(\gamma', z')\, g_4(\gamma, z) - 4g_1(\gamma', z')\, g_4(\gamma, z)}{2M^2 \left[\kappa^2 + \frac{M^2}{4}\lambda^2 + \gamma'v + \gamma(1-v) \right]^3} \right\} = 1\,, \tag{6.11}$$

where $\lambda = [vz' + (1-v)z]$. It is worth mentioning that the covariant normalization in Eq. (6.11) still contains the contributions beyond the valence state from the higher Fock components.

Once the BS amplitude is properly normalized, the valence probability and momentum distributions can be derived. The procedure passes through the evaluation

---

[2]The features observed due to scale invariance in Sec. 5.2 are avoided here due to the inclusion of the vertex form factor of Eq. (6.4), which introduces a new scale in the problem.

[3]See Appendix I.2 for more details on the numerical treatment.

of the valence wave function, which emerges from the elimination of the relative light front time between constituent particles defining the BS amplitude. The valence probability can be defined as [167, 168]:

$$p_{val} = \frac{1}{2^8 \pi^2} \int_{-1}^{1} dz \int_{0}^{\infty} d\gamma \int \frac{dk^-}{2\pi} \int \frac{dk'^-}{2\pi} \text{Tr} \left\{ \gamma^+ \, \Phi(k,p) \, \gamma^+ \, \bar{\Phi}(k',p) \right\} , \quad (6.12)$$

where $\gamma = k_\perp^2$, $z = 2\xi - 1$ and ξ is longitudinal momentum fraction.

After performing the traces and integrating over k^- and k'^-, one finds that (more details on the derivation of the equations below are given in Ref. [167])

$$p_{\text{val}} = \frac{1}{32\pi^2} \int_{-1}^{1} dz \int_{0}^{\infty} d\gamma \, \mathcal{P}_{val}(\gamma, z) , \quad (6.13)$$

where the valence probability density is [167]

$$\mathcal{P}_{val}(\gamma, z) = \tilde{\psi}(\gamma, z) \, \tilde{\psi}(\gamma, z) + \frac{\gamma}{M^2} \, \psi_4^{(0)}(\gamma, z) \, \psi_4^{(0)}(\gamma, z) , \quad (6.14)$$

and the other amplitudes, enclosing the longitudinal and transverse momentum distributions similarly to Eqs. (5.12) and (5.13), are defined as

$$\tilde{\psi}(\gamma, z) = \psi_2^{(0)}(\gamma, z) + \frac{z}{2} \psi_3^{(0)}(\gamma, z)$$
$$+ \frac{i}{M^3} \int_{0}^{\infty} d\gamma' \; \frac{\partial g_3(\gamma', z)/\partial z}{[\gamma + \gamma' + z^2 m^2 + (1 - z^2)\kappa^2]} \quad (6.15)$$

and

$$\psi_i^{(0)}(\gamma, z) = \int \frac{dk^-}{2\pi} \, \phi_i(k,p) = -\frac{1}{M} \int_{0}^{\infty} d\gamma' \frac{g_i(\gamma', z)}{[\gamma + \gamma' + m^2 z^2 + (1 - z^2)\kappa^2 - i\epsilon]^2} . \quad (6.16)$$

For the derivation of Eq. (6.15) it was also used that

$$\psi_i^{(1)}(\gamma, 2x - 1) \;\; = \;\; \int \frac{dk^-}{2\pi} \, k^- \, \phi_i(k,p) =$$
$$= \;\; \frac{2}{M^2} \int_{0}^{\infty} d\gamma' \frac{\partial g_i(\gamma', z)}{\partial z'} \frac{1}{[\gamma + \gamma' + m^2 z^2 + (1 - z^2)\kappa^2 - i\epsilon]}$$
$$- \;\; \frac{z}{2} \int_{0}^{\infty} d\gamma' g_i(\gamma', z) \frac{1}{[\gamma + \gamma' + m^2 z^2 + (1 - z^2)\kappa^2 - i\epsilon]^2} , \quad (6.17)$$

which is performed by applying the integral given by the formula in Eq. (6.9) and its derivative, which reads

$$\int_{-\infty}^{\infty} \frac{dk^-}{2\pi} \frac{k^-}{\left[\alpha \, k^- - \beta + i\epsilon \right]^3} = \frac{i}{2} \frac{\delta'(\alpha)}{\left[-\beta + i\epsilon \right]} . \quad (6.18)$$

Similarly to the procedure to obtain Eqs. (5.12) and (5.13), the longitudinal and transverse valence LF momentum distributions are obtained through

$$\phi(\xi) = \frac{1}{32\pi^2} \int_{0}^{\infty} d\gamma \, \mathcal{P}_{val}(\gamma, 2\xi - 1) \quad \text{and} \quad P(\gamma) = \frac{1}{32\pi^2} \int_{-1}^{1} dz \, \mathcal{P}_{val}(\gamma, z) . \quad (6.19)$$

6.1.1 LF distributions and pion decay constant

For illustrating the higher Fock contributions to the fermionic system, in Table 6.1 it is presented the valence probability (6.13) for three different values of the binding energy, $B/m = 0.01, 0.1$ and 1.0. In the chosen example, the exchanged boson mass $\mu/m = 0.15$ and the vertex form factor parameter is $\Lambda/m = 2$ have been adopted. The valence probability of the fermion-antifermion bound state, p_{val}^F, is compared with the one obtained for two-bosons, denoted by p_{val}^B. As it can be seen in the table, the value are very similar for both cases, indicating that the inclusion of the spin dof does not change the impact of contributions beyond the valence.

Table 6.1. Comparison between the valence probability for the fermionic p_{val}^F and bosonic p_{val}^B bound states. The exchanged boson mass is $\mu/m = 0.15$ and the vertex form factor parameter is $\Lambda/m = 2.0$.

B/m	p_{val}^F	p_{val}^B
0.01	0.96	0.94
0.1	0.78	0.80
1.0	0.68	0.67

Although the results of Table 6.1 are for a scalar exchange, simply for making the comparison with the bosonic case of Chap. 3, it was checked that the results are very similar when the vector exchange is considered. For strongly bound states, like the pion, the effect beyond the valence is about 30%, indicating that higher Fock components are extremely important and models based only on the valence component might be considerably limited.
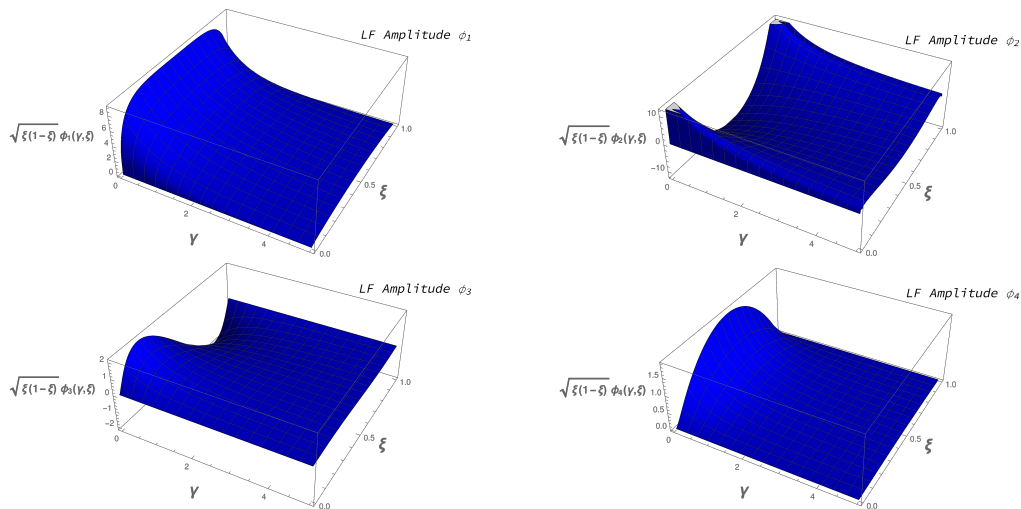
Figure 6.1. The four light-front components, related to the decomposition of the BS amplitude of Eq. (6.5), multiplied by the factor $\sqrt{\xi(1-\xi)}$. The adopted input parameters are $B/m = 1.35$, $\mu/m = 2.0$, $\Lambda/m = 1.0$ and $m=215$ MeV. The associated coupling constant is $g^2 = 26.718$.

As mentioned before, multiple structural observables are obtained through the valence LFWF components. Following the adopted decomposition for the BS amplitude (6.5) one has four LF components, obtained by integrating over k^- each component of the BS amplitude (6.16) independently. These components, multiplied by a factor of $\sqrt{\xi(1-\xi)}$, are presented in Fig. 6.1. The parameters, already chosen to provide a description of a mock pion, are $B/m = 1.35$, $\mu/m = 2.0$, $\Lambda/m = 1.0$ and $m = 215$ MeV. Other observables are straightforward to compute once the solution for the BS amplitude, which gives the components in Fig. 6.1, is known.

In order to study the effect from the parameters that can be adopted for the mock pion, Fig. 6.2 present the transverse (left frame) and longitudinal (right frame) LF distributions of Eq. (6.19). It is worth to point out that the ending points of the longitudinal distribution (right panel) present a small numerical oscillation and its improvement is due to be studied in the future. The coupling constant is tuned so that the pion mass is fixed at $M = M_\pi = 140$ MeV while the constituent quark mass is varied for fixing the binding energy $B/m = 1.35$. The exchanged gluon considered is 2.0 and the vertex form factor parameter is $\Lambda/m = 1.0$. Three sets of parameters were studied, namely $(B/m, \Lambda/m, \mu/m) = (1.25, 2.0, 1.5), (1.35, 2.0, 1.0)$ and $(1.35, 1.0, 2.0)$ were studied, with the LF momentum distributions being relatively similar for all the considered cases. The most significant effect happens when Λ is changed. The chosen set was the one returning the closest f_π to its experimental value.
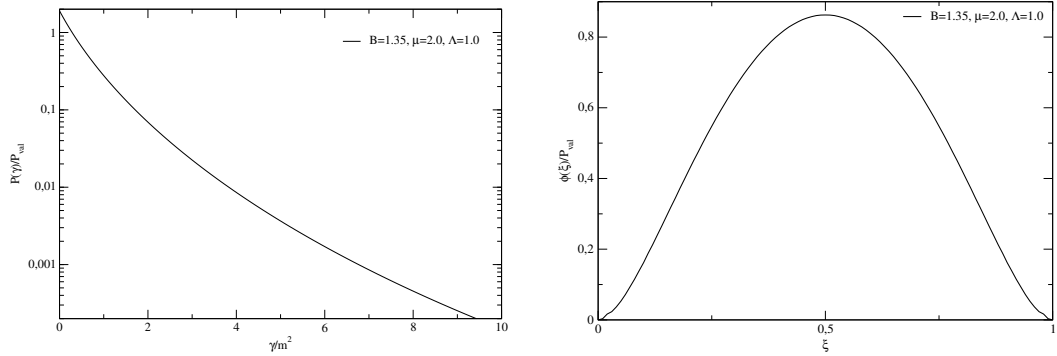
Figure 6.2. Transverse (left) and longitudinal (right) valence LF momentum distributions. The associated coupling constant is $g^2 = 26.718$.

After all, the input parameters for the mock pion are fixed as follows. For the effective mass of the gluon $\mu \approx 430$ MeV (equivalent to have $\mu/m = 2.0$ in the units adopted previously), following the result of Ref. [164] from LQCD in Landau gauge. This is obviously not ideal, since the vector boson is considered in the Feynman gauge here, but the non-trivial task of reformulating the BS approach in a general gauge will be left for the future. The quark mass, following Ref. [169], is fixed at $m \approx 215$ MeV, given that the pion mass is kept fixed as $M = M_\pi = 140$ MeV. This corresponds to a binding energy of $B/m = 1.35$ in the unit adopted formerly. For the vertex interaction parameter, it is chosen $\Lambda/m = 1$, which has the same order as

λ_{QCD}. The coupling constant is conveniently rescaled as

$$\alpha_s = \frac{g^2}{4\pi}(1 - \mu^2/\Lambda^2)^2,$$

where g^2 is fixed through the outcome of the eigenvalue problem. The form presented above is introduced in order to match the behavior in the infrared region [170]. Another relevant observable that can be computed is the pion decay constant, defined as

$$i\, p^2 f_\pi = N_C \int \frac{d^4k}{(2\pi)^4} \text{Tr}[\not{p}\,\gamma^5\,\Phi(p,k)],\qquad(6.20)$$

where N_C is the number of colors. More details on the formulation of the decay constant within the BS approach are presented in Appendix I.3. These parameters give for the pion decay constant $f_\pi = 96$ MeV, which is very close to the experimental value [1]. The obtained valence probability for this system is $p_{val} = 0.68$. The parameters, as well as the outcomes for p_{val} and f_π, are summarized in Table 6.2.

Table 6.2. Input parameters for the mock pion. The last two columns show the results for the valence probability p_{val} and decay constant f_π.

B/m	M_π (MeV)	g^2	μ (MeV)	Λ/m	m (MeV)	p_{val}	f_π (MeV)
1.35	140	26.718	430	1.0	215	0.68	96

6.1.2 GPD and elastic form factor

In order to access information inside hadrons, considering the quark and gluon dof, the so-called Generalized Parton Distributions (GPDs)[4] belong to the set of the elective quantities. It can be understood as a 3D picture of the hadrons, carrying the correlation between the transverse position and the longitudinal momentum of partons within the hadron, giving direct access to observables like form factors and parton distribution functions. One way of understanding the GPDs is as the off-shell parton-hadron scattering amplitude projected onto the LF, which reads [171]. Schematically, one has

$$H(x,\xi,t) = \frac{1}{2}\int dk^+ d^2k_\perp \delta\left(x - \frac{k^+}{P^+}\right)\int dk^- \mathcal{A}(k),\qquad(6.21)$$

with

$$\mathcal{A}(k) = \int d^4z e^{ik\cdot z}\langle P + \frac{\Delta}{2}|T\left[\bar{\psi}(-\frac{z}{2})\gamma^+\psi(\frac{z}{2})\right]|P - \frac{\Delta}{2}\rangle,\qquad(6.22)$$

where the light-cone gauge is considered, P is the momentum average of the hadron between the incoming and outgoing states, Δ is the transfered momentum and T is

---

[4]Worth pointing out that the Transverse Momentum Distributions (TMDs) are the relevant quantities for focusing on the momentum distributions. Their calculation will be done in a future study.

the time ordering operator. For the chiral-even quark distribution in a pseudoscalar hadron, the twist-2 GPD reads

$$H_\pi^q(x, \xi, t) = \frac{1}{2} \int \frac{dz^-}{2\pi} e^{ixP^+ z^-} \langle \pi, P + \frac{\Delta}{2} | \bar\psi^q(-\frac{z}{2}) \gamma^+ \psi^q(\frac{z}{2}) | \pi, P - \frac{\Delta}{2} \rangle |_{z^+ = z_\perp = 0}$$

(6.23)

Restricting ourselves to the DGLAP region ($|x| \geq \xi$, where $\xi = -\Delta^+/(2P^+)$), where the valence description holds (see Refs. [172, 173, 174, 175]), the GPD is simply an overlap of the LFWFs, which for the valence contribution reads [176]

$$H_\pi^u(x, \xi, t) = \int \frac{d^2 k_\perp}{16\pi^3} \left[\psi_{\uparrow\downarrow}^*(x', k_\perp') \, \psi_{\uparrow\downarrow}(x, k_\perp) + k_\perp' \cdot k_\perp \psi_{\uparrow\uparrow}^*(x', k_\perp') \, \psi_{\uparrow\uparrow}(x, k_\perp) \right],$$

(6.24)

where $\psi_{\uparrow\downarrow}$ and $\psi_{\uparrow\uparrow}$ are the two independent components of the LF wave function of the pion, corresponding to the possible spin configurations.

Following Ref. [177], the anti-parallel helicity component is defined as

$$2P^+ \psi_{\uparrow\downarrow}(k^+, k_\perp) = \int \frac{dk^-}{2\pi} Tr[\gamma^+ \gamma_5 \Phi(k, p)],$$

(6.25)

while for the parallel component one has

$$ik^i P^+ \psi_{\uparrow\uparrow}(k^+, k_\perp) = \int \frac{dk^-}{2\pi} Tr[\sigma^{+i} \gamma_5 \Phi(k, p)].$$

(6.26)

For the evaluation of Eqs. (6.25) and (6.26), it is used the decomposition of the BS amplitude given by Eq. (6.5). The scalar components ϕ_i are expressed by the Nakanishi integral representation, given in Eq. (6.7).

Computing the involved traces in Eqs. (6.25) and (6.26), one gets the following

$$Tr[\gamma \cdot n \gamma_5 \Phi(k, p)] = \frac{4}{M} \left(k \cdot n \, \phi_3 - \frac{n \cdot p \, k \cdot p}{M^2} \phi_3 - n \cdot p \, \phi_2 \right)$$

(6.27)

and

$$Tr[\sigma^{\mu\nu} n_\mu V_\nu \gamma_5 \Phi(k, p)] = \frac{i \, 4}{M^2} (n \cdot p \, k \cdot V - p \cdot V \, k \cdot n) \, \phi_4.$$

(6.28)

These expressions can be simplified by considering that $p^2 = M^2$, $n \cdot p = M$, $n \cdot k = k^+$, $k^2 = k^+ k^- - k_\perp^2$, $k \cdot p = M/2(k^+ + k^-)$, $k^0 = (k^+ + k^-)/2$, $k^3 = (k^+ - k^-)/2$, $p \cdot V = 0$, $k \cdot V = k^i$ and $k^+ = -Mz/2$, which leads to

$$Tr[\gamma \cdot n \gamma_5 \Phi(k, p)] = -\frac{(2k^- + Mz)}{M} \phi_3 - 4\phi_2$$

(6.29)

and

$$Tr[\sigma^{\mu\nu} n_\mu V_\nu \gamma_5 \Phi(k, p)] = \frac{i4k^i}{M} \phi_4,$$

(6.30)

where M is the bound state mass, i.e. the pion mass $M = M_\pi$. The next step is to perform the involved integrations over k^-. One basically needs to consider two terms, which are given by Eqs.(6.16) and (6.17).

The final result for the anti-parallel spin component of the light-front wave function is given by

$$
\begin{aligned}
\psi_{\uparrow\downarrow}(\gamma, x) &= -\frac{1}{2M^2}[4\,M\psi_2^{(0)}(\gamma, 2x-1) + 2\,\psi_3^{(1)}(\gamma, 2x-1) + M\,z\,\psi_3^{(0)}(\gamma, 2x-1)] \\
&= \frac{2}{M^4}\int_0^\infty d\gamma'\,\frac{\left[M^2 g_2(\gamma', z) + \left(\frac{zM^2}{2}\right)g_3(\gamma', z) - Dg_3'(\gamma', z)\right]}{D^2}
\end{aligned}
\tag{6.31}
$$

where $x \in [0,1]$, $g_3'(\gamma', z) = \frac{\partial g_3(\gamma', z)}{\partial z'}$ and $D = \gamma + \gamma' + m^2 z^2 + (1-z^2)\kappa^2$. For the parallel component, one has

$$
\psi_{\uparrow\uparrow}(k_\perp^2, x) = \frac{4}{M^2}\,\psi_4^{(0)}(\gamma, 2x-1).
\tag{6.32}
$$
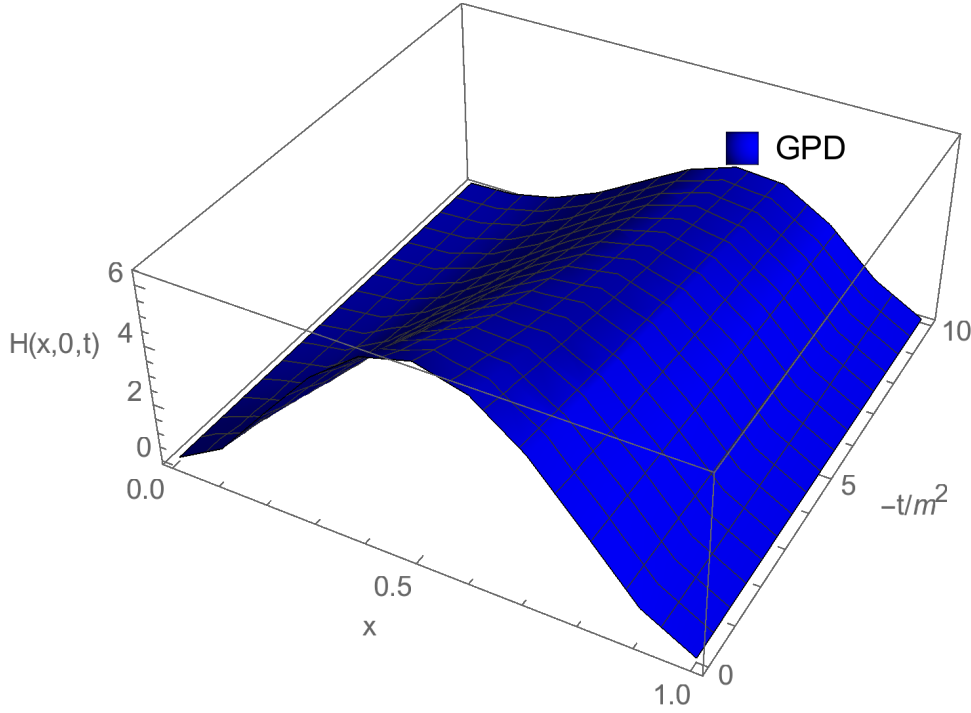
Figure 6.3. Chiral-even GPD of the pion in the DGLAP region (6.33), given by the overlap of LFWFs. The input parameters are presented in Table 6.2.

The final formulas for the GPD in the DGLAP region, i.e. valid in the region of the phase space where $|x| \geq \xi$, is given by

$$
H_\pi^{u;DGLAP}(x, \xi, t) = H_{\uparrow\downarrow}^u(x, \xi, t) + H_{\uparrow\uparrow}^u(x, \xi, t),
\tag{6.33}
$$

where

$$
H_{\uparrow\downarrow}^u(x, \xi, t) = \frac{1}{16\pi^3}\int_0^\infty k_\perp dk_\perp \int_{-\pi}^\pi d\theta\,\Psi_{\uparrow\downarrow}^*(x', k_\perp'^2)\,\Psi_{\uparrow\downarrow}(x'', k_\perp''^2)
\tag{6.34}
$$

and

$$H_{\uparrow\uparrow}^u(x, \xi, t) = \frac{1}{16\pi^3} \int_0^\infty k_\perp dk_\perp \int_{-\pi}^\pi d\theta \sqrt{|k_\perp'^2|}\sqrt{|k_\perp''^2|} \cos\theta \, \Psi_{\uparrow\uparrow}^*(x', k_\perp'^2) \, \Psi_{\uparrow\uparrow}(x'', k_\perp''^2).$$

$$(6.35)$$

The kinematical variables above read

$$x' = \frac{x - \xi}{1 - \xi}; \quad k_\perp'^2 = k_\perp^2 + \left(\frac{1-x}{1-\xi}\right)^2 \frac{\Delta_\perp^2}{4} + \frac{1-x}{1-\xi}\Delta_\perp k_\perp \cos\theta,$$

$$x'' = \frac{x + \xi}{1 + \xi}; \quad k_\perp''^2 = k_\perp^2 + \left(\frac{1-x}{1+\xi}\right)^2 \frac{\Delta_\perp^2}{4} - \frac{1-x}{1+\xi}\Delta_\perp k_\perp \cos\theta, \qquad (6.36)$$

$$-t = \frac{\Delta_\perp^2 + 4\xi^2 M^2}{1 - \xi^2},$$

where it is neglected the pion mass term, using the chiral limit where $M \to 0$, following what was done in Ref. [176].

Fig. 6.3 present the final result for the GPD of Eq. (6.33). The GPD obtained from the fermion-antifermion BSE in Minkowski space shows to be compatible with other results in the literature, as the ones presented in Refs. [175, 176].
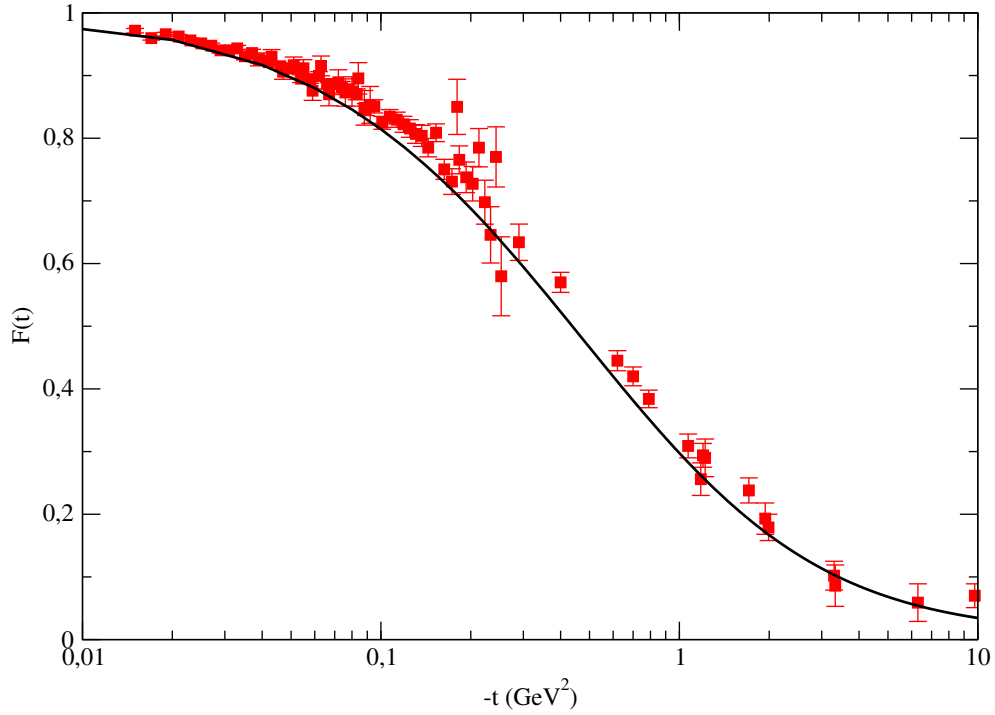
Figure 6.4. Pion electromagnetic valence form factor compared with data from [178]. The input parameters are presented in Table 6.2.

The valence form factor can be obtained simply by the following sum rule

$$F_\pi(t) = \int_{-1}^1 dx \, H_\pi(x, \xi, t), \qquad (6.37)$$

and its result can be seen in Fig. 6.4, where the normalization condition $F_\pi(-t = 0) = 1$ for the valence contribution was adopted. The result is compared with data from Ref. [178] and presents a very good agreement. As it is well-known, there is a correlation between the pion decay constant, f_π, and the charge radius, which dictates the low momentum region of the form factor. Therefore, this might be the reason for the nice agreement seen in Fig. 6.4, i.e. due to the pion form factor sensitiveness to basically only one parameter. The asymptotic region of the form factor should be analyzed with the model once the experimental data becomes available also for high momentum transfer. There are still further investigations to be done and the results are preliminary, but this indicates that the valence form factor can already represent very well the main features of the pion form factor for practical calculations, at least in the range of $t = -Q^2$ considered. The upcoming data beyond 10 GeV^2 will be extremely important, also to understand the role of the higher Fock states in the observables that might affect more the fall-off for high momentum transfer. The calculation of the electromagnetic form factor through the evaluation of the triangle diagram involving directly the BS amplitudes, as done in Sec. 3.1.3 for the two-boson case, is a work in progress. This calculation gives the form factor beyond the valence Fock-space component.

The reader should bear in mind that the results presented in this chapter are still preliminary, although promising. So far only the valence contribution to $H_\pi(x, \xi, t)$ and further development is necessary in order to obtain the ERBL domain [175], i.e. $|x| < |\xi|$. The model implicitly contains contributions from the higher Fock-space components with multiple intermediate gluons, part that corresponds to 32% of the total wave function, as given through the valence probability shown in Table 6.2. However, the formalism to account for the contributions from the higher Fock components in Eqs. (6.21)-(6.23) can be developed for the present model following the approaches developed Refs. [172, 173, 174, 175]. It will allow one to access, although indirectly, the physical content beyond the valence component in the dynamical observables. This can be done by computing, e.g., generalized transverse momentum distributions, GPDs, PDFs and form factors by means of the BS amplitude, without relying on the projection onto the LF.

In conclusion, a fully covariant non-perturbative model for the pion, without self-energy and vertex-corrections, was developed in Minkowski space through the solution of the fermion-antifermion BSE. The components of the valence LFWF were presented to illustrate the solution. By tuning the parameters of the model, namely the constituent quark masses, the effective gluon mass and the vertex interaction scale, it has been found 68% for the valence probability and, for the pion decay constant, $f_\pi = 96$ MeV. The GPD in the DGLAP region was then computed, from where it was obtained the pion valence form factor, which shows to be in fair agreement with the experimental data. This notable finding, by only using the valence component, is interpreted to be linked with the fact that only one parameter, f_π, is enough to determine the behavior of the form factor for low momentum transfer. Further analysis in the asymptotic region, then taking into account high Fock-space contributions, is expected to be performed in the near future. This model gives the essential input to evaluate the microscopic decay amplitudes containing the pion in the final state. These amplitudes are lacking in the CPV model discussed in Chap. 2. The study presented above, once performed for the kaon by repeating

the calculations for two different quark constituent masses, will provide the BS amplitudes for computing the partonic amplitudes for all the decay processes studied in Chap. 2.

Chapter 7

Summary and Outlook

The CP asymmetry generated by the presence of resonances and two-body final state interactions in charmless three-body $B^\pm$ decays was derived within a formalism explicitly constrained by CPT [20], extending the formulation proposed in Ref. [16]. All the possible interferences among the included resonant and non-resonant amplitudes were considered, except the ones involving products of the inelastic scattering and the resonant amplitudes. While summing up over the allowed kinematical phase space of all the considered decay channels, the CPT invariance is found by matching the condition $\sum_\lambda \Delta\Gamma_\lambda = 0$. Inelastic two-body final state interactions are included through a parametrization of the leading order s-wave scattering matrix elements $t_{\lambda,\lambda'}$, with $\lambda = \pi\pi$ and $\lambda' = KK$, fixed by the $\pi\pi \to KK$ scattering data. Naturally, the coupling between the $\pi\pi$ and KK channels happens in the region starting from the opening of the KK channel, i.e. around 1 GeV. The model is able to analyze the phase space up to two-body invariant masses $m_{\pi\pi'} \approx 1.6$ GeV. Below 1 GeV, the CPV within the model comes essentially from the interference among the ρ and $f_0(980)$ resonances and the non-resonant background related to the partonic amplitudes. The rescattering is responsible for coupling different decay channels and distribute CPV among them. Explicitly, the considered decay channels are $B^\pm \to \pi^\pm\pi^+\pi^-$, which gives as an outcome the asymmetry in the coupled channel $B^\pm \to \pi^\pm K^+K^-$, and $B^\pm \to K^\pm\pi^+\pi^-$, for which an equal amount of CP asymmetry, with opposite sign, arises in $B^\pm \to K^\pm K^+K^-$. The fit of the CP asymmetry formula is found to be in fair agreement with the LHCb experimental data [18].

Several improvements can be done in future studies with the CPV model. A simple extension is to consider the Bose symmetrization of the decay amplitude by the exchange of the identical pions or kaons. Moreover, the high-energy region can be explored, where likely the contribution of the double charm scattering and its coupling to the KK and $\pi\pi$ channels might play a role. One possible way of including these scattering amplitudes is to extend the ideas presented in Sec. 2.1.7, for parametrizing and fixing the T-matrix, as it corresponds to an essential input of the CPV model. The fit in the low mass region can also be improved by introducing the s-wave elastic scattering matrix $t_{\pi\pi,\pi\pi}$, which take into account, among other effects, the $f_0(500)$ (or σ) resonance [68].

Other two crucial structures, but more challenging to be implemented, are three-body final state interactions and realistic partonic amplitudes. For the first, the

model based on the inhomogeneous Faddeev-Bethe-Salpeter three-body equation presented in Sec. 2.3 and Ref. [25] must be brought into line with the CP asymmetry formula derived in Sec. 2. The development of realistic partonic amplitudes for three final state pions could start by considering the pion BS amplitude as obtained in Chap. 6. When kaons are involved, the fermion-antifermion BSE needs to be generalized by considering mass unbalanced systems, similarly to what was done for the fermion-boson bound state in Chap. 5 and Ref. [48].

Explicitly taking into account the CPT constraint is rarely done in calculations performed through short distance factorization approaches. The fact that decay channels are coupled by final state interactions implies, within the CPV model developed in this thesis, that the asymmetry generated by short distance mechanisms must be suppressed in specific B decay processes involving one pseudoscalar and one vector meson in the final state [24]. For testing this strong remark with experimental data, it is proposed a simple and practical method to extract the CP asymmetry of $B \to PV$ decays from the experimental three- body phase space. If the CPT constraint is implemented in the way it was presented in the CP violation formulation of Sec. 2.1, one can expect a strong suppression of the CP asymmetry in $B \to PV$ processes, as suggested by the toy Monte Carlo simulations performed in Ref. [24].

An alternative framework to account for three-body final state interactions in heavy meson decays has been developed, by describing the $B^+ \to K^- \pi^+ \pi^+$ decay amplitude through the s-wave $K\pi$ scattering amplitude and the Faddeev decomposition of the Bethe-Salpeter equation [25]. As the CPV model, this framework calls for the proper insertion of the short distance physics, which involves the evaluation of the microscopic decay amplitudes. The most challenging ingredients to obtain for the calculation are the proper representation of the mesonic vertexes, as their dynamical content needs to be accessed non-perturbatively and in Minkowski space.

The mesonic bound state vertexes, essential inputs necessary to evaluate the partonic decay amplitudes, created the demand for deeper understanding of the bound state structure. Properly representing such bound systems requires a non-perturbative approach and access to decay amplitudes which are defined in Minkowski space. All this has motivated the studies which are the backbone of the rest of the thesis. To embody the non-perturbative physics of the bound states, the homogeneous Bethe- Salpeter equation is adopted. A spinless two-body system was chosen as the starting point, aiming at exploring the effects of the truncation of the interaction kernel on the solutions. An ansatz was introduced for the BS amplitude, the Nakanishi integral representation, that allows one to make explicit its analytical structure. After that, the whole equation is projected onto the light-front to obtain a non-singular integral equation for the Nakanishi weight function, suitable to be solved numerically. Both the valence light-front and the elastic electromagnetic form factor are studied in detail after including both ladder and ladder plus cross-ladder kernels [41].

Although the impact of the inclusion of the cross-ladder is sizable, the valence wave function is found to be independent of the kernel at low transverse momentum, being determined by the given binding energy. Moreover, it was found that it is possible to naively factorize the dependencies of the valence wave function in terms of the longitudinal and transverse momentum distributions for the asymptotic large momentum behavior. For fixed binding energy and a proper normalization at zero

transverse momentum, the dependence on the longitudinal momentum fraction is found to be very well represented by an universal function in the asymptotic valence wave function. The functional form approaches the Wick-Cutkosky solution $|\xi(1-\xi)|^2$. As the impact from the generalized ladder kernel on the coupling constant was computed in Euclidean space in Ref. [105], one can predict the asymptotic form for large momentum of the valence wave function from the proposed conjecture.

Following from the gauging of the cross-ladder kernel, the two-body current contribution is computed for the elastic electromagnetic form factor. Due to the symmetry under the exchange of initial and final four-momenta in the photoabsorption amplitude, it was shown that the impulse and two-body contributions to the form factor conserve the current independently. Calculating the transition form factor, e.g. from the ground to the excited state, would be an intriguing and non-trivial check of the current conservation, as the matrix element of the current operator would depend on the overlap of both BS amplitudes of the initial and final states. Furthermore, the two-body current is found to be 15% of the elastic form factor at zero momentum transfer for strongly bound systems. In the large momentum region the behavior for the contributions from the impulse and two-body current to the form factor was derived analytically through counting rules. The asymptotic behavior found numerically agrees very well with counting rules, particularly when the log correction is introduced in the asymptotic formula for the contribution of the two-body current to the form factor.

The significant effect found by introducing one cross-ladder diagram in the BSE kernel implies that higher order non-planar graphs should be considered for the interaction kernel for practical calculations. Nevertheless, turning the approach into a scalar QCD model by means of the inclusion of the color degrees of freedom brings a completely different scenario in that regard [43]. As presented in Sec. 3.2, the impact of the cross-ladder contribution is highly suppressed for all the considered quantities, i.e binding energy, valence wave function and electromagnetic form factor. That happens already for $N_c = 3$ and by counting the color factors of higher order diagrams one can expect even strong suppression beyond the first non-planar diagrams. This finding is remarkable, as it supports rainbow-ladder truncations for practical calculations within continuous QCD.

A relatively simple, but extremely interesting, exploration that could be done in the future would be to consider the cross-ladder impact in unbalanced bosonic mass systems for different regimes of the ratio between the constituent boson masses. The Nakanishi representation for unequal particles was already introduced in Ref. [48] and could be used to represent the BS amplitude of such a system. The limiting case where $m_1 \to \infty$ with the other boson mass m_2 kept fixed and finite, can be investigated the fundamental role of the cross-ladder diagrams in order to recover the one-body limit of BSE, according to the theoretical expectation [179]. Further understanding of the impact on the spectrum, and momentum distributions of the excited states, for instance, would bring more robustness for the study.

In perspective, one can think on introducing the color degrees of freedom in the unbalanced mass system, to study how the suppression of the non-planar diagrams happens when $m_1 >> m_2$ is of interest. It could be investigated numerically the number of colors N_c needed to recover the one-body limit from the BSE in the ladder approximation. A more challenging problem, is how to enclose the essential features

from confinement in the BSE kernel. Following Refs. [158], one could introduce the spectral representation of the interaction kernel with derivatives of the Dirac delta to account for the behavior in the infrared region. This study is imperative in order to turn the BS approach into framework able to describe bound state hadronic systems.

After accumulating knowledge on the two-body BSE, the three-body Faddeev-Bethe-Salpeter equation with zero-range interaction has been for the first time addressed, both in Euclidean [45] and Minkowski [46] spaces. For studying the role of higher Fock-space contributions, the light-front equation has been also solved. The BSE implicitly incorporates effective three-body forces of relativistic origin, resulting in a huge attraction with strong effects on the observables, as seen for the spectrum and transverse momentum amplitudes in Sec. 4.1.4. The result suggests that valence inspired models hardly have the full dynamical content for practical purposes. Moreover, by tuning the two-body scattering amplitude it is found that, when it corresponds to a reasonably strong two-body interaction, a deeply bound three-body Borromean system arises as ground state. This feature was missed in previous light-front calculations [138, 139], as only interactions producing two-body bound states were considered.

In Minkowski space the three-body BSE has been solved by standard analytical and numerical methods [47], where (i) no ansatz or assumption has been introduced to represent the BS amplitude and (ii) the singularities from the kernel are treated analytically and numerically directly in the four-dimensional equation. The outcome for the amplitude is highly peaked, indicating the presence of a singular behavior as shown in Sec. 4.2.2, very different from the amplitude found through the Wick-rotated equation in Sec. 4.1.4. However, although the BS amplitudes from the solution in Euclidean and Minkowski spaces are fundamentally different, they can be compared by means of the transverse amplitude. The comparison shows a notable agreement, giving more confidence on the reliability of the direct integration method. One interesting direction for future explorations of the three-body system is to consider particles with non-equal masses. This allows to explore excited states and, therefore, the Efimov phenomena relativistically. The relativistic effect on the Efimov ratio, very well studied in non-relativistic approaches, is a promising example. Exploring how the ratio converges to the non-relativistic limit when higher excited levels are considered could bring interesting outcomes. Worth mentioning that the three-boson BSE in Minkowski space presents a kernel similar to the quark exchange diagrams in quark-diquark models [102] in the constituent quark picture. Therefore, the solutions obtained in this thesis for the Minkowski space equation can be interesting also in that context.

Noteworthy that due to the need of dealing with singularities numerically, the direct integration method can make challenging the extension of the approach for more sophisticated systems, e.g. involving finite range interactions or spin degrees of freedom. Therefore, the Faddeev-Bethe-Salpeter equation has been derived through the introduction of an integral representation in Sec. 4.3. In this case, the task should be numerically less demanding than the brute force integration of the Faddeev BSE. The integral representation of the amplitudes shows the presence of cuts and branching points, which could be responsible for the singular behavior found in the previous numerical studies [46, 144]. A formal aspect that requires further

elaboration is the relation of the proposed integral representation of the vertex and the NIR of the full three-body BS amplitude.

The treatment of spin dof is a major step forward while setting a Minkowskian framework, which would allow one to exploit in-depth phenomenological investigations, like CPV in heavy meson decays. In view of this, the BSE for the unequal mass system composed by a scalar boson and a fermion interacting through a scalar or vector boson was also solved in Minkowski and Euclidean spaces [48]. As in the two-boson case, the NIR together with the light-front projection are adopted to derive a non-singular integral equation, which is solved numerically. It is the first time that the NIR is considered for an unbalanced mass system. This formalism can be used to model baryons by means of an effective three-body quark-diquark system. The comparison between the coupling constants obtained in Euclidean and Minkowski spaces show fair agreement for $B/\bar{m} \lesssim 1.2$, for the scalar exchange, and for $B/\bar{m} \lesssim 0.5$, for the vector one. While further investigation is needed in the scalar exchange case, the limit on the binding where the solution can be obtained in the vector exchange case comes from the fact that the equation is scale invariant in the ultraviolet regime. As presented in Sec. 5.2, the scale invariant regime allows one to predict other features original BSE solution with the vector exchange kernel in the high momentum regime, where the equation becomes much simpler. For example, in the large transverse momentum region the fermion in the anti-aligned spin configuration prefers to carry most of the total longitudinal momentum, as follows from the enhancement of the corresponding Nakanishi weight function for $z \to 1$ shown in Sec. 5.2.2. Nevertheless, it remains to be investigated the case of the spin aligned configuration in the asymptotic momentum region. It should be pointed out the appealing presence of a feature that needs a careful analysis in the future: beyond the maximum real value of the coupling constant the solutions are log-periodic and proper analytical and numerical methods are required. Further developments of this study can also bring interesting outcomes showing an analogous behavior like the Efimov phenomena, but now in the relativistic context.

Finally, the fermion-antifermion homogeneous BSE is solved for a $J^\pi = 0^+$ state in Minkowski space through the same framework used for the two-boson and scalar-fermion systems. The ladder approximation is adopted, following the suppression found for the scalar QCD model for $N_c = 3$. The Dirac structure of the BS amplitude together with the fermion propagators bring extra end-point singularities that need to be properly treated while performing the light-front projection. Following the method developed in Ref. [50] that can be overcome. Since the goal now is to use the approach for phenomenological purposes, the covariant normalization of the BS amplitude was applied so that one can recover the probabilistic interpretation of the light-front wave function. The valence probability found for the fermionic system is very similar to the one found for the two-boson case [39], below 70% for strongly bound systems [167]. The effect from contributions beyond the valence component is not as dramatic as seen in the three-boson system, but a correction of about 30% still makes very challenging to apply valence inspired models for practical purposes. Obviously at the current status the approach still lacks of, e.g., dressed propagators, a confining kernel and considering the gauge invariance, and including those features, needed for dealing with realistic systems, could drastically change the conclusions obtained here.

The fermion-antifermion BSE for an unbalanced mass system, by using the NIR for different masses implemented for the boson-fermion system, is a natural upcoming problem to be solved. Although challenging, since the symmetry over the exchange of the fermions is lost, this is a fundamental step as it would pave the way to explore other mesons, beyond the pion. Furthermore, one could compute the inelastic form factor for the fermionic system and implement confinement in the BSE kernel, once the matter is clearly understood for the simpler two-boson equation.

Following the several aforementioned advancements, mostly formal, within the BS approach, a phenomenological model of the pion was further developed [163], following the first steps made in Ref. [51]. As the BSE equation for two fermions interacting through a vector boson exchange is also scale invariant in the asymptotic regime, introducing a new scale through a form factor to account for the vertex interaction is essential. This new parameter is chosen to be around Λ_{QCD}. The effective constituent masses are fixed from lattice QCD calculations available in the literature. The decay constant is found to be $f_\pi = 94$ MeV, in fair agreement with the experimental value. Moreover, the transverse and longitudinal amplitudes, the general parton distribution in the DGLAP region and the elastic electromagnetic form factor are computed, all from the valence light-front wave functions. The form factor is computed from the GPD, normalized to one at zero momentum transfer and compared with experimental data, showing a fair agreement. Although still rudimentary, the model presents a nice description of the pion and can be used as first dynamical input for the partonic decay amplitudes which enters the model for the CP violation. An important breakthrough would be to evaluate the partonic decay amplitudes using the BS amplitudes computed in Minkowski space, insert the result in the three-body FSI model presented in Sec. 2.3 and make the resulting decay amplitude compatible with the CPT invariant formalism for the CP asymmetry developed in Sec. 2.1. This model would enclose a quite complete description of heavy meson decays and could be used to analyzed various three-body phase spaces.

One essential point is the proper consideration of the dressed propagators and the vertex interaction through the gap-equation in Minkowski space, using spectral representations (see e.g. Refs. [180, 181]). Coupling gap-equation and BS equations in a framework fully established in Minkowski space, would bring the BS approach into a completely different level, i.e. analogous to the one already reached in the Euclidean space [155, 156]. This goal could make wider and sounder the application of the so-called *continuous QCD*, making possible to set a common playground with the lattice QCD community.

Appendix A

CPV formulas

The real and imaginary parts of $F_R^{\mathrm{BW}}(s)$ are given, respectively, by

$$\Re\left[F_R^{\mathrm{BW}}\right] = \frac{m_R^2 - s}{(m_R^2 - s)^2 + m_R^2 \Gamma_R(s)^2}, \tag{A.1}$$

and

$$\Im\left[F_R^{\mathrm{BW}}\right] = \frac{m_R \Gamma_R(s)}{(m_R^2 - s)^2 + m_R^2 \Gamma_R(s)^2}. \tag{A.2}$$

The square modulus is

$$|F_R^{\mathrm{BW}}|^2(s) = \frac{1}{(m_R^2 - s)^2 + m_R^2 \Gamma_R(s)^2}. \tag{A.3}$$

By using the relations

$$\Im(iz) = \Re(z), \quad \Im(z_1 z + z_2 z^*) = \Re(z)\Im(z_1 + z_2) + \Im(z)\Re(z_1 - z_2),$$
$$\Re(z_1^* z_2) = \Re(z_1)\Re(z_2) + \Im(z_1)\Im(z_2), \text{and} \Im(z_1^* z_2) = \Re(z_1)\Im(z_2) - \Im(z_1)\Re(z_2), \tag{A.4}$$

together with Eqs. (A.2)-(A.3), one can finally write Eq. (2.31) as it was written in Eq. (2.35).

An alternative to parametrize the decay amplitude, convenient for Monte-Carlo simulations, is to write Eq. (2.30) as

$$\mathcal{A}_{0\lambda}^{\pm} = a_{\pm}^{\rho} e^{i\delta_{\pm}^{\rho}} F_{\rho}^{\mathrm{BW}} k(s) \cos\theta + a_{\pm}^{f} e^{i\delta_{\pm}^{f}} F_f^{\mathrm{BW}} + \frac{a_{\pm\lambda}^{nr} e^{i\delta_{\pm\lambda}^{nr}}}{1 + \frac{s}{\Lambda_\lambda^2}}, \tag{A.5}$$

where $\delta_{\pm}^{\rho}$ and $\delta_{\pm}^{f}$ contain both the fixed weak and strong phases, with the Breit-Wigner functions introducing additional mass dependent strong phases as sketched above. The phase $\delta_{\pm}^{nr}$ comes from the partonic amplitude producing the three-body final state, excluding the strong phase from the rescattering process. The relation between the parameters is $a_{\pm}^{\rho} e^{i\delta_{\pm}^{\rho}} = a_0^{\rho} + b_0^{\rho} e^{\pm i\gamma}$, $a_{\pm}^{f} e^{i\delta_{\pm}^{f}} = a_0^{f} + b_0^{f} e^{\pm i\gamma}$, and $a_{\pm\lambda}^{nr} e^{i\delta_{\pm\lambda}^{nr}} = a_{0\lambda}^{nr} + b_{0\lambda}^{nr} e^{\pm i\gamma}$.

The parameters of the model can be written in terms of those in Eqs. (2.30) or (A.5), as explicitly presented below

$$\mathcal{A} = 4(\sin\gamma)\Im\,[a^{nr}_{0\lambda}b^{nr*}_{0\lambda}] = (a^{nr}_{+\lambda})^2 - (a^{nr}_{-\lambda})^2, \tag{A.6}$$

$$\mathcal{B} = 4(\sin\gamma)\Re\,[a^{nr}_{0\lambda'}b^{nr*}_{0\lambda} - a^{nr}_{0\lambda}b^{nr*}_{0\lambda'}], \tag{A.7}$$

$$\mathcal{B}' = -4(\sin\gamma)\Im\,[a^{nr}_{0\lambda'}b^{nr*}_{0\lambda} + a^{nr}_{0\lambda}b^{nr*}_{0\lambda'}], \tag{A.8}$$

$$\mathcal{C} = 4(\sin\gamma)\,\Im\,[a^{\rho}_{0}b^{\rho*}_{0}] = (a^{\rho}_{+})^2 - (a^{\rho}_{-})^2, \tag{A.9}$$

$$\begin{aligned}\mathcal{D} &= 4(\sin\gamma)\Im\,[a^{\rho}_{0}b^{nr*}_{0\lambda} + a^{nr}_{0\lambda}b^{\rho*}_{0}]\\ &= 2[a^{\rho}_{+}a^{nr}_{+\lambda}\cos(\delta^{\rho}_{+} - \delta^{nr}_{+\lambda}) - a^{\rho}_{-}a^{nr}_{-\lambda}\cos(\delta^{\rho}_{-} - \delta^{nr}_{-\lambda})],\end{aligned} \tag{A.10}$$

$$\begin{aligned}\mathcal{D}' &= 4(\sin\gamma)\Im\,[a^{\rho}_{0}b^{nr*}_{0\lambda'} + a^{nr}_{0\lambda'}b^{\rho*}_{0}]\\ &= 2[a^{\rho}_{+}a^{nr}_{+\lambda'}\cos(\delta^{\rho}_{+} - \delta^{nr}_{+\lambda'}) - a^{\rho}_{-}a^{nr}_{-\lambda'}\cos(\delta^{\rho}_{-} - \delta^{nr}_{-\lambda'})],\end{aligned} \tag{A.11}$$

$$\begin{aligned}\mathcal{E} &= 4(\sin\gamma)\Re\,[a^{\rho}_{0}b^{nr*}_{0\lambda} - a^{nr}_{0\lambda}b^{\rho*}_{0}]\\ &= -2[a^{\rho}_{+}a^{nr}_{+\lambda}\sin(\delta^{\rho}_{+} - \delta^{nr}_{+\lambda}) - a^{\rho}_{-}a^{nr}_{-\lambda}\sin(\delta^{\rho}_{-} - \delta^{nr}_{-\lambda})],\end{aligned} \tag{A.12}$$

$$\begin{aligned}\mathcal{E}' &= 4(\sin\gamma)\Im\,[-a^{\rho}_{0}b^{nr*}_{0\lambda'} + a^{nr}_{0\lambda'}b^{\rho*}_{0}]\\ &= 2[a^{\rho}_{+}a^{nr}_{+\lambda'}\sin(\delta^{\rho}_{+} - \delta^{nr}_{+\lambda'}) + a^{\rho}_{-}a^{nr}_{-\lambda'}\sin(\delta^{\rho}_{-} - \delta^{nr}_{-\lambda'})],\end{aligned} \tag{A.13}$$

$$\begin{aligned}\mathcal{F} &= 4(\sin\gamma)\Im\,\left[a^{f}_{0}b^{\rho*}_{0} + a^{\rho}_{0}b^{f*}_{0}\right]\\ &= 2[a^{\rho}_{+}a^{f}_{+}\cos(\delta^{\rho}_{+} - \delta^{f}_{+}) - a^{\rho}_{-}a^{f}_{-}\cos(\delta^{\rho}_{-} - \delta^{f}_{-})],\end{aligned} \tag{A.14}$$

$$\begin{aligned}\mathcal{G} &= 4(\sin\gamma)\Re\,\left[a^{f}_{0}b^{\rho*}_{0} - a^{\rho}_{0}b^{f*}_{0}\right]\\ &= 2[a^{\rho}_{+}a^{f}_{+}\sin(\delta^{\rho}_{+} - \delta^{f}_{+}) - a^{\rho}_{-}a^{f}_{-}\sin(\delta^{\rho}_{-} - \delta^{f}_{-})],\end{aligned} \tag{A.15}$$

$$\begin{aligned}\mathcal{H} &= 4(\sin\gamma)\Im\,\left[a^{f}_{0}b^{nr*}_{0\lambda} + a^{nr}_{0\lambda}b^{f*}_{0}\right]\\ &= 2[a^{f}_{+}a^{nr}_{+\lambda}\cos(\delta^{f}_{+} - \delta^{nr}_{+\lambda}) - a^{f}_{-}a^{nr}_{-\lambda}\cos(\delta^{f}_{-} - \delta^{nr}_{-\lambda})],\end{aligned} \tag{A.16}$$

$$\begin{aligned}\mathcal{H}' &= 4(\sin\gamma)\Im\,\left[a^{f}_{0}b^{nr*}_{0\lambda'} + a^{nr}_{0\lambda'}b^{f*}_{0}\right]\\ &= 2[a^{f}_{+}a^{nr}_{+\lambda'}\cos(\delta^{f}_{+} - \delta^{nr}_{+\lambda'}) - a^{f}_{-}a^{nr}_{-\lambda'}\cos(\delta^{f}_{-} - \delta^{nr}_{-\lambda'})],\end{aligned} \tag{A.17}$$

$$\begin{aligned}\mathcal{P} &= 4(\sin\gamma)\Re\,\left[a^{f}_{0}b^{nr*}_{0\lambda} - a^{nr}_{0\lambda}b^{f*}_{0}\right]\\ &= -2[a^{f}_{+}a^{nr}_{+\lambda}\sin(\delta^{f}_{+} - \delta^{nr}_{+\lambda}) - a^{f}_{-}a^{nr}_{-\lambda}\sin(\delta^{f}_{-} - \delta^{nr}_{-\lambda})],\end{aligned} \tag{A.18}$$

$$\begin{aligned}\mathcal{P}' &= 4(\sin\gamma)\Im\,\left[-a^{f}_{0}b^{nr*}_{0\lambda'} + a^{nr}_{0\lambda'}b^{f*}_{0}\right]\\ &= 2[a^{f}_{+}a^{nr}_{+\lambda'}\sin(\delta^{f}_{+} - \delta^{nr}_{+\lambda'}) + a^{f}_{-}a^{nr}_{-\lambda'}\sin(\delta^{f}_{-} - \delta^{nr}_{-\lambda'})],\end{aligned} \tag{A.19}$$

and

$$\mathcal{Q} = 4(\sin\gamma)\Im\,\left[a^{f}_{0}b^{f*}_{0}\right] = (a^{f}_{+})^2 - (a^{f}_{-})^2. \tag{A.20}$$

Appendix B

Three-body FSI in the LF framework

B.1 Parametrization of the S-matrix

The parametrization for the S-matrix, $S_{K\pi}^{1/2}$, is written as

$$S_{K\pi}^{1/2} = \frac{k\cot\delta + i\,k}{k\cot\delta - i\,k}\, \prod_{r=1}^{3} \frac{M_r^2 - M_{K\pi}^2 + iz_r\bar{\Gamma}_r}{M_r^2 - M_{K\pi}^2 - iz_r\Gamma_r} \tag{B.1}$$

where $z_r = k\,M_r^2/(k_r\,M_{K\pi})$. The center-of-mass momentum of the mesons in the $K\pi$ pair, following the system kinematics, is

$$k^2 = \left(\frac{M_{K\pi}^2 + m_\pi^2 - m_K^2}{2\,M_{K\pi}}\right)^2 - m_\pi^2\;. \tag{B.2}$$

The $K_0^*(1430)$, $K_0^*(1630)$ and $K_0^*(1950)$ resonances fix the parameters through the experimental data, i.e. $(M_r, \Gamma_r, \bar{\Gamma}_r)$, and quantitatively given by $(1.48, 0.25, 0.25)$, $(1.67, 0.1, 0.1)$ and $(1.9, 0.2,\ 0.14)$, respectively [99].

From the S-matrix of Eq. (B.1), including the proper kinematical factors, the τ amplitude entering in Eq. (2.52) reads

$$\tau_{I_{K\pi}}\left(M_{K\pi}^2\right) = 4\pi\,\frac{M_{K\pi}}{k}\left(S_{K\pi}^{I_{K\pi}} - 1\right). \tag{B.3}$$

The non-resonant part is parameterized through a simple effective range expansion, i.e. $k\cot\delta = \frac{1}{a} + \frac{1}{2}r_0\,k^2$, where $a = 1.6$ GeV^{-1} and $r_0 = 3.32$ GeV^{-1} are the fixed parameters. This parametrization gives a fair agreement when compared to the LASS experimental data for both modulus and phase shift, as discussed in detail in Ref. [59]. The $I = 3/2$ state is a non-resonant s-wave $K\pi$ amplitude, and will also be parametrized by an effective range expansion as follows

$$S_{K\pi}^{3/2} = \frac{k\cot\delta + i\,k}{k\cot\delta - i\,k} = \frac{\frac{1}{a_{I=3/2}} + \frac{1}{2}r_{0,I=3/2}\,k^2 + ik}{\frac{1}{a_{I=3/2}} + \frac{1}{2}r_{0,I=3/2}\,k^2 - ik},$$

with the effective range expansion parameters for this case fixed by $a_{I=3/2} = -1.00$ GeV^{-1} and $r_{0,I=3/2} = -1.76$ GeV^{-1}, from Ref. [182].

B.2 Further details on the LF equation

After the projection onto the LF hyperplane and some convenient manipulations, discussed in great detail in Ref. [59], the LF integral equation (2.52) reads

$$\xi^i(y, \vec{k}_\perp) = \xi_0^i(y, \vec{k}_\perp) + \tag{B.4}$$
$$+ \ \frac{i}{2(2\pi)^3} \int_0^{1-y} \frac{dx}{x(1-x-y)} \int d^2 q_\perp \left[\frac{\tau_j \left(M_{ik}^2(x, q_\perp) \right) \xi^j(x, \vec{q}_\perp)}{M^2 - M_0^2(x, \vec{q}_\perp; y, \vec{k}_\perp) + i\varepsilon} + (j \leftrightarrow k) \right],$$

where $M^2 = K^\mu K_\mu$, $y = k_i^+/K^+$ and $x = q_{j,k}^+/K^+$. The free LF three-body squared mass is given by

$$M_0^2(x, \vec{q}_\perp; y, \vec{k}_\perp) = \frac{k_\perp^2 + m_i^2}{y} + \frac{q_\perp^2 + m_j^2}{x} + \frac{(\vec{k}_\perp + \vec{q}_\perp)^2 + m_k^2}{1 - x - y}. \tag{B.5}$$

Moreover, in the LF, the argument of the two-body amplitude $\tau_j \left(M_{ik}^2(x, q_\perp) \right)$ is written as

$$M_{ik}^2(x, q_\perp) = (1 - x) \left(M^2 - \frac{q_\perp^2 + m_j^2}{x} \right) - q_\perp^2. \tag{B.6}$$

The driving term of Eq. (2.53) is rewritten in the LF as

$$\xi_0^i(y, \vec{k}_\perp) = \tag{B.7}$$
$$= \ \frac{i}{2(2\pi)^3} \int_0^{1-y} \frac{dx}{x(1-y-x)} \int d^2 q_\perp \frac{B_0(x, \vec{q}_\perp; y, \vec{k}_\perp)}{M^2 - M_0^2(x, \vec{q}_\perp; y, \vec{k}_\perp) + i\varepsilon} = B_0 \, \xi_0(y, k_\perp),$$

where B_0, the short-distance amplitude, is naively assumed to be a constant.

The integral in Eq. (B.8), over the transverse momentum, $\vec{q}_\perp = (q^1, q^2)$, is not finite and needs to be regularized. Therefore, a finite subtraction is made in the integration kernel and a finite parameter, $\lambda(\mu^2)$, introduced at the subtraction point. Applying this method one gets the following finite expression for the driving term,

$$\xi_0(y, k_\perp) = \lambda(\mu^2) + \frac{i}{2} \int_0^1 \frac{dx}{x(1-x)} \int_0^{2\pi} d\theta \int_0^\infty \frac{dq_\perp q_\perp}{(2\pi)^3} \times$$
$$\times \left[\frac{1}{M_{K\pi}^2(y, k_\perp) - M_{0,K\pi}^2(x, q_\perp) + i\varepsilon} - \frac{1}{\mu^2 - M_{0,K\pi}^2(x, q_\perp)} \right] \tag{B.8}$$

where the free squared-mass of the $K\pi$ system is given by

$$M_{0,K\pi}^2(x, q_\perp) = \frac{q_\perp^2 + m_\pi^2}{x} + \frac{q_\perp^2 + m_K^2}{1 - x}.$$

Now one can perform the integrations over θ and $q_\perp$ on Eq. (B.8) and finally obtain the following for the driving term

$$\xi_0(y, k_\perp) = \lambda(\mu^2) + \frac{i}{4} \int_0^1 \frac{dx}{(2\pi)^2} \ln \frac{(1-x)(x M_{K\pi}^2(y, k_\perp) - m_\pi^2 + ix\varepsilon) - x m_K^2}{(1-x)(x\mu^2 - m_\pi^2) - x m_K^2}. \tag{B.9}$$

Notice that the parameter ϵ is kept finite, to naively consider the absorption to other decay channels. This parameter also helps to achieve numerical stability more easily.

The last step before going through the numerical calculations is to perform the isospin decomposition of the decay amplitude. There are two possible total isospin states, namely, $I_T = 5/2$ and $3/2$. In the adopted notation, the bachelor amplitude has the total, I_T, the projection, I_T^z, and the interacting pairs, $I_{K\pi(K\pi')}$ isospin indexes, i.e. $\xi_{I_T,I_{K\pi}}^{I_T^z}(y, k_\perp)$. The state vector decomposed in terms of the source amplitude $(K\pi)$ isospin states, reads

$$|B_0\rangle = \sum_{I_T,I_{K\pi}} \alpha_{I_T,I_{K\pi}}^{I_T^z} |I_T, I_{K\pi}, I_T^z\rangle + \sum_{I_T,I_{K\pi'}} \alpha_{I_T,I_{K\pi'}}^{I_T^z} |I_T, I_{K\pi'}, I_T^z\rangle. \tag{B.10}$$

As said, there is no dependence on the momentum variables and the normalization is arbitrary. One can introduce re-coupling coefficients, defined as $R_{I_T,I_{K\pi},I_{K\pi'}}^{I_T^z} = \langle I_T, I_{K\pi}, I_T^z | I_T, I_{K\pi'}, I_T^z\rangle$ in the expressions. The set of isospin coupled integral equations can then be written as

$$\xi_{I_T,I_{K\pi}}^{I_T^z}(y, k_\perp) = \langle I_T, I_{K\pi}, I_T^z | B\rangle \, \xi_0(y, k_\perp)$$
$$+\frac{i}{2} \sum_{I_{K\pi'}} R_{I_T,I_{K\pi},I_{K\pi'}}^{I_T^z} \int_0^{1-y} \frac{dx}{x(1-y-x)} \int_0^\infty \frac{dq_\perp}{(2\pi)^3} K_{I_{K\pi'}}(y, k_\perp; x, q_\perp) \, \xi_{I_T,I_{K\pi'}}^{I_T^z}(x, q_\perp),$$

$$\tag{B.11}$$

where the free squared mass explicitly for the $K\pi\pi$ system reads

$$M_{0,K\pi\pi}^2(x, q_\perp, y, k_\perp) = \frac{k_\perp^2 + m_\pi^2}{y} + \frac{q_\perp^2 + m_\pi^2}{x} + \frac{q_\perp^2 + k_\perp^2 + 2q_\perp k_\perp \cos\theta + m_K^2}{1-x-y},$$

$$\tag{B.12}$$

and the squared-mass of the virtual $K\pi$ system is

$$M_{K\pi}^2(z, p_\perp) = (1-z)\left(M_B^2 - \frac{p_\perp^2 + m_\pi^2}{z}\right) - p_\perp^2.$$

And, finally, the kernel carrying the $K\pi$ interaction amplitude takes the following form

$$K_{I_{K\pi'}}(y, k_\perp; x, q_\perp) = \int_0^{2\pi} d\theta \, \frac{q_\perp \, \tau_{I_{K\pi'}}\left(M_{K\pi'}^2(x, q_\perp)\right)}{M_B^2 - M_{0,K\pi\pi}^2(x, q_\perp, y, k_\perp) + i\varepsilon}. \tag{B.13}$$

Appendix C

Derivation of the two-body scattering amplitude

The derivations presented in this appendix are based on Ref. [144]. For the contact interaction (with the vertex λ), the two-body amplitude $\mathcal{F}(M_{12}^2)$ is given by the infinite sum of graphs shown in Fig. 1(a) in [138]. The first contribution is simply $i\lambda$, the second one is $(i\lambda)^2\mathcal{B}$, where $\mathcal{B}$ is the amputated from $(i\lambda)^2$ the bubble graph, etc. That is:

$$i\mathcal{F}(M_{12}^2) = i\lambda + (i\lambda)^2\mathcal{B} + (i\lambda)^3\mathcal{B}^2 + \ldots =$$
$$\frac{i\lambda}{1 - (i\lambda)\mathcal{B}(M_{12}^2)} = \frac{1}{(i\lambda)^{-1} - \mathcal{B}(M_{12}^2)}, \tag{C.1}$$

or

$$\mathcal{F}(M_{12}^2) = \frac{1}{i[(i\lambda)^{-1} - \mathcal{B}(M_{12}^2)]} \tag{C.2}$$

where

$$\mathcal{B}(M_{12}^2) =$$
$$\int \frac{d^4k}{(2\pi)^4} \frac{i}{(k^2 - m^2 + i\epsilon)} \frac{i}{[(k-p)^2 - m^2 + i\epsilon]}. \tag{C.3}$$

Here m denotes the boson mass, and p now is the total 4-momentum of the two-body subsystem, $p^2 = M_{12}^2$. One way to calculate $\mathcal{B}(M_{12}^2)$ is to use the standard Feynman parametrization, i.e.

$$\frac{1}{a\,b} = \int_0^1 \frac{dv}{[va + (1-v)b]^2},$$

with $a = k^2 - m^2 + i\epsilon$, $b = (k-p)^2 - m^2 + i\epsilon$, and then compute the 4D integral in the Euclidean space. However, for $M_{12}^2 \geq 4\,m^2$, the integrand of this integral becomes singular and this method is not so convenient.

Therefore, to calculate the amplitude (especially for $M_{12}^2 > 4\,m^2$) in the most simple way, it can be used another method, not related to the Feynman parametrization, and the integration in the 4D Euclidean space. Namely, in the initial integral (C.3) (written in the c.m.-frame $\vec{p} = 0$) the integration over dk_0 will be carried out

by residues, i.e.

$$
\begin{aligned}
\mathcal{B}(M_{12}^2) &= -\int \frac{dk_0 d^3k}{(2\pi)^4} \frac{1}{(k_0^2 - \vec{k}^2 - m^2 + i\epsilon)} \\
&\times \frac{1}{[(k_0 - M_{12})^2 - \vec{k}^2 - m^2 + i\epsilon]} = \\
&2\pi i(res_1 + res_2).
\end{aligned}
\tag{C.4}
$$

Here $res_{1,2}$ are the residues of the integrand in one of the two poles in the upper half plane of the complex variable k_0. The positions of the poles are

$$
k_0^{(1)} = -\varepsilon_k + i\epsilon, \quad k_0^{(2)} = M_{12} - \varepsilon_k + i\epsilon
$$

and the corresponding residues are given by

$$
res_1 = \int_0^L \frac{k_v^2 dk_v}{(2\pi)^3} \frac{1}{\varepsilon_k} \frac{1}{[(\varepsilon_k + M_{12})^2 - \varepsilon_k^2 + i\epsilon]},
\tag{C.5}
$$

$$
res_2 = \int_0^L \frac{k_v^2 dk_v}{(2\pi)^3} \frac{1}{(\varepsilon_k)} \frac{1}{[M_{12}(M_{12} - 2\varepsilon_k) + i\epsilon]},
\tag{C.6}
$$

where the integrals were regularized by introducing the upper limit L. If $-\infty < M_{12}^2 < 4m^2$, the integrals (C.5), (C.6) are non-singular ones. On the other hand, if $M_{12} > 2m$, the second residue is represented as a sum of two contributions. Namely, the principal value of the integral over dk_v and the delta-function contribution, i.e.

$$
\begin{aligned}
res_2 &= res_{2a} + res_{2b} \\
&\int_0^L \frac{k_v^2 dk_v}{(2\pi)^3} \frac{1}{[M_{12}(M_{12} - 2\varepsilon_k) + i\epsilon]} \frac{1}{\varepsilon_k} \\
&= PV \int_0^L \frac{k_v^2 dk}{(2\pi)^3} \frac{1}{M_{12}(M_{12} - 2\varepsilon_k)} \frac{1}{\varepsilon_k} \\
&+ \int_0^L \frac{k_v^2 dk}{(2\pi)^3} (-i\pi)\delta[M_{12}(M_{12} - 2\varepsilon_k)] \frac{1}{\varepsilon_k} = \frac{1}{2\pi i} \frac{y''}{16\pi}.
\end{aligned}
\tag{C.7}
$$

As the integral in k_v diverges, it is necessary to perform a regularization process. By renormalizing one can express the bare parameters (in this context, the coupling constant λ) by observables (usually, in the field theory, via the "physical" coupling constant). From the condition that the two-body system has a bound state with the mass M_{2B} and the amplitude (C.2) has a pole at $M_{12} = M_{2B}$, one finds for the coupling constant λ

$$
(i\lambda)^{-1} = \mathcal{B}(M_{2B}^2) = 2\pi i(res_1 + res_2).
\tag{C.8}
$$

The denominator in (C.2) then becomes

$$
\begin{aligned}
i[(i\lambda)^{-1} - \mathcal{B}(M_{12}^2)] &= i[\mathcal{B}(M_{2B}^2) - \mathcal{B}(M_{12}^2)] = \\
&i[2\pi i\, res_1(M_{12} = M_{2B}) + 2\pi i\, res_2(M_{12} = M_{2B})] \\
&- i[2\pi i\, res_1(M_{12}) + 2\pi i\, res_2(M_{12})] = \\
&i\, PV \int_0^\infty \frac{(M_{2B}^2 - M_{12}^2)k_v^2 dk_v}{32\pi^2\, \varepsilon_k \left[k_v^2 - \left(\frac{1}{4}M_{12}^2 - m^2\right)\right]} \\
&\times \frac{1}{\left[k_v^2 + \left(m^2 - \frac{1}{4}M_{2b}^2\right)\right]} - 2\pi i\, res_{2b}
\end{aligned}
\tag{C.9}
$$

In Eq. (C.9), the principal value integral takes into account the singularity at $k_v = \sqrt{\frac{1}{4}M_{12}^2 - m^2}$.

The integral (C.9) is convergent in the limit $k_v \to \infty$. Its calculation in different domains of the variable M_{12} results in Eq. (4.3). It should be noticed that above threshold $M_{12} > 2\,m$, the amplitude obtains a imaginary part, i.e.

$$\mathcal{F}(M_{12}^2) = \frac{1}{\frac{1}{8\pi^2}\left(\frac{y''}{2}\log\frac{1+y''}{1-y''} - \frac{\arctan y_{M_{2B}}}{y_{M_{2B}}}\right) - i\frac{y''}{16\pi}} \tag{C.10}$$

where

$$y'' = \frac{\sqrt{M_{12}^2 - 4m^2}}{M_{12}}.$$

C.1 Unitarity check

The amplitude (C.10), if correct, must be unitary. More precisely, the partial wave amplitude corresponding to (C.10), must be unitary, i.e., it can be represented via a *real* phase shift δ. This property is checked in the following.

In the derivation of the two-body amplitude, it was followed the definitions and normalization of Ref. [128]. According to it, the partial wave is defined as

$$F_L(k) = \frac{1}{32\pi}\int_{-1}^{1} dz\; P_L(z)F(k,z). \tag{C.11}$$

From Eq. (C.10) it is obtained for the s-wave scattering amplitude (i.e $M_{12} > 2m$) that

$$F_0 = \frac{1}{16\pi}\mathcal{F}(M_{12}^2) =$$
$$\frac{1}{\frac{2}{\pi}\left(\frac{y''}{2}\log\frac{1+y''}{1-y''} - \frac{\arctan y_{M_{2B}}}{y_{M_{2B}}}\right) - iy''} \tag{C.12}$$
$$\equiv \frac{1}{g(y'') - iy''},$$

where $g(y'')$ is a real function given by

$$g(y'') \equiv \frac{2}{\pi}\left(\frac{y''}{2}\log\frac{1+y''}{1-y''} - \frac{\arctan y_{M_{2B}}}{y_{M_{2B}}}\right). \tag{C.13}$$

The scattering amplitude is related to the phase shift by [47])

$$F_0 = \frac{\varepsilon_k}{k}\exp(i\delta_0)\sin\delta_0, \tag{C.14}$$

which is unitarity if the phase shift δ_0 is real. That is,

$$\delta_0 = \frac{1}{2i}\log\left(1 + \frac{2ik}{\varepsilon_k}F_0\right). \tag{C.15}$$

Since

$$\frac{k}{\varepsilon_k} = y'', \tag{C.16}$$

one gets that

$$\delta_0 = \frac{1}{2i} \log\left(1 + 2iy'' F_0\right) = \frac{1}{2i} \log \frac{g(y'') + iy''}{g(y'') - iy''}, \tag{C.17}$$

and by complex conjugation:

$$\delta_0^* = \frac{1}{-2i} \log \frac{g(y'') - iy''}{g(y'') + iy''} = \frac{1}{2i} \log \frac{g(y'') + iy''}{g(y'') - iy''} = \delta_0. \tag{C.18}$$

Therefore, the two-body scattering amplitude is thus unitary.

C.1.1   Scattering length and the effective radius

In non-relativistic quantum mechanics one deals with the s-wave amplitude $f_0(k)$ related to the phase shift by

$$f_0(k) = \frac{1}{2ik}\left(\exp(2i\delta_0(k)) - 1\right) = \frac{1}{k}\exp(i\delta_0(k)\sin\delta_0(k), \tag{C.19}$$

which also can be represented as

$$f_0(k) = \frac{1}{g_0(k) - ik}. \tag{C.20}$$

From Eqs. (C.19) and (C.12), it can be written

$$f_0(k) = \frac{1}{\varepsilon_k} F_0 = \frac{1}{\varepsilon_k} \frac{1}{[g(y'') - iy'']} = \frac{1}{g_0(k) - ik}, \tag{C.21}$$

where $g(y'')$ is given by Eq. (C.13) and $g_0(k) = \varepsilon_k g(y'')$. Here it was used that $y'' \varepsilon_k = k$.

Next, the function $g_0(k) = \varepsilon_k g(y'')$ can be decomposed in a series in k

$$g_0(k) \approx -\frac{1}{a} + \frac{1}{2} r_0 k^2, \tag{C.22}$$

with

$$a = \frac{\pi y_{M_{2B}}}{2m \arctan(y_{M_{2B}})},$$
$$r_0 = \frac{2\left[2y_{M_{2B}} - \arctan(y_{M_{2B}})\right]}{\pi m \, y_{M_{2B}}}, \tag{C.23}$$

where a and r_0 are correspondingly the scattering length and the effective radius. Since both are proportional to $1/m$ they have a relativistic origin. However, for small binding energy $B \ll m$ the variable $y_{M_{2B}}$ increases as $y_{M_{2B}} \sim \sqrt{m/B}$. The scattering length a also increases, whereas the effective radius r_0 tends to a constant:

$$B \to 0: \quad a = \frac{1}{\sqrt{Bm}}, \quad r_0 = \frac{4}{\pi m}. \tag{C.24}$$

C.2 Renormalization via scattering length

Above it was required that the two-body scattering amplitude (4.3) has a pole at $M_{12} = M_{2B}$. Indeed, the expression given by the second line of (4.3) has this pole. This singularity complicates the numerical calculations and requires a special treatment. To avoid this difficulty, it will be put a different condition: the requirement that the scattering amplitude at zero energy is equal to $-a$, where a is the two-body scattering length. For some values of a the two-body system has no bound state and the amplitude has no pole. Whereas, the three-body system still can be bounded.

The (non-renormalized) two-body amplitude $\mathcal{F}(M_{12}^2)$ still have the form (C.2). Its argument can be written as $M_{12} = 2\varepsilon_k = 2\sqrt{k^2 + m^2}$. For simplicity, one can write $\mathcal{F} = \mathcal{F}(k)$. According to (C.12) and (C.21), the s-wave amplitude $f_0(k)$ can be introduced, i.e.

$$f_0(k) = \frac{1}{16\pi\varepsilon_k}\mathcal{F}(k), \tag{C.25}$$

and the new renormalization condition then reads

$$f_0(k = 0) = \frac{1}{16\pi m}\mathcal{F}(k = 0) = -a, \tag{C.26}$$

where a is the scattering length. By using (C.2), one obtains

$$\frac{1}{16\pi m}\frac{1}{i[(i\lambda)^{-1} - \mathcal{B}(k = 0)]} = -a, \tag{C.27}$$

and therefore

$$(i\lambda)^{-1} = \mathcal{B}(k = 0) - \frac{1}{16i\pi ma}. \tag{C.28}$$

The amplitudes are then given by

$$f_0(k) = \frac{1}{16\pi\varepsilon_k i\left[\mathcal{B}(k = 0) - \mathcal{B}(k)\right] - \frac{\varepsilon_k}{ma}},$$
$$\mathcal{F}(k) = \frac{1}{i\left[\mathcal{B}(k = 0) - \mathcal{B}(k)\right] - \frac{1}{16\pi ma}}. \tag{C.29}$$

For safety and a smooth transition to the case $k = 0$, instead of $\mathcal{B}(0) - \mathcal{B}(k)$ it will be first calculated the auxiliary function

$$h(k'', k) \equiv i[\mathcal{B}(k'') - \mathcal{B}(k)] \tag{C.30}$$

and then take the limit $k'' \to 0$. From the expressions (C.4), (C.5), (C.6), one gets

$$h(k'', k) = i[\mathcal{B}(k'') - \mathcal{B}(k)] =$$
$$i\frac{(2\pi i)(4\pi)}{(2\pi)^4}PV\int_0^\infty \frac{4(k''^2 - k^2)}{(k'^2 - k^2)(k'^2 - k''^2)}\frac{k'^2 dk'}{\sqrt{k'^2 + m^2}}. \tag{C.31}$$

This expression (up to a factor) can be also obtained from the first term in Eq. (C.9), if the integration variable is replaced as $k \to k'$ and, then, putting $M_{12}^2 = \varepsilon_k^2$

and $M_{2B}^2 = \varepsilon_{k''}^2$. The principal value takes into account two singularities at $k' = k$ and $k' = k''$. By calculating this integral, one finds that

$$
\begin{aligned}
h(k'', k) =& \frac{1}{16\pi^2} \frac{k}{\varepsilon_k} \log \frac{\varepsilon_k + k}{\varepsilon_k - k} - \frac{i}{16\pi} \frac{k}{\varepsilon_k} \\
& - \frac{1}{16\pi^2} \frac{k''}{\varepsilon_{k''}} \log \frac{\varepsilon_{k''} + k''}{\varepsilon_{k''} - k''} + \frac{i}{16\pi} \frac{k''}{\varepsilon_k''}
\end{aligned}
\tag{C.32}
$$

Then, by taking $k'' = 0$ and substituting it in (C.29), one obtains

$$
f_0(k) = \frac{1}{\frac{k}{\pi} \log \frac{\varepsilon_k + k}{\varepsilon_k - k} - \frac{\varepsilon_k}{ma} - ik},
$$

$$
\mathcal{F}(k) = \frac{1}{\frac{1}{16\pi^2} \frac{k}{\varepsilon_k} \log \frac{\varepsilon_k + k}{\varepsilon_k - k} - \frac{1}{16\pi ma} - \frac{i}{16\pi} \frac{k}{\varepsilon_k}}
\tag{C.33}
$$

The amplitude $f_0(k)$ still has the form (C.12) with

$$
g(k) = \frac{k}{\pi} \log \frac{\varepsilon_k + k}{\varepsilon_k - k} - \frac{\varepsilon_k}{ma},
\tag{C.34}
$$

and it is thus unitary. At small k it has the following decomposition

$$
g(k) \approx -\frac{1}{a} + \frac{1}{2} r_0 k^2
\tag{C.35}
$$

where

$$
r_0 = \frac{4am - \pi}{am^2\pi}
\tag{C.36}
$$

The above expression was derived for the region $M_{12}^2 > 4m^2$. Furthermore, the term

$$
\frac{1}{16\pi^2} \frac{k}{\varepsilon_k} \log \frac{\varepsilon_k + k}{\varepsilon_k - k}
\tag{C.37}
$$

coincides with the term

$$
\frac{1}{8\pi^2} \frac{y''}{2} \log \frac{1 + y''}{1 - y''},
\tag{C.38}
$$

in Eq. (4.3), which is also valid for $M_{12}^2 > 4m^2$.

For the other intervals of M_{12}^2, the corresponding analytical expressions are given by

$$
\text{If } 0 \leq M_{12}^2 \leq 4\,m^2, \quad y' = \frac{M_{12}}{\sqrt{4m^2 - M_{12}^2}},
$$

$$
(0 \leq y' < \infty), \text{ then:}
$$

$$
\frac{1}{16\pi^2} y'' \log \frac{1 + y''}{1 - y''} \Rightarrow \frac{1}{8\pi^2} \frac{\arctan y'}{y'},
$$

and

$$
\text{If } -\infty < M_{12}^2 \leq 0, \quad y = \frac{\sqrt{-M_{12}^2}}{\sqrt{4m^2 - M_{12}^2}},
$$

$$
(1 \leq y \leq 0), \text{ then:}
$$

$$
\frac{1}{16\pi^2} y'' \log \frac{1 + y''}{1 - y''} \Rightarrow \frac{1}{16\pi^2} \frac{1}{y} \log \frac{1 + y}{1 - y}.
$$

$$
\tag{C.39}
$$

The two-body scattering amplitude is thus given by

$$\text{If } -\infty < M_{12}^2 \leq 0, \quad y = \frac{\sqrt{-M_{12}^2}}{\sqrt{4m^2 - M_{12}^2}},$$

$$(1 \leq y \leq 0), \text{ then}:$$

$$\mathcal{F}(M_{12}^2) = \frac{1}{\frac{1}{16\pi^2 y} \log \frac{1+y}{1-y} - \frac{1}{16\pi ma}},$$

$$\text{If } 0 \leq M_{12}^2 \leq 4\,m^2, \quad y' = \frac{M_{12}}{\sqrt{4m^2 - M_{12}^2}},$$

$$(0 \leq y' < \infty), \text{ then}: \tag{C.40}$$

$$\mathcal{F}(M_{12}^2) = \frac{1}{\frac{1}{8\pi^2} \frac{\arctan y'}{y'} - \frac{1}{16\pi ma}}.$$

$$\text{If } 4m^2 \leq M_{12}^2 < \infty, \quad y'' = \frac{\sqrt{M_{12}^2 - 4m^2}}{M_{12}},$$

$$(0 \leq y'' \leq 1), \text{ then}:$$

$$\mathcal{F}(M_{12}^2) = \frac{1}{\frac{y''}{16\pi^2} \log \frac{1+y''}{1-y''} - \frac{1}{16\pi ma} - i\frac{y''}{16\pi}},$$

and for negative scattering length a this amplitude has no poles.

C.3 Behavior of $\mathcal{F}(M_{12}^2)$

For negative a, the function $\mathcal{F}(M_{12}^2)$ is non-singular and continuous. However, the function may change rapidly in the neighbourhood of the transition points $M_{12}^2 = 0$ and $M_{12}^2 = 4\,m^2$. In terms of q_0 (for a given q_v) these are

$$q_0 = M_3 \pm q_v, \quad q_0 = M_3 \pm \sqrt{q_v^2 + 4m^2} \tag{C.41}$$

In Fig. C.1 the real and imaginary parts of F are shown as functions of q_0 (for selected values of q_v) in the case of $M_3/m = 2.605$ corresponding to $am = -1.5$. It is seen in the figures that close to $q_0 = M_3 \pm \sqrt{q_v^2 + 4m^2}$ (i.e. $M_{12}^2 = 4\,m^2$), the amplitude has a non-smooth behavior.
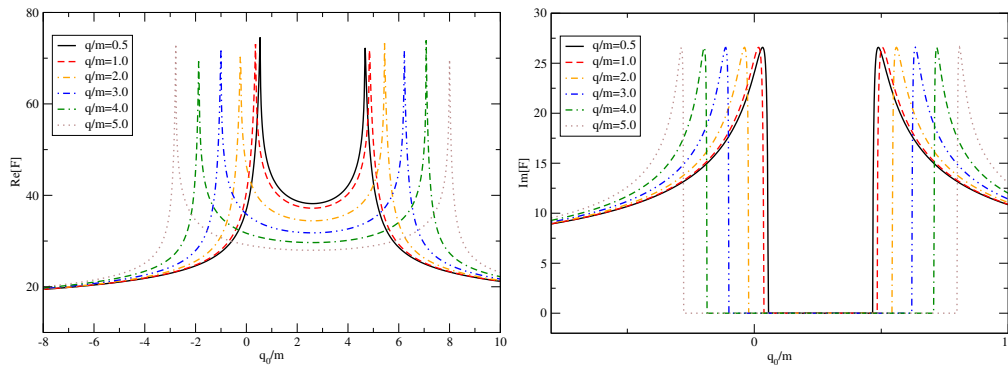
Figure C.1. Real and imaginary parts of $\mathcal{F}(M_{12}^2)$ with respect to q_0 for different fixed values of q_v.

Although the non-smoothness exists, this was shown to not be problematic in solving the equation. To show that, one can test solving the problem proposing a factorization of the form

$$v(q_0, q_v) = \mathcal{F}(M_{12}^2(q_0, q_v)) \, \tilde{v}(q_0, q_v), \tag{C.42}$$

by introducing

$$\tilde{\Pi}(q_0, q_v; k_0, k_v) = \mathcal{F}(M_{12}^2(q_0, q_v)) \, \Pi(q_0, q_v; k_0, k_v), \tag{C.43}$$

and obtaining an integral equation in terms of the function $\tilde{v}$ instead of v. The resulting equation was solved by expanding $\tilde{v}$ in splines. The result showed no significant difference between the solutions with and without the decomposition, with the convergence being achieved with a similar set of basis functions and integration points.

Appendix D

Spline decomposition

This appendix is based on Ref. [144].

Eqs. (4.9), (4.12) and (4.23) are solved by expanding the amplitude $v(q_0, q_v)$ in a bicubic spline basis, on a finite domain $\Omega = I_{q_0} \times I_{q_v} = [-q_0^{\max}, q_0^{\max}] \times [0, q_v^{\max}]$, i.e.

$$v(q_0, q_v) = \sum_{k=0}^{2N_{q_0}+1} \sum_{l=0}^{2N_{q_v}+1} A_{ij} S_k(q_0) S_l(q_v), \tag{D.1}$$

where the unknown coefficients A_{ij} are to determined. In the numerical implementation, the interval I_x ($x = q_0, q_v$) is partioned into N_x subintervals, so that the convergence is reached. The adopted spline functions, $S_j(x)$ are given by [183]

$$S_{2i}(x) = \begin{cases} 3\left(\frac{x-x_{i-1}}{h_i}\right)^2 - 2\left(\frac{x-x_{i-1}}{h_i}\right)^3 \\ \quad \text{if } x \in [x_{i-1}, x_i] \\ 3\left(\frac{x_{i+1}-x}{h_{i+1}}\right)^2 - 2\left(\frac{x_{i+1}-x}{h_{i+1}}\right)^3 \\ \quad \text{if } x \in [x_i, x_{i+1}] \\ 0 \quad \text{if } x \notin [x_{i-1}, x_{i+1}] \end{cases}$$

$$S_{2i+1}(x) = \begin{cases} \left[-\left(\frac{x-x_{i-1}}{h_i}\right)^2 + \left(\frac{x-x_{i-1}}{h_i}\right)^3\right] h_i \\ \quad \text{if } x \in [x_{i-1}, x_i] \\ \left[\left(\frac{x_{i+1}-x}{h_{i+1}}\right)^2 - \left(\frac{x_{i+1}-x}{h_{i+1}}\right)^3\right] h_{i+1} \\ \quad \text{if } x \in [x_i, x_{i+1}] \\ 0 \quad \text{if } x \notin [x_{i-1}, x_{i+1}] \end{cases}$$

$$\tag{D.2}$$

with $h_i = x_i - x_{i-1}$.

By using (D.1), Eq. (4.23) can be transformed to a generalized eigenvalue problem of the form

$$\sum_{i'j'} F_{iji'j'} A_{i'j'} = \lambda(M_3) \sum_{i'j'} V_{iji'j'} A_{i'j'}, \tag{D.3}$$

where

$$F_{iji'j'} = S_{i'}(q_0^{(i)})S_{j'}(q_v^{(j)}), \tag{D.4}$$

and the array $V_{iji'j'}$ is the right-hand side of (4.23) with v replaced by $S_{i'}(q_0^{(i)})S_{j'}(q_v^{(j)})$. The variable q_0 (q_v) has been here discretized on a mesh consisting of $2N_{q_0} + 2$ ($2N_{q_v} + 2$) points. The three-body mass M_3, or equivalently the three-body binding energy B_3, can subsequently be obtained from the condition

$$\lambda(M_3) = 1. \tag{D.5}$$

Eq. (D.5) constitutes a non-linear equation and is rather time-consuming to solve. For simplicity, it is used thus instead as inputs in the calculations the scattering length a and the M_3, obtained from the solution of the Euclidean BSE. Equation (D.3) is then solved for the eigenvalue λ and the coefficents A_{ij}.

The kernel $\Pi(q_0, q_v, k_0, k_v)$ (see Eq. (4.20)), which enters Eq. (4.23) has logarithmic singularities, and the analytic expressions for the singular points are given by Eqs. (4.24) and (4.25). The integrals over k_0 and k_v are computed by dividing a given integration interval into subintervals $I_i = [a_i, b_i]$, so that each subinterval contains at most one singular point that is at one of the end points. For each subinterval, the integrand is subsequently weakened by adopting a change of variables of the form

$$\int_{a_i}^{b_i} f(x)dx = \int_0^{\sqrt{b_i - a_i}} 2tf(a + t^2)dt, \tag{D.6}$$

for a subinterval with a singularity at a_i, and

$$\int_{a_i}^{b_i} f(x)dx = \int_0^{\sqrt{b_i - a_i}} 2tf(b - t^2)dt, \tag{D.7}$$

if the singularity is at the end point b_i. The resulting integrals involving smooth functions can then be performed by Gauss-Legendre integration.

Appendix E

Deriving the transverse amplitudes

E.1 Euclidean transverse amplitude

The expressions for the transverse amplitudes in the Euclidean space will be derived in more detail in this appendix. As mentioned, the following change of variables was performed,

$$k_i = k_i' + \frac{M_3}{3}, \quad (i = 1, 2, 3),$$ (E.1)

in order to allow the Wick-rotation without crossing any singularities. The primed momenta satisfy the relation

$$k_1' + k_2' + k_3' = 0.$$ (E.2)

The BS amplitude in Minkowski space can be written as

$$
\begin{aligned}
i\tilde{\Phi}_M(k_1', k_2', k_3'; M_3) &= \\
&= i^3 \frac{\tilde{v}_M(k_1') + \tilde{v}_M(k_2') + \tilde{v}_M(k_3')}{[(k_1' + \frac{p}{3})^2 - m^2 + i\epsilon][(k_2' + \frac{p}{3})^2 - m^2 + i\epsilon][(k_3' + \frac{p}{3})^2 - m^2 + i\epsilon]} = \\
&= i^3 \frac{\tilde{v}_M(k_1') + \tilde{v}_M(k_2') + \tilde{v}_M(-k_1' - k_2')}{[(k_1' + \frac{p}{3})^2 - m^2 + i\epsilon][(k_2' + \frac{p}{3})^2 - m^2 + i\epsilon]} \frac{1}{(k_1' + k_2' - \frac{p}{3})^2 - m^2 + i\epsilon},
\end{aligned}
$$ (E.3)

where

$$\tilde{\Phi}_M(k_1', k_2', k_3'; p) = \Phi_M\left(k_1' + \frac{p}{3}, k_2' + \frac{p}{3}, k_3' + \frac{p}{3}; p\right),$$ (E.4)

and $\tilde{v}(k_i') = v\left(k_i' + \frac{p}{3}\right)$.

One can now perform a two-dimensional Wick-rotation in the variables k_1' and k_2', i.e. $k_{10}' = ik_{14}'$ and $k_{20}' = ik_{24}'$, to get

$$
\begin{aligned}
i\tilde{\Phi}_E(k_{14}', k_{1z}', \vec{k}_{1\perp}'; k_{24}', k_{2z}', \vec{k}_{2\perp}') &= -i^3 \frac{\tilde{v}_E(k_{14}', k_{1v}') + \tilde{v}_E(k_{24}', k_{2v}') + \tilde{v}_E(k_{34}', k_{3v}')}{(k_{14}' - i\frac{M_3}{3})^2 + k_{1z}'^2 + m_1^2} \\
&\times \frac{1}{(k_{24}' - i\frac{M_3}{3})^2 + k_{2z}'^2 + m_2^2} \frac{1}{(k_{14}' + k_{24}' + i\frac{M_3}{3})^2 + (k_{1z}' + k_{2z}')^2 + m_3^2},
\end{aligned}
$$ (E.5)

where

$$k'_{iv} = \sqrt{k'^2_{i\perp} + k'^2_{iz}}, \quad m_i^2 = k'^2_{i\perp} + m^2 \quad (i = 1, 2, 3) \quad \text{and} \quad \vec{k}'_{3\perp} = -(\vec{k}'_{1\perp} + \vec{k}'_{2\perp}). \tag{E.6}$$

The full Euclidean transverse amplitude, corresponding to the Minkowski one given by (4.27), reads

$$L(\vec{k}'_{1\perp}, \vec{k}'_{2\perp}) = L_1(\vec{k}'_{1\perp}, \vec{k}'_{2\perp}) + L_2(\vec{k}'_{1\perp}, \vec{k}'_{2\perp}) + L_3(\vec{k}'_{1\perp}, \vec{k}'_{2\perp}) =$$
$$- \int_{-\infty}^{\infty} dk'_{10} \int_{-\infty}^{\infty} dk'_{1z} \int_{-\infty}^{\infty} dk'_{20} \int_{-\infty}^{\infty} dk'_{2z} i\tilde{\Phi}_E(k'_{14}, k'_{1z}, k'_{24}, k'_{2z}; \vec{k}'_{1\perp}, \vec{k}'_{2\perp}). \tag{E.7}$$

By insertion of Eq. (E.5) in (E.7), it is found that one of the contributions to the transverse amplitude is given by

$$L_1(\vec{k}'_{1\perp}, \vec{k}'_{2\perp}) = -i \int_{-\infty}^{\infty} dk'_{1z} \int_{-\infty}^{\infty} dk'_{10} \frac{\chi(k'_{14}, k'_{1z}; \vec{k}'_{1\perp}, \vec{k}'_{2\perp})}{(k'_{14} - i\frac{M_3}{3})^2 + k'^2_{1z} + m_1^2} \tilde{v}(k'_{1v}, k'_{14}), \tag{E.8}$$

with

$$\chi(k'_{14}, k'_{1z}; \vec{k}'_{1\perp}, \vec{k}'_{2\perp}) = \int_{-\infty}^{\infty} dk'_{20} \int_{-\infty}^{\infty} dk'_{2z} \frac{i}{(k'_{24} - i\frac{M_3}{3})^2 + k'^2_{2z} + m_2^2}$$
$$\times \frac{i}{(k'_{14} + k'_{24} + i\frac{M_3}{3})^2 + (k'_{1z} + k'_{2z})^2 + m_3^2}. \tag{E.9}$$

The two propagators in (E.9) can then be put together by using the Feynman parametrization

$$\frac{1}{A_1 A_2} = \int_0^1 \frac{dy}{[yA_1 + (1-y)A_2]^2}, \tag{E.10}$$

leading to the result

$$\frac{i}{(k'_{24} - i\frac{M_3}{3})^2 + k'^2_{2z} + m_2^2} \frac{i}{(k'_{14} + k'_{24} + i\frac{M_3}{3})^2 + (k'_{1z} + k'_{2z})^2 + m_3^2} = - \int_0^1 \frac{dy}{D^2}, \tag{E.11}$$

where the denominator reads

$$D = k'^2_{24} + k'^2_{2z} + (1-y)[k'^2_{14} + k'^2_{1z}] + \frac{2}{3}iM_3k'_{24}$$
$$+ 2(1-y)k'_{1z}k'_{2z} + \frac{2}{3}(1-y)k'_{14}(3k'_{24} + iM_3)$$
$$- \frac{4}{3}iyM_3k'_{24} + (1-y)m_3^2 + ym_2^2 - \frac{M_3^2}{9} = \tag{E.12}$$
$$= k'^2_{24} + k'^2_{2z} + (1-y)[k'^2_{14} + k'^2_{1z}] + 2\Big[(1-y)k'_{14} - \frac{iM_3}{3}(-1 + 2y)\Big]k'_{24}$$
$$+ 2(1-y)k'_{1z}k'_{2z} + \frac{2}{3}iM_3(1-y)k_{14} + (1-y)m_3^2 + ym_2^2 - \frac{M_3^2}{9}.$$

Now one can eliminate the terms linear in k'_{24} and k'_{2z}, by performing in Eqs. (E.9), (E.11) and (E.12) the transformations

$$k'_{24} \longrightarrow k'_{24} - \alpha,$$
$$k'_{2z} \longrightarrow k'_{2z} - \beta, \tag{E.13}$$

with

$$\alpha = (1-y)k'_{14} - \frac{iM_3}{3}(-1+2y) \quad \text{and} \quad \beta = (1-y)k'_{1z}. \tag{E.14}$$

After these transformations the denominator (E.12) is changed into

$$D \longrightarrow \tilde{D} = k'^2_{24} + k'^2_{2z} + A \tag{E.15}$$

where

$$A = y(1-y)\left[k'^2_{14} + k'^2_{1z}\right] + (1-y)m_3^2 + ym_2^2 + \frac{4}{3}iM_3y(1-y)k'_{14} - \frac{4}{9}M_3^2 y(1-y). \tag{E.16}$$

The integrals over k'_{24} and k'_{2z} in (E.9) can now be performed analytically, and the result is

$$\chi(k'_{14},k'_{1z}; \vec{k}'_{1\perp}, \vec{k}'_{2\perp}) = -\int_0^1 dy \int_{-\infty}^\infty dk'_{20} \int_{-\infty}^\infty dk'_{2z} \frac{1}{(k'^2_{24} + k'^2_{2v} + A)^2} =$$
$$= -2\pi \int_0^1 dy \int_0^\infty \frac{k'dk'}{(k'^2 + A)^2} = -\pi \int_0^1 \frac{dy}{A}. \tag{E.17}$$

Alternatively, one can write the quantity A in the form

$$A = ay^2 + by + c, \tag{E.18}$$

with

$$a = -k'^2_{1z} - \left(k'_{14} + \frac{2}{3}iM_3\right)^2, \quad b = k'^2_{1z} + \left(k'_{14} + \frac{2}{3}iM_3\right)^2 + m_2^2 - m_3^2, \quad c = m_3^2. \tag{E.19}$$

E.2 Minkowskian transverse amplitude

In this appendix the derivation of the transverse amplitude is presented in details. Furthermore, important properties of the equation are discussed. As said before, one of its components is enough for the comparison for the three identical bosons case. The Faddeev component is given by

$$L_1(\vec{k}_{1\perp}, \vec{k}_{2\perp}) = i \int_{-\infty}^\infty dk_{10} \int_{-\infty}^\infty dk_{1z} \frac{v_M(k_{10}, k_{1v})}{k_1^2 - m_1^2 + i\epsilon} \chi(k_{10}, k_{1z}; \vec{k}_{1\perp}, \vec{k}_{2\perp}), \tag{E.20}$$

with

$$\chi(k_{10}, k_{1z}; \vec{k}_{1\perp}, \vec{k}_{2\perp}) = i^2 \int \frac{d^2 k_2}{(k_2^2 - m_2^2 + i\epsilon)[(p' - k_2)^2 - m_3^2 + i\epsilon]} \tag{E.21}$$

where the following quantities enter $k_i = (k_{i0}, k_{iz})$ ($i = 1, 2$) and $d^2 k_i = dk_{i0}dk_{iz}$, with $i = 1, 2$. Moreover, $m_2^2 = m^2 + \vec{k}^2_{2\perp}$, $m_3^2 = m^2 + (\vec{p}_\perp - \vec{k}_{1\perp} - \vec{k}_{2\perp})^2$. and $p' = (p'_0, p'_z) = p - k_1 = (p_0 - k_{10}, p_z - k_{1z})$.

One can now perform the two-dimensional integral in (E.21), starting by introducing the Feynman parametrization as given in Eq. (E.10) and then making the

transformation $k_2 \to k_2 + (1-u)p'$ to eliminate the linear term in k_2, what makes Eq. (E.21) turn into

$$\chi(k_{10}, k_{1z}; \vec{k}_{1\perp}, \vec{k}_{2\perp}) = i^2 \int_0^1 du \int \frac{d^2 k_2}{(k_2^2 + D + i\epsilon)^2}, \qquad \text{(E.22)}$$

with

$$D = u(1-u)p'^2 - m_2^2 u - (1-u)m_3^2. \qquad \text{(E.23)}$$

One can now analytically perform the integral over k_2 in (E.17), starting by carrying out a Wick-rotation as $k_0 = ik_4$, leading to the result

$$\chi(k_{10}, k_{1z}; \vec{k}_{1\perp}, \vec{k}_{2\perp}) = \pi i^3 \int_0^1 du \int_0^\infty \frac{ds}{(-s + D + i\epsilon)^2} = -\pi i^3 \int_0^1 \frac{du}{D + i\epsilon}, \qquad \text{(E.24)}$$

where it was defined the quantity $s = k_{24}^2 + k_{2z}^2$.

The denominator D (E.23) is zero at

$$u_{\mp} = \frac{1}{2p'^2} \left[p'^2 - m_2^2 + m_3^2 \mp \sqrt{((m_2 - m_3)^2 - p'^2)((m_2 + m_3)^2 - p'^2)} \right], \qquad \text{(E.25)}$$

but for $p'^2 < (m_2 + m_3)^2$, the conditions above never happen in the interval $0 < u < 1$, so the term $i\epsilon$ can be dropped out in Eq. (E.24) and the integral over the Feynman parameter u can be performed safely analytically, giving the following

$$\chi(k_{10}, k_{1z}; \vec{k}_{1\perp}, \vec{k}_{2\perp}) = \frac{\pi i^3}{p'^2(u_- - u_+)} \int_0^1 du \left[\frac{1}{u - u_-} - \frac{1}{1 - u_+} \right] =$$
$$= -\frac{i\pi}{p'^2(u_- - u_+)} [\log(1 - u_-) - \log(-u_-) - \log(-1 + u_+) + \log(u_+)]$$
$$\text{(E.26)}$$

with $u_\pm$ give by (E.25).

In the situation where $p'^2 > (m_2 + m_3)^2$, the zeroes of the denominator, $u_\pm$, are placed on the real axis for the interval $u \in [0, 1]$. For that reason, one can separate χ in two terms, analogously to what was done in (4.18), i.e.

$$\chi(k_{10}, k_{1z}; \vec{k}_{1\perp}, \vec{k}_{2\perp}) = \chi'(k_{10}, k_{1z}; \vec{k}_{1\perp}, \vec{k}_{2\perp}) + \chi''(k_{10}, k_{1z}; \vec{k}_{1\perp}, \vec{k}_{2\perp}) \qquad \text{(E.27)}$$

where

$$\chi'(k_{10}, k_{1z}; \vec{k}_{1\perp}, \vec{k}_{2\perp}) = \frac{\pi i^3}{p'^2(u_- - u_+)} \left[\text{PV} \int_0^1 \frac{du}{u - u_-} - \text{PV} \int_0^1 \frac{du}{u - u_+} \right], \qquad \text{(E.28)}$$

and

$$\chi''(k_{10}, k_{1z}; \vec{k}_{1\perp}, \vec{k}_{2\perp}) = \frac{\pi i^3}{p'^2(u_- - u_+)} \left[-i\pi \int_0^1 du \delta(u - u_-) - i\pi \int_0^1 du \delta(u - u_+) \right]$$
$$= \frac{2\pi^2}{\sqrt{[p'^2 - (m_2 - m_3)^2][p'^2 - (m_2 + m_3)^2]}}.$$
$$\text{(E.29)}$$

The principal value integrals in Eq. (E.28) can be carried out analytically and one obtains for χ' the following expression

$$\chi'(k_{10}, k_{1z}; \vec{k}_{1\perp}, \vec{k}_{2\perp}) = i\pi \frac{\log \frac{m_2^2+m_3^2-p'^2-\sqrt{[p'^2-(m_2-m_3)^2][p'^2-(m_2+m_3)^2]}}{m_2^2+m_3^2-p'^2+\sqrt{[p'^2-(m_2-m_3)^2][p'^2-(m_2+m_3)^2]}}}{\sqrt{[p'^2-(m_2-m_3)^2][p'^2-(m_2+m_3)^2]}}. \tag{E.30}$$

The expression for χ'' is non-singular and can be treated numerically as presented in Eq. (E.29).

In the main text the contribution L_1 is given in its final form, after following the derivations of this appendix. Similarly to the treatment of the BS equation in Sec. 4.2.1, the propagators like $[k_1^2 - m_1^2 + i\epsilon]^{-1}$ were expressed in the form (4.18) and subtractions were made to eliminate the principal value singularities at $k_0 = \pm \tilde{k}_{10}$.

It should be noticed that the kernel χ in Eq. (4.28) has square-root singularities at $p'^2 = (m_2 \pm m_3)^2$. The kernels $\chi(\pm \tilde{k}_{10}, k_{1z}; \vec{k}_{1\perp}, \vec{k}_{2\perp})$ are thus singular at

$$k_{1z} = \pm \frac{2}{M_3} \sqrt{[(M_3 + m_1)^2 - (m_2 + m_3)^2][(M_3 - m_1)^2 - (m_2 + m_3)^2]}. \tag{E.31}$$

Furthermore, for fixed k_{1z}, the positions of the singular points of the kernels $\chi(-k_{10}, k_{1z}; \vec{k}_{1\perp}, \vec{k}_{2\perp})$ and $\chi(k_{10}, k_{1z}; \vec{k}_{1\perp}, \vec{k}_{2\perp})$ are given by

$$k_{10} = -M_3 + \sqrt{k_{1z}^2 + (m_2 + m_3)^2} \tag{E.32}$$

and

$$k_{10} = M_3 \pm \sqrt{k_{1z}^2 + (m_2 + m_3)^2}, \tag{E.33}$$

respectively. In this case only the singular points located on the positive k_0 axis need to be considered (see (4.28)). In fact, it turns out that the integrands in Eq. (4.28) are symmetric with respect to $k_{1z} \to -k_{1z}$. Therefore, one only needs to consider only the region where $k_{1z} > 0$ and multiply the equation by a factor 2. Furthermore, only the positive solutions of Eq. (E.31) are needed.

Appendix F

Non-relativistic limit

In this section, the non-relativistic limits of the three-body Euclidean BS and valence LF equations, Eqs. (4.9) and (4.12), respectively, are considered. The derivations presented in this appendix are based on Ref. [144]. The first analysis will be for the Euclidean BS equation. Representing the three-body mass M_3 as $M_3 = 3m - B_3$, with B_3 denoting the three-body binding energy, and truncating the denominator of Eq. (4.9), and the terms in the fraction of the argument of the log in Eq. (4.10), to the leading terms of momenta and the binding energies, one gets

$$
K = \frac{\widetilde{\Pi'}_E(q_4, q_v, k_4, k_v)}{\left(k_4 - \frac{i}{3}M_3\right)^2 + k_v^2 + m^2} = \frac{\frac{1}{2}\log\frac{\left(k_4+q_4+\frac{i}{3}M_3\right)^2+(q_v+k_v)^2+m^2}{\left(k_4+q_4+\frac{i}{3}M_3\right)^2+(q_v-k_v)^2+m^2}}{\left(k_4 - \frac{i}{3}M_3\right)^2 + k_v^2 + m^2}
$$

$$
\Rightarrow K_{nr} \approx \frac{\frac{1}{2}\log\frac{\frac{2}{3}B_3+\frac{(k_v+q_v)^2}{2m}+i(k_4+q_4)}{\frac{2}{3}B_3+\frac{(k_v-q_v)^2}{2m}+i(k_4+q_4)}}{2m\left(\frac{1}{3}B_3 - ik_4\right)}.
$$

(F.1)

At a first glance, one could neglect $\frac{(k_v \pm q_v)^2}{2m}$ in comparison to $(k_4 + q_4)$, however, this would results in $K_{nr} \equiv 0$, therefore it is necessary to keep them.

The two-body amplitude $\mathcal{F}(M_{12}^2)$ in the physical domain $(0 \leq M_{12}^2 \leq 4m^2)$ reads, in terms of the two-body bound state mass M_2

$$
\mathcal{F}(M_{12}^2) = \frac{8\pi^2}{\left(\frac{\arctan y'}{y'} - \frac{\arctan y_{M_2}}{y_{M_2}}\right)},
$$

where $y' = \frac{M_{12}}{\sqrt{4m^2-M_{12}^2}}$ and $y_{M_2} = \frac{M_2}{\sqrt{4m^2-M_2^2}}$ (see Eq. (4.3)). Following Ref. [138], one can introduce E_2 through $M_{12}^2 = (2m - E_2)^2$ and write the two-body bound state mass as $M_2 = 2m - B_2$. In the non-relativistic limit, $m \to \infty$, the $\mathcal{F}(M_{12}^2)$ amplitude becomes

$$
\mathcal{F}(M_{12}^2) = \frac{16\pi\sqrt{m}}{\sqrt{E_2} - \sqrt{B_2}}
$$

(F.2)

or, alternatively,

$$
\mathcal{F}(-M_{12}^2) = \frac{16\pi\sqrt{m}}{\sqrt{2m - \sqrt{-M_{12}^2}} - \sqrt{B_2}}.
$$

(F.3)

Since $M_{12}^2 = \left(\frac{2}{3}P - iq_4\right)^2 - q_v^2 = -(\frac{2}{3}iM_3 + q_4)^2 - q_v^2$, in the limit $m \to \infty$ one gets

$$E_2 = 2m - \sqrt{-\left[\frac{2}{3}i(3m - B3) + q_4\right]^2 - q_v^2} \approx \frac{3}{2}B_3 + iq_4 + \frac{\vec{q}^2}{4m}. \tag{F.4}$$

Substituting it in (F.2), one finds for the scattering amplitude

$$\mathcal{F}(M_{12}^2) = \frac{16\pi\sqrt{m}}{\sqrt{\frac{3}{2}B_3 + iq_4 + \frac{\vec{q}^2}{4m}} - \sqrt{B_2}} \tag{F.5}$$

After these manipulations, equation (4.9) reads

$$\tilde{v}'(q_4, q_v) = \frac{1}{\pi^2\sqrt{m}} \frac{1}{\sqrt{\frac{3}{2}B_3 + iq_4 + \frac{q_v^2}{4m}} - \sqrt{B_2}} \int_0^\Lambda dk_v \int_{-\infty}^\infty \frac{dk_4}{\left(\frac{1}{3}B_3 - ik_4\right)}$$

$$\times \log \frac{\frac{2}{3}B_3 + \frac{(k_v+q_v)^2}{2m} + i(k_4 + q_4)}{\frac{2}{3}B_3 + \frac{(k_v-q_v)^2}{2m} + i(k_4 + q_4)} \tilde{v}'(k_4, k_v), \tag{F.6}$$

where it was introduced a cutoff Λ to prevent the Thomas collapse [141]. In order to obtain the time independent equation, the integration over k_4 needs to be performed. Since this is a non-trivial task, this will not be done here.

For the three-body LF equation, given by Eq. (4.12), the non-relativistic limit, obtained by following the same steps as before, reads

$$\Gamma_{nr}(\vec{q}) = \frac{1}{\pi^2 m^{3/2}} \frac{1}{\sqrt{E_2} - \sqrt{B_2}} \int \frac{\Gamma_{nr}(\vec{k})d^3k}{B_3 + \frac{\vec{q}^2}{2m} + \frac{\vec{k}^2}{2m} + \frac{(\vec{q}+\vec{k})^2}{2m}}, \tag{F.7}$$

where

$$E_2 = 2m - M_{12} \approx B_3 + \frac{3}{4}\frac{\vec{q}^2}{m} \qquad \text{and}$$
$$M_{12}^2 = (1-x)M_3^2 - \frac{k_\perp^2 + (1-x)m^2}{x}. \tag{F.8}$$

Here, the factor $\frac{1}{\sqrt{E_2}-\sqrt{B_2}}$ is originated from the two-body amplitude (F.2) when $m \to \infty$. Equation (F.7) is the same as the one obtained in Eq. (18) of Ref. [138]. This equation is known as the Skornyakov-Ter-Martirosyan equation [184]. The non-relativistic equation can be also written in the form

$$\Gamma_{nr}(\vec{q}) = \frac{1}{\pi^2\sqrt{m}} \frac{1}{\sqrt{B_3 + \frac{3}{4}\frac{\vec{q}^2}{m}} - \sqrt{B_2}} \int \frac{\Gamma_{nr}(\vec{k})d^3k}{\vec{k}^2 + \vec{k}\cdot\vec{q} + \vec{q}^2 + mB_3}, \tag{F.9}$$

and, for the s-wave, after integrating over the angles, it reads

$$\Gamma_{nr}(q_v) = \frac{\frac{2}{\pi\sqrt{m}}}{\sqrt{B_3 + \frac{3}{4}\frac{q_v^2}{m}} - \sqrt{B_2}} \int_0^\Lambda \log\left(\frac{k_v^2 + k_v q_v + q_v^2 + mB_3}{k_v^2 - k_v q_v + q_v^2 + mB_3}\right) \Gamma_{nr}(k_v)\frac{k_v dk_v}{q_v} \tag{F.10}$$

Equation (F.10), like Eq. (F.6), requires a cutoff in order to find a physical solution by avoiding the Thomas collapse.

Appendix G

Derivation of the three-body BSE: ansatz and uniqueness

This chapter aims to derive in detail the Faddeev-Bethe-Salpeter equation by means of an ansatz for the integral representation and the uniqueness conjecture of its spectral function, analogous to the conjecture for the Nakanishi weight function [38]. The content of this appendix is based on Ref. [185].

From Eq. (4.34) one can define, after using Feynman parametrization, the kernel as

$$
I(q, \gamma', z'; p) = \int \frac{d^4k}{(2\pi)^4} \frac{i}{(\frac{p}{3}+k)^2 - m^2 + i\epsilon}
$$

$$
\times \frac{i}{(\frac{p}{3}-q-k)^2 - m^2 + i\epsilon} \frac{1}{\gamma' - k^2 - (p \cdot k)z' - i\epsilon} = 2 \int_0^1 d\alpha_2 \int_0^1 d\alpha_3 \int \frac{d^4k}{(2\pi)^4} \frac{1}{D^3},
\tag{G.1}
$$

where the denominator D is given by

$$
D = [(1 - \alpha_2 - \alpha_3)((\frac{p}{3}+k)^2 - m^2) + \alpha_2((\frac{p}{3}-q-k)^2 - m^2)
$$
$$
- \alpha_3(\gamma' - k^2 - (p \cdot k)z') + i\epsilon].
\tag{G.2}
$$

The denominator in Eq. (G.1) can be re-written as

$$
D = k^2 + \left(\frac{2}{3} - \frac{4\alpha_2}{3} - \frac{2\alpha_3}{3} + \alpha_3 z'\right)(k \cdot p) + 2\alpha_2(k \cdot q) + (\alpha_3 - 1)\left(m^2 - \frac{p^2}{9}\right)
$$
$$
- \frac{2\alpha_2}{3}(p \cdot q) + \alpha_2 q^2 - \alpha_3 \gamma' = k^2 + k \cdot \left[\left(\frac{2}{3}(1 - 2\alpha_2 - \alpha_3) + \alpha_3 z'\right)p + 2\alpha_2 q\right]
$$
$$
- m^2 + \frac{p^2}{9} - \alpha_2 q \cdot \left(\frac{2}{3}p - q\right) + \alpha_3\left(-\gamma' + m^2 - \frac{p^2}{9}\right)
$$
$$
= \left\{k - \frac{1}{2}\left[\left(\frac{2}{3}(1 - 2\alpha_2 - \alpha_3) + \alpha_3 z'\right)p + 2\alpha_2 q\right]\right\}^2
$$
$$
- \frac{1}{4}\left[\left(\frac{2}{3}(1 - 2\alpha_2 - \alpha_3) + \alpha_3 z'\right)p + 2\alpha_2 q\right]^2 - m^2 + \frac{p^2}{9} - \alpha_2 q \cdot \left(\frac{2}{3}p - q\right)
$$
$$
+ \alpha_3\left(-\gamma' + m^2 - \frac{p^2}{9}\right).
\tag{G.3}
$$

Subsequently, the term linear in k is eliminated by doing the transformation

$$k \longrightarrow k + \frac{1}{2}\Big[\Big(\frac{2}{3}(1 - 2\alpha_2 - \alpha_3) + \alpha_3 z'\Big)p + 2\alpha_2 q\Big], \tag{G.4}$$

and perform the loop integral using

$$\int \frac{d^4 k}{(k^2 - M^2 + i\epsilon)^3} = -\frac{i}{2}\frac{\pi^2}{M^2 - i\epsilon}, \tag{G.5}$$

with

$$\begin{aligned}
M^2 &= \alpha_2(\alpha_2 - 1)q_-^2 + \alpha_2\alpha_3\Big(\frac{2}{3} - z'\Big)p \cdot q_- \\
&\quad + \alpha_3^2 \frac{p^2}{4}\Big(\frac{2}{3} - z'\Big)^2 + \alpha_3\Big[\gamma' - m^2 + \frac{p^2}{9}(3z' - 1)\Big] + m^2 \\
&= -\alpha_2(1 - \alpha_2)[q_-^2 + z''(\alpha_2, \alpha_3, z')p \cdot q_- - \Gamma(\alpha_2, \alpha_3, \gamma', z'; p)],
\end{aligned} \tag{G.6}$$

In Eq. (G.6) it was defined the following quantities

$$q_- = \frac{2}{3}p - q, \tag{G.7}$$

$$z''(\alpha_2, \alpha_3, z') = \frac{\alpha_2\alpha_3\big(\frac{2}{3} - z'\big)}{\alpha_2(\alpha_2 - 1)}, \tag{G.8}$$

and

$$\begin{aligned}
\Gamma(\alpha_2, \alpha_3, \gamma', z'; p) &= \\
&= \frac{1}{\alpha_2(1 - \alpha_2)}\Big\{\alpha_3^2\frac{p^2}{4}\Big(\frac{2}{3} - z'\Big)^2 + \alpha_3\Big[\gamma' - m^2 + \frac{p^2}{9}(3z' - 1)\Big] + m^2\Big\} \\
&= \frac{1}{\alpha_2(1 - \alpha_2)}\Big\{\alpha_3\Big[\gamma' - m^2 + p^2\Big(\frac{1}{9}(3z' - 1) + \frac{\alpha_3}{4}\Big(\frac{2}{3} - z'\Big)^2\Big)\Big] + m^2\Big\}.
\end{aligned} \tag{G.9}$$

The result for the integral $I(q, \gamma', z'; p)$ thus is

$$I(q, \gamma', z'; p) = \frac{i}{(4\pi)^2}\int_0^1 \frac{d\alpha_2}{\alpha_2(1 - \alpha_2)}\int_0^{1-\alpha_2} \frac{d\alpha_3}{D_1}, \tag{G.10}$$

where the denominator D_1 is defined as

$$D_1 = q_-^2 + z''(\alpha_2, \alpha_3, z')p \cdot q_- - \Gamma(\alpha_2, \alpha_3, \gamma', z'; p) + i\epsilon \tag{G.11}$$

The next step is to introduce the scattering two-body amplitude and define the following integral

$$\begin{aligned}
\bar{I}(q, \gamma', z'; p) &= \mathcal{F}(M_{12}^2)I(q, \gamma', z'; p) = \\
&= \int_{4m^2}^\infty \frac{\rho(\gamma'')d\gamma''}{q_-^2 - \gamma'' + i\epsilon}I(q, \gamma', z'; p) = \frac{-i}{(4\pi)^2}\int_{4m^2}^\infty \frac{\rho(\gamma'')d\gamma''}{q_-^2 - \gamma'' + i\epsilon} \\
&\quad \times \int_0^1 \frac{d\alpha_2}{\alpha_2(1 - \alpha_2)}\int_0^{1-\alpha_2} \frac{d\alpha_3}{\Gamma(\alpha_2, \alpha_3, \gamma', z'; p) - q_-^2 - z''(\alpha_2, \alpha_3, z')p \cdot q_- - i\epsilon}.
\end{aligned} \tag{G.12}$$

One can now use Feynman parametrization to put the denominators together and, then, Eq. (G.12) can be re-written as

$$
\bar{I}(q,\gamma',z';p) = \frac{i}{(4\pi)^2} \int_{4m^2}^{\infty} \rho(\gamma'')d\gamma'' \int_0^1 d\alpha_1 \int_0^1 \frac{d\alpha_2}{\alpha_2(1-\alpha_2)}
$$
$$
\times \int_0^{1-\alpha_2} \frac{d\alpha_3}{[\bar{\Gamma}(\alpha_1,\alpha_2,\alpha_3,\gamma'',\gamma',z';p) - q_-^2 - z'''(\alpha_1,\alpha_2,\alpha_3,z')p\cdot q_- - i\epsilon]^2}
$$
(G.13)

where

$$
\bar{\Gamma}(\alpha_1,\alpha_2,\alpha_3,\gamma'',\gamma',z';p) = \alpha_1\gamma'' + (1-\alpha_1)\Gamma(\alpha_2,\alpha_3,\gamma',z';p), \qquad \text{(G.14)}
$$

and

$$
z'''(\alpha_1,\alpha_2,\alpha_3,z') = (1-\alpha_1)z''(\alpha_2,\alpha_3,z'). \qquad \text{(G.15)}
$$

From Eqs. (4.34) and (G.13), one can obtain the following integral equation for $g(\gamma,z)$

$$
\int_0^{\infty} \int_{-\frac{4}{3}}^{\frac{2}{3}} dz \frac{g(\gamma,z)}{\gamma - q^2 - (p\cdot q)z - i\epsilon} =
$$
$$
= -\frac{2}{(4\pi)^2} \int_{4m^2}^{\infty} \rho(\gamma'')d\gamma'' \int_0^1 d\alpha_1 \int_0^1 \frac{d\alpha_2}{\alpha_2(1-\alpha_2)} \int_0^{1-\alpha_2} d\alpha_3 \int_0^{\infty} d\gamma' \int_{-\frac{4}{3}}^{\frac{2}{3}} dz'
$$
$$
\times \frac{g(\gamma',z')}{[\bar{\Gamma}(\alpha_1,\alpha_2,\alpha_3,\gamma'',\gamma',z';p) - (\frac{2}{3}-q)^2 - z'''(\alpha_1,\alpha_2,\alpha_3,z')p\cdot(\frac{2}{3}-q) - i\epsilon]^2}
$$
(G.16)

To be able to apply the uniqueness conjecture, the denominator on the right-hand side needs to be manipulated into the same form as the one on the left-hand side. To this end, it is defined

$$
z''''(\alpha_1,\alpha_2,\alpha_3,z') = -\frac{4}{3} - z'''(\alpha_1,\alpha_2,\alpha_3,z') = -\frac{4}{3} + \frac{(1-\alpha_1)\alpha_3(\frac{2}{3}-z')}{1-\alpha_2}, \quad \text{(G.17)}
$$

and

$$
\bar{\Gamma}'(\alpha_1,\alpha_2,\alpha_3,\gamma'',\gamma',z';p) = \bar{\Gamma}(\alpha_1,\alpha_2,\alpha_3,\gamma'',\gamma',z';p) - \frac{4}{9}p^2 - \frac{2}{3}z'''(\alpha_1,\alpha_2,\alpha_3,z')p^2
$$
$$
= \alpha_1\gamma'' + \frac{(1-\alpha_1)}{\alpha_2(1-\alpha_2)}\left\{\alpha_3\left[\gamma' - \frac{p^2}{9} - m^2 + z'\frac{p^2}{3} + \frac{\alpha_3}{4}\left(\frac{2}{3}-z'\right)^2 p^2\right] + m^2\right\}
$$
$$
- \frac{2}{3}p^2\left(\frac{2}{3} - \frac{(1-\alpha_1)\alpha_3(\frac{2}{3}-z')}{(1-\alpha_2)}\right) = \alpha_1\gamma'' + \frac{(1-\alpha_1)}{\alpha_2(1-\alpha_2)}
$$
$$
\times \left\{\alpha_3\left[\gamma' - \frac{p^2}{9} - m^2 + z'\frac{p^2}{3} + \frac{\alpha_3}{4}\left(\frac{2}{3}-z'\right)^2 p^2\right] + m^2\right\}
$$
$$
+ \frac{2}{3}p^2\left[z''''(\alpha_1,\alpha_2,\alpha_3,z') + \frac{2}{3}\right].
$$
(G.18)

With these definitions, Eq. (G.16) then takes the form

$$
\int_0^\infty \int_{-\frac{4}{3}}^{\frac{2}{3}} dz \frac{g(\gamma, z)}{\gamma - q^2 - (p \cdot q)z - i\epsilon} =
$$
$$
= -\frac{2}{(4\pi)^2} \int_{4m^2}^\infty \rho(\gamma'')d\gamma'' \int_0^1 d\alpha_1 \int_0^1 \frac{d\alpha_2}{\alpha_2(1-\alpha_2)} \int_0^{1-\alpha_2} d\alpha_3
$$
$$
\times \int_0^\infty d\gamma' \int_{-\frac{4}{3}}^{\frac{2}{3}} dz' \frac{g(\gamma', z')}{[\bar{\Gamma}'(\alpha_1, \alpha_2, \alpha_3, \gamma'', \gamma', z'; p) - q^2 - z''''(\alpha_1, \alpha_2, \alpha_3, z')p \cdot q - i\epsilon]^2}
$$
$$
= -\frac{2}{(4\pi)^2} \int_0^\infty d\gamma \int_{-\frac{4}{3}}^{\frac{2}{3}} \frac{dz}{\gamma - q^2 - z(p \cdot q) - i\epsilon} \int_0^\infty d\gamma' \int_{-\frac{4}{3}}^{\frac{2}{3}} dz' g(\gamma', z') \int_{4m^2}^\infty \rho(\gamma'')d\gamma''
$$
$$
\times \int_0^1 d\alpha_1 \int_0^1 \frac{d\alpha_2}{\alpha_2(1-\alpha_2)} \int_0^{1-\alpha_2} d\alpha_3
$$
$$
\times \delta'(\gamma - \bar{\Gamma}'(\alpha_1, \alpha_2, \alpha_3, \gamma'', \gamma', z'; p))\delta(z - z''''(\alpha_1, \alpha_2, \alpha_3, z')).
$$
$$(G.19)$$

By assuming that the uniqueness conjecture [35, 38] (which was proved for transition amplitudes for bosonic systems in the perturbative regime in Ref. [35]) holds for the weight function $g(\gamma, z)$ of the ansatz for the integral representation introduced here, one can simplify the LH-side of the equation. The conjecture implies that the weight function of the integral representation, $g_i(\gamma, z)$, is unique, encoding all the non-perturbative dynamical information. This enables to solve it as a standard eigenvalue problem. Therefore, one finally obtain the following

$$
g(\gamma, z) = -\frac{2}{(4\pi)^2} \int_0^\infty d\gamma' \int_{-\frac{4}{3}}^{\frac{2}{3}} dz' g(\gamma', z') \int_{4m^2}^\infty \rho(\gamma'')d\gamma'' \int_0^1 d\alpha_1 \int_0^1 \frac{d\alpha_2}{\alpha_2(1-\alpha_2)}
$$
$$
\times \int_0^{1-\alpha_2} d\alpha_3 \delta'(\gamma - \bar{\Gamma}'(\alpha_1, \alpha_2, \alpha_3, \gamma'', \gamma', z'; p))\delta(z - z''''(\alpha_1, \alpha_2, \alpha_3, z')),
$$
$$(G.20)$$

where z'''' and $\bar{\Gamma}'$ are defined by Eqs. (G.17) and (G.18), respectively.

Kernel for the three-body integral equation

The arguments of the δ functions can be written in such a way that the kernel of the integral equation in (G.20) reads

$$
K(\gamma, z, \gamma', z'; p) = -\frac{2}{(4\pi)^2} \frac{\partial}{\partial \gamma} \int_{4m^2}^\infty \rho(\gamma'')d\gamma'' \int_0^1 d\alpha_1 \int_0^1 d\alpha_3 \int_0^{1-\alpha_3} (1-\alpha_2)d\alpha_2
$$
$$
\times \delta\left(\left[\gamma - \alpha_1\gamma'' - \frac{2}{3}p^2\left(\frac{2}{3} + z\right)\right]\alpha_2(1-\alpha_2) - (1-\alpha_1)\left\{\alpha_3\left[\gamma' - \frac{p^2}{9} - m^2 + z'\frac{p^2}{3}\right.\right.\right.
$$
$$
\left.\left.\left. + \frac{\alpha_3}{4}\left(\frac{2}{3} - z'\right)^2 p^2\right] + m^2\right\}\right)\delta\left(\left(z + \frac{4}{3}\right)(1-\alpha_2) - (1-\alpha_1)\alpha_3\left(\frac{2}{3} - z'\right)\right).
$$
$$(G.21)$$

The integration over α_2 is straightforward to carry out, by using that

$$(1-\alpha_2)\left(z+\frac{4}{3}\right) - (1-\alpha_1)\alpha_3\left(\frac{2}{3}-z'\right) = 0 \iff \alpha_2 = 1 - (1-\alpha_1)\frac{\alpha_3(\frac{2}{3}-z')}{(z+\frac{4}{3})},$$

$$\bar{\alpha}_2(\alpha_1,\alpha_3,z,z') = \alpha_2(1-\alpha_2) = \left[1 - (1-\alpha_1)\frac{\alpha_3(\frac{2}{3}-z')}{z+\frac{4}{3}}\right],$$

$$\alpha_2 \geqslant 0 \iff 1 - (1-\alpha_1)\frac{\alpha_3(\frac{2}{3}-z')}{(z+\frac{4}{3})} \geqslant 0,$$

$$\alpha_2 \leqslant 1-\alpha_3 \iff -1 + (1-\alpha_1)\frac{(\frac{2}{3}-z')}{z+\frac{4}{3}} \geqslant 0.$$

(G.22)

One then obtains that

$$K(\gamma,z,\gamma',z';p) = -\frac{2}{(4\pi)^2}\frac{(\frac{2}{3}-z')}{(z+\frac{4}{3})^2}\frac{\partial}{\partial\gamma}\int_{4m^2}^{\infty}\rho(\gamma'')d\gamma''\int_0^1 d\alpha_1\alpha_1\int_0^1 d\alpha_3\alpha_3$$

$$\times \delta\left(\left[\gamma - (1-\alpha_1)\gamma'' - \frac{2}{3}p^2\left(\frac{2}{3}+z\right)\right]\hat{\alpha}_2(\alpha_1,\alpha_3,z,z')\right.$$

$$\left. - \alpha_1\left\{\alpha_3\left[\gamma' - \frac{p^2}{9} - m^2 + z'\frac{p^2}{3} + \frac{\alpha_3}{4}\left(\frac{2}{3}-z'\right)^2 p^2\right] + m^2\right\}\right)$$

$$\times \theta\left(1 - \alpha_1\frac{\alpha_3(\frac{2}{3}-z')}{(z+\frac{4}{3})}\right)\theta\left(-1 + \alpha_1\frac{(\frac{2}{3}-z')}{(z+\frac{4}{3})}\right)\theta\left(\left(\frac{2}{3}-z'\right) - \left(z+\frac{4}{3}\right)\right),$$

(G.23)

where the transformation $(1-\alpha_1) \longrightarrow \alpha_1$ was done and the following quantity was defined

$$\hat{\alpha}_2(\alpha_1,\alpha_3,z,z') = \frac{\alpha_1\alpha_3(\frac{2}{3}-z')}{(z+\frac{4}{3})^2}\left[\left(z+\frac{4}{3}\right) - \alpha_1\alpha_3\left(\frac{2}{3}-z'\right)\right].$$

(G.24)

The θ functions in Eq. (G.23) lead to the following constraints on α_1 and α_3

$$1 - \alpha_1\frac{\alpha_3(\frac{2}{3}-z')}{(z+\frac{4}{3})} \geqslant 0 \iff \alpha_3 \leqslant \frac{(z+\frac{4}{3})}{\alpha_1(\frac{2}{3}-z')},$$

$$-1 + \alpha_1\frac{(\frac{2}{3}-z')}{(z+\frac{4}{3})} \geqslant 0 \iff \alpha_1 \geqslant \frac{(z+\frac{4}{3})}{(\frac{2}{3}-z')}.$$

(G.25)

Furthermore, one can simplify the argument of the δ function, perform the integration over γ'' in (G.23) and transform $\alpha_3 \longrightarrow \alpha_3/\alpha_1$, which leads to

$$K(\gamma,z,\gamma',z';p) = -\frac{2}{(4\pi)^2}\theta\left(\left(\frac{2}{3}-z'\right) - \left(z+\frac{4}{3}\right)\right)$$

$$\int_{\frac{z+\frac{4}{3}}{\frac{2}{3}-z'}}^1 \frac{d\alpha_1}{\alpha_1(1-\alpha_1)}\int_0^{\frac{z+\frac{4}{3}}{\frac{2}{3}-z'}} \frac{d\alpha_3}{(z+\frac{4}{3}) - \alpha_3(\frac{2}{3}-z')}$$

$$\times \frac{\partial}{\partial\gamma}[\rho(\gamma_0(\alpha_1,\alpha_3,\gamma,z,\gamma',z'))]\theta(\gamma_0(\alpha_1,\alpha_3,\gamma,z,\gamma',z') - 4m^2),$$

(G.26)

with γ_0 given by

$$
\begin{aligned}
\gamma_0(\alpha_1, \alpha_3, \gamma, z, \gamma', z') &= \frac{\gamma - \frac{2}{3}p^2(\frac{2}{3}+z)}{1-\alpha_1} \\
&- \left(z+\frac{4}{3}\right)^2 \frac{\alpha_3[\gamma' - \frac{p^2}{9} - m^2 + z'\frac{p^2}{3} + \frac{1}{4}\frac{\alpha_3}{\alpha_1}(\frac{2}{3}-z')^2 p^2] + m^2\alpha_1}{(1-\alpha_1)\alpha_3(\frac{2}{3}-z')[(z+\frac{4}{3}) - \alpha_3(\frac{2}{3}-z')]}.
\end{aligned}
\tag{G.27}
$$

Moreover, the condition $\gamma_0 \geqslant 4m^2$ leads to the following constrain on γ'

$$
\begin{aligned}
0 &\leqslant \gamma' \leqslant \gamma'_{\max}(\alpha_1, \alpha_3, \gamma, z, z') \\
&= \frac{\frac{2}{3}-z'}{(z+\frac{4}{3})^2}\left[z+\frac{4}{3} - \alpha_3\left(\frac{2}{3}-z'\right)\right]\left[\gamma - \frac{2}{3}p^2\left(\frac{2}{3}+z\right) - 4m^2(1-\alpha_1)\right] \\
&+ \frac{p^2}{9} + m^2 - \frac{p^2}{3}z' - \frac{1}{4}\frac{\alpha_3}{\alpha_1}\left(\frac{2}{3}-z'\right)^2 p^2 - \frac{\alpha_1}{\alpha_3}m^2.
\end{aligned}
\tag{G.28}
$$

It should also be noticed that the derivative $\frac{\partial}{\partial\gamma}[\rho(\gamma_0)]$ is weakly singular at $\gamma' = \gamma'_{\max}$, corresponding to the lower threshold $\gamma_0 = 4\,m^2$.

It turns out that the numerical calculation of the kernel given by Eq. (G.26) can present some difficulties due to the singular behavior as $\alpha_1 \to 1$. One can therefore derive an alternative equation by simply performing the integration over γ' in Eq. (G.20) instead of over γ'', as done in Eq. (G.26).

After integration over γ' and performing the transformation $\alpha_3 \to \alpha_3/\alpha_1$, Eq. (G.20) can be re-written in a more suitable way to be solved numerically. The final equations to be solved are presented in Eqs. (4.35) and (4.36).

Appendix H

Derivations for the boson-fermion BSE

The derivations presented in this appendix are based on Refs. [148, 149].

H.1 Coefficients of the BSE in Minkowski space

After performing the traces, following the derivations given in Refs. [48, 116], one finds for the coefficients of the scalar boson exchange BSE:

$$
\begin{aligned}
\mathcal{C}^s_{11} &= \frac{1}{2}M + m_F \\
\mathcal{C}^s_{12} &= \frac{k^2(p \cdot k')(\frac{1}{2}M + m_F) + (p \cdot k)(k \cdot k')(\frac{1}{2}M - m_F)}{M^2 k^2 - (p \cdot k)^2} \\
&\quad + \frac{M k^2(k \cdot k') - \frac{1}{M}(p \cdot k)^2(p \cdot k') - \frac{k^2}{M}(p \cdot k)(p \cdot k')}{M^2 k^2 - (p \cdot k)^2} \\
\mathcal{C}^s_{21} &= M \\
\mathcal{C}^s_{22} &= \frac{k^2 M(p \cdot k') + (\frac{1}{2}M - m_F)(p \cdot k)(p \cdot k')}{M^2 k^2 - (p \cdot k)^2} \\
&\quad + \frac{M^2(k \cdot k')(m_F - \frac{1}{2}M) - M(p \cdot k)(k \cdot k')}{M^2 k^2 - (p \cdot k)^2}
\end{aligned}
\tag{H.1}
$$

while for the vector exchange (5.5) they read

$$
\begin{aligned}
\mathcal{C}_{11}^{v} &= -\left[(k^2 - \left(\frac{1}{2} + \frac{m_F}{M} \right) M^2 + k \cdot p + v k' \cdot p \right] \\
&\quad - \frac{M^2 \left[k^2 + \left(\frac{1}{2} - \frac{m_F}{M} \right) k \cdot p \right] k \cdot k' - k^2 \left[\left(\frac{1}{2} - \frac{m_F}{M} \right) M^2 + k \cdot p \right] k' \cdot p}{M^2 k^2 - (p \cdot k)^2}, \\
\mathcal{C}_{12}^{v} &= -(k \cdot k' + k'^2 - k' \cdot p) \left(\frac{1}{2} + \frac{m_F}{M} \right) \\
&\quad - \frac{\left[k^2 + \left(\frac{1}{2} - \frac{m_F}{M} \right) p \cdot k \right] \left[(p \cdot k') k^2 - (k \cdot k')(p \cdot k) - (p \cdot k')(p \cdot k) + (k \cdot k') M^2 \right]}{M^2 k^2 - (p \cdot k)^2}, \\
\mathcal{C}_{21}^{v} &= -\left(\frac{m_F}{M} - \frac{3}{2} \right) M^2 \\
&\quad - M^2 \frac{\left[k^2 + \left(\frac{1}{2} - \frac{m_F}{M} \right) p \cdot k \right] p \cdot k' - \left[\left(\frac{1}{2} - \frac{m_F}{M} \right) M^2 + p \cdot k \right] k \cdot k'}{M^2 k^2 - (p \cdot k)^2}, \\
\mathcal{C}_{22}^{v} &= -(k' \cdot k + k'^2 - p \cdot k') \\
&\quad - \frac{\left[\left(\frac{1}{2} - \frac{m_F}{M} \right) M^2 + p \cdot k \right] \left[(k' \cdot k)(p \cdot k) - (p \cdot k') k^2 - (k' \cdot k) M^2 + (p \cdot k')(p \cdot k) \right]}{M^2 k^2 - (p \cdot k)^2}.
\end{aligned}
$$
(H.2)

The superscript $s(v)$ will be kept for the moment to indicate the coefficients in the kernel of the bound state equation for the scalar (vector) exchange.

H.1.1   Final coefficients with NIR and LF projection

The final form of the coefficients, after introducing the NIR, the LF variables and performing the integration on k^-, is given below. For the scalar case one has that the coefficients in Eq. (5.10) are given by

$$
\begin{aligned}
c_{11}^{(0)} &= \frac{M}{2} + m_F; \\
c_{12}^{(0)} &= -\frac{z'v}{2} \left(\frac{M}{2} + m_F \right) - (1 - v) \frac{1}{M} \left(\gamma + \frac{z M^2}{4} \right), \qquad c_{12}^{(1)} = \frac{(1 - v)}{2} (1 - z); \\
c_{21}^{(0)} &= M; \\
c_{22}^{(0)} &= -M \frac{z'v}{2} - (1 - v) \left(\frac{M}{2} - m_F \right),
\end{aligned}
$$
(H.3)

while for the vector exchange the final coefficients read

$$c_{11}^{(0)} = \frac{M^2}{2}\left[a + vz'\frac{a}{2} + (2-v)\frac{z}{2}\right] + (2-v)\gamma$$

$$c_{11}^{(1)} = -\frac{M}{2}(2-v)(1-z)$$

$$c_{12}^{(0)} = \frac{a}{2}\left\{\gamma(1-v)(2+v) + 2v(\gamma'+\kappa^2) + 2(1-v)\mu^2 \quad + \frac{M^2}{4}(vz'-2)[z-v(z-z')]\right\}$$

$$\qquad + \left(\gamma + z\frac{M^2}{4}\right)\ \left(1 - v - z'\frac{v}{2}\right)$$

$$c_{12}^{(1)} = \frac{M}{2}\ \left\{a(1-v)\left[1 + z + (z-z')\frac{v}{2}\right] - (1-z)\ \left(1 - v - z'\frac{v}{2}\right)\right\}$$

$$c_{21}^{(0)} = \frac{M^2}{2}\left[(2-v)(2-a) + 2 + z'v\right]$$

$$c_{22}^{(0)} = \gamma(1-v)(2+v) + 2v(\gamma'+\kappa^2) + 2(1-v)\mu^2$$

$$\qquad + \frac{M^2}{2}\left[(1-v)\left(zz'\frac{v}{2} - z + 2 - a\right) + z'\frac{v}{2}\ (z'v - 4 + a)\right]$$

$$c_{22}^{(1)} = \frac{M}{2}\ (1-v)\left[v(z-z') + 2(1+z)\right]$$

$$\text{(H.4)}$$

where $a = 1 + 2m_F/M$.

H.2   Wick-rotated coefficients for the boson-fermion BSE

The Wick-rotated equation for the boson-fermion BSE with a vector boson exchanged is derived in this appendix. The first step is to carry out the Wick-rotation in Eq. (H.2), by performing the following transformations: $k^2 \to k_E^2 = -(k_4^2 + \vec{k}^2)$, $p\cdot k \to p\cdot k_E = iMk_4$, $p\cdot k' \to p\cdot k'_E = iMk'_4$, $k\cdot k' \to k_E\cdot k'_E = -(k_4k'_4 + \vec{k}\cdot\vec{k'})$ and

$k'^2 \rightarrow k_E'^2 = -(k_4'^2 + \vec{k}'^2)$, what gives

$$
\begin{aligned}
\mathcal{C}_{11}^E &= \frac{-2\,\vec{k}^4 - \vec{k}^2\,(2\,k_4^2 - 2\,i\,k_4\,M + 2\,\vec{k}\cdot\vec{k}' + (M - ik_4')(M + 2\,m_F))}{2\,\vec{k}^2} \\
&\quad + \frac{k_4\,\vec{k}\cdot\vec{k}'\,(-2\,k_4 + i(M - 2\,m_F))}{2\,k^2} \\
\mathcal{C}_{12}^E &= \frac{-2\,i\vec{k}^4\,k_4' + \vec{k}^2\,(-2\,ik_4^2\,k_4' + 2\,ik_4(\vec{k}\cdot\vec{k}' + ik_4'\,M) - \vec{k}\cdot\vec{k}'(3\,M + 2\,m_F)}{2\,\vec{k}^2\,M} \\
&\quad + \frac{-(M + 2\,m_F)(\vec{k}'^2 + k_4'^2 + ik_4'\,M)) + k_4\,\vec{k}\cdot\vec{k}'\,(k_4 + iM)(2\,ik_4 + M - 2\,m_F)}{2\,\vec{k}^2\,M} \\
\mathcal{C}_{21}^E &= -\frac{M(\vec{k}^2(-2\,ik_4' + 3\,M - 2\,m_F) + \vec{k}\cdot\vec{k}'\,(2\,ik_4 + M - 2\,m_F))}{2\,\vec{k}^2} \\
\mathcal{C}_{22}^E &= -\frac{\vec{k}^2\,(2\,\vec{k}\cdot\vec{k}' + 2\,k'^2 + k_4'(2\,k_4' + 3\,iM - 2\,i\,m_F))}{2\,\vec{k}^2} \\
&\quad - \frac{\vec{k}\cdot\vec{k}'\,(k_4 + iM)(2k_4 - i(M - 2\,m_F))}{2\,\vec{k}^2}.
\end{aligned}
\tag{H.5}
$$

H.2.1 Angular integration

Since $\vec{k}\cdot\vec{k}' = |\vec{k}||\vec{k}'|\cos\theta$ and considering the angular dependence in the interaction kernel, i.e.

$$
\frac{1}{(k - k')^2 + \mu^2} = \frac{1}{(k_4 - k_4')^2 + \vec{k}^2 + \vec{k}'^2 - 2\,|\vec{k}||\vec{k}'|\cos\theta + \mu^2},
\tag{H.6}
$$

leading to the definitions of the auxiliary functions a and b,

$$
\begin{aligned}
a &= (k_4 - k_4')^2 + \vec{k}^2 + \vec{k}'^2 + \mu^2 \\
\text{and}\quad b &= 2\,|\vec{k}||\vec{k}'|.
\end{aligned}
\tag{H.7}
$$

These expressions are introduced since the angular integration can be performed through the following compact formulas

$$
\begin{aligned}
\int_{-1}^{1} d\cos\theta\,\frac{1}{a - b\cos\theta} &= \frac{1}{b}\ln\frac{a + b}{a - b} \\
\text{and}\quad \int_{-1}^{1} d\cos\theta\,\frac{\cos\theta}{a - b\cos\theta} &= -\frac{2}{b} + \frac{a}{b^2}\ln\frac{a + b}{a - b}.
\end{aligned}
\tag{H.8}
$$

For the sake of simplicity, from now on it will be adopted $\vec{k} \rightarrow k$ and $\vec{k}' \rightarrow k'$ for the notation, since here no more four-vectors are involved.

After performing the angular integrations, i.e. the one over θ and the one over the azimuthal angle (which trivially leads to a factor of 2π), the integral equation

reads

$$\phi_i(k_4, k) = -\frac{\alpha}{(2\pi)^2}$$

$$\times \sum_{j=1,2} \int dk'_4 dk' \frac{b\left(c^{(0)}_{ij} + \frac{a}{2}c^{(1)}_{ij}\right)\ln\frac{a+b}{a-b} - b^2 c^{(1)}_{ij}}{k^2 \left[m_F^2 + k^2 + (k_4 - iM/2)^2\right]\left[m_S^2 + k^2 + (k_4 + iM/2)^2\right]} \phi_j(k'_4, k') \tag{H.9}$$

and the final coefficients are

$$c^{(0)}_{11} = -k^2 - k_4^2 + ik_4 M + iM(k'_4 + iM)\left(\frac{1}{2} + \frac{m_F}{M}\right),$$

$$c^{(1)}_{11} = \frac{-k^2 - k_4^2 + ik_4 M\left(\frac{1}{2} - \frac{m_F}{M}\right)}{k^2};$$

$$c^{(0)}_{12} = -\left(i\frac{k'_4}{M}(k^2 + k_4^2) + k_4 k'_4 + (k'^2 + k_4^2 + ik'_4 M)\left(\frac{1}{2} + \frac{m_F}{M}\right)\right),$$

$$c^{(1)}_{12} = i\frac{k_4}{M} - \left(\frac{3}{2} + \frac{m_F}{M}\right) + \frac{k_4}{k^2}(k_4 + iM)\left(i\frac{k_4}{M} + \left(\frac{1}{2} - \frac{m_F}{M}\right)\right); \tag{H.10}$$

$$c^{(0)}_{21} = M\left[ik'_4 - M\left(\frac{3}{2} - \frac{m_F}{M}\right)\right], \qquad c^{(1)}_{21} = -\frac{M}{k^2}\left[ik_4 + M\left(\frac{1}{2} - \frac{m_F}{M}\right)\right];$$

$$c^{(0)}_{22} = -(k_4'^2 + k'^2) - ik'_4 M\left(\frac{3}{2} - \frac{m_F}{M}\right),$$

$$c^{(1)}_{22} = -1 - \frac{1}{k^2}(k_4 + iM)\left(k_4 - iM\left(\frac{1}{2} - \frac{m_F}{M}\right)\right).$$

This equation is non-singular and therefore suitable to be solved numerically.

H.3 Manipulations for the Wick-rotated asymptotic equation

With the ansatz presented in Eq. (5.22), the set of integral equations becomes

$$K^{\eta+7} F_1(\varphi) = -\frac{\alpha}{(2\pi)^2} \int_0^\infty dK' K'^{\eta+2} \int_0^\pi \frac{d\varphi'}{\sin^2 \varphi'} \left\{\left[b\left(\bar{c}^{(0)}_{11} + \frac{a}{2}\bar{c}^{(1)}_{11}\right)L - b^2 \bar{c}^{(1)}_{11}\right] F_1(\varphi')\right.$$

$$\left. + K'^{-1}\left[b\left(\bar{c}^{(0)}_{12} + \frac{a}{2}\bar{c}^{(1)}_{12}\right)L - b^2 \bar{c}^{(1)}_{12}\right]F_2(\varphi')\right\}$$

$$K^{\eta+6} F_2(\varphi) = -\frac{\alpha}{(2\pi)^2} \int_0^\infty dK' K'^{\eta+1} \int_0^\pi \frac{d\varphi'}{\sin^2 \varphi'} \left\{\left[b\left(\bar{c}^{(0)}_{22} + \frac{a}{2}\bar{c}^{(1)}_{22}\right)L - b^2 \bar{c}^{(1)}_{22}\right] F_2(\varphi')\right.$$

$$\left. + K'\left[b\left(\bar{c}^{(0)}_{21} + \frac{a}{2}\bar{c}^{(1)}_{21}\right)L - b^2 \bar{c}^{(1)}_{21}\right]F_1(\varphi')\right\}, \tag{H.11}$$

where

$$L = \ln\frac{a+b}{a-b} = \ln\frac{1 + y^2 - 2y\cos\varphi \, \cos\varphi' + 2y\sin\varphi \, \sin\varphi'}{1 + y^2 - 2y\cos\varphi \, \cos\varphi' - 2y\sin\varphi \, \sin\varphi'}$$

$$= \ln\frac{1 + y^2 - 2y\cos(\varphi + \varphi')}{1 + y^2 - 2y\cos(\varphi - \varphi')}. \tag{H.12}$$

Substituting the coefficients (5.21) in Eq. (H.11), one obtains the following set of coupled integral equations

$$
K^{\eta+7} F_1(\varphi) = -\frac{\alpha}{(2\pi)^2} \int_0^\infty dK' \, K'^{\eta+2} \int_0^\pi \frac{d\varphi'}{\sin^2 \varphi'} \Big\{ H'_{11} F_1(\varphi') + \imath \, H'_{12} F_2(\varphi') \Big\},
$$

$$
K^{\eta+6} F_2(\varphi) = -\frac{\alpha}{(2\pi)^2} \int_0^\infty dK' \, K'^{\eta+1} \int_0^\pi \frac{d\varphi'}{\sin^2 \varphi'} \Big\{ H'_{21} F_1(\varphi') - \imath \, H'_{22} F_2(\varphi') \Big\},
$$

$$
\text{(H.13)}
$$

where

$$
\begin{aligned}
H'_{11} &= -KK' \sin \varphi \sin \varphi' \left(\csc^2 \varphi \left(-2KK' \cos \varphi \cos \varphi' + K^2 + K'^2 \right) + 2K^2 \right) L \\
&\quad + 4K^2 K'^2 \sin \varphi'^2 \\
H'_{12} &= K^2 \csc \varphi \sin \varphi' \left((K^2 + K'^2) \cos \varphi - 2KK' \cos \varphi' \right) L - 4K^3 K' \cos \varphi \sin^2 \varphi' \\
H'_{21} &= K'^2 \csc \varphi \sin \varphi' \left((K^2 + K'^2) \cos \varphi - 2KK' \cos \varphi' \right) L - 4KK'^3 \cos \varphi \sin^2 \varphi' \\
H'_{22} &= -KK' \sin \varphi \sin \varphi' \left(2K'^2 + (K^2 + K'^2 - 2KK' \cos \varphi \cos \varphi') \csc^2 \varphi \right) L \\
&\quad + 4K^2 K'^2 \sin^2 \varphi'
\end{aligned}
$$

$$
\text{(H.14)}
$$

Then, by the transformation $K' \to K y$ the equation simplifies to:

$$
\begin{aligned}
F_1(\varphi) = -\frac{\alpha}{(2\pi)^2} \int_0^\infty dy \, y^{\eta+2} \int_0^\pi \frac{d\varphi'}{\sin^2 \varphi'} \\
\times \Big\{ \Big[-y \sin \varphi \sin \varphi' \left(\csc^2 \varphi \left(-2y \cos \varphi \cos \varphi' + 1 + y^2 \right) + 2 \right) L + 4y^2 \sin^2 \varphi' \Big] F_1(\varphi') \\
+ \imath \Big[\csc \varphi \sin \varphi' \left((1 + y^2) \cos \varphi - 2y \cos \varphi' \right) L - 4y \cos \varphi \sin^2 \varphi' \Big] F_2(\varphi') \Big\}
\end{aligned}
$$

$$
\begin{aligned}
F_2(\varphi) = -\frac{\alpha}{(2\pi)^2} \int_0^\infty dy \, y^{\eta+1} \int_0^\pi \frac{d\varphi'}{\sin^2 \varphi'} \\
\times \Big\{ \Big[-y \sin \varphi \sin \varphi' \left(2y^2 + (1 + y^2 - 2y \cos \varphi \cos \varphi') \csc^2 \varphi \right) L + 4y^2 \sin^2 \varphi' \Big] F_2(\varphi') \\
- \imath \Big[y^2 \csc \varphi \sin \varphi' \left((1 + y^2) \cos \varphi - 2y \cos \varphi' \right) L - 4y^3 \cos \varphi \sin^2 \varphi' \Big] F_1(\varphi') \Big\}.
\end{aligned}
$$

$$
\text{(H.15)}
$$

Introducing $\imath F_2 \to F_2$ and further simplifying the equations one gets Eq. (5.23).

H.4   High momentum limit in Minkowski space

The coefficients of the BSE in Minkowski space, presented in Eq. (H.4), become, in the high momentum limit,

$$
\begin{aligned}
c_{11}^{(0)} &= (2-v)\gamma, & \text{(H.16)}\\
c_{11}^{(1)} &= -\frac{M}{2}(2-v)(1-z),\\
c_{12}^{(0)} &= \frac{a}{2}\left\{\gamma(1-v)(2+v)+2v\gamma'\right\} \quad +\gamma\left(1-v-z'\frac{v}{2}\right),\\
c_{12}^{(1)} &= \frac{M}{2}\left\{a(1-v)\left[1+z+(z-z')\frac{v}{2}\right]-(1-z)\left(1-v-z'\frac{v}{2}\right)\right\},\\
c_{21}^{(0)} &= \frac{M^2}{2}\left[(2-v)(2-a)+2+z'v\right],\\
c_{22}^{(0)} &= \gamma(1-v)(2+v)+2\,v\,\gamma',\\
c_{22}^{(1)} &= \frac{M}{2}(1-v)\left[v(z-z')+2(1+z)\right].
\end{aligned}
$$

Moreover, Eq.(5.11) now reads

$$
k_u^- = -\frac{2\,\gamma}{(1+z)M}\ ,\quad k_d^- = \frac{2\,\gamma}{(1-z)M}\ \ . \tag{H.17}
$$

and for Eq. (5.10) one has that

$$
\begin{aligned}
&B_{11}(k_{u(d)}^-)=c_{11}^{(0)}+c_{11}^{(1)}k_{u(d)}^-\ , &\qquad &B_{12}(k_{u(d)}^-)=c_{12}^{(0)}+c_{12}^{(1)}k_{u(d)}^-\\
&B_{21}(k_{u(d)}^-)=c_{21}^{(0)}\ , & &B_{22}(k_{u(d)}^-)=c_{22}^{(0)}+c_{22}^{(1)}k_{u(d)}^-
\end{aligned}\quad , \tag{H.18}
$$

Finally, one should consider here that the equations decouple, based on the conclusion found in Sec. 5.2.1 for the Wick-rotated equation. Consequently, the BSE (5.8) for ϕ_2 becomes

$$
\int_0^\infty d\gamma' \frac{g_2(\gamma',z)}{[\gamma'+\gamma-i\epsilon]^2} = \frac{\alpha}{4\pi}\,\frac{1}{\gamma}\,\int_0^1 dv\,v^2 \int_0^\infty d\gamma' \int_{-1}^1 dz'\ g_2(\gamma',z')
$$

$$
\times \left\{\left[\gamma(1-v)v-\gamma(1-v)v\frac{z-z'}{1+z}+2\,v\,\gamma'\right]\frac{(1+z)^2\,\theta(z'-z)}{D_u^2(z',z)}\right.
$$

$$
\left.+\left[\gamma(1-v)(2+v)+2\,v\,\gamma'+\frac{\gamma}{1-z}(1-v)\left[v(z-z')+2(1+z)\right]\right]\frac{(1-z)^2\,\theta(z-z')}{D_d^2(z',z)}\right\}
$$

$$
= \frac{\alpha}{4\pi}\,\frac{1}{\gamma}\,\int_0^1 dv\,v^2 \int_0^\infty d\gamma' \int_{-1}^1 dz'\,g_2(\gamma',z')\left\{\left[\gamma(1-v)v\frac{1+z'}{1+z}+2\,v\,\gamma'\right]\frac{(1+z)^2\,\theta(z'-z)}{D_u^2(z',z)}\right.
$$

$$
\left.+\left[\gamma(1-v)\frac{4+v(1-z')}{1-z}+2\,v\,\gamma'\right]\frac{(1-z)^2\,\theta(z-z')}{D_d^2(z',z)}\right\},\quad \text{(H.19)}
$$

where the value of the coupling constant α was already obtained through the Wick-rotated equation given by (5.32). The denominator D_u (for $z'>z$) is

$$
\begin{aligned}
D_u(z',z) &= v(1-v)\,(z'-z)\,\gamma+(1+z)\,[v(1-v)\gamma+v\,\gamma']\\
&= v(\gamma'(1+z)+\gamma(1-v)(1+z')), \tag{H.20}
\end{aligned}
$$

Considering the scale invariance of Eqs. (H.19) and (5.35), one can use the ansatz for the Nakanishi weight function presented in Eq. (5.40), i.e. $g_2(\gamma, z) = \gamma^r f(z)$, where $r = 2 + \frac{\eta}{2}$ with the constraint that

$$-1 < r < 0,$$

which is equivalent to (5.27).

Substituting (5.40) in (5.8) and making the transformation $\gamma' \to \gamma\, y$:

$$
\pi r \csc(\pi r)\, f(z) = \frac{\alpha}{4\pi} \int_{-1}^{1} dz'\, f(z') \int_0^1 dv \int_0^\infty dy\, y^r
$$
$$
\times \left\{ \left[(1-v)v\frac{1+z'}{1+z} + 2\,v\,y \right] \frac{(1+z)^2\,\theta(z'-z)}{(y(1+z)+(1-v)(1+z'))^2} \right.
$$
$$
\left. + \left[(1-v)\frac{4+v(1-z')}{1-z} + 2\,v\,y \right] \frac{(1-z)^2\,\theta(z-z')}{(y(1-z)+(1-v)(1-z'))^2} \right\}
$$
$$
= \frac{\alpha}{4\pi} \int_{-1}^{1} dz'\, f(z') \int_0^1 dv \int_0^\infty dy\, y^r
$$
$$
\times \left\{ v\left[(1-v)(1+z') + 2\,y(1+z) \right] \frac{(1+z)\,\theta(z'-z)}{(y(1+z)+(1-v)(1+z'))^2} \right.
$$
$$
\left. + \left[(1-v)(4+v(1-z')) + 2\,v\,y(1-z) \right] \frac{(1-z)\,\theta(z-z')}{(y(1-z)+(1-v)(1-z'))^2} \right\}
$$
$$
= \frac{\alpha}{4\pi} \int_{-1}^{1} dz'\, f(z') \int_0^1 dv \int_0^\infty dy\, y^r
$$
$$
\times \left\{ \frac{v}{1+z} \left[(1-v)(1+z') + 2\,y(1+z) \right] \frac{\theta(z'-z)}{(y+(1-v)\frac{1+z'}{1+z})^2} \right.
$$
$$
\left. + \frac{1}{1-z} \left[(1-v)(4+v(1-z')) + 2\,v\,y(1-z) \right] \frac{\theta(z-z')}{(y+(1-v)\frac{1-z'}{1-z})^2} \right\}, \quad \text{(H.21)}
$$

where it was used the following integral,

$$
\int_0^\infty dx\, \frac{x^a}{(x+y)^2} = y^{a-1}\pi a \csc(\pi a). \quad \text{(H.22)}
$$

After some manipulations, one has that

$$
f(z) = \frac{\alpha}{4\pi r} \int_{-1}^{1} dz'\, f(z') \int_0^1 dv \left\{ \frac{v}{1+z} K'_{(z'-z)}\theta(z'-z) + \frac{1}{1-z} K'_{(z-z')}\theta(z-z') \right\}
$$
$$
= \frac{\alpha}{4\pi r} \int_{-1}^{1} dz'\, f(z') \int_0^1 dv \left\{ -v \left[(1-v)\frac{1+z'}{1+z} \right]^r [2+r]\,\theta(z'-z) \right.
$$
$$
\left. + \left[(1-v)\frac{1-z'}{1-z} \right]^r \left[\frac{4r}{1-z'} - v(2+r) \right] \theta(z-z') \right\}, \quad \text{(H.23)}
$$

where

$$
K'_{(z'-z)} = r \left[(1-v)\frac{1+z'}{1+z} \right]^{r-1} (1-v)(1+z') - 2(1+r)(1+z) \left[(1-v)\frac{1+z'}{1+z} \right]^{r}
$$

$$
K'_{(z-z')} = r(1-v) \left[(1-v)\frac{1-z'}{1-z} \right]^{r-1} (4+v(1-z'))
$$

$$
- 2\,v(1+r)(1-z) \left[(1-v)\frac{1-z'}{1-z} \right]^{r}
$$

(H.24)

and after integrating over v, one obtains

$$
f(z) = \frac{\alpha}{4\pi|r|} \int_{-1}^{1} dz' f(z') \Bigg\{ \left[\frac{1+z}{1+z'} \right]^{|r|} \frac{2+r}{2+3r+r^2} \theta(z'-z)
$$

$$
+ \left[\frac{1-z}{1-z'} \right]^{|r|} \left[\frac{2+r}{2+3r+r^2} + \frac{4|r|}{(1+r)(1-z')} \right] \theta(z-z') \Bigg\}. \quad \text{(H.25)}
$$

Eq. (H.25) can be further simplified to

$$
f(z) = \frac{\alpha}{4\pi|r|(1+r)}
$$

$$
\times \int_{-1}^{1} dz' f(z') \Bigg\{ \left[\frac{1+z}{1+z'} \right]^{|r|} \theta(z'-z) + \left[\frac{1-z}{1-z'} \right]^{|r|} \left[1 + \frac{4|r|}{(1-z')} \right] \theta(z-z') \Bigg\},
$$

(H.26)

where the value of α depends on r according to (5.32) and can be written as

$$
\alpha = -\frac{2\pi r(1-r^2)}{1-2r}. \quad \text{(H.27)}
$$

An analogous development could be done for ϕ_1 and the corresponding g_1.

Appendix I

Fermion-antifermion BSE: Kernel and numerics

The formalism for the solution of the fermion-antifermion (0^-) Bethe-Salpeter equation is briefly summarized, focusing on the numerical treatment of the problem. The LF projection and NIR are used to obtain a non-singular generalized eigenvalue problem, which when can be solved by adopting a basis expansion. The content of this appendix is based on Ref. [186].

I.1 Non-singular contribution to the kernel

The non-singular contribution to the kernel in Eq. (6.8) is for the scalar exchange given by

$$
\begin{aligned}
\mathcal{L}_{ij}^{(ns)}(\gamma, z, \gamma', z') = & \frac{m^2(\mu^2 - \Lambda^2)^2}{2\pi[\gamma + z^2 m^2 + (1 - z^2)\kappa^2]} \int_0^1 dv v^2 (1 - v)^2 \\
& \times \left\{ \theta(-k_D^+) \frac{C_{ij}(\gamma, z; v)[3k_d^- k_D^+ + 3\ell_D + (1 - v)(\mu^2 - \Lambda^2)]}{[k_D^+ k_d^- + \ell_D + (1 - v)(\mu^2 - \Lambda^2) + i\epsilon]^3 [k_D^+ k_d^- + \ell_D + i\epsilon]^2} \right. \\
& \left. + \sigma_{ij}[z \to -z; z' \to -z'] \right\}.
\end{aligned}
\tag{I.1}
$$

Moreover, in the case of pseudo-scalar exchange one has

$$
\begin{aligned}
(\mathcal{L}_{14}^{(ns)})^{(PS)} = -\mathcal{L}_{14}^{(ns)}, \quad (\mathcal{L}_{22}^{(ns)})^{(PS)} = \mathcal{L}_{22}^{(ns)}, \quad (\mathcal{L}_{24}^{(ns)})^{(PS)} = -\mathcal{L}_{24}^{(ns)} \\
(\mathcal{L}_{33}^{(ns)})^{(PS)} = \mathcal{L}_{33}^{(ns)}, \quad (\mathcal{L}_{23}^{(ns)})^{(PS)} = \mathcal{L}_{23}^{(ns)}
\end{aligned}
\tag{I.2}
$$

and for the massless vector exchange

$$
\begin{aligned}
(\mathcal{L}_{14}^{(ns)})^{(V)} = 0, \quad (\mathcal{L}_{22}^{(ns)})^{(V)} = -2\mathcal{L}_{22}^{(ns)}, \quad (\mathcal{L}_{24}^{(ns)})^{(V)} = 0 \\
(\mathcal{L}_{33}^{(ns)})^{(V)} = -2\mathcal{L}_{33}^{(ns)}, \quad (\mathcal{L}_{23}^{(ns)})^{(V)} = -2\mathcal{L}_{23}^{(ns)}.
\end{aligned}
\tag{I.3}
$$

In Eq. (I.1) it was also introduced the quantities

$$
k_D^+ = v(1 - v)M(z' - z)/2,
\tag{I.4}
$$

$$\ell_D = -v(1-v)\big[\gamma + \frac{M^2}{4}z'(z-z')\big] - v\big[\gamma' + z'^2m^2 + (1-z'^2)\kappa^2\big] - (1-v)\mu^2, \quad \text{(I.5)}$$

$$k_d^- = -\frac{M}{2} + \frac{2}{M(1-z)}(\gamma + m^2), \quad \text{(I.6)}$$

and

$$k_u^- = \frac{M}{2} - \frac{2}{M(1+z)}(\gamma + m^2), \quad \text{(I.7)}$$

which under the transformation $(z \to -z, z' \to -z')$ obey the relations

$$k_D^+ \to -k_D^+, \quad \text{(I.8a)}$$
$$\ell_D \to \ell_D, \quad \text{(I.8b)}$$
$$k_d^- \to -k_u^-. \quad \text{(I.8c)}$$
$$\text{(I.8d)}$$

Furthermore, the matrix σ is defined as

$$\sigma = \begin{pmatrix} 1 & 1 & -1 & 1 \\ 1 & 1 & -1 & 1 \\ -1 & -1 & 1 & -1 \\ 1 & 1 & -1 & 1 \end{pmatrix}. \quad \text{(I.9)}$$

The denominator $D(\gamma, z, \gamma', z', v)$ used in [49] is given by

$$\begin{aligned} D(\gamma, z, \gamma', z', v) = -(1-z)(k_D^+ k_d^- + \ell_D) = \\ v(1-z')\gamma + vm^2[(1-v)(1-z')z^2 + vz'^2(1-z)] \\ + v\kappa^2(1-z)(1-z')[1+z-v(z-z')] + (1-z)[(1-v)\mu^2 + v\gamma'] =, \quad \text{(I.10)} \\ v(1-v)(1-z')[\gamma + z^2m^2 + (1-z^2)\kappa^2] + \\ v^2(1-z)[z'^2m^2 + (1-z'^2)\kappa^2] + (1-z)[v\gamma' + (1-v)\mu^2]. \end{aligned}$$

The coefficients C_{ij} in Eq. (I.1) which are non-vanishing read

$$C_{11}(\gamma, z; v) = \frac{Q_+}{4m^2(1-z)} \tag{I.11a}$$

$$C_{12}(\gamma, z; v) = \frac{M}{4m} \tag{I.11b}$$

$$C_{14}(\gamma, z; v) = -\frac{(1-v)}{(1-z)^2} \frac{[Q_+^2 - m^2 M^2 (1-z)^2]}{4m^2 M^2} \tag{I.11c}$$

$$C_{21}(\gamma, z; v) = C_{12}(\gamma, z; v) \tag{I.11d}$$

$$C_{22}(\gamma, z; v) = -\frac{[Q_+ \, Q_- - (1-z)^2 m^2 M^2]}{2m^2 M^2 (1-z)^2} \tag{I.11e}$$

$$C_{23}(\gamma, z; v) = -\frac{(1-v)}{(1-z)^3} \frac{Q_- \, [Q_+^2 - (1-z)^2 m^2 M^2]}{2m^2 M^4} \tag{I.11f}$$

$$C_{24}(\gamma, z; v) = \frac{2m}{M} C_{14}(\gamma, z; v) \tag{I.11g}$$

$$C_{32}(\gamma, z; v) = \frac{Q_-}{2m^2(1-z)} \tag{I.11h}$$

$$C_{33}(\gamma, z; v) = \frac{(1-v)}{(1-z)^2} \frac{Q_+ \, Q_-}{2m^2 M^2} \tag{I.11i}$$

$$C_{34}(\gamma, z; v) = (1-v) \frac{m}{M} C_{32}(\gamma, z; v) \tag{I.11j}$$

$$C_{41}(\gamma, z; v) = \frac{M}{m} C_{12}(\gamma, z; v) \tag{I.11k}$$

$$C_{42}(\gamma, z; v) = 2 C_{12}(\gamma, z; v) \tag{I.11l}$$

$$C_{43}(\gamma, z; v) = C_{34}(\gamma, z; v) \tag{I.11m}$$

$$C_{44}(\gamma, z; v) = -\frac{(1-v)}{(1-z)} \frac{[Q_+ - 2m^2(1-z)]}{4m^2} \tag{I.11n}$$

with

$$
\begin{aligned}
Q_+ = {}& \gamma + m^2 + \frac{M^2}{4}(1-z)^2 = \frac{M(1-z)}{2} \, k_d^- + \frac{M^2}{4} \, (1-z) \, (2-z) = \\
& \frac{M(1-z)}{2} \left(k_d^- - \frac{M}{2} z + M \right)
\end{aligned} \tag{I.12}
$$

and

$$
\begin{aligned}
Q_- = {}& \gamma + m^2 - \frac{M^2}{4}(1-z^2) = \gamma + z^2 m^2 + (1-z^2)\kappa^2 = \\
& \frac{M(1-z)}{2} \, k_d^- - \frac{M^2}{4} \, z(1-z) = \frac{M(1-z)}{2} \left(k_d^- - \frac{M}{2} z \right).
\end{aligned} \tag{I.13}
$$

From the numerical point of view, to avoid instabilities from the end-point

behavior close to $z = 1$, it can be advantageous to instead introduce the coefficients

$$\tilde{C}_{11}(\gamma, z) = \frac{(1-z)^3}{4m^2} Q_+ \tag{I.14a}$$

$$\tilde{C}_{12}(\gamma, z) = \frac{M}{4m}(1-z)^4 \tag{I.14b}$$

$$\tilde{C}_{14}(\gamma, z) = -\frac{(1-z)^2}{4m^2 M^2}[Q_+^2 - m^2 M^2 (1-z)^2] \tag{I.14c}$$

$$\tilde{C}_{21}(\gamma, z) = \tilde{C}_{12}(\gamma, z) \tag{I.14d}$$

$$\tilde{C}_{22}(\gamma, z) = -\frac{(1-z)^2}{2m^2 M^2}[Q_+ \, Q_- - (1-z)^2 m^2 M^2] \tag{I.14e}$$

$$\tilde{C}_{23}(\gamma, z) = -\frac{(1-z)}{2m^2 M^4} \, Q_- \, [Q_+^2 - (1-z)^2 m^2 M^2] \tag{I.14f}$$

$$\tilde{C}_{24}(\gamma, z) = \frac{2m}{M}\tilde{C}_{14}(\gamma, z) \tag{I.14g}$$

$$\tilde{C}_{32}(\gamma, z) = \frac{(1-z)^3}{2m^2} Q_- \tag{I.14h}$$

$$\tilde{C}_{33}(\gamma, z) = \frac{(1-z)^2}{2m^2 M^2} Q_+ \, Q_- \tag{I.14i}$$

$$\tilde{C}_{34}(\gamma, z) = \frac{m}{M}\tilde{C}_{32}(\gamma, z) \tag{I.14j}$$

$$\tilde{C}_{41}(\gamma, z) = \frac{M}{m}\tilde{C}_{12}(\gamma, z) \tag{I.14k}$$

$$\tilde{C}_{42}(\gamma, z) = 2\tilde{C}_{12}(\gamma, z) \tag{I.14l}$$

$$\tilde{C}_{43}(\gamma, z) = \tilde{C}_{34}(\gamma, z) \tag{I.14m}$$

$$\tilde{C}_{44}(\gamma, z) = -\frac{(1-z)^3}{4m^2}[Q_+ - 2m^2(1-z)], \tag{I.14n}$$

which are related to the coefficients C_{ij} according to

$$
\begin{aligned}
C_{11} &= \frac{1}{(1-z)^4}\tilde{C}_{11}, & C_{12} &= \frac{1}{(1-z)^4}\tilde{C}_{12}, & C_{14} &= \frac{(1-v)}{(1-z)^4}\tilde{C}_{14}, \\
C_{21} &= \frac{1}{(1-z)^4}\tilde{C}_{21}, & C_{22} &= \frac{1}{(1-z)^4}\tilde{C}_{22}, & C_{23} &= \frac{(1-v)}{(1-z)^4}\tilde{C}_{23}, \\
C_{24} &= \frac{(1-v)}{(1-z)^4}\tilde{C}_{24} & C_{32} &= \frac{1}{(1-z)^4}\tilde{C}_{32}, & C_{33} &= \frac{(1-v)}{(1-z)^4}\tilde{C}_{33}, \\
C_{34} &= \frac{(1-v)}{(1-z)^4}\tilde{C}_{34}, & C_{41} &= \frac{1}{(1-z)^4}\tilde{C}_{41}, & C_{42} &= \frac{1}{(1-z)^4}\tilde{C}_{42}, \\
C_{43} &= \frac{(1-v)}{(1-z)^4}\tilde{C}_{43}, & C_{44} &= \frac{(1-v)}{(1-z)^4}\tilde{C}_{44}.
\end{aligned}
\tag{I.15}
$$

The non-singular part can then be written in the form

$$
\mathcal{L}_{ij}^{(ns)}(\gamma, z, \gamma', z') = \frac{m^2(\mu^2 - \Lambda^2)^2}{2\pi[\gamma + z^2 m^2 + (1-z^2)\kappa^2]}
$$
$$
\times \{\theta(-k_D^+)\tilde{C}_{ij}(\gamma, z)\chi^{(k)}(\gamma, z, \gamma', z') + \sigma_{ij}[z \longrightarrow -z; z' \longrightarrow -z']\},
\tag{I.16}
$$

where it was defined the integrals

$$\chi^{(1)}(\gamma, z, \gamma', z') = \int_0^1 \frac{dv v^2 (1-v)^2 \left[3D(\gamma, z, \gamma', z', v) - (1-v)(1-z)(\mu^2 - \Lambda^2)\right]}{\left[D(\gamma, z, \gamma', z', v) - (1-v)(1-z)(\mu^2 - \Lambda^2)\right]^3 D^2(\gamma, z, \gamma', z', v)},$$
(I.17)

and

$$\chi^{(2)}(\gamma, z, \gamma', z') = \int_0^1 \frac{dv v^2 (1-v)^3 \left[3D(\gamma, z, \gamma', z', v) - (1-v)(1-z)(\mu^2 - \Lambda^2)\right]}{\left[D(\gamma, z, \gamma', z', v) - (1-v)(1-z)(\mu^2 - \Lambda^2)\right]^3 D^2(\gamma, z, \gamma', z', v)},$$
(I.18)

where $D(\gamma, z, \gamma', z')$ is defined by Eq. (I.10).

The index k in Eq. (I.16) depends on i and j as is shown in Table I.1.

Furthermore, by introducing the coefficients

$$\hat{C}_{ij}(\gamma, z) = \frac{m^2 (\mu^2 - \Lambda^2)^2}{2\pi[\gamma + z^2 m^2 + (1-z^2)\kappa^2]} \tilde{C}_{ij}(\gamma, z),$$
(I.19)

the expression for the non-singular part of the kernel can be written in the compact form

$$\mathcal{L}_{ij}^{(ns)}(\gamma, z, \gamma', z') = \theta(-k_D^+)\hat{C}_{ij}(\gamma, z)\chi^{(k)}(\gamma, z, \gamma', z') + \sigma_{ij}[z \longrightarrow -z; z' \longrightarrow -z'].$$
(I.20)

i	j	k
1	1	1
1	2	1
1	4	2
2	1	1
2	2	1
2	3	2
2	4	2
3	2	1
3	3	2
3	4	2
4	1	1
4	2	1
4	3	2
4	4	2

Table I.1. Values of k for the different combinations of i and j.

I.1.1   Singular contribution

For the singular part $\mathcal{L}_{ij}^{(s)}$ in Eq. (6.8) one has in the scalar case the following non-vanishing contributions

$$\mathcal{L}_{14}^{(s)}(\gamma, z, \gamma', z') = -\frac{(\mu^2 - \Lambda^2)^2}{2\pi M^2}\frac{\delta(z' - z)}{2(1 - z^2)}\int_0^1 dv\frac{v(1 - v)^2}{D_\ell}, \tag{I.21a}$$

$$\mathcal{L}_{22}^{(s)}(\gamma, z, \gamma', z') = -\frac{(\mu^2 - \Lambda^2)^2}{2\pi M^2}\frac{\delta(z' - z)}{(1 - z^2)}\int_0^1 dv\frac{v(1 - v)}{D_\ell}, \tag{I.21b}$$

$$\mathcal{L}_{24}^{(s)}(\gamma, z, \gamma', z') = -\frac{(\mu^2 - \Lambda^2)^2}{2\pi M^2}\frac{m}{M}\frac{\delta(z' - z)}{(1 - z^2)}\int_0^1 dv\frac{v(1 - v)^2}{D_\ell}, \tag{I.21c}$$

$$\mathcal{L}_{33}^{(s)}(\gamma, z, \gamma', z') = \frac{(\mu^2 - \Lambda^2)^2}{2\pi M^2}\frac{\delta(z' - z)}{(1 - z^2)}\int_0^1 dv\frac{v(1 - v)^2}{D_\ell}, \tag{I.21d}$$

$$\mathcal{L}_{23}^{(s)}(\gamma, z, \gamma', z') = \mathcal{L}_{23}^{(s,a)}(\gamma, z, \gamma', z') + \mathcal{L}_{23}^{(s,b)}(\gamma, z, \gamma', z'), \tag{I.21e}$$

where

$$\mathcal{L}_{23}^{(s,a)}(\gamma, z, \gamma', z') = -\frac{(\mu^2 - \Lambda^2)^2}{2\pi M^2}\frac{2z\delta(z' - z)}{M^2(1 - z^2)^2}\left[\frac{M^2(1 - z^2)}{8} + \gamma + m^2\right]\int_0^1 dv\frac{v(1 - v)^2}{D_\ell}, \tag{I.22}$$

and

$$\mathcal{L}_{23}^{(s,b)}(\gamma, z, \gamma', z') = -\frac{1}{2\pi M^4(1 - z^2)}\left[\frac{\partial}{\partial z'}\delta(z' - z)\right]\int_0^1\frac{dv}{(1 - v)}$$
$$\times\left[\frac{(1 - v)(\mu^2 - \Lambda^2)}{\ell_D + (1 - v)(\mu^2 - \Lambda^2)} + \log\left(\frac{\ell_D}{\ell_D + (1 - v)(\mu^2 - \Lambda^2)}\right)\right]. \tag{I.23}$$

In the above expressions it was defined

$$D_\ell = \tilde{\ell}_D[\tilde{\ell}_D + (1 - v)(\mu^2 - \Lambda^2) + i\epsilon]^2 \tag{I.24a}$$

$$\tilde{\ell}_D = -v(1 - v)\gamma - v(\gamma' + z^2 m^2 + (1 - z^2)\kappa^2) - (1 - v)\mu^2, \tag{I.24b}$$

i.e $\tilde{\ell}_D = \ell_D|_{z=z'}$.

Furthermore, for the pseudo-scalar exchange one has

$$(\mathcal{L}_{14}^{(s)})^{(PS)} = -\mathcal{L}_{14}^{(s)}, \quad (\mathcal{L}_{22}^{(s)})^{(PS)} = \mathcal{L}_{22}^{(s)}, \quad (\mathcal{L}_{24}^{(s)})^{(PS)} = -\mathcal{L}_{24}^{(s)}$$
$$(\mathcal{L}_{33}^{(s)})^{(PS)} = \mathcal{L}_{33}^{(s)}, \quad (\mathcal{L}_{23}^{(s)})^{(PS)} = \mathcal{L}_{23}^{(s)} \tag{I.25}$$

and for the massless vector exchange

$$(\mathcal{L}_{14}^{(s)})^{(V)} = 0, \quad (\mathcal{L}_{22}^{(s)})^{(V)} = -2\mathcal{L}_{22}^{(s)}, \quad (\mathcal{L}_{24}^{(s)})^{(V)} = 0$$
$$(\mathcal{L}_{33}^{(s)})^{(V)} = -2\mathcal{L}_{33}^{(s)}, \quad (\mathcal{L}_{23}^{(s)})^{(V)} = -2\mathcal{L}_{23}^{(s)} \tag{I.26}$$

I.2   Numerical methods

I.2.1   Explicit removal of the theta and delta functions

From the numerical point of view, it is important to explicitly remove the theta functions in Eq. (I.1), and the delta functions in Eqs.(I.21). This can be easily done by carefully considering the integrations over z' in Eq. (6.8).

Starting by considering the non-singular contribution, by using the relations (I.8), one can rewrite (I.1) as

$$\mathcal{L}_{ij}^{(ns)}(\gamma, z, \gamma', z') = \theta(z-z')\mathcal{L}_{ij}^{(ns,1)}(\gamma, z, \gamma', z') + \sigma_{ij}\theta(z'-z)\mathcal{L}_{ij}^{(ns,2)}(\gamma, z, \gamma', z'), \quad (I.27)$$

where

$$
\begin{aligned}
\mathcal{L}_{ij}^{(ns,1)}(\gamma, z, \gamma', z') &= \frac{m^2(\mu^2 - \Lambda^2)^2}{2\pi[\gamma + z^2 m^2 + (1-z^2)\kappa^2]} \int_0^1 dv\, v^2(1-v)^2 \\
&\times \frac{C_{ij}(\gamma, z; v)[3k_d^- k_D^+ + 3\ell_D + (1-v)(\mu^2 - \Lambda^2)]}{[k_D^+ k_d^- + \ell_D + (1-v)(\mu^2 - \Lambda^2) + i\epsilon]^3 [k_D^+ k_d^- + \ell_D + i\epsilon]^2},
\end{aligned}
\quad (I.28)
$$

and

$$
\begin{aligned}
\mathcal{L}_{ij}^{(ns,2)}(\gamma, z, \gamma', z') &= \frac{m^2(\mu^2 - \Lambda^2)^2}{2\pi[\gamma + z^2 m^2 + (1-z^2)\kappa^2]} \int_0^1 dv\, v^2(1-v)^2 \\
&\times \frac{C_{ij}(\gamma, -z; v)[3k_u^- k_D^+ + 3\ell_D + (1-v)(\mu^2 - \Lambda^2)]}{[k_D^+ k_u^- + \ell_D + (1-v)(\mu^2 - \Lambda^2) + i\epsilon]^3 [k_D^+ k_u^- + \ell_D + i\epsilon]^2}.
\end{aligned}
\quad (I.29)
$$

Consequently,

$$
\begin{aligned}
\mathcal{H}_{ij}^{(ns)}(\gamma, z) &= \int_{-1}^1 dz' \int_0^\infty d\gamma' \mathcal{L}_{ij}^{(ns)}(\gamma, z, \gamma', z')g_j(\gamma', z') = \\
&\int_0^\infty d\gamma' \Big[\int_{-1}^z dz' \mathcal{L}_{ij}^{(ns,1)}(\gamma, z, \gamma', z')g_j(\gamma', z') + \int_z^1 dz' \sigma_{ij}\mathcal{L}_{ij}^{(ns,2)}(\gamma, z, \gamma', z')g_j(\gamma', z') \Big],
\end{aligned}
\quad (I.30)
$$

It should be noted here that one has to avoid the point $z = z'$. This can be done by replacing z in the upper limit in the first term and the lower limit in the second term, by $z - \epsilon$ and $z + \epsilon$ respectively. But since the integration over z' using Gaussian quadrature, it is not needed.

It is seen from Eqs. (I.21) one has a singular contribution for $(i, j) = (1, 4), (2, 2), (2, 4), (3, 3), (2, 3)$ when $z = z'$. The first four cases are straightforward and one can write

$$
\begin{aligned}
\mathcal{H}_{14}^{(s)}(\gamma, z) &= \int_{-1}^1 dz' \int_0^\infty d\gamma' \mathcal{L}_{14}^{(s)}(\gamma, z, \gamma', z')g_4(\gamma', z') = \\
&- \frac{(\mu^2 - \Lambda^2)^2}{2\pi M^2} \frac{1}{2(1-z^2)} \int_0^\infty d\gamma' \int_0^1 dv \frac{v(1-v)^2}{D_\ell} g_4(\gamma', z),
\end{aligned}
\quad (I.31)
$$

$$
\begin{aligned}
\mathcal{H}_{22}^{(s)}(\gamma, z) &= \int_{-1}^1 dz' \int_0^\infty d\gamma' \mathcal{L}_{22}^{(s)}(\gamma, z, \gamma', z')g_2(\gamma', z') = \\
&- \frac{(\mu^2 - \Lambda^2)^2}{2\pi M^2} \frac{1}{(1-z^2)} \int_0^\infty d\gamma' \int_0^1 dv \frac{v(1-v)}{D_\ell} g_2(\gamma', z),
\end{aligned}
\quad (I.32)
$$

$$
\begin{aligned}
\mathcal{H}_{24}^{(s)}(\gamma, z) &= \int_{-1}^1 dz' \int_0^\infty d\gamma' \mathcal{L}_{24}^{(s)}(\gamma, z, \gamma', z')g_4(\gamma', z') = \\
&- \frac{(\mu^2 - \Lambda^2)^2}{2\pi M^2} \frac{m}{M} \frac{1}{(1-z^2)} \int_0^\infty d\gamma' \int_0^1 dv \frac{v(1-v)^2}{D_\ell} g_4(\gamma', z),
\end{aligned}
\quad (I.33)
$$

and

$$\mathcal{H}_{33}^{(s)}(\gamma, z) = \int_{-1}^{1} dz' \int_{0}^{\infty} d\gamma' \mathcal{L}_{33}^{(s)}(\gamma, z, \gamma', z') g_3(\gamma', z') =$$

$$\frac{(\mu^2 - \Lambda^2)^2}{2\pi M^2} \frac{1}{(1 - z^2)} \int_{0}^{\infty} d\gamma' \int_{0}^{1} dv \frac{v(1 - v)^2}{D_\ell} g_3(\gamma', z). \tag{I.34}$$

Similarly, for the contribution coming from $\mathcal{L}_{23}^{(s,a)}$:

$$\mathcal{H}_{23}^{(s,a)}(\gamma, z) = \int_{-1}^{1} dz' \int_{0}^{\infty} d\gamma' \mathcal{L}_{23}^{(s,a)}(\gamma, z, \gamma', z') g_3(\gamma', z') =$$

$$- \frac{(\mu^2 - \Lambda^2)^2}{2\pi M^2} \frac{2z}{M^2(1 - z^2)^2} \left[\frac{M^2(1 - z^2)}{8} + \gamma + m^2 \right] \tag{I.35}$$

$$\times \int_{0}^{\infty} d\gamma' \int_{0}^{1} dv \frac{v(1 - v)^2}{D_\ell} g_3(\gamma', z).$$

On the contrary, the contribution coming from $\mathcal{L}_{23}^{(s,b)}$ is proportional to $\frac{\partial}{\partial z'} \delta(z' - z)$ and has to be handled with more care. By a partial integration one obtains

$$\mathcal{H}_{23}^{(s,b)}(\gamma, z) = \int_{-1}^{1} dz' \int_{0}^{\infty} d\gamma' \mathcal{L}_{23}^{(s,b)}(\gamma, z, \gamma', z') g_3(\gamma', z') =$$

$$- \frac{1}{2\pi M^4(1 - z^2)} \int_{0}^{1} \frac{dv}{(1 - v)} \int_{0}^{\infty} d\gamma' \left\{ \left[\delta(z' - z) \right. \right.$$

$$\times \left[\frac{(1 - v)(\mu^2 - \Lambda^2)}{\ell_D + (1 - v)(\mu^2 - \Lambda^2)} + \log\left(\frac{\ell_D}{\ell_D + (1 - v)(\mu^2 - \Lambda^2)} \right) \right] g_3(\gamma', z') \right]_{-1}^{1}$$

$$- \int_{-1}^{1} dz' \delta(z' - z) \left[\frac{\partial g_3(\gamma', z')}{\partial z'} \left[\frac{(1 - v)(\mu^2 - \Lambda^2)}{\ell_D + (1 - v)(\mu^2 - \Lambda^2)} \right. \right.$$

$$+ \log\left(\frac{\ell_D}{\ell_D + (1 - v)(\mu^2 - \Lambda^2)} \right) \right] + g_3(\gamma', z') \frac{\partial}{\partial z'} \left[\frac{(1 - v)(\mu^2 - \Lambda^2)}{\ell_D + (1 - v)(\mu^2 - \Lambda^2)} \right.$$

$$\left. \left. \left. + \log\left(\frac{\ell_D}{\ell_D + (1 - v)(\mu^2 - \Lambda^2)} \right) \right] \right] \right\}. \tag{I.36}$$

The surface term in (I.36) vanish since

$$[\delta(z' - z) g_3(\gamma', z')]_{-1}^{1}$$
$$= \delta(1 - z) g_3(\gamma', 1) - \delta(-1 - z) g_3(\gamma', -1) = g_3(\gamma', 1)[\delta(1 - z) + \delta(-1 - z)], \tag{I.37}$$

and $g_3(\gamma', 1) = 0$. Here it was used the property $g_3(\gamma', -z') = -g_3(\gamma', z')$. Moreover, the required derivative in (I.36) is

$$\frac{\partial}{\partial z'} \left[\frac{(1 - v)(\mu^2 - \Lambda^2)}{\ell_D + (1 - v)(\mu^2 - \Lambda^2)} + \log\left(\frac{\ell_D}{\ell_D + (1 - v)(\mu^2 - \Lambda^2)} \right) \right] =$$

$$\frac{\partial \ell_D}{\partial z'} \left[\frac{-(1 - v)(\mu^2 - \Lambda^2}{[\ell_D + (1 - v)(\mu^2 - \Lambda^2]^2} + \frac{(1 - v)(\mu^2 - \Lambda^2)}{\ell_D[\ell_D + (1 - v)(\mu^2 - \Lambda^2)]} \right] = \tag{I.38}$$

$$\frac{-v(1 - v)^2(\mu^2 - \Lambda^2)^2[z(1 - v) + 2z'v]M^2}{4\ell_D[\ell_D + (1 - v)(\mu^2 - \Lambda^2]^2}.$$

Consequently,

$$
\mathcal{H}_{23}^{(s,b)}(\gamma, z) = \frac{1}{2\pi M^4 (1 - z^2)} \int_0^\infty d\gamma' \left\{ \frac{\partial g_3(\gamma', z)}{\partial z} \right.
$$

$$
\times \int_0^1 \frac{dv}{(1 - v)} \left[\frac{(1 - v)(\mu^2 - \Lambda^2)}{\tilde{\ell}_D + (1 - v)(\mu^2 - \Lambda^2)} + \log\left(\frac{\tilde{\ell}_D}{\tilde{\ell}_D + (1 - v)(\mu^2 - \Lambda^2)} \right) \right]
$$

$$
\left. - \frac{zM^2}{4} (\mu^2 - \Lambda^2)^2 g_3(\gamma', z) \int_0^1 dv \frac{v(1 - v^2)}{D_l} \right\}.
$$

$$(I.39)$$

I.2.2 Basis expansion

The Nakanishi weight function of each component i is expanded in the following form

$$
g_i(\gamma, z) = \sum_{k=1}^{N_z} \sum_{n=1}^{N_\gamma} A_{kn}^i G_{2(k-1)+r_i}^{\lambda_i}(z) \mathcal{L}_{n-1}(\gamma),
$$

$$(I.40)$$

where A_{kn}^i are the coefficients to be determined and the functions $G_{2m+r_i}^{\lambda_i}$, and $\mathcal{L}_n$ are defined by

$$
G_n^\lambda(z) = (1 - z^2)^{(2\lambda-1)/4} \Gamma(\lambda) \sqrt{\frac{n!(n + \lambda)}{2^{1-2\lambda} \pi \Gamma(n + 2\lambda)}} C_n^\lambda(z),
$$

$$
\mathcal{L}_n(\gamma) = \sqrt{a} L_n(a\gamma) e^{-a\gamma/2},
$$

$$(I.41)$$

where C_n^λ denotes Gegenbauer polynomial and L_n is a Laguerre polynomial. It should be noticed that because of the symmetry under $z \to -z$ one has

$$
r_i = \begin{cases} 0 & ; i = 1, 2, 4, \\ 1 & ; i = 3. \end{cases}
$$

$$(I.42)$$

The basis functions defined by (I.41) obey the orthogonality relations

$$
\int_{-1}^1 dz G_l^{\lambda_i}(z) G_n^{\lambda_i}(z) = \delta_{ln}
$$

$$
\int_0^\infty d\gamma \mathcal{L}_j(\gamma) \mathcal{L}_l(\gamma) = \delta_{jl}.
$$

$$(I.43)$$

Furthermore, in the applications $\lambda = \lambda_i$ will be a half-integer, i.e. $\lambda = l + 1/2$. Therefore,

$$
G_n^{(l+1/2)}(z) = (2l - 1)!! \sqrt{\frac{(n + l + 1/2)}{\prod_{j=1}^{2l} (n + j)}} (1 - z^2)^{l/2} C_n^{(l+1/2)}(z).
$$

$$(I.44)$$

In the calculation of the singular contribution $\mathcal{L}^{(s)}$ one needs also the derivative of $G_n^{l+1/2}$, which is given by

$$
\frac{\partial G_n^{(l+1/2)}}{\partial z} = (2l - 1)!! \sqrt{\frac{(n + l + 1/2)}{\prod_{j=1}^{2l} (n + j)}} (1 - z^2)^{l/2} \left[(2l + 1) C_{n-1}^{(l+3/2)}(z) - \frac{lz C_n^{(l+1/2)}(z)}{(1 - z^2)} \right],
$$

$$(I.45)$$

with $C_{-1}^{l+3/2}(z) = 0$ if $n = 0$.

Additionally, the second derivative of the $G_n^{l+1/2}(z)$ takes the form

$$
\frac{\partial^2 G_n^{(l+1/2)}}{\partial z^2} = (2l-1)!! \sqrt{\frac{(n+l+1/2)}{\prod_{j=1}^{2l}(n+j)}} (1-z^2)^{l/2-2} \left[(l(l-1)z^2 - n(n+1)(1-z^2) \right.
$$
$$
\left. - l(1 + 2n(1-z^2)))C_n^{(l+1/2)}(z) + 2z(1-z^2)(2l+1)C_{n-1}^{(l+3/2)}(z) \right],
$$
(I.46)

which can be derived from the Gegenbauer differential equation

$$
(1-z^2)\frac{\partial^2 C_n^{(\lambda)}(z)}{\partial z^2} - (2\lambda+1)z\frac{\partial C_n^{(\lambda)}(z)}{\partial z} + n(n+2\lambda)C_n^{(\lambda)}(z) = 0.
$$
(I.47)

I.2.3 Eigenvalue equation for the Nakanishi weight functions

The next step is to write Eq. (6.8) in matrix form by using the basis introduced in the previous subsection. For this purpose one can define

$$
\mathcal{A}_{kn}^{(i)}(\gamma, z) = G_{2(k-1)+r_i}^{(l_i+1/2)}(z) \int_0^\infty d\gamma' \frac{\mathcal{L}_{n-1}(\gamma')}{[\gamma + \gamma' + m^2 z^2 + (1-z^2)\kappa^2]^2},
$$
(I.48)

and

$$
\mathcal{B}_{kn}^{(ij)}(\gamma, z) = \mathcal{B}_{kn}^{(ij,ns)}(\gamma, z) + \mathcal{B}_{kn}^{(ij,s)}(\gamma, z),
$$
(I.49)

where

$$
\mathcal{B}_{kn}^{(ij,ns)}(\gamma, z) = \int_0^\infty d\gamma' \mathcal{L}_{n-1}(\gamma') \int_{-1}^z dz' \mathcal{L}_{ij}^{(ns,1)}(\gamma, z, \gamma', z') G_{2(k-1)+r_j}^{(l_j+1/2)}(z') +
$$
$$
\sigma_{ij} \int_0^\infty d\gamma' \mathcal{L}_{n-1}(\gamma') \int_z^1 dz' \mathcal{L}_{ij}^{(ns,2)}(\gamma, z, \gamma', z') G_{2(k-1)+r_j}^{(l_j+1/2)}(z'),
$$
(I.50)

$$
\mathcal{B}_{kn}^{(14,s)}(\gamma, z) = -\frac{(\mu^2 - \Lambda^2)^2}{2\pi M^2} \frac{1}{2(1-z^2)} G_{2(k-1)}^{(l_4+1/2)}(z) \int_0^\infty d\gamma' \mathcal{L}_{n-1}(\gamma') I_1(\gamma, z, \gamma'),
$$
(I.51)

$$
\mathcal{B}_{kn}^{(22,s)}(\gamma, z) = -\frac{(\mu^2 - \Lambda^2)^2}{2\pi M^2} \frac{1}{(1-z^2)} G_{2(k-1)}^{(l_2+1/2)}(z) \int_0^\infty d\gamma' \mathcal{L}_{n-1}(\gamma') I_2(\gamma, z, \gamma'),
$$
(I.52)

$$
\mathcal{B}_{kn}^{(24,s)}(\gamma, z) = -\frac{(\mu^2 - \Lambda^2)^2}{2\pi M^2} \frac{m}{M} \frac{1}{(1-z^2)} G_{2(k-1)}^{(l_4+1/2)}(z) \int_0^\infty d\gamma' \mathcal{L}_{n-1}(\gamma') I_1(\gamma, z, \gamma'),
$$
(I.53)

$$
\mathcal{B}_{kn}^{(33,s)}(\gamma, z) = \frac{(\mu^2 - \Lambda^2)^2}{2\pi M^2} \frac{1}{(1-z^2)} G_{2(k-1)+1}^{(l_3+1/2)}(z) \int_0^\infty d\gamma' \mathcal{L}_{n-1}(\gamma') I_1(\gamma, z, \gamma'),
$$
(I.54)

and

$$
\mathcal{B}_{kn}^{(23,s)}(\gamma, z) = -\frac{(\mu^2 - \Lambda^2)^2}{2\pi M^2} \frac{2z}{M^2(1-z^2)^2} \left[\frac{M^2(1-z^2)}{8} + \gamma + m^2 \right]
$$
$$
\times G_{2(k-1)+1}^{(l_3+1/2)}(z) \int_0^\infty d\gamma' \mathcal{L}_{n-1}(\gamma') I_1(\gamma, z, \gamma')
$$
$$
+ \frac{1}{2\pi M^4(1-z^2)} \frac{\partial G_{2(k-1)+1}^{(l_3+1/2)}(z)}{\partial z} \int_0^\infty d\gamma' \mathcal{L}_{n-1}(\gamma') I_3(\gamma, z, \gamma')
$$
$$
- \frac{z(\mu^2 - \Lambda^2)^2}{8\pi M^2(1-z^2)} G_{2(k-1)+1}^{(l_3+1/2)}(z) \int_0^\infty d\gamma' \mathcal{L}_{n-1}(\gamma') I_4(\gamma, z, \gamma').
$$
(I.55)

In the above equations the integrals I_1, I_2, I_3 and I_4 are defined by

$$I_1(\gamma, z, \gamma') = \int_0^1 dv \frac{v(1-v)^2}{D_\ell(\gamma, z, \gamma')}, \tag{I.56a}$$

$$I_2(\gamma, z, \gamma') = \int_0^1 dv \frac{v(1-v)}{D_\ell(\gamma, z, \gamma')}, \tag{I.56b}$$

$$I_3(\gamma, z, \gamma') = \int_0^1 \frac{dv}{(1-v)} \left[\frac{(1-v)(\mu^2 - \Lambda^2)}{\tilde{\ell}_D + (1-v)(\mu^2 - \Lambda^2)} + \log\left(\frac{\tilde{\ell}_D}{\tilde{\ell}_D + (1-v)(\mu^2 - \Lambda^2)} \right) \right], \tag{I.56c}$$

$$I_4(\gamma, z, \gamma') = \int_0^1 dv \frac{v(1-v^2)}{D_\ell(\gamma, z, \gamma')}. \tag{I.56d}$$

$$\tilde{I}_1(\gamma, z, \gamma') = \frac{(\mu^2 - \Lambda^2)^2}{2\pi M^2 (1 - z^2)} I_1(\gamma, z, \gamma') \tag{I.57a}$$

$$\tilde{I}_2(\gamma, z, \gamma') = \frac{(\mu^2 - \Lambda^2)^2}{2\pi M^2 (1 - z^2)} I_2(\gamma, z, \gamma') \tag{I.57b}$$

$$\tilde{I}_3(\gamma, z, \gamma') = \frac{1}{2\pi M^4 (1 - z^2)} I_3(\gamma, z, \gamma') \tag{I.57c}$$

$$\tilde{I}_4(\gamma, z, \gamma') = \frac{z(\mu^2 - \Lambda^2)^2}{8\pi M^2 (1 - z^2)} I_4(\gamma, z, \gamma') \tag{I.57d}$$

$$\tilde{I}_5(\gamma, z, \gamma') = \frac{2z(\mu^2 - \Lambda^2)^2}{2\pi M^4 (1 - z^2)} \left[\frac{M^2}{8} + \frac{\gamma + m^2}{(1 - z^2)} \right] I_1(\gamma, z, \gamma'). \tag{I.57e}$$

The Eqs. (I.51)-(I.55) can then be written in the more compact form

$$\mathcal{B}_{kn}^{(14,s)}(\gamma, z) = -\frac{1}{2} G_{2(k-1)}^{(l_4+1/2)}(z) \int_0^\infty d\gamma' \mathcal{L}_{n-1}(\gamma') \tilde{I}_1(\gamma, z, \gamma'), \tag{I.58}$$

$$\mathcal{B}_{kn}^{(22,s)}(\gamma, z) = -G_{2(k-1)}^{(l_2+1/2)}(z) \int_0^\infty d\gamma' \mathcal{L}_{n-1}(\gamma') \tilde{I}_2(\gamma, z, \gamma'), \tag{I.59}$$

$$\mathcal{B}_{kn}^{(24,s)}(\gamma, z) = -\frac{m}{M} G_{2(k-1)}^{(l_4+1/2)}(z) \int_0^\infty d\gamma' \mathcal{L}_{n-1}(\gamma') \tilde{I}_1(\gamma, z, \gamma'), \tag{I.60}$$

$$\mathcal{B}_{kn}^{(33,s)}(\gamma, z) = G_{2(k-1)+1}^{(l_3+1/2)}(z) \int_0^\infty d\gamma' \mathcal{L}_{n-1}(\gamma') \tilde{I}_1(\gamma, z, \gamma'), \tag{I.61}$$

$$\begin{aligned} \mathcal{B}_{kn}^{(23,s)}(\gamma, z) &= -G_{2(k-1)+1}^{(l_3+1/2)}(z) \int_0^\infty d\gamma' \mathcal{L}_{n-1}(\gamma') \tilde{I}_5(\gamma, z, \gamma') \\ &+ \frac{\partial G_{2(k-1)+1}^{(l_3+1/2)}(z)}{\partial z} \int_0^\infty d\gamma' \mathcal{L}_{n-1}(\gamma') \tilde{I}_3(\gamma, z, \gamma') \\ &- G_{2(k-1)+1}^{(l_3+1/2)}(z) \int_0^\infty d\gamma' \mathcal{L}_{n-1}(\gamma') \tilde{I}_4(\gamma, z, \gamma'). \end{aligned} \tag{I.62}$$

Equation (6.8) can subsequently be rewritten as

$$\sum_{kn} \mathcal{A}_{kn}^{(i)}(\gamma, z) A_{kn}^i = \alpha \sum_j \sum_{kn} \mathcal{B}_{kn}^{(ij)}(\gamma, z) A_{kn}^j, \quad i = 1, 2, 3, 4. \tag{I.63}$$

One then act on each side by the operator $\int_0^\infty d\gamma \int_{-1}^1 dz G_{2(k'-1)+r_i}^{(l_i+1/2)}(z)\mathcal{L}_{n'-1}(\gamma)$

$$\sum_{kn} \int_0^\infty d\gamma \mathcal{L}_{n'-1}(\gamma) \int_{-1}^1 dz G_{2(k'-1)+r_i}^{(l_i+1/2)}(z)\mathcal{A}_{kn}^{(i)}(\gamma,z)A_{kn}^i =$$

$$\alpha \sum_j \sum_{kn} \int_0^\infty d\gamma \mathcal{L}_{n'-1}(\gamma) \int_{-1}^1 dz G_{2(k'-1)+r_i}^{(l_i+1/2)}(z)\mathcal{B}_{kn}^{(ij)}(\gamma,z)A_{kn}^j, \quad i = 1,2,3,4. \tag{I.64}$$

By defining the tensors

$$\tilde{\mathcal{A}}_{k'n',kn}^{ij} = \delta_{ij} \int_0^\infty d\gamma \mathcal{L}_{n'-1}(\gamma) \int_{-1}^1 dz G_{2(k'-1)+r_i}^{(l_i+1/2)}(z)\mathcal{A}_{kn}^{(i)}(\gamma,z), \tag{I.65}$$

and

$$\tilde{\mathcal{B}}_{k'n',kn}^{ij} = \int_0^\infty d\gamma \mathcal{L}_{n'-1}(\gamma) \int_{-1}^1 dz G_{2(k'-1)+r_i}^{(l_i+1/2)}(z)\mathcal{B}_{kn}^{(ij)}(\gamma,z), \tag{I.66}$$

the following equation is obtained for the coefficents

$$\sum_j \sum_{kn} \tilde{\mathcal{A}}_{k'n',kn}^{ij}A_{kn}^j = \alpha \sum_j \sum_{kn} \tilde{\mathcal{B}}_{k'n',kn}^{ij}A_{kn}^j. \tag{I.67}$$

Here δ_{ij} was introduced in (I.65) in order to write the left-hand and right-hand sides of the same form.

For a given j, the numbers A_{kn}^j form a two-dimensional array of size $N_z \times N_\gamma$. By defining the new index

$$l = (k-1)N_\gamma + n, \tag{I.68}$$

the coefficients for one value of j can be stored in a one-dimensional vector $\hat{A}_{k'}^j$. Here $k = 1,...,N_z$ and $n = 1,...,N_\gamma$ and therefore $k' = 1,...,N_zN_\gamma$. This process can be then repeated and the following can be introduced

$$l' = (j-1)N_zN_\gamma + l = (j-1)N_zN_\gamma + (k-1)N_\gamma + n, \tag{I.69}$$

where $l' = 1,...,4N_zN_\gamma$ since $j = 1,...,4$. In this way, all the coefficients A_{kn}^j can be stored in a one-dimensional vector $a_{l'}$. The same "trick" can be done for the triples (i,k',n') and (j,k,n), i.e.

$$\tilde{\mathcal{A}}_{k'n',mn}^{ij} \longrightarrow \hat{A}_{l'l''}, \quad \tilde{\mathcal{B}}_{k'n',mn}^{ij} \longrightarrow \hat{B}_{l'l''}, \tag{I.70}$$

where the index l'' is obtained by doing the replacements $(k \to k', n \to n', j \to i)$ in Eq. (I.69).

The coefficients for the Nakanishi weight functions and the coupling constant α are thus obtained by solving a generalized eigenvalue problem of the form

$$\hat{A}a = \alpha\hat{B}a, \tag{I.71}$$

where the one-dimensional vector a contains the unknown coefficients.

I.3   Pion Decay Constant

As mentioned in the main text, the pion decay constant in terms of the BS amplitude is defined by

$$i\,p^2 f_\pi = N_C \int \frac{d^4k}{(2\pi)^4} \text{Tr}[\not{p}\,\gamma^5\,\Phi(p,k)]\,, \tag{I.72}$$

where N_C is the number of colors. Using the decomposition of BS amplitude given by Eq. (6.5), one can perform the trace and obtain

$$i\,M^2 f_\pi = -4\,M\,N_C \int \frac{d^4k}{(2\pi)^4}\phi_2(k,p) \tag{I.73}$$

The amplitude $\phi_2(k,p)$ is then written in terms of the Nakanishi integral representation

$$\phi_2(k,p) = \tilde{N} \int_{-1}^{1} dz' \int_0^\infty d\gamma' \frac{g_2(\gamma',z';\kappa^2)}{[k^2 + z'p\cdot k - \gamma' - \kappa^2 + i\epsilon]^3}\,,$$

where the factor $\tilde{N}$ comes from the covariant normalization of the BS amplitude. Introducing Eq. (I.74) in (I.73) one gets

$$i\,M f_\pi = -4\,N_C\tilde{N} \int_{-1}^{1} dz' \int_0^\infty d\gamma' g_2(\gamma',z';\kappa^2) \int \frac{d^4k}{(2\pi)^4} \frac{1}{[k^2 + z'p\cdot k - \gamma' - \kappa^2 + i\epsilon]^3} \tag{I.74}$$

Then the four-dimensional integration can be performed as follows

$$\int \frac{d^4k}{(2\pi)^4} \frac{1}{[k^2 + z'p\cdot k - \gamma' - \kappa^2 + i\epsilon]^3} = \int \frac{d^4q}{(2\pi)^4} \frac{1}{[q^2 - \gamma' - \kappa^2 - z'^2\,M^2/4 + i\epsilon]^3}$$
$$= \frac{i}{(2\pi)^4} \frac{\pi^2}{2} \frac{1}{[-\gamma' - \kappa^2 - z'^2\,M^2/4]}\,, \tag{I.75}$$

where it was used the following change of variables: $q = k + p/2\,z'$.

The final expression for the pion decay constant is given by

$$f_\pi = \frac{N_C\tilde{N}}{8\pi^2\,M} \int_{-1}^{1} dz' \int_0^\infty d\gamma' \frac{g_2(\gamma',z';\kappa^2)}{[\gamma' + \kappa^2 + z'^2\,M^2/4]} \tag{I.76}$$

Where $M = M_\pi$ is the pion mass and $\tilde{N}$ comes from the normalization of the Bethe-Salpeter amplitude.

Bibliography

[1] M. Tanabashi *et al.* (Particle Data Group), *Review of Particle Physics*, Phys. Rev. D **98**, 030001 (2018).

[2] CERN, *Large Hadron Collider*, `http://home.web.cern.ch/about/accelerators/large-hadron-collider` (2019).

[3] N. Cabibbo, *Unitary Symmetry and Leptonic Decays*, Phys. Rev. Lett. **10**, 531–533 (1963); M. Kobayashi and T. Maskawa, *CP-Violation in the Renormalizable Theory of Weak Interaction*, Prog. Theor. Phys **49**, 652–657 (1973).

[4] L. Wolfstein, *CP Violation* (North-Holland, 1989).

[5] J. H. Christenson, J. W. Cronin, V. L. Fitch and R. Turlay, *Evidence for the 2π Decay of the $K20$ Meson*, Phys. Rev. Lett. **13**, 138 (1964).

[6] M. Bander, D. Silverman, A. Soni, *CP noninvariance in the decays of heavy charged quark systems*, Phys. Rev. Lett. **43**, 242 (1979).

[7] I. Bediaga, I. I. Bigi, A. Gomes, G. Guerrer, J. Miranda, A. C. dos Reis, *On a CP anisotropy measurement in the Dalitz plot*, Phys. Rev. D **80**, 096006 (2009).

[8] I. Bediaga, J. Miranda, A. C. dos Reis, I. I. Bigi , A. Gomes, J. M. Otalora Goicochea, A. Veiga, *Second generation of "Miranda procedure" for CP violation in Dalitz studies of B (and D and τ) decays* Phys.Rev. D **86**, 036005 (2012).

[9] B. Bhattacharya, M. Gronau, J. L. Rosner, *CP asymmetries in three-body $B^{\pm}$ decays to charged pions and kaons* Phys. Lett. B **726**, 337 (2013).

[10] H. Y. Cheng and C. K. Chua, *Branching fractions and direct CP violation in charmless three-body decays of B mesons*, Phys. Rev. D **88**, 114014 (2013).

[11] H.-Y. Cheng, C. -K. Chua, K.-C. Yang, Z. -Q. Zhang, *Revisiting charmless hadronic B decays to scalar mesons*, Phys. Rev. D **87**, 114001 (2013).

[12] L. Wolfenstein, *Final-state interactions and CP violation in weak decays*, Phys. Rev. D **43**, 151 (1991).

[13] I. I. Bigi, A. I. Sanda, *CP Violation* (Cambridge University Press, Cambridge, England, 2009), 2nd ed.

[14] R. E. Marshak, Riazuddin, and C. P. Ryan, *Theory of Weak Interactions in Particle Physics* (Wiley-Interscience, New York, 1969).

[15] G. C. Branco, L. Lavoura, J. P. Silva, *CP Violation* (Oxford University Press, New York, 1999).

[16] I. Bediaga, T. Frederico and O. Lourenço, *CP violation and CPT invariance in B decays with final state interactions*, Phys. Rev. D **89**, 094013 (2014).

[17] D. Atwood, A. Soni, *Possibility of large direct* CP *violation in $\vec{B}$ $K\pi$-like modes because of long distance rescattering effects and implications for the angle γ*, Phys. Rev. D **58**, 036005 (1998); H.-Y. Cheng, C.-K. Chua, A. Soni, *Final state interactions in hadronic B decays*, Phys. Rev. D **71**, 014030 (2005).

[18] R. Aaiji *et al.* (LHCb Collaboration), *Measurements of CP violation in the three-body phase space of charmless $B^{\pm}$ decays* Phys. Rev. D **90**, 112004 (2014) (Additional figures in LHCb-PAPER-2014-044, `https://cds.cern.ch/record/1751517?ln=en`).

[19] C. Wang, Z. H. Zhang, Z. Y. Wang, and X. H. Guo, *Localized direct CP violation in $B^{\pm} \to \rho^0(\omega)\pi^{\pm} \to \pi^+\pi^-\pi^{\pm}$*, Eur. Phys. J. C **75**, 536 (2015).

[20] J. H. Alvarenga Nogueira, I. Bediaga, A. B. R. Cavalvante, T. Frederico and O. Lourenço, *CP violation: Dalitz interference, CPT and FSI*, Phys. Rev. D **92**, 054010 (2015).

[21] J. H. Alvarenga Nogueira, I. Bediaga, A. B. R. Cavalvante, T. Frederico and O. Lourenço, *Charmless Three-Body B-decays: final state interaction and CP violation*, J. Phys.: Conf. Ser. **706**, 042010 (2016).

[22] T. Frederico, J. H. Alvarenga Nogueira, I. Bediaga, A. B. R. Cavalvante and O. Lourenço, *CPT, Final State Interaction and CP Violation*, arXiv:1605.03889 (2016).

[23] J. H. Alvarenga Nogueira, T. Frederico, I. Bediaga and P.C. Magalhães, *CP Violation in the three-body $B^{\pm}$ phase-space*, PoS ICHEP2016, 635 (2016).

[24] J. H. Alvarenga Nogueira, I. Bediaga, T. Frederico, P. C. Magalhães and J. Molina Rodriguez, *Suppressed $B \to PV$ CP asymmetry: CPT constraint*, Phys. Rev. D **94**, 054028 (2016).

[25] J. H. Alvarenga Nogueira, T. Frederico and O. Lourenço, *$B^+ \to K^-\pi^+\pi^+$: three-body final state interactions and $K\pi$ isospin states*, Few Body Syst. **58**, 98 (2017).

[26] E. E. Salpeter and H. A. Bethe, *A Relativistic Equation for Bound-State Problems*, Phys. Rev. **84**, 1232 (1951).

[27] S. J. Brodsky, H.-C. Pauli, and S. S. Pinsky, *Quantum chromodynamics and other field theories on the light cone*, Phys. Rept. **301**, 299 (1998).

[28] J. Carbonell, B. Desplanques, V. A. Karmanov, J. F. Mathiot, *Explicitly covariant light-front dynamics and relativistic few-body systems*, Phys. Report **300**, 215 (1998).

[29] M. Gell-Man and F. Low, *Bound States in Quantum Field Theory*, Phys. Rev. **84**, 350 (1951).

[30] G. C. Wick, *Properties of Bethe-Salpeter Wave Functions*, Phys. Rev. **96**, 1124 (1954).

[31] C. D. Roberts, A. G. Williams, *Dyson-Schwinger equations and their application to hadronic physics* , Prog. Part. Nucl. Phys. **33**, 477 (1994).

[32] J. Carbonell, V. A. Karmanov, M. Mangin-Brinet, *Electromagnetic form factor via Bethe-Salpeter amplitude in Minkowski space* , Eur. Phys. J. A **39**, 53 (2009).

[33] R. E. Cutkosky, *Solutions of a Bethe-Salpeter Equation*, Phys. Rev. **96**, 1135 (1954).

[34] K. Kusaka and A. G. Williams, *Solving the Bethe-Salpeter equation for scalar theories in Minkowski space*, Phys. Rev. D **51**, 7026 (1995); K. Kusaka, K. Simpson and A. G. Williams, *Solving the Bethe-Salpeter equation for bound states of scalar theories in Minkowski space*, Phys. Rev. D **56**, 5071 (1997).

[35] N. Nakanishi, *Partial-Wave Bethe-Salpeter Equation*, Phys. Rev. **130**, 1230 (1963); Erratum Phys. Rev. **131**, 2841 (1963); N. Nakashi, *A General Survey of the Theory of the Bethe-Salpeter Equation*, Prog. Theor. Phys. Suppl. **43**, 1 (1969); *Graphy Theory and Feynman Integrals* (Gordon and Breach, New York, 1971).

[36] V. A. Karmanov and J. Carbonell, *Solving Bethe-Salpeter equation in Minkowski space*, Eur. Phys. J. A **27**, 1 (2006).

[37] J. Carbonell and V. A. Karmanov, *Cross-ladder effects in Bethe-Salpeter and light-front equations*, Eur. Phys. J. A **27**, 11 (2006).

[38] T. Frederico, G. Salmè and M. Viviani, *Two-body scattering states in Minkowski space and the Nakanishi integral representation onto the null plane*, Phys. Rev. D **85**, 036009 (2012).

[39] T. Frederico, G. Salmè and M. Viviani, *Quantitative studies of the homogeneous Bethe-Salpeter equation in Minkowski space*, Phys. Rev. D **89**, 016010 (2014).

[40] V. Gigante, C. Gutierrez, J. H. Alvarenga Nogueira and E. Ydrefors, *A short review about the Bethe-Salpeter equation and the solution for the $\chi^2\phi$ model in Minkowski space*, PoS ICHEP2016, 1107 (2017).

[41] V. Gigante, J. H. Alvarenga Nogueira, E. Ydrefors, C. Gutierrez, V.A. Karmanov and T. Frederico, *Bound state structure in Minkowski space: beyond the ladder approximation*, Phys. Rev. D **95**, 056012 (2017).

[42] V. Gigante, J. H. Alvarenga Nogueira, E. Ydrefors and C. Gutierrez, *Study of the bound-state Bethe-Salpeter equation in 2+1 Minkowski space*, Int. J. Mod. Phys. Conf. Ser. **45**, 1760055 (2017).

[43] J. H. Alvarenga Nogueira, Chueng-Ryong Ji, E. Ydrefors and T. Frederico, *Color-suppression of non-planar diagrams in bosonic bound states*, Phys. Lett. B **777**, 207 (2018).

[44] J. H. Alvarenga Nogueira, E. Ydrefors, T. Frederico, G. Salmè, *Relativistic Studies of Few-Body Systems Using the Bethe-Salpeter*, Few Body Syst. **59**, 94 (2018).

[45] E. Ydrefors, J. H. Alvarenga Nogueira, V. Gigante, T. Frederico and V.A. Karmanov, *Three-body bound states with zero-range interaction in the Bethe-Salpeter approach*, Phys.Lett. B **770**, 131 (2017).

[46] E. Ydrefors, J. H. Alvarenga Nogueira, V.A. Karmanov and T. Frederico, *Solving the three-body bound-state Bethe-Salpeter equation in Minkowski space*, Phys. Lett. B **791**, 276 (2019).

[47] J. Carbonell and V. A. Karmanov, *Solving Bethe-Salpeter scattering state equation in Minkowski space*, Phys. Rev. D **90**, 056002 (2014).

[48] J. H. Alvarenga Nogueira, V. Gherardi, T. Frederico, G. Salmè, D. Colasante and E. Pace, *Solving the Bethe-Salpeter equation in Minkowski space for a fermion-scalar system*, Phys. Rev. D **100**, 016021 (2019).

[49] J. Carbonell, V. A. Karmanov, *Solving Bethe-Salpeter equation for two fermions in Minkowski space*, Eur. Phys. J. A **46**, 387 (2010).

[50] W. de Paula, T. Frederico, G. Salmè, M. Viviani, *Advances in solving the two-fermion homogeneous Bethe-Salpeter equation in Minkowski space*, Phys. Rev. D **94**, 071901 (2016).

[51] W. de Paula, T. Frederico, G. Salmè, M. Viviani, R. Pimentel, *Fermionic bound states in Minkowski space: light-cone singularities and structure*, Eur. Phys. J. C **77**, 764 (2017).

[52] A. D. Sakharov, *Violation of cp invariance, c asymmetry and baryon asymmetry of the universe*, J. of Exp. and Theor. Phys., **5** 24 (1967).

[53] CERN, *LHCb - Large Hadron Collider beauty experiment*, `http://lhcb-public.web.cern.ch/lhcb-public/` (2019).

[54] R. Aaiji *et al.* (LHCb Collaboration), *Measurement of CP Violation in the Phase Space of $B^{\pm} \to K^{\pm}\pi^+\pi^-$ and $B^{\pm} \to K^{\pm}K^+K^-$ Decays*, Phys. Rev. Lett. **111**, 101801 (2013).

[55] G. Grayer *et al.*, *High statistics study of the reaction $\pi^- p \to \pi^-\pi^+ n$: Apparatus, method of analysis, and general features of results at 17 GeV/c*, Nucl. Phys. B **75**, 189 (1974); D. Aston *et al.* (LASS Collaboration), *A Study of $K^-\pi^+$ Scattering in the Reaction $K^- p \to K^-\pi^+ n$ at $11 GeV/c$*, Nucl. Phys. B **296**, 493 (1988).

[56] D. Cohen, D. S. Ayres, R. Diebold, S. L. Kramer, A. J. Pawlicki, and A. B. Wicklund, *Amplitude analysis of the K^-K^+ system produced in the reactions $\pi^- p \to K^-K^+ n$ and K^-K^+ at 6 GeV/c*, Phys. Rev. D **22**, 2595 (1980); W. Wang, Int. J. Mod. Phys. A 29, 1430040 (2014).

[57] J. R. Peláez, F. J. Ynduráin, *Pion-pion scattering amplitude*, Phys. Rev. D **71**, 074016 (2005); R. García-Martín, R. Kamiński, J.R. Peláez, J. Ruiz de Elvira, F. J. Ynduráin, *Pion-pion scattering amplitude. IV. Improved analysis with once subtracted Roy-like equations up to 1100 MeV*, Phys. Rev. D **83**, 074004 (2011).

[58] P. C. Magalhães, M. R. Robilotta, K. S. F. F. Guimarães, T. Frederico, W. de Paula, I. Bediaga, A. C. dos Reis, C. M. Maekawa, and G. R. S. Zarnauskas, *Towards three-body unitarity in $D^+ \to K^-\pi^+\pi^+$*, Phys. Rev. D **84**, 094001 (2011).

[59] K. S. F. F. Guimarães, O. Lourenço, W. de Paula, T. Frederico and A. C. dos Reis, *Final state interaction in $D^+ \to K^-\pi^+\pi^+$ with $K\pi$ $I = 1/2$ and $3/2$ channels*, J. High Energy Phys. **08**, 135 (2014).

[60] T. Frederico, K. S. F. F. Guimarães, O. Lourenço, W. de Paula, I. Bediaga, and A. C. dos Reis, *Heavy Meson Decay in Three-Mesons and FSI*, Few Body Syst. **55**, 441 (2014).

[61] A. J. Bevan *et al*, *The Physics of the B Factories*, Eur. Phys. J. C **74**, 3026 (2014).

[62] C. W. Salgado and D. P. Weygand, *On the partial-wave analysis of mesonic resonances decaying to multiparticle final states produced by polarized photons*, Phys. Rep. **537**, 1 (2014).

[63] R. Aaiji *et al.* (LHCb Collaboration), *Measurements of CP violation in the three-body phase space of charmless $B^\pm$ decays*, Phys. Rev. D **90**, 112004 (2014).

[64] A. Garmash *et al.* (Belle Collaboration), *Evidence for Large Direct CP Violation in $B^\pm \to \rho(770)^0 K^\pm$ from Analysis of Three-Body Charmless $B^\pm \to K^\pm \pi^\pm \pi^\pm$ Decays*, Phys. Rev. Lett. **96**, 251803 (2006).

[65] B. Aubert *et al.* (BABAR Collaboration), *Dalitz-plot analysis of the decays $B^\pm \to K^\pm \pi^\pm \pi^\pm$*, Phys. Rev. D **72**, 072003 (2005) [Erratum-ibid. D **74**, 099903 (2006)]; *Evidence for direct CP violation from Dalitz-plot analysis of $B^\pm \to K^\pm \pi^\pm \pi^\pm$*, Phys. Rev. D **78**, 012004 (2008).

[66] E. M. Aitala *et al.* (E791 Collaboration), *Study of the $D_s^+ \to \pi^-\pi^+\pi^+$ Decay and Measurement of f_0 Masses and Widths*, Phys. Rev. Lett. **86**, 765 (2001).

[67] N. Brambilla *et al.*, *QCD and strongly coupled gauge theories: challenges and perspectives*, Eur. Phys. J. C **74**, 2981 (2014).

[68] J. R. Pelaez, *From controversy to precision on the sigma meson: a review on the status of the non-ordinary $f_0(500)$ resonance*, Phys. Rept. **658**, 1 (2016).

[69] X. W. Kang, B. Kubis, C. Hanhart, U.G. Meißner, B_{l4} *decays and the extraction of* $|V_{ub}|$, Phys. Rev. D, **89**, 053015 (2014).

[70] J.-M. Gérard and W.-S. Hou, *CP Nonconservation and CPT: Reassessment of Loop Effects in Charmless B Decays*, Phys. Rev. Lett. **62**, 855 (1989); G. W.-S. Hou, *CP and CPT: Reassessment of Penguin Induced CP Violation in Decays*, Nucl. Phys. B (Proc. Suppl.) **16**, 371 (1990).

[71] J.-M. Gérard and W.-S. Hou, *CP violation in inclusive and exclusive charmless B decays*, Phys. Rev. D **43**, 2909 (1991).

[72] J. D. Bjorken, *New Developments in High-Energy Physics*, Nucl. Phys. B (Proc. Suppl.) **11**, 325 (1989).

[73] J. F. Donoghue, E. Golowich, A. A. Petrov, and J. M. Soares, *Systematics of Soft Final-State Interactions in B Decays*, Phys. Rev. Lett. **77**, 2178 (1996).

[74] M. Suzuki, L. Wolfenstein, *Final state interaction phase in B decays*, Phys. Rev. D **60**, 074019 (1999).

[75] A. F. Falk, A. L. Kagan, Y. Nir, and A. A. Petrov, *Final state interactions and new physics in* $\vec{B} \to \pi K$ *decays,* Phys. Rev. D **57**, 4290 (1998); B. Blok, M. Gronau, and J. L. Rosner, *Annihilation, Rescattering, and CP Asymmetries in B Meson Decays*, Phys. Rev. Lett. **78**, 3999 (1997).

[76] P. Zenczykowski, *Coupled-channel final-state interactions through Reggeon exchange for* $D(B) \to \pi\pi, K\bar{K}$, Phys. Lett. B **460**, 390 (1999); A. Furman, R. Kaminski, L. Lesniak, P. Zenczykowski, *Final state interactions in* $B^{\pm} \to K^+K^-K^{\pm}$ *decays*, Phys. Lett. B **699**, 102 (2011).

[77] M. Beneke, G. Buchalla, M. Neubert, and C. T. Sachrajda, *QCD Factorization for* $B \to \pi\pi$ *Decays: Strong Phases and CP Violation in the Heavy Quark Limit*, Phys. Rev. Lett. **83**, 1914 (1999); *QCD factorization for exclusive, non-leptonic B meson decays: General arguments and the case of heavy-light final states*, Nucl. Phys. B **591**, 313 (2000); *QCD Factorization in* $B \to \pi K$, $\pi\pi$ *Decays and Extraction of Wolfenstein Parameters,* Nucl. Phys. B **606**, 245 (2001).

[78] A. J. Buras, R. Fleischer, S. Recksiegel and F. Schwab, $B \to \pi\pi$, *New Physics in* $B \to \pi K$, *and Implications for Rare K and B Decays,* Phys. Rev. Lett. **92**, 101804 (2004).

[79] M. Gronau, D. London, and J. L. Rosner, *Rescattering contributions to rare B-meson decays,* Phys. Rev. D **87**, 036008 (2013).

[80] C. D. Lu, Y.-L. Shen and W. Wang, *Final state interaction in* $B \to KK$ *decays*, Phys. Rev. D **73**, 034005 (2006)

[81] D. J. Wilson, R. A. Briceño, J. J. Dudek, R. G. Edwards, and C. E. Thomas, *Coupled* $\pi\pi$, $K\bar{K}$ *scattering in P-wave and the* ρ *resonance from lattice QCD*, Phys. Rev. D **92**, 094502 (2015); G. Moir, M. Peardon, S. M. Ryan, C. E. Thomas, D. J. Wilson, Coupled-Channel $D\pi$, $D\eta$ and $D_s K^-$ Scattering from Lattice QCD, J. High Energy Phys. **10**, 011 (2016).

[82] C. Smith, *Searching for dominant rescattering sources in decays of B to two pseudoscalars*, Eur. Phys. J. C **33**, 523 (2004).

[83] S. Kränkl, T. Mannel, J. Virto, *Three-Body Non-Leptonic B Decays and QCD Factorization,* Nucl. Phys. B **899**, 247 (2015).

[84] X. Ji, J.-P. Ma, and F. Yuan, *Generalized Counting Rule for Hard Exclusive Processes,* Phys. Rev. Lett. **90**, 241601 (2003).

[85] R. García-Martín, R. Kamiński, J. R. Peláez and J. Ruiz de Elvira, *Precise Determination of the $f_0(600)$ and $f_0(980)$ Pole Parameters from a Dispersive Data Analysis*, Phys. Rev. Lett. **107**, 072001 (2011).

[86] I. Bediaga, T. Frederico, P. C Magalhães, *Charm Penguin in $B^\pm \to K^\pm K^+ K^-$: partonic and hadronic loops*, Phys. Lett. B **780**, 357 (2018); *Charm rescattering contribution in rare $B_c^+ \to K^+ K^- \pi^+$ decay* Phys. Lett. B **785**, 581 (2018).

[87] M. Wirbel, B. Stech, and M. Bauer, *Exclusive semileptonic decays of heavy mesons*, Z. Phys. C **29**, 637 (1985); M. Bauer, B. Stech, and M. Wirbel, *Exclusive non-leptonic decays of D-, D_s- and B-mesons*, Z. Phys. C **34**, 103 (1987).

[88] G. P. Lepage and S. J. Brodsky, *Exclusive processes in perturbative quantum chromodynamics*, Phys. Rev. D **22**, 2157 (1980).

[89] M. Beneke, G. Buchalla, M. Neubert, and C. Sachrajda, *QCD Factorization for $B \to \pi\pi$ decays: strong phases and CP violation in the heavy quark limit*, Phys. Rev. Lett. **83**, 1914 (1999); *QCD factorization for exclusive non-leptonic B-meson decays: general arguments and the case of heavy–light final states*, Nucl. Phys. B **591**, 313 (2000).

[90] Y. Keum, H. Li, and A. Sanda, *Fat penguins and imaginary penguins in perturbative QCD*, Phys. Lett. B **504**, 6 (2001); *Penguin enhancement and $\vec{B}K\pi$ decays in perturbative QCD*, Phys. Rev. D **63**, 054008 (2001).

[91] C. Bauer, S. Fleming, and M. Luke, *Summing Sudakov logarithms in $\vec{B}X_s\gamma$ in effective field theory*, Phys. Rev. D **63**, 014006 (2000); C. Bauer, S. Fleming, D. Pirjol, and I. Stewart, *An effective field theory for collinear and soft gluons: Heavy to light decays*, Phys. Rev. D **63**, 114020 (2001); C. Bauer and I. Stewart, *Invariant Operators in Collinear Effective Theory*, Phys. Lett. B **516**, 134 (2001); C. Bauer, D. Pirjol, and I. Stewart, *Soft-collinear factorization in effective field theory*, Phys. Rev. D **65**, 054022 (2002).

[92] A. Furman, R. Kamiński, L. Leśniak and B. Loiseau, *Long-distance effects and final state interactions in $B \to \pi\pi K$ and $B \to K\bar{K}K$ decays*, Phys. Lett. B **622**, 207 (2005); B. El-Bennich, A. Furman, R. Kamiński, L. Leśniak and B. Loiseau, *Interference between $f_0(980)$ and $\rho^0(770)$ resonances in $B \to \pi^+\pi^- K$ decays*, Phys. Rev. D **74**, 114009 (2006); B. El-Bennich, A. Furman, R. Kamiński, L. Leśniak, B. Loiseau, B. Moussallam, *CP violation and kaon-pion interactions in $B \to K\pi^+\pi^-$ decays*, Phys. Rev. D **79**, 094005 (2009); A. Furman, R. Kamiński, L. Leśniak, P. Zenczykowski, *Final state interactions in $B^\pm \to K^+ K^- K^\pm$

decays, Phys. Lett. B **699**, 102 (2011); J.-P. Dedonder, A. Furman, R. Kaminski, L. Lesniak, B. Loiseau, *S-, P- and D-wave $\pi\pi$ final state interactions and CP violation in $B^{\pm} \to \pi^{\pm}\pi^{\mp}\pi^{\pm}$ decays*, Acta Phys. Pol. B **42**, 2013 (2011).

[93] D. Zeppenfeld, *SU(3) Relations for B Meson Decays*, Z. Phys. C **8**, 77 (1981); L. L. Chau and H. Y. Cheng, *Quark-Diagram Analysis of Two-Body Charm Decays*, Phys. Rev. Lett. **56**, 1655 (1986); L. L. Chau and H. Y. Cheng, *Analysis of two-body decays of charm mesons using the quark-diagram scheme*, Phys. Rev. D **36**, 137 (1987); M. J. Savage and M. B. Wise, *SU(3) predictions for nonleptonic B-meson decays*, Phys. Rev. D **39**, 3346 (1989) [Erratum-ibid. D **40**, 3127 (1989)]; L. L. Chau, H. Y. Cheng, W. K. Sze, H. Yao and B. Tseng, *Charmless nonleptonic rare decays of B mesons*, Phys. Rev. D **43**, 2176 (1991) [Erratum-ibid. D **58**, 019902 (1998)].

[94] I. I. Bigi, *"Could charm (& τ) transitions be the 'poor princess' providing a deeper understanding of fundamental dynamics ?" or: "Finding novel forces"*, Front. Phys. **10**, 101203 (2015).

[95] H.-Y. Cheng, C.-W. Chiang, and A.-L. Kuo, *Updating $B \to PP, VP$ decays in the framework of flavor symmetry*, Phys. Rev. D **91**, 014011 (2015).

[96] P. C. Magalhães and M. R. Robilotta, *$D^+ \to K^-\pi^+\pi^+$: The weak vector curren*, Phys.Rev. D **92**, 094005 (2015).

[97] E. Byckling and K. Kajantie, *Particle Kinematics*, (John Wiley and Sons, 1973).

[98] R. Aaij, *et al.* (LHCb collaboration), *Study of B_c^+ decays to the $K^+K^-\pi^+$ final state and evidence for the decay $B_c^+ \to \chi_{c0}\pi^+$*, Phys. Rev. D **94**, 091102(R) (2016)

[99] K. S. F. F. Guimarães, I. Bediaga, A. Delfino, T. Frederico, A. C. dos Reis, L. Tomio, *Three-body model of the final state interaction in heavy meson decay*, Nucl. Phys. B Proc. Suppl. **199**, 341 (2010).

[100] J. H. O. Sales, T. Frederico, B. V. Carlson, P. U. Sauer, *Light front Bethe-Salpeter equation*, Phys. Rev. C **61**, 044003 (2000).

[101] R. J. Perry, A. Harindranath, K. G. Wilson, *Light front Tamm-Dancoff field theory*, Phys. Rev. Lett. **65**, 2959 (1990).

[102] G. Eichmann, H. Sanchis-Alepuz, R. Williams, R. Alkofer, and C. S. Fischer, *Baryons as relativistic three-quark bound states*, Prog. Part. Nucl. Phys. **91**, 1 (2016).

[103] S. Mandelstam, *Dynamical Variables in the Bethe-Salpeter Formalism*, Proc. Roy. Soc. **A233**, 248 (1955).

[104] E. zur Linden and H. Mitter, *Bound-state solutions of the Bethe-Salpeter equation in momentum space*, Nuovo Cimento B **61**, 389 (1969).

[105] T. Nieuwenhuis and J. A. Tjon, *Nonperturbative Study of Generalized Ladder Graphs in a $\phi^2\chi$ Theory*, Phys. Rev. Lett. **77**, 814 (1996).

[106] M. Mangin-Brinet and J. Carbonell, *Solutions of the Wick-Cutkosky model in the Light-Front Dynamics*, Phys. Lett. B **474**, 237 (2000).

[107] M. S. Dorkin *et al.*, *Two-fermion bound states within the Bethe-Salpeter approach*, Few-Body Systems **42**, 1 (2008); M. S. Dorkin *et al.*, *Solving Bethe-Salpeter Equation in Euclidean Space*, Few-Body Systems **49**, 233 (2011).

[108] M. J. Levine, J. Wright, J. A. Tjon, *Solution of the Bethe-Salpeter Equation in the Inelastic Region*, Phys. Rev. **154**, 1437 (1967).

[109] C. Schwartz and C. Zemach, *Theory and Calculation of Scattering with the Bethe-Salpeter Equation*, Phys. Rev. **141**, 1454 (1966).

[110] J. Carbonell, T. Frederico and V. A. Karmanov, *Euclidean to Minkowski Bethe–Salpeter amplitude and observables*, Eur. Phys. J. C **77**, 58 (2017).

[111] J. Carbonell, V. A. Karmanov, *Solutions of the Bethe-Salpeter equation in Minkowski space and applications to electromagnetic form factors*, Few-Body Syst. **49**, 205 (2011).

[112] L. Chang *et al.*, *Imaging dynamical chiral symmetry breaking: pion wave function on the light front*, Phys. Rev. Lett. **110**, 132001 (2013);

[113] X. Ji, *Parton Physics on a Euclidean Lattice*, Phys. Rev. Lett. **110**, 262002 (2013).

[114] G. C. Rossi and M. Testa, *Euclidean versus Minkowski short distance* , Phys. Rev. D **98**, 054028 (2018).

[115] J. Carbonell, T. Frederico, V. A. Karmanov, *Bound state equation for the Nakanishi weight function*, Phys. Lett. B **769**, 418 (2017).

[116] V. Gherardi, *Solving the homogeneous Bethe-Salpeter equation for a fermion-scalar system in Minkowski space*, Master Thesis, Facoltà di Scienze Matematiche, Fisiche e Naturali Sapienza Università di Roma (2017).

[117] V. Sauli and J. Adam, Jr., *Study of relativistic bound states for scalars theories in the Bethe-Salpeter and Dyson-Schwinger formalism*, Phys. Rev. D **67**, 085007 (2003).

[118] V. Gigante, T. Frederico, C. Gutierrez, L. Tomio, *Bound States in Minkowski Space in 2 + 1 Dimensions*, Few-Body Syst. **56**, 375 (2015).

[119] L. D. Landau, E. M. Lifshitz, *Quantum Mechanics Non-Relativistic Theory*, 3rd ed.(Pergamon Press, 1977).

[120] V. Gigante, *Equação de Bethe-Salpeter em 2+1 dimensões para estado ligado de duas partículas no espaço de Minkowski*. PhD Thesis — Instituto Tecnológico de Aeronáutica, São José dos Campos, Brazil (2014).

[121] C. L. Gutiérrez Gómez, *Minkowski space Bethe-Salpeter equation within Nakanishi representation*, PhD thesis- Instituto de Física Teórica Universidade Estadual Paulista, São Paulo, Brazil (2016).

[122] S. J. Brodsky, C.-R. Ji, *Exclusive Production of Higher-Generation Hadrons and Form-Factor Zeros in Quantum Chromodynamics*, Phys. Rev. Lett. **55**, 2257 (1985).

[123] S. J. Brodsky and J. R. Hiller, *Universal properties of the electromagnetic interactions of spin-one systems*, Phys. Rev. D **46**, 2141 (1992).

[124] A. P. Kobushkin and A. I. Syamtomov, *High-Q^2 elastic ed scattering and QCD predictions*, Phys. Rev. D **49**, 1637 (1994).

[125] A. P. Kobushkin and A. I. Syamtomov, *Deuteron electromagnetic form-factors in the transitional region between nucleon-meson and quark-gluon pictures*, Phys. Atom. Nucl. **58**, 1477 (1995).

[126] J. P. B. C. de Melo, Chueng-Ryong Ji, T. Frederico, *The ρ-meson time-like form factors in sub-leading pQCD*, Phys. Lett. B **763**, 87 (2016).

[127] C.-R.Ji and Y. Tokunaga, *Light-front dynamic analysis of bound states in a scalar field model*, Phys. Rev. D **86**, 054011 (2012).

[128] C. Itzykson and J.-B. Zuber, *Quantum field theory*, (Dover Publications, NY, 1980).

[129] C.-R. Ji, *Interpolation Between the Instant Form and the Front Form of Relativistic Dynamics*, Few Body Syst. **58**, 42 (2017).

[130] C. Gutierrez, V. Gigante, T. Frederico, G. Salmè, M. Viviani, L. Tomio, *Bethe–Salpeter bound-state structure in Minkowski space*, Phys. Lett. B **759**, 131 (2016).

[131] D. S. Hwang and V. A. Karmanov, *Many-body Fock sectors in Wick-Cutkosky model*, Nucl. Phys. B **696**, 413 (2004).

[132] J. Carbonell and V. A. Karmanov, *Transition electromagnetic form factor and current conservation in the Bethe-Salpeter approach*, Phys. Rev. D **91**, 076010 (2015).

[133] G.'t Hooft, *A planar diagram theory for strong interactions* Nucl. Phys. B **72**, 461 (1974).

[134] G.'t Hooft, *A two-dimensional model for mesons* Nucl. Phys. B **75**, 461 (1974).

[135] K. Hornbostel, S. J. Brodsky and H.-C. Pauli, *Light-cone-quantized QCD in 1+1 dimensions*, Phys. Rev. D **41**, 3814 (1990).

[136] P. Cvitanović, *Group theory for Feynman diagrams in non-Abelian gauge theories*, Phys. Rev. D **14**, 1536 (1976).

[137] G. Baym, *Inconsistency of Cubic Boson-Boson Interactions*, Phys. Rev. **117**, 886 (1960).

[138] T. Frederico, *Null-plane model of three bosons with zero-range interaction*, Phys. Lett. B **282**, 409 (1992).

[139] J. Carbonell, V. A. Karmanov, *Three-boson relativistic bound states with zero-range interaction*, Phys. Rev. **C 67**, 037001 (2003).

[140] V. A. Karmanov and P. Maris, *Manifestation of three-body forces in three-body Bethe-Salpeter and light-front equations*, Few-Body Syst., **46**, 95 (2009).

[141] L. H. Thomas, *The Interaction Between a Neutron and a Proton and the Structure of H^3*, Phys. Rev. **47**, 903 (1935).

[142] T. Frederico, A. Delfino, L. Tomio and M. T. Yamashita, *Universal aspects of light halo nuclei*, Prog. Part. Nucl. Phys. **67**, 939 (2012).

[143] V. Efimov, *Energy levels arising from resonant two-body forces in a three-body system*, Phys. Lett. B **33**, 563 (1970); *Qualitative treatment of three-nucleon properties*, Nucl. Phys. A **362**, 45 (1981).

[144] E. Ydrefors, J. H. Alvarenga Nogueira, V. A. Karmanov, and T. Frederico, in preparation (2019).

[145] E. F. Suisso, J. P. B. C. de Melo, and T. Frederico, *Relativistic dynamics of Qqq systems*, Phys. Rev. D **65**, 094009 (2002).

[146] D. B. Kaplan, J.-W. Lee, D. T. Son, M. A. Stephanov, *Conformality lost*, Phys. Rev. D **80**, 125005 (2009).

[147] M. Margin-Brinet, J. Carbonell, V. A. Karmanov, *Stability of bound states in the light-front Yukawa model*, Phys. Rev. D **64**, 027701 (2001); *Relativistic bound states in the Yukawa model*, Phys. Rev. D **64**, 125005 (2001).

[148] J. H. Alvarenga Nogueira, T. Frederico, E. Pace, G. Salmè and E. Ydrefors, in preparation (2019).

[149] J. H. Alvarenga Nogueira and T. Frederico, notes on *The fermion-boson BSE in the ultraviolet region* (2019).

[150] T. Frederico, W. de Paula, A. Delfino, M. T. Yamashita, L. Tomio, *Four-boson continuous scale symmetry breaking*, Few body Syst. **60**, 46 (2019).

[151] C. Shi, I. C. Cloët, *Intrinsic Transverse Motion of the Pion's Valence Quarks*, Phys. Rev. Lett. **122**, 082301 (2019).

[152] J. Dudek *et al.*, *Physics opportunities with the 12 GeV upgrade at Jefferson Lab*, Eur. Phys. J. A **48**, 187 (2012).

[153] C. Adolph *et al.* (COMPASS), *Hadron transverse momentum distributions in muon deep inelastic scattering at 160 GeV/c*, Eur. Phys. J. **8**, 2531 (2013) [Erratum: Eur. Phys. J. C 75(2), 94 (2015)].

[154] A. Accardi and A. Bacchetta, *Accessing the nucleon transverse structure in inclusive deep inelastic scattering*, Phys. Lett. B **773**, 632 (2017).

[155] S. R. Beane, W. Detmold, K. Orginos, M. J. Savage, *Nuclear Physics from Lattice QCD*, Prog. Part. Nucl. Phys. **66**, 1 (2011).

[156] I. C. Cloët, C. D. Roberts, *Explanation and Prediction of Observables using Continuum Strong QCD*, Prog. Part. Nucl. Phys. **77**,1 (2014).

[157] I. C. Cloët, L. Chang, C. D. Roberts, S. M. Schmidt, and P. C. Tandy, *Pion Distribution Amplitude from Lattice QCD*, Phys. Rev. Lett. **111**, 092001 (2013); L. Chang, I. C. Cloët, C. D. Roberts, S. M. Schmidt, and P. C. Tandy, *Pion Electromagnetic Form Factor at Spacelike Momenta*, Phys. Rev. Lett. **111**, 141802 (2013).

[158] P. Lowdon, *Conditions on the violation of the cluster decomposition property in QCD*, J. Math. Phys. **57**, 102302 (2016); *Non-perturbative constraints on the quark and ghost propagators*, Nucl. Phys. B **935**, 242 (2018) 242; *Dyson–Schwinger equation constraints on the gluon propagator in BRST quantised QCD*, Phys. Lett. B **786**, 399 (2018).

[159] J. H. O. Sales, T. Frederico, B. V. Carlson and P. U. Sauer, *Light front Bethe-Salpeter equation*, Phys. Rev. C **61**, 044003 (2000); J. H. O. Sales, T. Frederico, B. V. Carlson and P. U. Sauer, *Renormalization of the ladder light front Bethe-Salpeter equation in the Yukawa model*, Phys. Rev. C **63**, 064003 (2001).

[160] J. P. Vary *et al.*, *Hamiltonian light-front field theory in a basis function approach*, Phys. Rev. C **81**, 035205 (2010); J. P. Vary, L. Adhikari, G. Chen, Y. Li, P. Maris and X. Zhao, *Basis Light-Front Quantization: Recent Progress and Future Prospects*, Few Body Syst. **57**, 695 (2016); J. P. Vary *et al.*, *Trends and Progress in Nuclear and Hadron Physics: a straight or winding road*, Few Body Syst. **58**, 56 (2017).

[161] F. Gross, *Three-Dimensional Covariant Integral Equations for Low-Energy Systems*, Phys. Rev. **186**, 1448 (1969); F. Gross, *Relativistic few-body problem. I. Two-body equations*, Phys. Rev. C **26**, 2203 (1982); C. Savkli, F. Gross, *Quark - anti-quark bound states in the relativistic spectator formalism*, Phys. Rev. C **63**, 035208 (2001); F. Gross, *The CST: Its Achievements and Its Connection to the Light Cone*, Few Body Syst. **58**, 39 (2017).

[162] W. Broniowski, S. Prelovsek, L. Santelj, E. Ruiz Arriola, *Pion wave function from lattice QCD vs. chiral quark models*, Phys. Lett. B **686**, 313 (2010).

[163] W. de Paula, J. H. Alvarenga Nogueira, E. Ydrefors, C. Mezrag, H. Moutarde, G. Salmè and T. Frederico, in preparation (2019).

[164] O. Oliveira, P. Bicudo, *Running gluon mass from a Landau gauge lattice QCD propagator*, J. Phys. G **38**, 045003 (2011); A. G. Duarte, O. Oliveira, and P. J. Silva, *Lattice gluon and ghost propagators and the strong coupling in pure SU(3) Yang-Mills theory: Finite lattice spacing and volume effects*, Phys. Rev. D **94**, 014502 (2016).

[165] T. M. Yan, *Quantum Field Theories in the Infinite-Momentum Frame. IV. Scattering Matrix of Vector and Dirac Fields and Perturbation Theory*, Phys. Rev. D **7**, 1780 (1973).

[166] J. P. B. C. de Melo, J. H. O. Sales, T. Frederico, P. U. Sauer, *Pairs in the light-front and covariance*, Nuc. Phys. A **631** (1998) 574; J. P. B. C. de Melo, T. Frederico, *Light-Front projection of spin-1 electromagnetic current and zero-modes*, Phys. Lett. B **708**, 87 (2012).

[167] W. de Paula, J. H. Alvarenga Nogueira, E. Ydrefors, G. Salmè and T. Frederico, in preparation (2019).

[168] J. A. O. Marinho, T. Frederico, E. Pace, G. Salme and P. Sauer, *Light-front Ward-Takahashi Identity for Two-Fermion Systems*, Phys. Rev. D **77**, 116010 (2008).

[169] M. B. Parappilly *et al.*, *Scaling behavior of the quark propagator in full QCD*, Phys. Rev. D **73**, 054504 (2006).

[170] A. Deur, S.J. Brodsky, G.F. de Teramond, *The QCD Running Coupling*, Prog. Part. Nucl. Phys. **90**, 1 (2016).

[171] M. Diehl, *Generalized Parton Distributions*, Phys. Rep. **388**, 41 (2003).

[172] T. Frederico, E. Pace, B. Pasquini and G. Salmè, *Pion generalized parton distributions with covariant and light-front constituent quark models*, Phys. Rev. D **80**, 054021 (2009).

[173] C. Fanelli, E. Pace, G. Romanelli, G. Salmè, M. Salmistraro, *Pion generalized parton distributions within a fully covariant constituent quark model*, Eur. Phys. J. C **76**, 253 (2016).

[174] Clayton S. Mello, J.P.B.C. de Melo, T. Frederico, *Minkowski space pion model inspired by lattice QCD running quark mass*, Phys. Lett. B **766**, 86 (2017).

[175] N. Chouika, C. Mezrag, H. Moutarde, J. Rodríguez-Quintero, *A Nakanishi-based model illustrating the covariant extension of the pion GPD overlap representation and its ambiguities*, Phys.Lett. B **780**, 287 (2018).

[176] N. Chouika, *Distributions de Parton Généralisées et extension covariante: vers une tomographie du nucléon*, PhD thesis, IRFU, SPhN, Saclay (2018).

[177] C. Mezrag, H. Moutarde, J. Rodriguez-Quintero, *From Bethe–Salpeter Wave functions to Generalised Parton Distributions*, Few-Body Syst. **57**, 729 (2016).

[178] R. Baldini *et al.*, *Nucleon time-like form factors below the $N\bar{N}$ threshold*, Eur. Phys. J. C **11**, 709 (1999); Nucl. Phys. A **666** & **667** 3 (2000).

[179] F. Gross, *Relativistic Quantum Mechanics and Field Theory* (Wiley, 1999).

[180] T. Frederico, D. C. Duarte, W. de Paula, E. Ydrefors, S. Jia, P. Maris, *Towards Minkowski space solutions of Dyson-Schwinger Equations through un-Wick rotation*, arXiv:1905.00703 (2019).

[181] V. Sauli, J. Adam and P. Bicudo, *Dynamical chiral symmetry breaking with Minkowski space integral representations*, Phys. Rev. D **75**, 087701 (2007).

[182] P. Estabrooks, R. K. Carnegie, A. D. Martin, W. M. Dunwoodie, T. A. Lasinski, D. W. G. S. Leith, *Study of $K\pi$ scattering using the reactions $K^- + p \to K^- + \pi^+ n$ and $K^- + p \to K^- + \pi^- \Delta^{++}$ at 13 GeV/c*, Nucl. Phys. B **133**, 490 (1978).

[183] J. Carbonell, V. A. Karmanov, *Solutions of the Bethe–Salpeter Equation in Minkowski Space and Applications to Electromagnetic Form Factors*, Few-Body Syst. **49** (2011) 205.

[184] G. V. Skornyakov and K. A. Ter-Martirosyan, *Three body problem for short range forces. I. Scattering of low energy neutrons by deuterons*, Sov. Phys. JETP **4**, 648 (1957).

[185] E. Ydrefors, J. H. Alvarenga Nogueira, T. Frederico and V. Karmanov, notes on *Solving the three-body BSE with the NIR* (2019).

[186] E. Ydrefors and J. H. Alvarenga Nogueira, notes on *Solving the fermion-antifermion Bethe-Salpeter equation* (2018).